T2K off-axis near detector ν_μ flux measurement and absolute momentum scale calibration of the off-axis near detector tracker

Flor de María BLASZCZYK

Institut de Recherche sur les lois Fondamentales de l'Univers (IRFU)

Université Paris 7 Denis Diderot

A thesis submitted for the degree of

DOCTEUR EN SCIENCES,
Spécialité:
Physique des Particules

Defended on September 20th 2011

Defense committee:
Thomas PATZAK (président du jury)
Marcos DRACOS (rapporteur)
Hirohisa TANAKA (rapporteur)
Gérard SAJOT
Cristina VOLPE
Sandrine EMERY (directrice)

Résumé

Dans cette thèse les résultats de la mesure du spectre en énergie des neutrino muoniques auprès du détecteur proche hors-axe de T2K et la calibration de l'échelle en impulsion absolue du trajectographe du détecteur proche sont présentés. Nous rappelons d'abord l'histoire et l'état des connaissances actuelles sur la physique du neutrino. Nous donnons aussi le cadre théorique requis à la compréhension des analyses présentées, en particulier le paramétrage des oscillations de neutrino et les modèles d'interaction neutrino-matière. Nous présentons ensuite T2K, une expérience hors-axe à longue ligne de base au Japon, qui envoie un faisceau de neutrinos muoniques depuis J-PARC vers Super-Kamiokande, avec un détecteur proche situé à 280m du site de production des neutrinos. Les objectifs principaux sont la mesure de l'angle theta13 et la mesure précise des paramètres dits atmosphériques. Nous décrivons les différents détecteurs, en particulier le trajectographe du détecteur proche et ses performances. Les outils requis pour les analyses, comme les techniques de reconstruction et de sélection de l'échantillon d'interactions courant chargé pour effectuer la mesure des flux énergétiques, sont expliqués. L'objectif principal de cette thèse, la mesure du spectre énergétique des neutrinos muoniques, est ensuite détaillé, en présentant les motivations de la mesure, les résultats obtenus avec le premier échantillon de données de T2K et les différentes erreurs systématiques étudiées. Finalement, nous présentons la calibration de l'échelle en impulsion absolue du trajectographe du détecteur proche obtenue par la reconstruction de la masse invariante des kaons neutres.

Abstract

In this thesis we present the results from the ν_μ energy spectrum measurement at T2K's near detector and T2K's near detector tracker absolute momentum scale calibration. First we review the main historical steps and the current state of the art of neutrino physics as well as the theoretical framework required to understand the thesis physics analyses presented later on. In particular we focus on the neutrino oscillation parametrization and the neutrino-matter interaction models. We then describe T2K, an off-axis long baseline neutrino oscillation experiment in Japan which consists of a muon neutrino beam sent from J-PARC to Super-Kamiokande, with a magnetized near detector located at 280m from the neutrino production site. T2K's main goals are measuring the last unknown angle of the PMNS matrix θ_{13} through the search of ν_e appearance in the ν_μ beam and measuring precisely the atmospheric parameters through muon neutrino disappearance. We briefly describe the detectors, in particular the near detector tracker and its performance. We then present the analyses tools, such as the reconstruction techniques used and how the neutrino charged current interaction events needed for the energy spectrum measurement are selected. The main goal of the thesis, the muon neutrino energy spectrum measurement done with the first T2K data is explained next. We give the motivations for such measurement, the results obtained with the first T2K data sample, and the different systematic errors studied. Finally, the absolute momentum scale calibration of T2K's near detector tractor, done through the reconstruction of the neutral kaon invariant mass, is explained.

Contents

Introduction

Produced naturally in the Sun, in supernovae, in the Earth or artificially in beams or nuclear reactors, neutrinos are one of the biggest subjects of interest in modern physics. First studied to understand their peculiar proprieties, neutrinos and in particular neutrino oscillations have turned out to be a crucial tool to survey physics beyond the Standard Model. Indeed, in the Standard Model they are massless particles, but the existence of the oscillation phenomenon which violates the lepton number conservation proves they are massive. Nevertheless, it is not yet understood how their masses are generated and most of the theoretical models that describe it predict the existence of particles beyond the Standard Model such as heavy right-handed neutrinos. Should we measure a non-zero complex phase in their mixing matrix, neutrinos would then violate the CP symmetry and consequently could be the first step towards the understanding of the matter-antimatter asymmetry observed in the Universe, through the leptogenesis mechanism. Despite the great progress in neutrino physics these last 20 years, many of their proprieties are not understood. For example, whether neutrinos are their own antiparticle or not - the Majorana vs Dirac nature debate - or whether sterile neutrinos exist, implying there are the more than three neutrino families.

Neutrino physics are of great interest also in astrophysics, cosmology and even nuclear physics. They can be considered as messengers from the core of various cosmic sources, like the Sun or exploding Supernovae, thus carrying unique information on the processes that have occurred far away in the Galaxy. As for nuclear physics, the study of the double beta neutrinoless decay that is the best experimental way to test the neutrino nature is of great interest since it is a forbidden process within the Standard Model.

The T2K experiment aims to measure the last unknown mixing angle θ_{13}, leaving the door open to explore the CP-violation in the leptonic sector should the complex phase of the mixing matrix δ be different from zero. The second main goal is to measure with great precision the

oscillation parameters Δm^2_{32} and θ_{23}, also called the atmospheric oscillation parameters. The θ_{13} angle will be measured through the appearance of ν_e in a ν_μ beam, whereas the atmospheric parameters will be measured through the ν_μ disappearance. To do these measurements, T2K sends an off-axis ν_μ beam produced with the new proton accelerator facility J-PARC in Tokai to the well-known water Čerenkov detector Super-Kamiokande, 295 km away. The unoscillated beam is characterized by an off-axis near detector, located at 280 m from the neutrino beam production point. This magnetized near detector is made of various detector types. In this thesis, I will focus on the description of the near detector's tracker, which is optimized to study charged current interactions, since both of my analyses are based on the data taken by the tracker.

To be able to accomplish T2K physics goals, it is important to understand the different sources of systematic errors. It is within this context that this thesis is presented. Both oscillation measurements, through ν_μ disappearance which depends on the ratio of the oscillated and unoscillated neutrino energy spectra, and through ν_e appearance, are sensitive to both the absolute momentum scale and the neutrino muon flux before oscillation. From the measured momentum of the particles in the tracker, it is possible to compute the neutrino energy. Thus the absolute momentum scale has a direct impact on the unoscillated spectrum. The shape of the spectrum must be well defined as well, therefore the unoscillated neutrino muon flux must be measured as precisely as possible.

The first chapter of this thesis begins with the history of neutrino physics, from their discovery to the current state of the art, with an explanation of the oscillation mechanism, the generation of their masses, and CP-violation. In the second chapter, we will focus on the neutrino -nucleus interactions which are fundamental to understanding how neutrinos are detected and understand how the cross-sections of the different interaction types are computed. The third chapter will describe the T2K experiment goals, layout, beam production and the various detectors. The fourth chapter will focus on the off-axis near detector tracker, which is made of three time projection chambers and two fined grained detectors, since the analyses use mainly the information provided by these detectors. This will take us to the fifth chapter, where the tools and selection cuts used for the neutrino muon flux measurement will be presented, as well as the validation of the selection tools. In the sixth chapter we will move on to the flux measurement analysis, including the description of the systematic errors. Finally, the absolute momentum scale calibration of the near detector tracker will be presented.

Chapter 1

Neutrino physics

Neutrinos are the lightest elementary fermions discovered up to now. They are produced by many different natural sources such as the Sun, the Earth's nuclear background radiation, the cosmic ray interactions with the atmosphere, or supernovae. Since they are neutral and colorless, they can only interact through the weak interaction thus are difficult to detect. There are three different neutrino families or flavors, associated respectively to the electron, the muon and the tau leptons in charged current weak interactions. Although the first neutrino models stated that neutrinos were massless, these theories were proved to be inaccurate when neutrino oscillations were observed, since oscillations imply massive neutrinos.

Up to now, only the differences of the squared masses have been measured (through neutrino oscillations) since measuring their individual masses is proving to be a real challenge. The strictest upper limit on neutrino masses has been set by cosmology, where the sum of neutrino masses varies between 0.2 and 1 eV/c^2 depending on the model used [1, 2]. Although there has been great progress on the neutrino physics field in the last decades, neutrino physicists have yet to understand many of the neutrino proprieties. For instance, what the true nature of the neutrino is, whether neutrinos are their own antiparticle (Majorana neutrinos) or not (Dirac neutrinos).

The first part of this chapter will focus on the main neutrino history stages. The second part will describe the oscillations mechanism in vacuum with a two-flavor mixing and three flavor approach as well as the matter effects. The third part will briefly discuss the neutrino nature and neutrino mass related issues. In the fourth part we will address the possibility of

CP violation in the neutrino mixing matrix, which is a key point to understanding one of the major unanswered questions today: the baryon asymmetry in the Universe. Finally the last part of this chapter will deal with the state of the art of neutrino oscillation parameters and future neutrino experiments.

1.1 Neutrino history

In this section we will review the main events that marked neutrino physics history. To begin with we will see how the hypothesis of the neutrino particle was born, and how it was discovered almost thirty years later (Sec. 1.1.1). We will then move on to the discovery of the neutrino oscillation phenomenon (Sec. 1.1.2), which solved the solar neutrino problem and that proved that neutrinos had a mass, as opposed to what the Standard Model stated. Since then, neutrino oscillations have proved to be a very useful tool, not only to understand neutrino proprieties but also to probe the Standard Model and look for new physics.

1.1.1 The origin and discovery of the neutrinos

During the late 20s, scientists studying β-decays described the process as a two-body decay, where a nucleus X decayed via ${}^{A}_{Z}X \rightarrow {}^{A}_{Z+1}X' + e^{-}$. Nevertheless, the measured electron energy spectrum was continuous instead of being a monoenergetic spectrum as expected for a two-body decay (Fig. 1.1). Physicists were facing then either an energy conservation violation or new physics. In 1930, W. Pauli postulated in his well-known letter beginning with 'Dear radioactive ladies and gentlemen' that β-decays were actually a three-body decay, where the third body, that he called "neutron", was a very light neutral fermion which carried part of the energy but could hardly be detected [3]. In 1934 E. Fermi in his β-decay theory renamed Pauli's hypothetical particle into neutrino, meaning in Italian the 'small neutral one' [4] because the neutron, as we know it today and which is a completely different particle, had been discovered by J. Chadwick [5] shortly after Pauli had made his hypothesis.

A few years later, in 1936, E. Majorana suggested that the neutrino could be its own antiparticle [6], opposed to the Dirac model where particles are different from their antiparticles. This is a question that has yet to be answered, even though many years have passed since then.

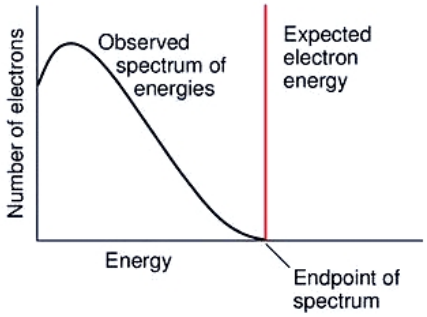

Figure 1.1: The expected and observed electron spectrum for a single β-decay.

It is only in 1956 that F. Reines and C. Cowan proved the neutrino's existence [7]. They detected the $\overline{\nu_e}$ produced by the Savannah River reactor (South Carolina, USA) using a detector filled with water and cadmium chloride through the $\overline{\nu_e} + p \rightarrow e^+ + n$ reaction.

In 1962, a neutrino that did not behave in the same way as the neutrino produced in the β-decays was discovered while studying pion decays at the Brookhaven National Laboratory [8]. This neutrino was the ν_μ associated to the muon, whereas the previously discovered neutrino was a ν_e, associated to the electron. The third generation neutrino ν_τ was discovered much later, in the year 2001 by the DONUT experiment at Fermilab [9].

The current Standard Model (SM) [10, 11, 12] requires three neutrino flavors, ν_e, ν_μ, and ν_τ. The LEP experiments [13] proved by measuring the invisible width of the Z^0 boson that there were only three neutrino flavors that coupled with the Z^0. These neutrinos are described as massless neutral and colorless (color is the strong interaction charge) elementary particles , which implies that neutrinos interact only through weak interaction. Together with the charged leptons, they form the weak interaction doublets. This is the current elementary fermion table:

Leptons		Quarks	
e^-	ν_e	u	d
μ^-	ν_μ	c	s
τ^-	ν_τ	t	b

Table 1.1: The electro-weak doublets and quark doublets.

Neutrinos are therefore produced and detected through weak interaction, i.e. they couple with the $W^{\pm}$ bosons (charged current interactions) or with the Z^0 boson (neutral current interactions). The most commonly used channel to detect them at energies of the order of the GeV is the charged current quasi-elastic channel $\nu_l + n \rightarrow l^- + p$, where the outgoing lepton corresponds to the incoming neutrino flavor. T2K, which focus on the searches for ν_μ disappearance and ν_e appearance, will use this process. A more detailed explanation of the neutrino interactions with matter will be given in section 1.2.2 and chapter 2.

1.1.2 The discovery of neutrino oscillations

A great deal of evidence for neutrino oscillations has been collected from many sources, over a wide range of neutrino energies and with many different detector technologies. It all started with the solar neutrinos problem, when the number of neutrinos observed did not match the number of neutrinos expected. As we will see later on in sections 1.2 and 1.4, neutrino oscillations play a key role in the search for new physics, in particular they hint there could be CP violation in the leptonic sector, which would be a first step towards the understanding of the baryonic asymmetry observed in the Universe.

We will first focus on the solar neutrino problem and the birth of the neutrino oscillation hypothesis. We will then present the first experimental proof of neutrino oscillations with atmospheric neutrinos, by Super-Kamiokande.

1.1.2.1 The solar neutrino deficit

In the late 1960s, the chlorine-based Homestake Experiment, led by R. Davis Jr. and J.N. Bahcall, was the first to measure the flux of solar neutrinos [14] through inverse β-decay. The measured flux showed a deficit with respect to the expected number of solar neutrinos. The fusion reactions that take place in the Sun produce only ν_e (Fig. 1.2). As it was understood then, the average solar ν_e flux expected on Earth was 10^8 $\nu_e/\text{s/m}^2$. Nevertheless only one third of the expected neutrinos were detected. This could mean only two things, either neutrinos had some unexpected properties or the solar model was not well understood. The figure 1.3 shows the Standard Solar Model neutrino energy spectra.

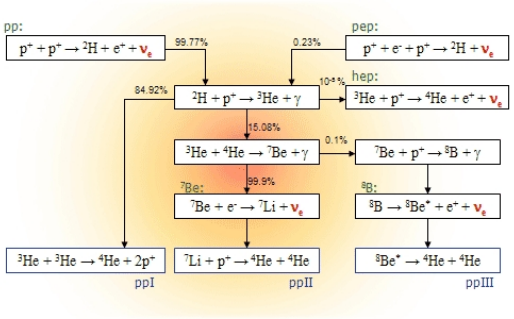

Figure 1.2: The Sun nuclear reactions chain leading to neutrino production.

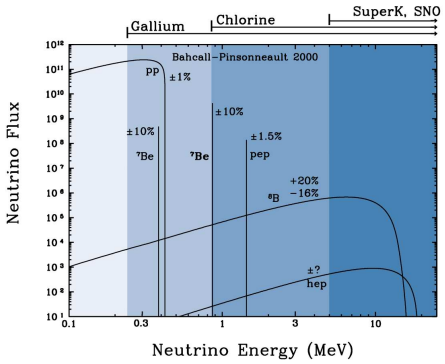

Figure 1.3: The Standard Solar Model neutrino fluxes and energy range sensibility for different experiments.

A few years prior to the Homestake experiment, B. Pontecorvo suggested the idea of neutrino oscillations, where a neutrino could oscillate into an antineutrino and vice-versa, in analogy with the $K^0 - \overline{K^0}$ system [15]. One year after the solar neutrino deficit was observed, V. Gribov and B. Pontecorvo published in 1969 their famous paper where they described in detail the neutrino oscillation mechanism [16]. In the meantime, when the ν_μ was discovered, Z. Maki, M. Nakagawa, and S. Sakata introduced an oscillation mechanism, similar to the one Pontecorvo had suggested, but between different neutrino flavors [17]. This mechanism will be detailed in the 1.2 section.

The solar neutrino deficit was confirmed by several other radiochemical and water Čerenkov detectors which were sensitive to different energy ranges (Fig. 1.3) and thus able to observe neutrinos from different stages of the Sun nuclear reaction chain, including GALLEX [18], Sage [19], GNO [20], Kamiokande [21] and Super-Kamiokande [22]. These detectors, which used only charged current interactions to detect the neutrinos, had only one possible explanation left: the ν_e had transformed into something that could not be detected by such detectors (muons and taus have a mass which is beyond the solar neutrino energy scale thus charged current interactions are not possible).

The oscillation hypothesis remained controversial until 2002, when the Sudbury Neutrino Observatory experiment (SNO)[23] measured the total neutrino flux and observed that it did

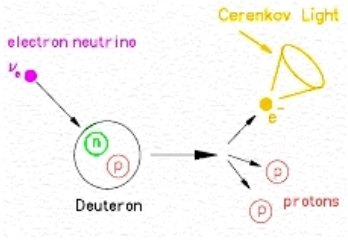

Figure 1.4: Charged current reaction used by SNO to detect ν_e.

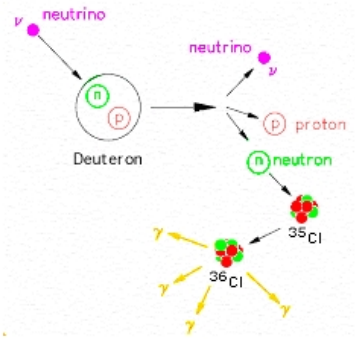

Figure 1.5: Neutral current reaction used by SNO to measure the total solar neutrino flux.

not have only a ν_e component, but had also a ν_μ and a ν_τ components. The SNO detector used heavy water (deuterium) which allowed the detection of neutrinos through charged current (Fig. 1.4) - measurement of the ν_e component - but also through neutral current (Fig. 1.5). The neutral current reactions break apart the deuterium, liberating a neutron that would later be captured by another nucleus (producing detectable light). Since the neutral current process is equally sensitive to all three neutrino types, the total neutrino flux could be measured. The total neutrino flux measured was conserved and in agreement with the expected numbers.

Precise measurements of the solar neutrino oscillation parameters were obtained by combining the SNO results and those of KamLAND [24], a neutrino experiment that studied the $\overline{\nu_e}$ produced by 16 nuclear reactors in Japan as well as the solar ν_e disappearance. Although both experiments used very different techniques, the results were in very good agreement as it can be seen in section 1.5.

1.1.2.2 The atmospheric neutrino puzzle

Cosmic rays, which are mostly high energy protons, are another main source of neutrinos. They arrive on the Earth's upper atmosphere and interact with it, producing a large amount of secondary particles. Most of these secondary particles are pions which decay via $\pi^\pm \rightarrow \mu^\pm + \nu_\mu(\overline{\nu_\mu})$. These muons decay in turn through $\mu^\pm \rightarrow e^\pm + \nu_e(\overline{\nu_e}) + \overline{\nu}_\mu(\nu_\mu)$ thus leading to an expected neutrino flux that on average has twice as many ν_μ as ν_e. Since these neutrinos are produced all over the atmosphere (Fig. 1.6), experiments aiming to detect them have to be

able to determine the direction of the incident neutrino.

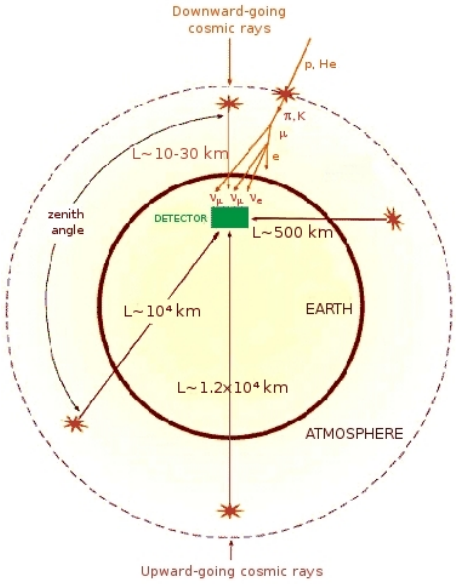

Figure 1.6: Different flight distances between the cosmic ray interaction point and the detector.

In the 80s, the Kamiokande and the IMB [25] experiments, both based on large water Čerenkov detectors put forward a problem with the atmospheric neutrinos. The measured ratio between the upward and downward going ν_μ was different from the expected value. It is only in 1998 that Super-Kamiokande (SK) proved the atmospheric neutrinos oscillation [26]. More precisely, SK studied the dependence of the ν_μ and ν_e spectra on the zenith angle. A deficit in the ν_μ flux coming from the nadir with respect to the expected value for the no-oscillation hypothesis was observed, while the ν_e flux coming from the same direction remained on average the expected unoscillated one (Fig. 1.7). Therefore the ν_μ disappearance was not due to an interaction with the Earth's matter otherwise a similar deficit or excess would have been observed on the ν_e flux. The only explanation left was that ν_μ had mainly oscillated into a neutrino type which was not the electron one, possibly ν_τ (although the sterile neutrino hypothesis was not discarded). It was the first solid evidence of neutrino oscillations, and it proved simultaneously that neutrinos were massive since oscillations cannot occur in a massless neutrino framework as we will see in the next section. These results along with those obtained by SNO solved the solar neutrino problem as well. Years later, K2K[27] and OPERA[28], which directly observed

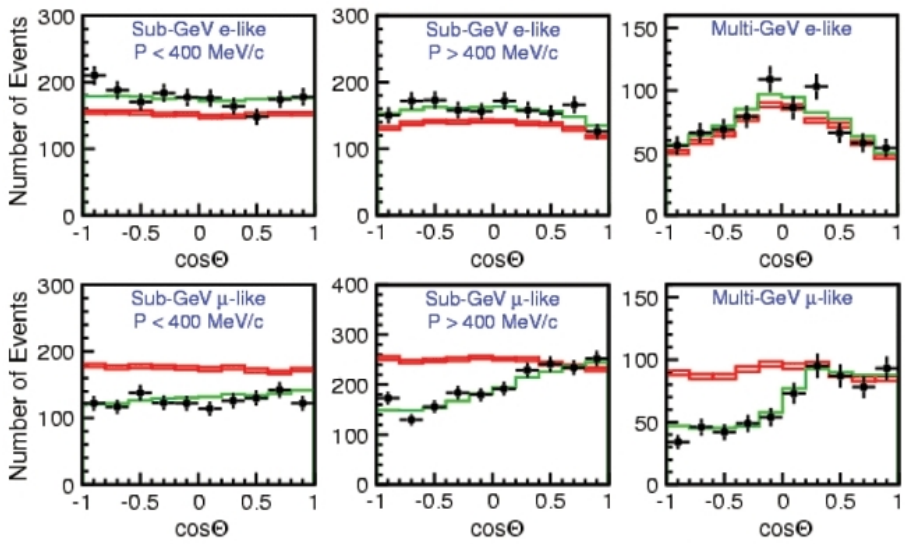

Figure 1.7: Super-Kamiokande atmospheric neutrino spectra as a function of the zenith angle θ. The top row shows the electron-like events and the bottom row the muon-like events. The energy range increases from left to right. Green histograms (resp. red) are the expected number of events for the oscillation (resp. no oscillation) hypothesis and the dots are the data from SK.

the ν_τ appearance, confirmed that the atmospheric ν_μ oscillated into ν_τ (Sec. 1.5).

1.2 Oscillations mechanism

Neutrinos are produced and detected by weak interaction in a given flavor eigenstate (ν_e, ν_μ, or ν_τ). The neutrino mass eigenstates (propagation eigenstates named ν_1, ν_2, and ν_3) are different from the flavor eigenstates (interaction eigenstates), thus leading to a 'mixing' process i.e. the latter are a linear combination of the mass eigenstates. While propagating in vacuum or in matter, the mixing evolves since each mass eigenstate has its own phase. This causes a phase difference between the mass eigenstates after an elapsed time, that might eventually lead to the detection of a differently flavored neutrino than the one that was initially produced. This flavor changing process is known as 'neutrino oscillation' and it violates the flavor conservation.

The oscillation phenomenon is a crucial tool to study neutrino properties. So far it is the field that has rewarded us with the most results. The most important result, other than the constraint of the oscillation parameters, is that they are the only experimental evidence that neutri-

nos have a mass different from zero – through the constraint of the squared masses difference – and that the lepton numbers are not conserved. The next most awaited result is whether there is CP violation in the leptonic sector or not. If there is, it will be a key point to understand the origin of the baryonic asymmetry in the universe (Sec. 1.4). We will see in chapter 3 that the T2K experiment is a first step towards the understanding of this asymmetry and that the results presented in this thesis will be useful for the different measurements.

Nevertheless, neutrino oscillations are not sensitive to the nature of the neutrinos (Dirac or Majorana) and are only sensitive to the squared-mass difference. Thus, they cannot be used to directly measure the neutrino masses or determine the neutrino nature.

Section 1.2.1 will detail oscillations in vacuum, with both a two-flavor approximation and three-flavor mixing. Section 1.2.2 will briefly describe the matter induced effects on the oscillations.

In the following sections, the mass eigenstates propagation will be simply described with plane wave solutions. A full wave packet treatment can be found in the literature [29, 30][31]. The Greek indexes will refer to the flavor eigenstates whereas the Latin ones will describe the mass eigenstates. All the following equations will be expressed in natural units ($\hbar = c = 1$).

1.2.1 Vacuum oscillations

In this section we will describe the theory of the oscillation mechanism when neutrinos propagate in vacuum, first with a two-flavor approach and then with the three flavor mixing.

1.2.1.1 Two flavor mixing

As a first approach, let us consider a simple case with only two flavor eigenstates, ν_α and ν_β, and two mass eigenstates ν_1 and ν_2.

If the initial state $|\nu_i(0)\rangle$ at the time $t = 0$ was a propagation eigenstate, then the propagation could be simply described by the time-dependent Schrödinger equation

$$|\nu_i(\vec{r}, t)\rangle = e^{-i(E_i t - \vec{p_i} \cdot \vec{r})} |\nu_i(0)\rangle \tag{1.1}$$

where:

- t is the elapsed time from the start of the propagation ;
- E_i is the energy of the mass eigenstate i ;
- $\overrightarrow{p_i}$ is the 3-dimensional momentum of the mass eigenstate i ;
- $\overrightarrow{r}$ is the current position of the particle relative to its starting position.

Neutrinos propagation eigenstates (in vacuum or matter) are the mass eigenstates, whereas flavor eigenstates are a linear combination of the mass eigenstates given by a simple unitary - the total number of neutrinos must be conserved - mixing matrix M:

$$\begin{pmatrix} \nu_\alpha \\ \nu_\beta \end{pmatrix} = M \begin{pmatrix} \nu_1 \\ \nu_2 \end{pmatrix} = \begin{pmatrix} \cos\theta & \sin\theta \\ -\sin\theta & \cos\theta \end{pmatrix} \begin{pmatrix} \nu_1 \\ \nu_2 \end{pmatrix} \tag{1.2}$$

where there is only one mixing angle θ. Using this relationship between flavor and mass eigenstates and the equation 1.1, one obtains the following:

$$\begin{pmatrix} |\nu_\alpha(\vec{r},t)\rangle \\ |\nu_\beta(\vec{r},t)\rangle \end{pmatrix} = M \cdot \begin{pmatrix} e^{-i(E_1 t - \vec{p_1}\cdot\vec{r})} & 0 \\ 0 & e^{-i(E_2 t - \vec{p_2}\cdot\vec{r})} \end{pmatrix} \cdot M^{-1} \begin{pmatrix} |\nu_\alpha(0)\rangle \\ |\nu_\beta(0)\rangle \end{pmatrix} \tag{1.3}$$

If at $t = 0$ there was $|\nu_\alpha(0)\rangle = 1$ and $|\nu_\beta(0)\rangle = 0$ then the probability for the ν_α to have oscillated into a ν_β is:

$$\begin{aligned} P(\nu_\alpha \to \nu_\beta; \vec{r}, t) &= |\langle \nu_\alpha(0) | \nu_\beta(\vec{r},t)\rangle|^2 \\ &= 4\sin^2\theta\cos^2\theta\sin^2\frac{(E_1 t - \vec{p_1}\cdot\vec{r}) - (E_2 t - \vec{p_2}\cdot\vec{r})}{2} \\ &= \sin^2(2\theta)\sin^2\frac{(\phi_2 - \phi_1)}{2} \end{aligned} \tag{1.4}$$

with $\phi_i = E_i t - p_i r$. We consider that the propagation is along a given axis, and by choosing that axis as the reference axis, we can reduce the three-dimensional equation to a single dimension propagation (space-wise). The following approximations can be made to simplify the oscillation probability formula:

- Neutrinos are highly relativistic: their momentum is typically of the order of a few keV or MeV whilst their masses m_i are below the eV according to the cosmological limits [1, 2]:

$$m_i \ll p_i \Rightarrow m_i \ll E_i \Rightarrow p_i = \sqrt{E_i^2 - m_i^2} \simeq E_i\left(1 - \frac{m_i^2}{2E_i^2}\right) \tag{1.5}$$

- The only eigenstates that can interfere with each other are the ones having the same energy [29, 30] therefore $E_1 = E_2 = E$
- ϕ_i depends on both the propagation time t and the propagation distance $|\vec{r}| = L$. According to B. Kayser [31], we can consider that $t \simeq L$ for all defined mass eigenstates.

Therefore:

$$\begin{aligned}\phi_i &= E_i t - p_i L \\ &= E_i t - E_i L \left(1 - \frac{m_i^2}{2E_i^2}\right) \\ &= E_i(t - L) + \frac{m_i^2 L}{2E_i} \\ &\simeq \frac{m_i^2 L}{2E_i}\end{aligned} \tag{1.6}$$

Finally, we can write the oscillation probability:

$$P(\nu_\alpha \to \nu_\beta; L, E) = \sin^2(2\theta)\sin^2(\frac{(m_1^2 - m_2^2)L}{4E}) = \sin^2(2\theta)\sin^2(\frac{\Delta m^2}{4}\frac{L}{E}) \tag{1.7}$$

where $\Delta m^2 = m_1^2 - m_2^2$. As we can see on equation 1.7, if an oscillation is observed either through ν_α disappearance – the measured number of ν_α is smaller than the initial amount of ν_α – or through ν_β appearance, then Δm^2 is necessarily different from zero. Consequently, at least one of the mass eigenstates has a mass different from zero thus meaning neutrinos are massive.

Neutrino oscillation experiments aim to measure the squared masses difference Δm^2 and the mixing angle θ. Since the probability depends only on two experimental parameters, the initial neutrino energy E and the propagation distance L, the experiments will choose the appropriate L (and eventually E if a neutrino beam is used) to observe a maximal oscillation. T2K which uses a ν_μ beam of 600 MeV chose a baseline of 295 km to measure a maximal $\nu_\mu \to \nu_e$ oscillation. More details will be given in chapter 3.

1.2.1.2 Three flavor mixing

Let us consider now the real case with three neutrino flavors. Once again, the total number of neutrinos must be conserved so the connection between the mass eigenstates to the flavor

eigenstates is given by the unitary matrix V:

$$\begin{pmatrix} \nu_e \\ \nu_\mu \\ \nu_\tau \end{pmatrix} = \begin{pmatrix} V_{e1} & V_{e2} & V_{e3} \\ V_{\mu 1} & V_{\mu 2} & V_{\mu 3} \\ V_{\tau 1} & V_{\tau 2} & V_{\tau 3} \end{pmatrix} \begin{pmatrix} \nu_1 \\ \nu_2 \\ \nu_3 \end{pmatrix} \text{ where } V^\dagger V = 1$$

V can be broken down into two matrices as follows:

$$V = U_{PMNS} A_M$$

where

$$A_M = \begin{pmatrix} e^{i\alpha} & 0 & 0 \\ 0 & e^{i\beta} & 0 \\ 0 & 0 & 1 \end{pmatrix}$$

is the Majorana phases matrix, phases that do not have any impact on the oscillation probabilities and U_{PMNS} is the Pontecorvo-Maki-Nakagawa-Sakata matrix (also called the PMNS or MNS matrix)[17]. The Majorana matrix is considered only if neutrino are Majorana particles (Sec. 1.3). The PMNS matrix, which is similar to the Cabibbo-Kobayashi-Maskawa matrix (CKM matrix) in the quark sector [32, 33], can be parametrized with three mixing angles and one complex phase as follows:

$$U_{PMNS} = \begin{pmatrix} 1 & 0 & 0 \\ 0 & c_{23} & s_{23} \\ 0 & -s_{23} & c_{23} \end{pmatrix} \begin{pmatrix} c_{13} & 0 & s_{13}e^{-i\delta} \\ 0 & 1 & 0 \\ -s_{13}e^{i\delta} & 0 & c_{13} \end{pmatrix} \begin{pmatrix} c_{12} & s_{12} & 0 \\ -s_{12} & c_{12} & 0 \\ 0 & 0 & 1 \end{pmatrix} \quad (1.8)$$

with $c_{ij} = \cos\theta_{ij}$, $s_{ij} = \sin\theta_{ij}$ and δ the CP violation phase in the leptonic sector. Measuring the δ phase, which requires first the measurement of θ_{13}, plays a key role in the search of the origin of the baryonic asymmetry in the Universe. More details can be found in section 1.4.

By computing the probabilities in a similar way as described in the previous section, we obtain that the oscillation probability for a flavor eigenstate α to oscillate into a flavor eigenstate β is given by

$$\begin{aligned} P(\nu_\alpha \to \nu_\beta; L, E) = \delta_{\alpha\beta} &- 4\sum_{i>j} \Re(U^*_{\alpha i} U_{\beta i} U_{\alpha j} U^*_{\beta j}) \sin^2[1.27\Delta m^2_{ij}(L/E)] \\ &+ 2\sum_{i>j} \Im(U^*_{\alpha i} U_{\beta i} U_{\alpha j} U^*_{\beta j}) \sin[2.54\Delta m^2_{ij}(L/E)] \end{aligned} \quad (1.9)$$

with Δm^2_{ij} expressed in eV^2, the propagation or oscillation length L expressed in km, and the initial neutrino energy E in GeV (including the previously omitted factors $\hbar$ and c).

Most of the PMNS matrix parameters have been measured, except for the mixing angle θ_{13} and the CP-violation phase δ. T2K's main goal is measuring θ_{13} through the search for ν_e appearance in a ν_μ beam. Assuming that $\Delta m^2_{32} \sim \Delta m^2_{31}$ (Sec.1.5), the probability of ν_e appearance from a ν_μ beam is

$$\begin{aligned} P(\nu_\mu \to \nu_e) = & \sin^2(\theta_{23}) \sin^2(2\theta_{13}) sin^2(1.27\Delta m^2_{32} L/E_\nu) \\ & + \cos^2(\theta_{23}) \sin^2(2\theta_{13}) \sin^2(1.27\Delta m^2_{21} L/E_\nu) \\ & - J \sin(\delta) \sin(1.27\Delta m^2_{32} L/E_\nu) \\ & + J \cos(\delta) \cos(1.27\Delta m^2_{32} L/E_\nu) \end{aligned} \tag{1.10}$$

where

$$J = \cos(\theta_{13}) \sin(2\theta_{12}) \sin(2\theta_{13}) \sin(2\theta_{23}) \sin(1.27\Delta m^2_{32} L/E_\nu) \sin(1.27\Delta m^2_{21} L/E_\nu)$$

Furthermore, if we assume that $\delta = 0$ and if we neglect matter effects (Sec.1.2.2) then the oscillation probabilities can be simplified into

$$P(\nu_\mu \to \nu_e) = \sin^2(2\theta_{13}) \sin^2(\theta_{23}) \sin^2\left(1.27\Delta m^2_{13} \frac{L}{E_\nu}\right) \tag{1.11}$$

$$P(\nu_\mu \to \nu_\mu) = 1 - \cos^4(\theta_{13}) \sin^2(2\theta_{23}) \sin^2\left(1.27\Delta m^2_{32} \frac{L}{E_\nu}\right) \tag{1.12}$$

Although the exact value of θ_{13} is not yet known, the existing upper limit on it shows that the angle is smaller than 11°(Sec.1.5). Therefore, the central matrix in equation 1.8 is often replaced by the identity matrix when looking for the solar neutrino oscillations (dominated by θ_{12} and Δm^2_{21}) or the atmospheric neutrino oscillations (ruled by θ_{23} and Δm^2_{32}). By applying this approximation on equations 1.11 and 1.12, we obtain that $P(\nu_\mu \to \nu_e) \simeq 0$ and

$$\begin{aligned} P(\nu_\mu \to \nu_\mu) &= 1 - \sin^2(2\theta_{23}) \sin^2\left(1.27\Delta m^2_{32} \frac{L}{E_\nu}\right) \\ &= 1 - P_{2flavors}(\nu_\mu \to \nu_\tau) \end{aligned} \tag{1.13}$$

where $P_{2flavors}(\nu_\mu \to \nu_\tau)$ is similar to the oscillation probability computed considering only two neutrino flavors, ν_μ and ν_τ. As we can see, the two-flavor approach is not just a simplification, it actually is a good approximation of the three-flavor mixing when we consider the real values of the parameters. This approximation has been often used in the solar and reactor neutrino experiments (SNO, KamLAND), as well as in the atmospheric neutrino or long baseline experiments.

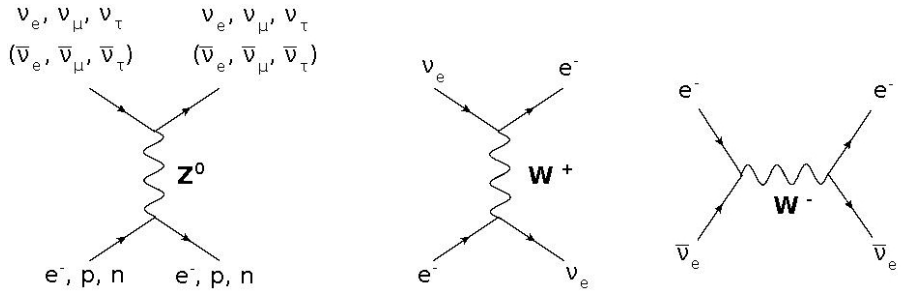

Figure 1.8: Neutral current scattering (left) and charged current scattering (middle and right) Feynman diagrams at tree level for all neutrino and antineutrino flavors.

1.2.2 Oscillations in matter

Until now, we made the approximation that neutrinos propagated in vacuum. In fact, neutrinos propagate in environments that have variable matter density profiles, such as the Earth, the Sun or supernovae. The matter-neutrino scattering, which can be either through charged current or neutral current, can be interpreted as potentials that depend on the neutrino flavor. Such perturbations have an effect on the mixing of neutrino flavor eigenstates, which can lead to a resonant enhancement of the mixing angle and thus increase the oscillation probability even if the vacuum mixing angle is small. This matter effect is commonly known as the Mikheyev-Smirnov-Wolfenstein effect (MSW)[34, 35].

Neutral current scattering terms on electrons, protons, and neutrons have the same amplitude for all neutrino and antineutrino flavors, whereas there is only one charged current scattering diagram that does not violate the lepton number conservation and that has a neutrino in the final state (Fig.1.8, right-hand side). This diagram generates an additional term that has to be taken into account for electron neutrinos exclusively since ordinary matter has only one leptonic flavor. If the matter is electrically neutral and distributed in a random way, then the potentials for the charged current scattering V_{CC} and neutral current scattering V_{NC} can be written as a function of the electron density ρ_e, the neutron density ρ_n, and the Fermi constant G_F:

$$V_{CC} = \sqrt{2} G_F \rho_e \text{ and } V_{NC} = -\frac{1}{\sqrt{2}} G_F \rho_n. \tag{1.14}$$

The neutral current contribution depends only on the neutron density since the proton and electron contributions cancel.

These contributions have to be added to the propagation Hamiltonian. Let us consider once again a two-flavor mixing, ν_e and ν_X (where ν_X is a linear combination of ν_μ and ν_τ), with one mixing angle in vacuum θ_v, one squared mass splitting Δm^2 and two mass eigenstates, ν_1 and ν_2. The Hamiltonian that takes into account the matter-induced potentials is the sum of the vacuum Hamiltonian and the matter effect terms:

$$H = \frac{\Delta m^2}{4E} \begin{pmatrix} -\cos 2\theta_v & \sin 2\theta_v \\ \sin 2\theta_v & \cos 2\theta_v \end{pmatrix} + V_{CC} \begin{pmatrix} 1 & 0 \\ 0 & 0 \end{pmatrix} + V_{NC} \bullet \mathrm{Id} \tag{1.15}$$

The neutral current contribution is the same for all flavor eigenstates i.e. the contribution matrix is proportional to the identity matrix. It can be demonstrated such terms do not modify the oscillation probability if only active neutrino flavors exist, thus we will neglect the neutral current term.

New mass eigenstates, ν_1' and ν_2', can be written as a function of a new mixing angle θ_m and a new squared mass splitting Δm_m^2 that include matter effects, thus different from θ_v, and the flavor eigenstates ν_e and ν_X:

$$\begin{pmatrix} \nu_1' \\ \nu_2' \end{pmatrix} = \begin{pmatrix} \cos\theta_m & \sin\theta_m \\ -\sin\theta_m & \cos\theta_m \end{pmatrix} \begin{pmatrix} \nu_e \\ \nu_X \end{pmatrix} \tag{1.16}$$

We can deduce from equations 1.15 and 1.16 an expression for θ_m and Δm_m^2:

$$\sin^2(2\theta_m) = \frac{\sin^2(2\theta_v)}{\sin^2(2\theta_v) + (\cos(2\theta_v) - R)^2} \tag{1.17}$$

and

$$\Delta m_m^2 = \Delta m_v^2 \sqrt{\sin^2(2\theta_v) + (\cos(2\theta_v) - R)^2} \tag{1.18}$$

where R is an dimensionless ratio and can be written as

$$R = \frac{2\sqrt{2} G_F \rho_e E_\nu}{\Delta m_v^2} \tag{1.19}$$

Remarks:

- There is a case where the oscillation is resonant, thus leading to a maximal mixing. The critical electron density ρ_e^R at which the resonance happens is:

$$\rho_e^R = \frac{\Delta m^2 \cos 2\theta_v}{2\sqrt{2} G_F E} \Leftrightarrow \theta_m = \frac{\pi}{4} \tag{1.20}$$

For a given density ρ_e, the maximum oscillation will happen when the neutrino energy is:

$$E_R = \frac{\Delta m^2 \cos 2\theta_v}{2\sqrt{2} G_F \rho_e} \tag{1.21}$$

The existence of such resonance depends on whether neutrinos or antineutrinos are being detected, and on the sign of the mass splitting. Consequently, experiments sensitive to matter effects are useful to determine the neutrino mass hierarchy (Sec.1.3.3).

- If ρ_e is uniform along the neutrino path, the oscillation probability is similar to the equation 1.7 with θ_m instead of θ_v and Δm^2_m instead of Δm^2_v:

$$P(\nu_e \to \nu_X; L, E) = \sin^2(2\theta_m) \sin^2(\frac{\Delta m^2_m}{4} \frac{L}{E}) \tag{1.22}$$

Matter effects only modify the propagation of the ν_e, so they might have an impact on the search for ν_e appearance. For T2K, the neutrino propagation distance is 295 km, the neutrino energy range is $\sim$0.25 - 2 GeV, and the electron density can be considered as constant along the baseline – the neutrino beam is fairly close to the Earth's surface – with an average value of $\sim$3.2 g/cm^3. The ratio R defined in equation 1.19 is therefore of the order of 10 %. Given the small number of expected ν_e at T2K's far detector Super-Kamiokande (Sec.3.1.2), the contribution from matter effects in the T2K ν_e appearance analysis is small with respect to the expected statistical error. This is not the case for longer baseline experiments such as MINOS or NOνA, where the matter effects are approximately three times more important.

In the solar neutrino case, the electron density profile changes along the neutrino path, modifying simultaneously the effective mass, and leading to a mixing of the effective mass eigenstates as well as the flavor eigenstates. This problem can hardly be solved analytically, which means experiments are fundamental to understand the mechanism. For further details, refer to [36] and [37].

1.3 Neutrino mass and nature

Although it does not concern the work presented in this thesis, the neutrino nature, i.e. whether it is its own particle or not, and the smallness of the neutrino masses are questions that have yet to be answered so we will briefly discuss the status on these matters. Both subjects are closely

linked together, since the most widely accepted theoretical frame which explains the neutrino mass generation – the see-saw mechanism – requires a sterile right handed heavy neutrino, which is part of the Majorana neutrino framework.

The Standard Model (SM) requires three neutrino families that together with their respective charged leptons form the weak interaction doublets. Neutrinos are described in this framework as massless colorless neutral particles, thus interacting only through weak interaction. If there were more than three neutrinos, the extra neutrinos would not have a charged lepton partner and consequently would not couple to the W bosons. Moreover, measurements of the Z^0 boson invisible width at the LEP showed that there are only three neutrino families lighter than the Z^0 boson [13]. Nevertheless, the existence of heavier neutrinos that would not have any Standard Model weak coupling is not excluded yet. These neutrinos referred to as "sterile" neutrinos are required by most theories to explain the neutrino mass.

In section 1.3.1 we will define what Majorana and Dirac fields are, to introduce the neutrino mass terms in the Lagrangian and briefly explain the see-saw mechanism. Section 1.3.2 will present an experimental technique to test the neutrino nature. Finally, section 1.3.3 will review the current status on the direct neutrino mass measurement.

1.3.1 Neutrino mass terms in the Lagrangian

There are several approaches to build a fermion field $\psi = \psi_L + \psi_R$, where the left-handed and right-handed chiral components are defined by $\psi_L = \frac{1-\gamma_5}{2}\psi$ and $\psi_R = \frac{1+\gamma_5}{2}\psi$. We will focus on two:

- a Dirac field, where ψ_L and ψ_R are independent ;
- a Majorana field, where ψ_L and ψ_R are linked by the charge conjugation symmetry C, implying that the particle is its own antiparticle i.e.

$$C\psi_L = \psi_L^C = \pm\psi_R \text{ and } C\psi_R = \psi_R^C = \pm\psi_L \tag{1.23}$$

The usual mass term (referred to as the Dirac mass term) for a field ψ is given by

$$\mathcal{L}_m = m_D\overline{\psi}\psi = m_D(\overline{\psi}_L\psi_R + \overline{\psi}_R\psi_L) \tag{1.24}$$

where m_D is the Dirac masses matrix, which conserves the leptonic number but not the chirality. However, in the Standard Model (SM), each lepton generation is described by an $SU(2)$ doublet and a singlet

$$\psi_L = \begin{pmatrix} \nu_l \\ l \end{pmatrix}_L ; l_R \text{ where } l = e, \mu, \tau. \tag{1.25}$$

Since the ψ_L doublet cannot be contracted with the singlet to yield a numerical result, the terms in the equation 1.24 cannot exist in the SM Lagrangian. By introducing the SM Higgs doublet $\phi = (\phi^+, \phi^0)$, which allows fermion masses to be generated through interactions with the Higgs vacuum expectation value (vev), it is possible to write a mass term for the charged leptons

$$m_D \bar{l} l = m_D(\bar{l}_L l_R + \bar{l}_R l_L) \tag{1.26}$$

A similar mass term can be written for neutrinos if a right-handed neutrino N_R is introduced to the SM, although such neutrinos have never been observed yet.

It is also possible to build Lorentz invariant scalars for the Majorana fields with a similar $-m\overline{\psi}\psi$ structure, directly coupling the left-handed neutrino to the right-handed antineutrino and vice versa:

$$\begin{aligned} \mathcal{L}^L &= \frac{m_L}{2}\left(\overline{\psi}_L \psi_R^C + \overline{\psi}_R^C \psi_L\right) \\ \mathcal{L}^R &= \frac{m_R}{2}\left(\overline{\psi}_R \psi_L^C + \overline{\psi}_L^C \psi_R\right) \end{aligned} \tag{1.27}$$

where m_L and m_R are the left and right mass states, called Majorana mass matrices, which conserve chirality but violate lepton number conservation by two units. By adding the equation 1.27 to 1.24, we can rewrite the full mass term as follows:

$$L_m = -\frac{1}{2}\begin{pmatrix} \overline{\psi}_L^C & \overline{\psi}_R \end{pmatrix} M \begin{pmatrix} \psi_L \\ \psi_R^C \end{pmatrix} - \frac{1}{2}\begin{pmatrix} \overline{\psi}_L & \overline{\psi}_R^C \end{pmatrix} M \begin{pmatrix} \psi_L^C \\ \psi_R \end{pmatrix} \tag{1.28}$$

with

$$M = \begin{pmatrix} m_L & m_D \\ m_D & m_R \end{pmatrix} \tag{1.29}$$

The mass matrix defined in equation 1.29 can be broken down into:

- the Dirac mass m_D, which requires a right-handed (sterile since the number of active neutrino flavors is constrained to three) neutrino N_R to be coupled with a $SU(2)_L$ doublet and the Higgs doublet C-conjugate : $h_D(\overline{\nu_L}\overline{l_L})\phi^C N_R$ where h_D is the Yukawa coupling constant ;

- the left Majorana mass m_L , which couples left-handed fields only. This coupling can be done only if a Higgs triplet is introduced, which implies the existence of a Goldstone boson called Majoron. Nevertheless, this boson was excluded by the LEP measurements. It is also possible to generate m_L with the standard Higgs doublet but this leads to a non-renormalizable interaction. This is why this term is very often set to zero, even when considering a right Majorana term ;
- the right Majorana mass m_R, which couples right-handed fields only. This requires the introduction of a neutral Higgs singlet and a right-handed neutrino N_R. By adding a Higgs singlet, we add also a Goldstone boson that is not coupled to the Z^0 and thus hasn't been excluded by any measure yet.

The most common model to explain neutrinos small masses in a natural way is the 'see-saw' mechanism [38]. In this model $m_L = 0$ for the reasons mentioned above, m_D is of the order of the Standard Model elementary particles masses (a few MeV - GeV), and $m_R \gg m_D$. If we consider only one neutrino flavor, after diagonalizing the M matrix we obtain two mass eigenstates $m_{heavy} \sim m_R$ and $m_{light} \sim m_D^2/m_R$ that are mixed with a mixing angle $\theta \sim -m_D/m_R$. The heavy mass corresponds to the right-handed sterile neutrino singlet N_R and the light mass corresponds to the standard left-handed neutrino ν_l. Since the sterile neutrino mass is expected to be comparable to the grand unification scale (10^{16} GeV) and thus at an energy scale far beyond the explored energy ranges up to now, its existence has yet to be proved.

1.3.2 Neutrinoless double beta decay

The most promising test of the Majorana versus Dirac nature of the neutrino is the neutrinoless double-beta decay $\beta\beta0\nu$ (Fig.1.9), i.e., the detection of the decay of a nucleus, with charge Z and A nucleons through

$$(Z, A) \rightarrow (Z + 2, A) + 2e^- \tag{1.30}$$

This process violates the lepton number conservation by two units and is therefore forbidden in the Standard Model. If neutrinos are Majorana particles then this process is not forbidden. Two experiments searching for the $\beta\beta0\nu$ process but who have not observed it yet, have provided limits on the effective electron neutrino – because neutrino flavor eigenstates are not mass eigenstates – Majorana mass:

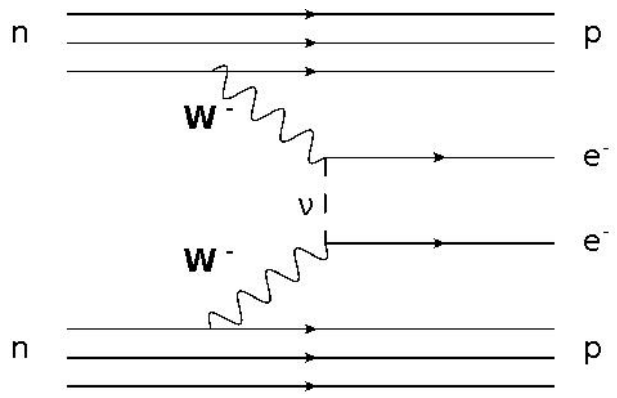

Figure 1.9: Neutrinoless double β-decay Feynman diagram at tree level.

- NEMO3 [39], whose limit depends on the model used to compute the nuclear matrix elements

$$\langle m_{\nu_e} \rangle < 0.7 - 2.8 \text{ eV}/c^2 \text{ ;}$$

- Heidelberg-Moscow [40] whose limit considers a 50% error on the nuclear matrix elements

$$\langle m_{\nu_e} \rangle < 0.35 \text{ eV}/c^2 \text{ (90\% C.L.).}$$

Currently several other experiments are or will also be searching for the $\beta\beta0\nu$ such as CUORE [41], GERDA [42], EXO [43], and NEMO3/SUPER-NEMO [39].

1.3.3 Direct neutrino mass measurement and mass hierarchy

The most stringent limit on the sum of neutrino masses is given today by cosmology

$$\sum_i m_i < 0.2 - 1 \text{ eV}/c^2.$$

This limit, which is model dependent, is obtained through the analysis of the Cosmic Microwave Background (CMB) anisotropies and the power spectrum of the large universe structures density fluctuations[1, 2].

Direct measurements of the neutrino masses have been attempted by several experiments, the main results being

- $m(\nu_e) < 2.5 - 2.8 \text{ eV}/c^2$ (@ 95 % C.L.), measured by the Mainz [44] and Troitsk [45] tritium β-decay experiments ;

- $m(\nu_\mu) < 0.17\ \mathrm{MeV}/c^2$ (@ 90 % C.L.), measured by a pion decay experiment at the Paul Scherrer institute [46] ;

- $m(\nu_\tau) < 18.2\ \mathrm{MeV}/c^2$ (@ 95 % C.L.), measured by ALEPH [47]).

The KATRIN [48] experiment in Germany, inspired of the Mainz and Troistk experiments, is under construction and will measure or at least improve the limit on the effective mass of the $\overline{\nu}_e$ with sub-eV precision by examining the spectrum of electrons emitted from the tritium β-decays.

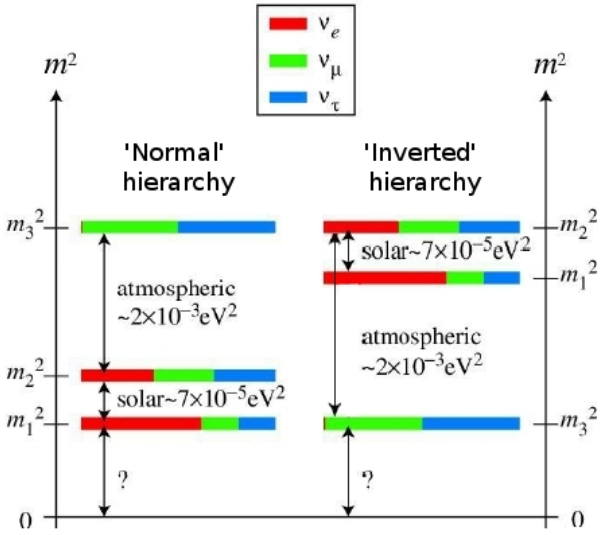

Figure 1.10: Three-neutrino squared-mass spectrum. The colors indicate the fraction of each neutrino flavor.

Another issue related to the neutrino mass is whether the mass hierarchy is normal or inverted (Fig.1.10). Only the sign of Δm^2_{21} (solar pair) is known, while the sign of Δm^2_{23} (atmospheric pair) has yet to be determined. Long baseline neutrino oscillation experiments should be able to discriminate its sign using the matter induced effects. Grand unified theories favor the 'normal' hierarchy where the solar pair is at the bottom since the neutrino spectrum would be then similar to the quark spectra. On the contrary, if the solar pair is at the top, it would suggest the existence of a new symmetry that would lead to the near degeneracy at the top of the spectrum [49].

1.4 CP violation and leptogenesis

Neutrino physics can be the key to understanding the baryon asymmetry of the Universe, in other words why we observe more matter than antimatter. This matter excess is described by the parameter η:

$$\eta = \frac{n_B - n_{\overline{B}}}{n_\gamma} = (6.21 \pm 0.16) \times 10^{-10} \tag{1.31}$$

where n_B (resp. $n_{\overline{B}}$) is the number of baryons (resp. antibaryons) in the Universe and n_γ is the number of photons. It is unlikely that this excess comes from initial conditions of the Universe's birth, with an asymmetric Big Bang between baryons and antibaryons, since it implies a strong fine tuning of the η parameter and an initial asymmetry of the order of 10^{-7}.

Another explanation to this, the baryogenesis, starts with a symmetric hot Big Bang and the baryon asymmetry is the result of a dynamical evolution. The baryogenesis is possible if three conditions, known as the Sakharov conditions [50], are fulfilled:

- the baryon number B is violated ;
- C and CP are violated, otherwise the baryons and antibaryon would be generated at the same rate ;
- $n_B = e^{-m/kT}$ and $n_{\overline{B}} = e^{-\overline{m}/kT}$ so if CPT is conserved, which imposes $m = \overline{m}$ (m being the baryon mass and $\overline{m}$ the antibaryon mass), there must be a departure from the thermal equilibrium along the history of the Universe, otherwise $n_B = n_{\overline{B}}$.

The first condition is fulfilled by a nonperturbative SM process known as the sphaleron, which converts three baryons into three antileptons and violates the lepton (L) and baryon (B) numbers by three units [51]. The SM conserves only the number B-L. This processes are no longer observed because of their small amplitude at the current temperatures, but they were not suppressed earlier in the Universe history, when the temperatures where higher.

As for the second condition, the only known source of CP violation is in the quark sector where the weak interactions violate C and CP via the Kobayashi-Maskawa mechanism (complex phase in the CKM matrix). This mechanism produces an asymmetry of 10^{-20}, which is 10 orders of magnitude below the observed value of η.

Finally, the departure from the thermal equilibrium occurs at the electroweak phase transition.

Since the second and third conditions are only fulfilled qualitatively but not quantitatively, leptonic CP violation could also contribute to the asymmetry development through the propagation of an asymmetry in the leptons to an asymmetry in the baryons via the sphaleron processes. This model is the leptogenesis theory [52] and requires neutrinos to be Majorana particles as well as the introduction of a heavy right-handed singlet neutrino N_R.

This heavy Majorana neutral lepton N_R predicted by the see-saw mechanism, required by the leptogenesis theory, and produced in the Big Bang can have decay modes that violate CP. These decays would lead to the inequality

$$\Gamma(N_R \to l^+ + ...) \neq \Gamma(N_R \to l^- + ...), \tag{1.32}$$

resulting in unequal numbers of l^+ and l^-. This asymmetry can be then propagated to the baryon through nonperturbative SM processes (sphalerons) and finally lead to the observed baryon asymmetry.

Let us explain how to test the CP violation in the leptonic sector with neutrino oscillations, which would support the leptogenesis hypothesis. If we assume that the CPT invariance holds, then the probability P for a antineutrino $\overline{\nu}_\alpha$ to oscillate into a $\overline{\nu}_\beta$ should be the same as the probability for a neutrino ν_β to oscillate into a ν_α:

$$P(\overline{\nu}_\alpha \to \overline{\nu}_\beta) = P(\nu_\beta \to \nu_\alpha)$$

From the probability expression given by the equation 1.9, we can write

$$P(\nu_\beta \to \nu_\alpha; U_{PMNS}) = P(\nu_\alpha \to \nu_\beta; U^*_{PMNS})$$

where U_{PMNS} is the PMNS matrix given in the equation 1.8. Thus if CPT is not violated,

$$P(\overline{\nu}_\alpha \to \overline{\nu}_\beta; U) = P(\nu_\alpha \to \nu_\beta; U^*) \tag{1.33}$$

In other words, the antineutrino oscillation probability is the same as that for a neutrino, except that the mixing matrix U_{PMNS} has to be replaced by its complex conjugate. Therefore, if

U_{PMNS} is not real i.e. $\delta \neq 0$, the neutrino and antineutrino oscillation probabilities differ as long as θ_{13} is also not naught. This would prove there is CP violation in the leptonic sector. But the difference between the oscillation probabilities does not depend on whether neutrinos are Dirac or Majorana particles, since the Majorana phases disappear when computing the oscillation amplitude. Depending on the θ_{13} value and whether it is measurable or not, current or future experiments should be able to measure the CP violation phase δ. If T2K successfully measures the θ_{13} angle, its plans are to move on to a second phase to measure δ.

1.5 Neutrino oscillations state of the art

In this section I will first summarize the results obtained on the oscillation parameters i.e. θ_{ij} and Δm^2_{ji} as well as the experiments that provided the most precise measurements.

If there are only three mass eigenstates, ν_1, ν_2, and ν_3, the squared masses differences Δm^2_{ij} satisfy

$$\Delta m^2_{32} + \Delta m^2_{21} + \Delta m^2_{13} = 0. \tag{1.34}$$

thus Δm^2_{13} can be deduced if the sign of the other two squared masses difference is known.

1.5.1 Solar neutrino oscillation parameters

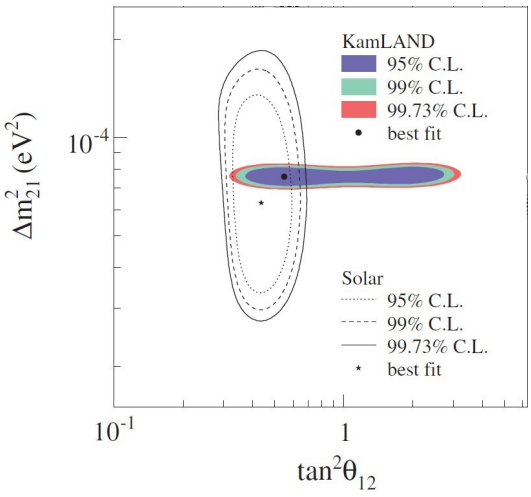

Figure 1.11: Allowed regions forΔm^2_{12} and $\tan^2\theta_{12}$. Combined results of KamLAND and solar neutrino experiments[53].

Solar neutrino oscillation experiments are sensitive to ν_e disappearance and allow the constraint of the parameters θ_{12} and Δm^2_{21}. The typical L/E for these oscillations is of the order of 10^5 km/GeV. The best fits were provided by the combination of the results of all solar neutrino experiments and KamLAND. Figure 1.11 shows that the solar experiments constrained mainly the θ_{12} angle while KamLAND had more precision on the Δm^2_{21} measurement, therefore both results complement each other and yield a precise measurement of both parameters.

$$\sin^2(2\theta_{12}) = 0.87 \pm 0.03 \text{ and } \Delta m^2_{21} = 7.59^{+0.19}_{-0.21} \times 10^{-5} \text{ eV}^2/c^4. \quad (1.35)$$

1.5.2 Atmospheric neutrino oscillation parameters

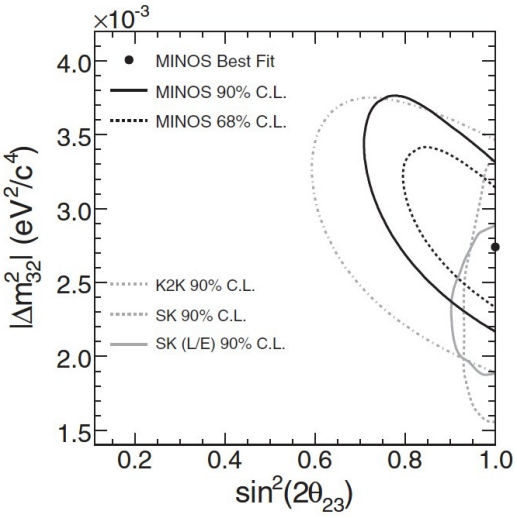

Figure 1.12: Allowed regions for Δm^2_{32} and $\sin^2 2\theta_{23}$ by SK, K2K and MINOS[54].

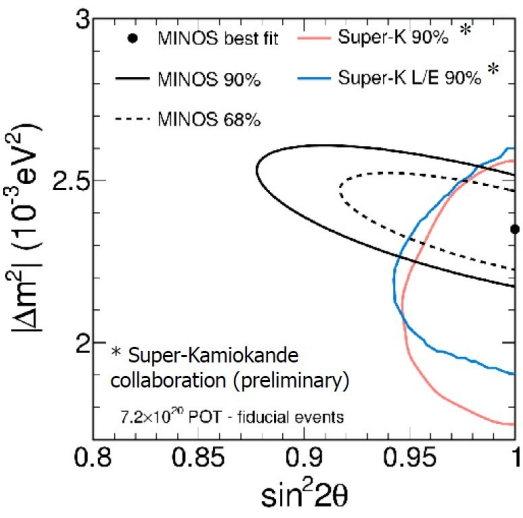

Figure 1.13: Latest preliminary results provided by MINOS and SK at the Neutrino 2010 Conference.

The atmospheric neutrino oscillations allow the constraint of the parameters θ_{23} and Δm^2_{32} since they are dominated by the $\nu_\mu \rightarrow \nu_\tau$ oscillation (Eq.1.13). Measurements are done through ν_μ disappearance. After SK confirmed the oscillation hypothesis in 1998, two long baseline experiments using artificial neutrino beams have also provided measurements for the above parameters :

- KEK to Kamioka (K2K) [27] in Japan, that used a ν_μ beam produced at KEK which was first analyzed by a water Čerenkov near detector at KEK and then by the far detector SK at 250 km ;

- MINOS [55] in the U.S.A., which uses the Fermilab's NuMi ν_μ beamline and two steel-scintillator sampling calorimeters as near and far detectors, with a baseline of 735 km. MINOS is currently running and has provided the most precise results on the atmospheric parameters.

The results of SK, K2K and MINOS can be seen in figures 1.12 and 1.13. The best fitted values for the combined results are

$$\sin^2 2\theta_{23} > 0.92 \text{ (@ 90 \% C.L.) and } |\Delta m^2_{32}| = 2.43 \pm 0.13 \times 10^{-3} \text{ eV}^2/c^4. \quad (1.36)$$

The sign of Δm^2_{32} has not been discriminated yet since it can only be measured if matter effects are observed.

All of the previously mentioned experiments only study the ν_μ disappearance. It was expected that most of these neutrinos oscillated into ν_τ, but the appearance of the latter had never been directly observed until OPERA [28], an emulsion based experiment which uses the CNGS beam in Italy, detected for the first time the appearance of a ν_τ from a ν_μ oscillation in 2010 (Fig.1.14) [56].

One of T2K's main goals is measuring with even greater precision the parameters Δm^2_{32} and θ_{23}. MINOS results were very useful to tune and optimize the T2K experiment on the search for ν_μ disappearance and ν_e appearance. More details on how T2K will measure these parameters will be given in section 3.1.3.

1.5.3 The θ_{13} search

The only mixing angle that has not been measured yet is θ_{13}. The most significant limit up to now has been given by CHOOZ [57], a short baseline reactor antineutrino experiment in France that used a liquid scintillator based detector at $\sim$ 1 km of the two nuclear reactors at Chooz and searched for $\overline{\nu}_e$ disappearance, whose probability does not depend on δ. No evidence of $\overline{\nu}_e$ disappearance was found, thus yielding the most stringent superior limit on $sin^2 2\theta_{13}$ for $\delta = 0$ until now (Fig.1.15)

$$\sin^2(2\theta_{13}) < 0.15 \text{ (@ 90 \% C.L.).} \quad (1.37)$$

Currently, three experiments are running and aim to measure or at least improve the existing limit on θ_{13}:

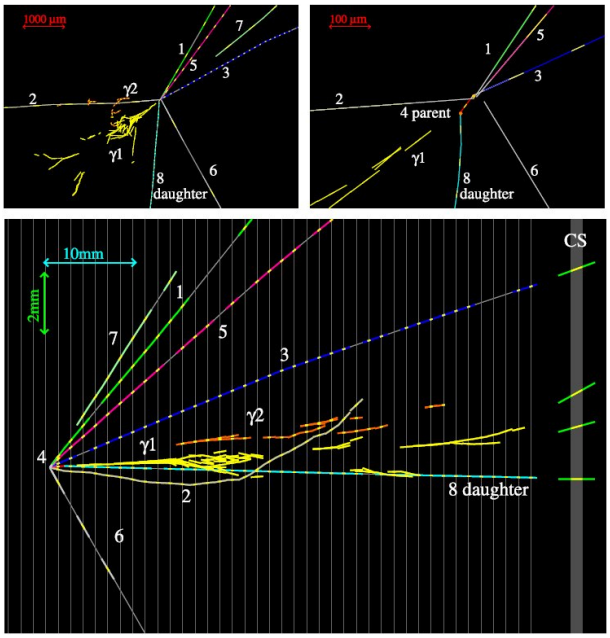

Figure 1.14: Event display of the OPERA τ^- candidate event, where track 4 would be the τ^- track and track 8 the kink daughter track. Top left: view transverse to the neutrino direction. Top right: same view zoomed on the vertices. Bottom: longitudinal view. [56]

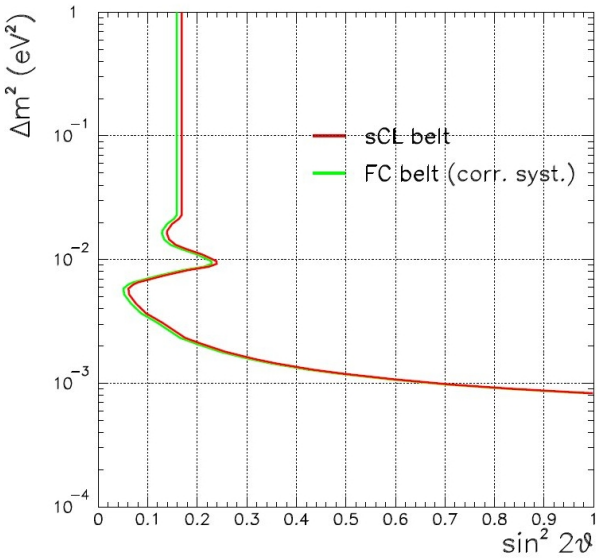

Figure 1.15: Exclusion plot at 90 % C.L. for the Chooz results [57].

- MINOS. Although it is not its main goal since it is an experiment optimized for the ν_μ disappearance search, MINOS can provide results on θ_{13} through the search of ν_e appearance in the ν_μ beam. So far the ν_e appearance has not been observed [58, 59] ;
- Double-Chooz [60]. Based on the same principle as its predecessor Chooz, Double Chooz will use two identical liquid scintillator detectors, one near the reactors and the other at $\sim$1 km to search for $\overline{\nu}_e$ disappearance to directly measure θ_{13}, without any correlation to the δ phase. So far the experiment is running only with its far detector, the near detector should start the data taking in 2012 ;
- T2K [61]. Using the new accelerator facility J-PARC at Tokai (Japan) to produce a ν_μ beam, T2K uses a near detector at 280 m from the proton target and SK as far detector at 295 km. One of T2K's main goals is measuring the angle θ_{13} through the search of ν_e appearance in a ν_μ beam, which also allows in a second stage to measure the δ phase. A detailed description of T2K will be given in chapter 3.

Since Double-Chooz can measure θ_{13} directly but not measure δ and T2K measures θ_{13} with a correlation to δ, both experiments are complementary.

1.6 Future neutrino projects

I will now give a brief overview of the future neutrino projects that aim to determine the still unknown oscillation parameters such as θ_{13} and the CP violation phase δ or to improve the precision on the already measured ones.

We will first focus on the near future reactor neutrino experiments which aim to measure θ_{13}. We will then present medium and long-term future detectors and enhanced neutrino beams.

1.6.1 Near future reactor experiments

Two short baseline experiments which search for reactor $\overline{\nu}_e$ disappearance to measure the mixing angle θ_{13}, similar to Double Chooz, are on their way: Daya Bay [62] in China and RENO [63] in Korea.

Daya Bay will study the $\overline{\nu}_e$ produced by six nuclear reactors (total thermal power of 11.6 GW) with six identical liquid scintillator detectors, divided into two near detectors close

to each of the two main blocks of reactors, and four far detectors at a distance of approximately 2 km from each block. The near detectors should start data taking during fall 2011 while the far detectors should be ready by fall 2012.

RENO will also study $\overline{\nu}_e$ produced by six nuclear reactors (total thermal power of 17.3 GW), and will have one near ($\sim$300 m) and one far ($\sim$1.5 km) gadolinium doped liquid scintillator detectors of $\sim$500 tons each. RENO is scheduled to start taking in spring 2011.

The expected sensitivities to θ_{13} for Daya-Bay and RENO are given in figure 1.16.

1.6.2 Medium and long-term neutrino projects

For improving the precision on the already measured oscillation parameters and to measure the unknown parameters with long baseline neutrino oscillation experiments, two types of improvements must be done: the neutrino beam production must be enhanced and detectors must be upgraded.

We will first describe which techniques are being investigated for neutrino beam production and then we will present the main mid-term and longer-term future detector projects.

1.6.2.1 Future neutrino beams

To be able to increase the current sensitivities and to answer the remaining questions about the neutrino proprieties, in particular measuring the CP-violation phase, the neutrino beam production must be enhanced. For this, the upgrade of the current neutrino beam production technique and two new techniques to produce intense neutrino beams for long or short baseline neutrino oscillation experiments are under development.

Currently only ν_μ ($\overline{\nu}_\mu$) beams are produced, by having a proton beam collide onto a target. The collision produces multiple secondary particles such as pions, which through their decay produce the neutrino beam. Although the energy of the secondary particles cannot be controlled, which leads to a large neutrino energy spectrum, pions can be focused to direct the beam towards the detectors and select whether the beam is a neutrino or antineutrino beam. Nevertheless, the neutrino beam is not 100 % pure in ν_μ since some secondary particle decays can produce ν_e and $\overline{\nu}_e$. Also, there can be a contamination from selected wrong sign pions,

which adds a $\overline{\nu}_\mu$ component to the beam. The most powerful ν_μ beam built is the T2K beam (peak $E_\nu \simeq 600$ MeV), which uses a 30 GeV proton beam with a nominal power of 750 kW. T2K beam power had reached a power of 150 kW before the 2011 Japan earthquake. Studies are underway to find how to improve this type of beam production, in particular to increase the beam power. This upgraded technique is called the superbeam technique.

The first new technique is the neutrino factories, which aim to produce intense neutrino beams coming from muon decays. Prior to decay, muons can be accumulated in storage rings and then accelerated. They will then decay via $\mu^- \rightarrow \nu_\mu + \overline{\nu}_e + e^-$ or $\mu^+ \rightarrow \overline{\nu}_\mu + \nu_e + e^+$ depending on the stored muon type. This method is optimized to search for $\nu_\mu \leftrightarrow \nu_e$ oscillations (resp. $\overline{\nu_\mu} \leftrightarrow \overline{\nu}_e$), through the detection of a 'wrong sign' muon. Indeed, if an initial ν_μ oscillates into a ν_e, the latter will be detected as an electron whereas the $\overline{\nu}_e$ produced along with the ν_μ are detected as positrons. For this, the use of a magnetized detector is required, to distinguish the charge of the muons. The possibility of studying both neutrinos and antineutrinos oscillations is optimal to measure the phase δ and study CP violation in the leptonic sector if $\delta \neq 0$. The energy of the beam, the baseline distance and the detector type are under investigation to obtain the maximum possible sensitivity.

The second new technique is the beta beams. The β radioactivity is a perfectly pure source of ν_e or $\overline{\nu}_e$ and it can be used to produce pure electron (anti)neutrino beams. The principle is based on the acceleration of an ionized β-decaying source, leading to a very focalized beam whose energy spectrum is well known. They are adapted to search for $\nu_e \rightarrow \nu_\mu$ or $\overline{\nu}_e \rightarrow \overline{\nu}_\mu$ oscillations through the detection of the outgoing muon, and they do not require a magnetized detector since the purity of the beam is 100 % thus there cannot be a wrong sign muon. As neutrino factories, beta beams can be used to study the CP violation. The energy of the neutrino beam depends of the energy at which the ions are accelerated, which ranges from 0.5 to 1 GeV/c. Nevertheless, beta beams pose a technological problem that resides in the production and storing of a large number of ions, which is necessary to have an intense neutrino beam. Possible technologies, detectors and baseline are under study.

1.6.2.2 Future detectors

Several projects are ongoing for future neutrino detectors all over the planet, for studying accelerator neutrinos with short or long baselines as well as reactor antineutrinos with working

principles similar to CHOOZ.

A mid-term future project in the United States is the long baseline neutrino oscillation experiment NOνA [64], which will replace the currently running experiment MINOS. Its main goals are to measure θ_{13} through the $\nu_\mu \rightarrow \nu_e$ oscillation, and to determine the mass hierarchy (sign of Δm^2_{32}) through the study of matter effects. It will use the existing NuMI beamline and new near and far detectors, with a baseline length of 810 km. Unlike MINOS which is an on-axis experiment – the detectors are at 0°with respect to the beam direction – NOνA will use an off-axis configuration (Sec.3.2.3), and a higher energy neutrino beam with a peak energy at the far detector of 5 GeV. The near and far detectors will be similar liquid scintillator based detectors (total mass of $\sim$15 kton for the far detector), to minimize systematic errors when extrapolating the measurements between them.

In Europe, the project that addresses the feasibility of a deep underground neutrino detector is LAGUNA [65]. The objective is to build a larger and more sensitive detector than the currently existing ones to study a large range of topics related to neutrino physics, including diffuse supernova neutrino background, galactic supernova bursts, solar and atmospheric neutrinos, reactor neutrinos, beta-beam neutrinos as well as to search for proton decays and dark matter. This project is in charge of choosing both the best site in Europe to build the infrastructure and the type of detector to be used. Three different detector designs are being considered:

- MEMPHYS, a water Čerenkov detector of $\sim$730 kton, divided into up to five shafts of 65 m diameter and 65 m height each, containing separate tanks. The technology is well known since it has been used in several experiments such as Kamiokande and Super-Kamiokande, and has good resolution on energy, position and angle reconstruction.

- GLACIER, an up to 100 kton liquid argon time projection chamber. This type of detector is known for its uniform and high accuracy imaging but presents a technology challenge which is to drift ionization tracks over long paths of several meters and having the complete detector immersed in a magnetic field. Monte Carlo studies have shown that, for neutrino energies ranging from 0 to 5 GeV, the efficiency on ν_e appearance signal is very high (90 %) while reducing to the permil level one of the main sources of background, the misidentified π^0 produced through neutral current neutrino interactions.

- LENA, a liquid scintillator detector similar to the currently existing detector Borexino. The scintillator is arranged in cylindrical shells around the central volume, with a target volume of 100 m height and 26 m diameter. The scintillation light will be gathered by the photomultipliers (PMT) installed on the inner walls, with a surface coverage of 15 % which can be increased to up to 30 % by adding conical light reflecting mirrors around the PMTs. This type of detector proves to be highly efficient at low neutrino energies, and can study $\overline{\nu}_e$ signal with almost no background by tagging inverse beta decays in coincidence. The detector can nevertheless be used to cover an neutrino energy range from $\sim$10 MeV to 10-20 GeV.

Since none of the existing underground laboratories in Europe can host such large detectors, seven sites are currently being investigated to build new underground facilities.

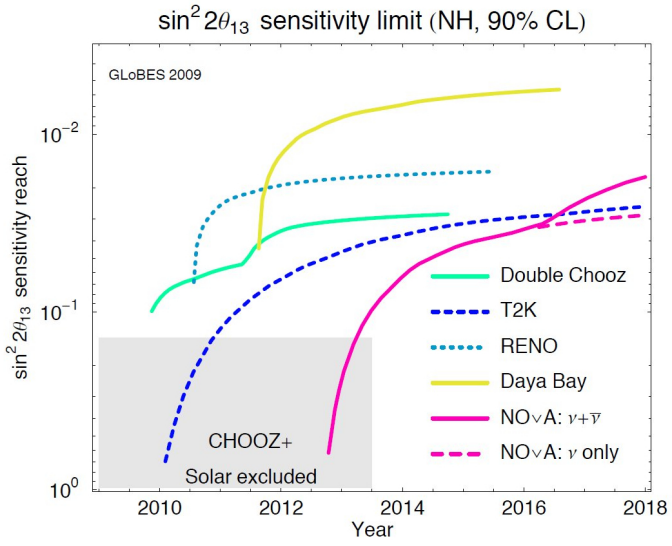

Figure 1.16: Sensitivity to $\sin^2 2\theta_{13}$ as a function of time for current and future experiments searching for θ_{13}. Note that the starting dates of the experiments are not up to date, most of them have been shifted.

Sensitivities for T2K, Double Chooz, NOνA, RENO, and Daya-Bay to θ_{13} as a function of time are given on figure 1.16.

Chapter 2

Neutrino-nucleus interactions

Neutrinos interact with matter only through weak interaction i.e. by exchanging a Z^0 or $W^{\pm}$ boson with a nucleon, a nucleus or a lepton. Their detection is very difficult since the typical neutrino interaction cross-section is of the order of a few 10^{-39} cm^2/GeV (Fig.2.1). Since their detection is done through interactions with the nuclei present in the detector, long baseline neutrino oscillation experiments aiming for precision study of oscillations, such as T2K, require an accurate knowledge on neutrino-nucleus interactions, in particular the ability to reconstruct the neutrino fluxes and to be able to predict the neutral current π^0 production, one of the main backgrounds in the search for ν_e appearance.

The complexity of the problem is double, since neutrinos interact with a quark which is part of a nucleon, which in turn is part of a nucleus. Therefore, a good understanding of the nuclear environment has to be reached to measure the neutrino interaction cross sections [66]. Determining how the nuclear environment responds when interacting with a neutrino requires the knowledge of nuclear matrix elements, but the description of the nuclear structure and dynamics involves severe difficulties which arise from both the nature of strong interactions and the complexity of the quantum mechanical many-body problem. Therefore the theoretical model chosen to describe the nucleus and the nucleon-nucleon interactions will have a great impact on both the predictions and the systematic errors, consequently limiting the precision of any measurement which involves the interaction with a nucleus.

Since it is very challenging to compute the exact solution of the many-body Schrödinger equation, it is possible to describe the most important features of nuclear dynamics using an

independent particle model, where the nucleon-nucleon potential is replaced with a mean field. The simplest model which uses the independent particle approach is the relativistic Fermi gas model (RFG), in which the nucleus is seen as a degenerate Fermi gas of neutrons and protons, bound with constant energy. This average binding energy and the Fermi momentum of the nucleus are specific to each nucleus. The model takes into account the fermionic nature of the nucleons by including Pauli blocking, i.e. that two identical nucleons may not occupy the same quantum state simultaneously. The most commonly used version of this model is the Smith and Moniz model [67]. Although electron scattering experiments proved that this simple model was inadequate for describing electron-nucleus scattering, previous neutrino scattering experiments have not yet demonstrated model deficiencies.

The T2K experiment uses the NEUT neutrino Monte Carlo generator[68] to predict the rates and kinematics of the various neutrino interaction modes that contribute to the T2K neutrino events. This generator is based on the Smith and Moniz prescription to model the nuclear environment.

Throughout this chapter we will point out the choices made in NEUT, briefly explaining the different theoretical models and giving the corresponding experimental results. For this, we will review the most common neutrino-nucleon/nucleus interaction channels that are used in neutrino detection, and that will be used in the analyses described later on. In particular, we will describe the charged current interactions for the ν_μ flux measurement in chapters 5-6 and both neutral and charged current deep inelastic scattering for the tracker absolute momentum scale calibration with K^0_s in chapter 7. We will first focus on the charged current interactions and then we will move on to the neutral current ones.

2.1 Charged current interactions

The first neutrino interaction was discovered at the Savannah River reactor in 1956, through a charged current reaction (Sec. 1.1.1). Charged current interactions are the ones where the neutrino exchanges a $W^\pm$ boson with a nucleon or a nucleus from the detector, and turns into its corresponding charged lepton partner after the interaction. At the lowest order of approximation, i.e. with the exchange of one intermediate boson and the assumption that the neutrino

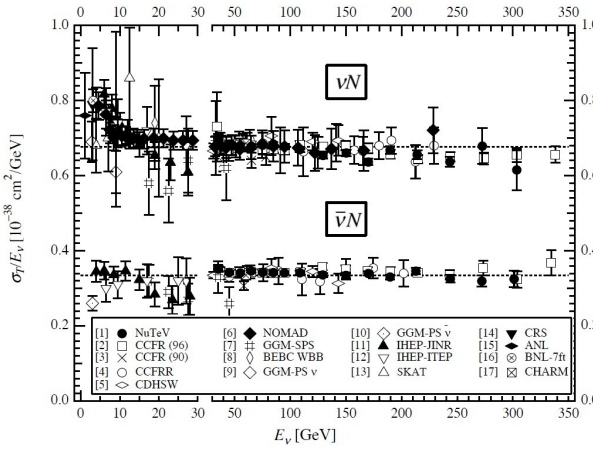

Figure 2.1: σ_T/E_ν as a function of neutrino energy E_ν for the muon neutrino and anti-neutrino, where σ_T is the charged current total cross section. The error bars include both statistical and systematic errors [49].

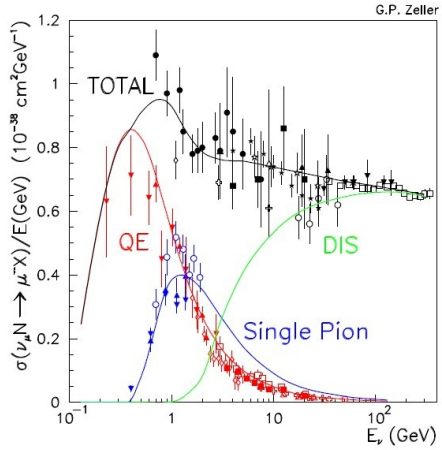

Figure 2.2: Charged current ν_μ cross-sections measured by past experiments [69].

and outgoing charged lepton can be described as a plane wave free state (Born approximation), the cross section of the weak charged current process $\nu_l + A \to l^- + X$ can be written as

$$\frac{d^2\sigma}{d\Omega_l dE_l} = \frac{G_F^2 |V_{ud}|^2}{16\pi^2} \frac{|\overrightarrow{k}_l|}{|\overrightarrow{k}|} L_{\mu\nu} W_A^{\mu\nu} \tag{2.1}$$

where the tensor $L_{\mu\nu}$ is specified by the measured lepton kinematical variables, the tensor $W^{\mu\nu}$ contains all the target structure information including the initial and final nuclear states, G_F is the Fermi constant, V_{ud} is the CKM matrix element coupling the up and down quarks, and $\overrightarrow{k}$ and $\overrightarrow{k}_l$ denote the momenta of the incoming neutrino and the outgoing charged lepton respectively [66]. The total charged current cross section for muon neutrino and anti-neutrino is on average a few 10^{-39} cm^2/GeV (Fig.2.1).

We will review the interaction channels only for muon neutrinos since the analyses presented in this thesis focus on ν_μ interactions which are the main component of the T2K neutrino beam. The cross-sections of the different processes must be well modeled and understood to avoid biasing the neutrino energy reconstruction described in section 6.3.3.4. First, we will look at the quasi-elastic channel, which is the most frequent at T2K's energy scale (Fig.2.2, Sec.3.1.1) and also the most useful to precisely reconstruct the neutrino energy. We will then

describe the channels which lead to the production of a single pion in the final state, which are the second most important interaction channel around the 1 GeV region. Finally we will focus on the deep inelastic process and multi-pion production.

2.1.1 Charged current quasi-elastic interactions

The charged current quasi-elastic (CCQE) process, $\nu_\mu + n \rightarrow \mu^- + p$ (Fig.2.3), is the main signal reaction for oscillation experiments in the 1 GeV region because it has the largest neutrino-nucleus cross section for energies below 2 GeV (Fig.2.2). Its simple final state allows an accurate reconstruction of the neutrino energy using only the measured energy and angle of the outgoing lepton with respect to the incoming neutrino.

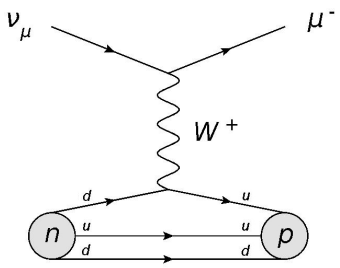

Figure 2.3: Charged current quasi-elastic Feynman diagram.

In this case, the neutrino energy can be written as

$$E_\nu^{CCQE} = \frac{m_P^2 - m_\mu^2 - E_N^2 + 2E_\mu E_N - 2\boldsymbol{p}_\mu \cdot \boldsymbol{p}_N + |\boldsymbol{p}_N|^2}{2(E_N - E_\mu + |\boldsymbol{p}_\mu| \cos\theta_\mu - |\boldsymbol{p}_N| \cos\theta_N)} \tag{2.2}$$

where E_μ and $\boldsymbol{p}_\mu$ are the energy and momentum of the outgoing muon, θ_μ is the angle of the muon with respect to the incoming neutrino, m_P and m_μ denote the proton and muon mass, and $\boldsymbol{p}_N$ and E_N are the momentum and energy carried by the struck neutron. If we consider that the neutron is at rest, i.e. $|\boldsymbol{p}_N| = 0$, and that the neutron binding energy correction from the relativistic Fermi gas model used is a constant value ϵ then the energy of the neutrino can be written as $E_N = m_N - \epsilon$, where m_N is the neutron mass. The equation 2.2 can therefore be reduced to

$$E_\nu^{CCQE} = \frac{m_P^2 - m_\mu^2 - E_N^2 + 2E_N E_\mu}{2(E_N - E_\mu + \boldsymbol{p}_\mu \cos\theta_\mu)} \tag{2.3}$$

We will use this procedure to compute the neutrino energy for the neutrino muon flux measurement in chapter 6. The momentum and angle of the muon with respect to the neutrino will be mainly measured by the time projection chambers (TPCs) of the T2K off-axis near detector tracker (Chap.4), while the fine grained detectors (FGDs) of the tracker will play the role of neutrino targets and will be useful to reconstruct the neutrino interaction vertices. Since the FGDs are mainly made of plastic scintillator bars, the most abundant nuclei are carbon nuclei. Thus, the binding energy we will use is $\epsilon = 25$ MeV, as measured by electron scattering experiments [70].

The neutrino-nucleon CCQE scattering cross section is very often written according to the Llewelyn-Smith formalism [71], which parametrizes the cross section in terms of several Lorentz-invariant form factors which are functions of Q^2, the squared four-momentum transferred to the nuclear system. These form factors can be divided into two types: the vector form factors and the axial form factor. While the vector form factors can be extracted from electron scattering measurements on proton and deuteron targets with great accuracy, the axial form factor must be measured by neutrino scattering experiments. This axial form factor is assumed to have a dipole form and can be written as

$$F_A(Q^2) = \frac{F_A(Q^2 = 0)}{[1 + Q^2/(M_A^{QE})^2]^2} \tag{2.4}$$

where M_A^{QE} is the axial mass parameter. The value for the axial mass can be extracted from reconstructed Q^2 distributions. More details of the neutrino-nucleus scattering theory can be found in detail in [72].

Several past experiments have measured the axial mass. Global fits from bubble chamber data on deuterium yield a value of $M_A^{QE} = 1.014 \pm 0.026$ GeV/c^2[73]. Once this parameter was measured, the CCQE cross-section could be extracted. Figure 2.4 shows the CCQE scattering cross-sections as measured by ANL[74], Gargamelle [75, 76, 77], BNL[78], Serpukhov[79], and SKAT[80] for muon neutrinos and antineutrinos.

However, recent results from the K2K, MINOS, and MiniBooNE experiments on nuclear targets at low energy, i.e. $E_\nu < 10$ GeV, yield higher values of the axial mass parameter. The best fit values from the K2K experiment are $M_A^{QE} = 1.20 \pm 0.12$ GeV/c^2 from ν_μ-oxygen

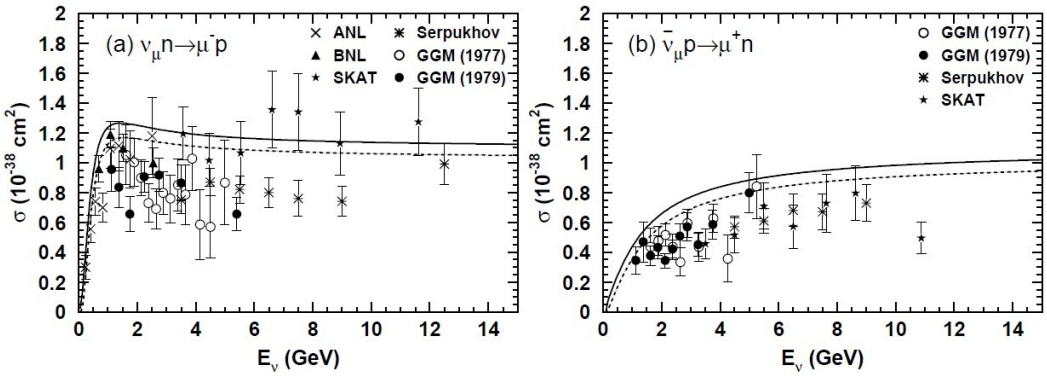

Figure 2.4: Charged current quasi-elastic cross-sections. The solid lines show the calculated cross-sections for free targets and dashed lines are for bound targets (oxygen).

CCQE data taken with the SciFi detector[81] and $M_A^{QE} = 1.14^{+0.14}_{-0.11}$ GeV/c^2 from ν_μ-carbon data taken with the SciBar detector[82]. MINOS fitted the ν_μ-Fe CCQE enhanced Q^2 distributions and extracted a value of $M_A^{QE} = 1.19 \pm 0.17$ GeV/c^2 at a mean neutrino energy of 3 GeV [83].

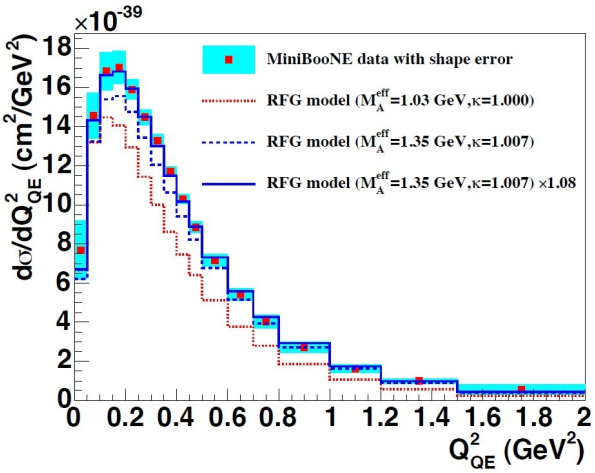

Figure 2.5: MiniBooNE's flux integrated single differential cross section per target neutron for the ν_μ CCQE process [84].

MiniBooNE, a mineral oil based Čerenkov detector which studied the ν_μ produced by BNB (Booster Neutrino Beamline) at Fermilab, fitted the shape of the Q^2 spectrum from ν_μ-carbon

CCQE data for a mean neutrino energy of 0.7 GeV. The ν_μ CCQE data presented a cross section suppression at very low Q^2 (< 0.3 GeV/c^2). To address the discrepancy between the prediction and the data, MiniBooNE introduced a scale factor κ on the lower bound of the nucleon sea which controls the size of the nucleon phase space relevant for Pauli blocking, reducing the predicted interaction rate at low Q^2. The results are shown in figure 2.5. The single differential cross section measured by MiniBooNE is best fitted by an RFG model with a high axial mass value $M_A^{QE} = 1.35 \pm 0.17$ GeV/c^2 and a scale factor $\kappa = 1.007$. The data favors an additional normalization increase of $\sim$8 % with respect to the expected normalization increase implied by the high value of the axial mass. The overall normalization error is 10.7 %, where 8.66 % comes from neutrino flux prediction, 4.32 % from background cross-sections and 4.60 % from detector model [84].

Nevertheless, at higher neutrino energies (3-100 GeV), the NOMAD experiment measured a value of $M_A^{QE} = 1.05 \pm 0.02$ (stat) ± 0.06 (syst) GeV/c^2 [85] which is in agreement with the old measurements of the axial mass. It is not yet known how to reconcile this value with the K2K, MINOS and MiniBooNE observations.

Given the discrepancies between the different experimental results and taking into account the theoretical model differences, NEUT's choice for the axial mass value is $M_A^{QE} = 1.21 \pm 0.20$ GeV/c^2, with an overall normalization error on the CCQE cross-section of 25 % [86]. This value will be used to compute the systematic errors on the flux measurement in chapter 6.

2.1.2 Charged current single pion production

The second most abundant processes in the 1 GeV neutrino energy region are the charged-current single pion (CC1π^+) production processes, $\nu_\mu + n/p \rightarrow \mu^- + n/p + \pi^+$ (Fig.2.2). These events are simple to tag and reconstruct experimentally since they have only one additional particle in the final state.

Nevertheless, once the neutrino has interacted with the nucleon (primary interaction), the produced particles including the knocked out nucleon are scattered by the nuclear medium and can eventually be re-absorbed by the medium. These interactions with the nuclear medium are

known as the final state interactions (FSI) and are important since they might mask the true topology of the event [87]. Therefore, if the final state pion is absorbed by the nuclear medium, it cannot be detected and thus forms one of the main and irreducible backgrounds in the ν_μ disappearance analyses because it mimics a CCQE event. The FSI exist also for the final state proton in CCQE processes but they are relatively better understood than in the case of single pion production. These FSI add an extra level of complexity to the cross-section calculation, and when they can be computed, corrections are applied to take them into account since they can bias the measured total cross-section as well as the shape of the cross-section as a function of the neutrino energy.

Single pion production can be broken down into two broad phenomenological categories: coherent and incoherent scattering.

2.1.2.1 Incoherent pion production

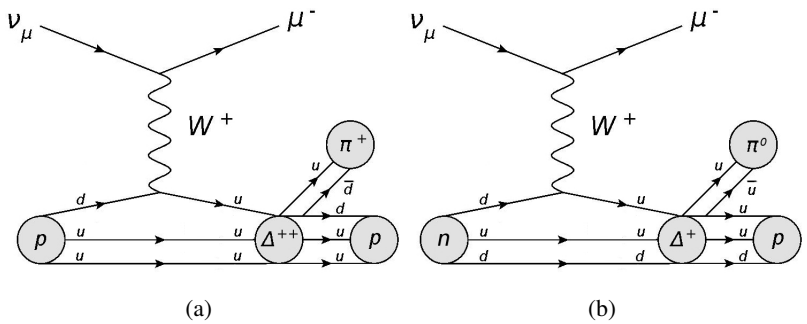

Figure 2.6: Single pion production Feynman diagrams: (a) π^+ production through Δ^{++} resonance (similar diagram for $\nu_\mu + n \rightarrow \mu^- + \Delta^+ \rightarrow \mu^- + n + \pi^+$), (b) π^0 production through Δ^+ resonance.

Incoherent scattering consists in creating a resonance (a Δ^{++} or a Δ^+) via the interaction of the neutrino with a single nucleon, followed by the decay of the resonance into a proton or neutron, and a pion (Fig.2.6). The most commonly used model for predicting the CC1π^+ cross-section, rate, and kinematics of the final state particles, is the Rein and Sehgal (RS) model [88].

Please note that this model is also used to describe the neutral current single pion and charged current single kaon production processes. At T2K energy range, the dominant single kaon production channel is $\nu_\mu + n \rightarrow \mu^- + K^+ + \Lambda$. However, we will not discuss this channel

since the momentum scale calibration presented in chapter 7 requires neutral kaons exclusively, which are mainly produced through deep inelastic scattering.

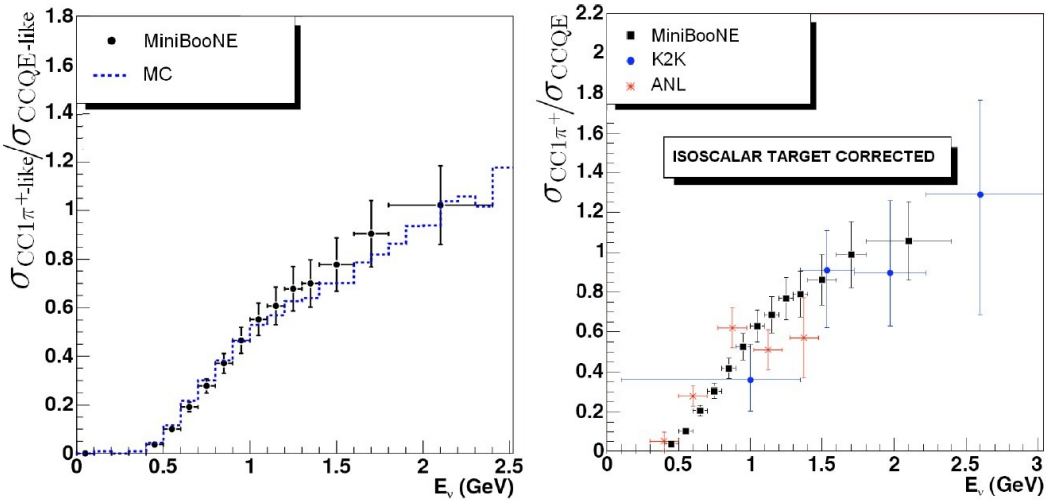

Figure 2.7: MiniBooNE effective ν_μ-carbon CC1π^+/CCQE ratio measurement without the final state interaction corrections (left) and comparison of the corrected MiniBooNE, K2K, and ANL CC1π^+/CCQE ratio measurements.

Similar to the CCQE cross section parametrization, the RS model uses form factors which are assumed to have dipole forms dependent on mass parameters. So far, there are no direct measurements of the resonant axial mass $M_A^{RES\pi}$. However, MiniBooNE successfully extracted a high statistics and purity sample of CC1π^+ from ν_μ-carbon interactions. With this sample, they extracted two cross section ratios. Their main result is the ratio $\sigma_{CC1\pi-like}/\sigma_{CCQE-like}$ where CC1π-like is defined as an event with exactly one μ^- and one π^+ exiting from the struck nucleus, and CCQE-like is defined as an event with only one μ^- and no pions. This ratio, called the effective cross section ratio, is shown on the left hand panel of figure 2.7 [89] along with the `nuance` [90] MC generator prediction which is also based on the RS model. The right hand panel of figure 2.7 shows the final state interaction (FSI) corrected ratio of CC1π^+/CCQE for the MiniBooNE, K2K-SciBar [91], and ANL [92] measurements. The MiniBooNE measurement has an uncertainty of $\sim$11 % while for K2K the uncertainty is $\sim$19 %. The effective ratio, since it does not make any correction for nuclear effects, is less model-dependent than the FSI-corrected cross section ratio. It is reasonable to conclude that $M_A^{RES\pi}$ is larger than

1 GeV/c^2 since the M_A^{QE} measured by the experiments is large.

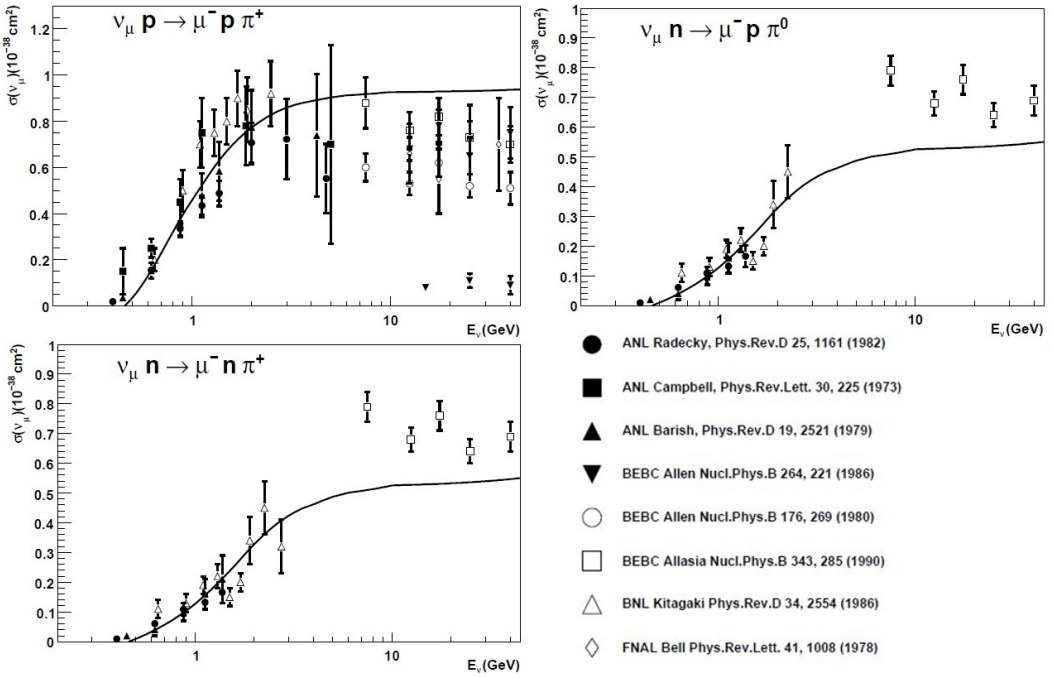

Figure 2.8: Single pion production cross-sections for $\nu_\mu + p \rightarrow \mu^- + p + \pi^+$ (top left), $\nu_\mu + n \rightarrow \mu^- + n + \pi^0$ (top right), and $\nu_\mu + n \rightarrow \mu^- + n + \pi^+$ (bottom left). Solid lines show the calculated cross-sections.

Charged current single pion cross-sections measured prior to MiniBooNE and K2K can be found in figure 2.8.

Single neutral pions can also be produced through charged current incoherent scattering, via a Δ^+ resonance (Fig.2.6). The MiniBooNE measurement of the absolutely normalized cross section of $CC1\pi^0$ production on carbon can be found in [93]. These measurements showed a 30 % higher cross section with respect to one the predicted by the RS model, using an inclusive signal i.e. any event with one muon and one π^0 in the final state with no other mesons. This confirms once again the choice of a high $M_A^{RES\pi}$ value.

Taking into account the previous results, the chosen $M_A^{RES\pi}$ in NEUT is 1.21 ± 0.20 GeV/c^2 and we will consider that the uncertainty on the CC1π cross-section is 30 % for neutrino ener-

gies below 2 GeV and 20 % for higher neutrino energies [86].

2.1.2.2 Coherent scattering

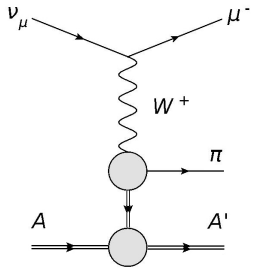

Figure 2.9: Coherent π production.

Coherent scattering is when the neutrino interacts with the nucleus as a whole i.e. interacts with all nucleons coherently to produce a pion (Fig.2.9). The nucleus is left in its ground state after the scattering, thus the process has a low momentum transfer. Once again, the model used is the Rein and Sehgal one, and the cross section and final state interactions depend on an axial mass parameter $M_A^{COH\pi}$. This parameter has a value of 1.0 ± 0.5 GeV/c^2 in NEUT, which is the default value recommended by the RS model. The uncertainty assumed for $M_A^{COH\pi}$, a rather large uncertainty, is based on the limits on CC coherent pion production in the T2K energy region published by both K2K ($\sigma_{CCcoh\pi}/\sigma_{CCinc} < 0.60 \times 10^{-2}$ at 90 % C.L. for $Q^2 < 0.1$ (GeV/c)^2)[94] and SciBooNE ($\sigma_{CCcoh\pi}/\sigma_{CCinc} < 0.67 \times 10^{-2}$ at 90 % C.L. for $E_\nu = 1.1$ GeV and $\sigma_{CCcoh\pi}/\sigma_{CCinc} < 1.36 \times 10^{-2}$ at 90 % C.L. for $E_\nu = 2.2$ GeV)[95] which are below the level predicted by the RS model (Fig.2.10). Since coherent pion production has not been experimentally observed yet, we will assign a 100 % error on the CC1π coherent pion production cross-section when computing the systematic errors on the ν_μ flux measurement in chapter 6.

2.1.3 Deep inelastic scattering and multi-pion production

The deep inelastic scattering (DIS) process has been used for a long time to validate the Standard Model and to probe the insides of hadrons. With a perturbative QCD approach, the structure of the nucleons can be determined by measuring the structure functions (SF) $2xF_1(x, Q^2)$, $F_2(x, Q^2)$, and $xF_3(x, Q^2)$. The scattering particle, which can be an electron, a muon, or a

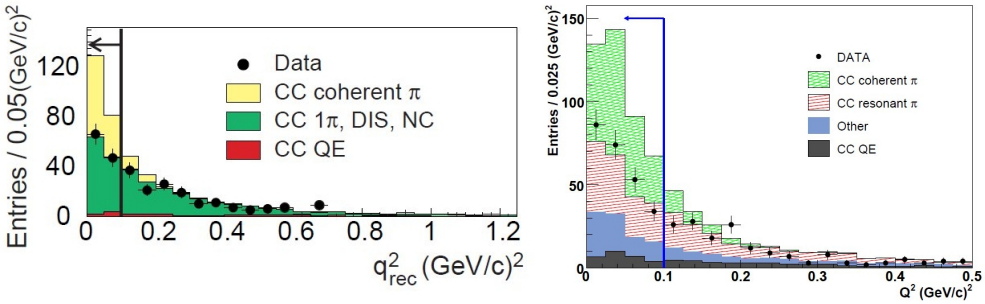

(a) (b)

Figure 2.10: K2K and SciBooNE neutrino coherent pion search data.(a) shows K2K SciBar data with best MC fit and (b) shows SciBooNE data with best MC fit. Both results are compatible with the background predictions.

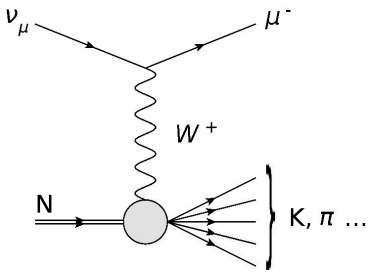

Figure 2.11: Charged current deep inelastic scattering Feynman diagram.

neutrino, collides onto the neutron or proton and shatters it, producing several kaons, pions, and other particles. In our case, the scattering particle is a neutrino muon and the CCDIS process can be written as $\nu_\mu + N \rightarrow \mu^- + X$ (Fig.2.11).

The kinematics of the DIS can be described by the Bjorken scaling variable x, the inelasticity y, and the squared four momentum transferred to the hadronic system Q^2. In terms of the lab frame variables, these Lorentz invariants can be expressed as:

$$x = \frac{4E_\nu E_\mu \sin^2 \frac{\theta_\mu}{2}}{2ME_{HAD}} \text{ , } y = \frac{E_{HAD}}{E_\nu} \text{ , and } Q^2 = 2MxyE_\nu \tag{2.5}$$

where E_ν is the incident neutrino energy, E_μ and θ_μ are the energy and the angle of the outgoing muon, E_{HAD} is the energy of the hadronic system, and M is the mass of the nucleon. With these variables, the neutrino CC double differential cross section can be written as a function of the nucleon SF:

$$\frac{d^2\sigma}{dxdy} = \frac{G_F^2 M E_\nu}{\pi} \left(\left[1 - y\left(1 + \frac{Mx}{2E_\nu}\right) + \frac{y^2}{2} \frac{1 + \left(\frac{2Mx}{Q}\right)^2}{1 + R_L} \right] F_2 \pm \left[y - \frac{y^2}{2} \right] xF_3 \right) \tag{2.6}$$

where G_F is the Fermi weak coupling constant and $R_L(x, Q^2)$ is the ratio of the longitudinal and transverse cross sections. A review of the theory and neutrino-nucleus DIS experimental results can be found in [96].

Deep inelastic scattering processes require a minimum energy. For example, the NEUT generator requires the hadronic invariant mass W to be larger than 1.3 GeV/c^2. The cross-section predictions for this process are computed with the GRV98 parton distribution functions [97]. The Bodek and Yang corrections[98] are used in the low Q^2 region. The multiplicity of pions is restricted to be larger than or equal to two for 1.3 < W <2.0 GeV/c^2 since single pion production is already covered by the RS model as described in the previous section. The estimated uncertainties on the cross-sections for both processes, multi-pion production and DIS, are 30 % for neutrino energies below 2 GeV and 25 % for higher energies.

Neutrinos above 800 MeV can lead to the production of strange mesons such as kaons. In particular, K_s^0 can be produced and their decay via $K_s^0 \rightarrow \pi^+ + \pi^-$ will interest us for calibrating the absolute momentum scale of the tracker by reconstructing the K^0 invariant mass.

Since T2K peak neutrino energy is 600 MeV, the neutrinos which will produce these kaons are part of the high energy tail of the neutrino spectrum and thus the statistics expected for DIS events containing kaons is very low (Sec.7).

2.2 Neutral current interactions

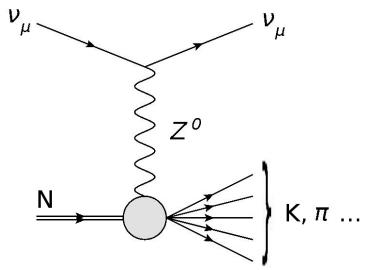

Figure 2.12: Neutral current deep inelastic scattering Feynman diagram.

Neutral current interactions are the ones where the neutrino exchanges a Z^0 with a nucleon or a nucleus. In this case there is no outgoing charged lepton, only multiple hadron are produced.

Neutral current π^0 production, $\nu_\mu + N \rightarrow \nu_\mu + N + \pi^0$, is an important process for experiments searching for the $\nu_\mu \rightarrow \nu_e$ oscillation since it is one of the main sources of background in the appearance search. T2K, whose main goal is studying this oscillation, has a dedicated detector in the near detector – the π^0 detector or P0D – to study the production of these neutral pions (Sec.3.4.2). This process is also usually described with the RS model. Although it is one of the main sources of contamination for the ν_e appearance analyses, it is not a problem for neither the ν_μ flux measurement which uses an inclusive charged current sample with very low neutral current contamination, nor the calibration analysis.

Experimental results from neutral current cross-section measurements are usually presented as a ratio to the charged current cross-sections. In NEUT, the following simplifications of the cross-sections extracted from various experiments are used:

- for neutral current elastic scattering [99, 100]:

$$\begin{aligned}\sigma(\nu_\mu p \to \nu_\mu p) &= 0.153 \times \sigma(\nu_\mu n \to \mu^- p),\\ \sigma(\overline{\nu}_\mu p \to \overline{\nu}_\mu p) &= 0.218 \times \sigma(\overline{\nu}_\mu p \to \mu^+ n),\end{aligned} \tag{2.7}$$

- for deep inelastic scattering [101, 102]:

$$\begin{aligned}\frac{\sigma(\nu N \to \nu X)}{\sigma(\nu N \to \mu^- X)} &= 0.26 \text{ for } E_\nu \leq 3 \text{ GeV},\\ &= 0.26 + 0.04 \times (\frac{E_\nu}{3} - 1) \text{ for } 3 < E_\nu < 6 \text{ GeV},\\ &= 0.30 \text{ for } E_\nu \geq 6 \text{ GeV},\end{aligned} \tag{2.8}$$

$$\begin{aligned}\frac{\sigma(\overline{\nu} N \to \overline{\nu} X)}{\sigma(\overline{\nu} N \to \mu^+ X)} &= 0.39 \text{ for } E_\nu \leq 3 \text{ GeV},\\ &= 0.39 - 0.02 \times (\frac{E_\nu}{3} - 1) \text{ for } 3 < E_\nu < 6 \text{ GeV},\\ &= 0.37 \text{ for } E_\nu \geq 6 \text{ GeV}.\end{aligned} \tag{2.9}$$

The neutral current scattering cross-sections on neutrons are estimated from the ones on protons with Monte Carlo simulations based on the Weinberg-Salam model [103, 104, 105] as follows:

$$\begin{aligned}\sigma(\nu n \to \nu n) &= 1.5 \times \sigma(\nu p \to \nu p),\\ \sigma(\overline{\nu} n \to \overline{\nu} n) &= 1.0 \times \sigma(\overline{\nu} p \to \overline{\nu} p).\end{aligned} \tag{2.10}$$

Again, neutrinos that have an energy greater than the DIS threshold ($\sim$800 MeV) can produce kaons through neutral current DIS (Fig.2.12). These interactions will therefore also be used for calibrating the absolute momentum scale of the T2K near detector tracker. The overall uncertainty assigned to the total neutral current cross-section is 36 %.

Chapter 3

The Tokai to Kamioka experiment

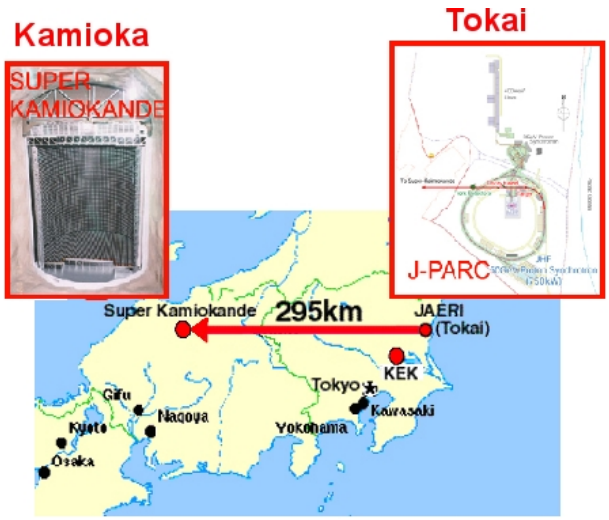

Figure 3.1: The T2K experiment, from Tokai to Kamioka (Japan).

Tokai to Kamioka (T2K) [61] is a long baseline neutrino oscillation experiment in Japan, the first of its kind to be specifically designed to look explicitly for the appearance of electron neutrinos in a ν_μ beam.

T2K's main goal is measuring θ_{13}, the last unknown mixing angle of the PMNS matrix. This will be done by studying the $\nu_\mu \rightarrow \nu_e$ oscillation, and more precisely by looking for the appearance of ν_e in a ν_μ beam. The measurement of θ_{13} plays a key role for studying CP violation in the leptonic sector. By searching for ν_μ disappearance, T2K will also measure with

precision the atmospheric oscillation $\nu_\mu \rightarrow \nu_\tau$ parameters Δm^2_{23} and θ_{23}.

The T2K experiment uses an intense ν_μ beam produced at J-PARC[106] which links the Tokai site to the Kamioka site (Fig. 3.1). The beam goes first into a near detector located at 280 m from the neutrino production site in Tokai and 295 km away it reaches the far detector Super-Kamiokande (Kamioka)[107]. The near detector has been designed to characterize the unoscillated beam as well as to measure various neutrino-nuclei cross-sections and backgrounds.

T2K presents various technological and scientific interest points other than the measurement of the oscillation parameters:

- it is an experiment that uses a high intensity proton beam (0.75 MW nominal power) used to produce the neutrino beam. In accelerator based neutrino experiments, the proton beam intensity is directly linked to the number of neutrinos produced (Sec.3.2) and thus to the amount of data taken which is given as a function of the number of protons that hit the target (Protons On Target, POT). At nominal power, T2K expects 10^{21} POT per year which is equivalent to $\sim$3000 hours of operation. The first phase of T2K has been approved for a total of 5×10^{21} POT taken over five years ;

- it uses a high performance magnetized near detector with two novel technologies - the multi-pixel photon counters and the Micromegas bulks (Chap.4) ;

- it is the first time that the world-wide known and well understood water Čerenkov detector Super Kamiokande will be used after its readout electronics upgrade.

This technology progress will be useful for future experiments. The T2K beam was commissioned in April 2009 and the experiment's first physics run lasted from January to June 2010.

In this chapter we will first discuss the T2K physics goals and how they can be reached. Section 3.2 will briefly describe the neutrino beam production. We will then move on to the description of the various detectors: the on-axis near detector in section 3.3, the off-axis near detector in section 3.4, and the off-axis far detector Super-Kamiokande in section 3.5.

3.1 T2K physics goals

In chapter 1, we introduced a parametrization of the neutrino oscillations with three mixing angles, two squared-mass splittings and one CP-violation phase δ. So far only θ_{13} and δ have not been measured, while Δm^2_{32} and θ_{23} need to be measured with greater precision. As mentioned above, the measurement of these parameters is T2K's main goal. The strategy used by T2K is typical of long baseline neutrino oscillation experiments, and consists in combining the measurements of an unoscillated neutrino beam at the near detector and the measurements of the oscillated neutrino beam at the far detector. The results at the near detector are extrapolated to the far detector and then are compared to the ones obtained at the far detector. This extrapolation requires a good understanding of all the experimental elements: the beam, the near detector, and the far detector. In particular, the neutrino flux extrapolation is done using a simulation based on the measured flux at the near detector and the results of a hadroproduction dedicated experiment, SHINE/NA61 at CERN, which uses a replica of T2K's target. The flux simulation and SHINE will be discussed in further detail in section 6.2.

In this section we will first describe the general neutrino oscillation measurement principle. The second part will focus on the θ_{13} measurement, what the main background sources are and what sensitivity to this parameter can be reached by T2K. Similarly, we will then look at how T2K measures the atmospheric oscillation parameters θ_{23} and Δm^2_{32}. Finally, we will briefly dicuss the possibility of measuring the δ phase with the T2K experiment.

3.1.1 General measurement principle

The search of neutrino interactions at Super Kamiokande uses mainly charged current quasi-elastic channel (Sec.2.1.1) i.e. $\nu_l + n \rightarrow l^- + p$ which is the dominant neutrino interaction mode at T2K energy range (Fig.3.2). The outgoing lepton is a muon if the incoming neutrino is a ν_μ and respectively an electron for ν_e. If the CCQE hypothesis is assumed for all of the detected neutrinos, then the neutrino energy spectrum at both the near and far detectors can be obtained from the charged lepton energy:

$$E_\nu^{CCQE} = \frac{m_P^2 - m_l^2 - m_{Neff}^2 + 2m_{Neff}E_l}{2(m_{Neff} - E_l + |\boldsymbol{p}_l|\cos\theta_l)} \tag{3.1}$$

where m_P is the proton mass, m_{Neff} is the neutron mass minus the binding energy correction, E_l and p_l are respectively the energy and momentum of the outgoing lepton, and θ_l is the angle

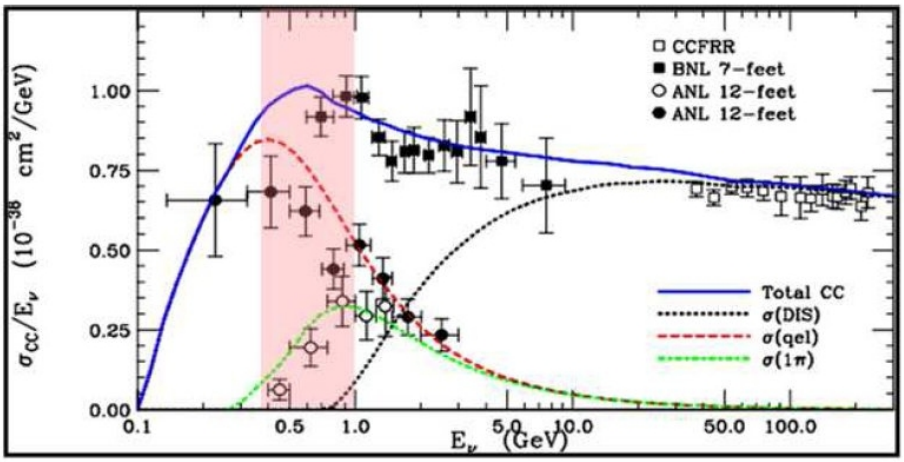

Figure 3.2: Neutrino cross-sections vs neutrino energy. The T2K neutrino energy range is shown in red.

between the outgoing lepton and the incoming neutrino. A detailed explanation of the neutrino energy reconstruction will be given in section 6.3.3.4.

The off-axis far detector SK measures the oscillated ν_μ and ν_e energy spectra, and the off-axis near detector ND280 measures the unoscillated ν_μ and intrinsic ν_e energy spectra (Sec.3.1.2). The spectra measured at the near detector are then extrapolated and compared to the ones obtained with the far detector, to measure the oscillation parameters. So far, the first T2K oscillation analyses use the near detector measurements for computing the near/far detector normalization while the flux shape is provided by the simulation.

The first analysis of this thesis, which will be presented in chapter 6, is meant to measure the unoscillated ν_μ flux, which plays a key role in the ν_μ disappearance analysis and is a source of systematic error (8.6 %, [108]) in the ν_e appearance analysis, and simultaneously validate the flux simulation. In chapter 7, the second analysis will focus on studying one main sources of uncertainty, the absolute energy scale which will have great impact on the search for ν_μ disappearance and a smaller impact on the search for ν_e appearance.

Since Super-Kamiokande takes cosmic data simultaneously, the first criterion to select a T2K neutrino candidate event is that it has to be in a window of ± 500 µsec with respect to the

T2K beam trigger (Sec.3.2). The other selection cuts will depend on whether one is looking for ν_e appearance (Sec.3.1.2) or for ν_μ disappearance (Sec.3.1.3).

3.1.2 θ_{13} measurement

The main goal of T2K is measuring the last unknown mixing angle of the PMNS matrix, θ_{13}. The best upper limit on this parameter is $\sin^2 2\theta_{13} < 0.15$ (90 % C.L.), given by the CHOOZ reactor[57] experiment which did not find any evidence of $\overline{\nu}_e$ disappearance (Sec.1.5).

The measurement of θ_{13} is based on the search of the appearance of ν_e in the ν_μ beam. In chapter 1 we explained that the $\nu_\mu \rightarrow \nu_e$ oscillation probability could be written as

$$\begin{aligned} P(\nu_\mu \rightarrow \nu_e) = & \sin^2(\theta_{23}) \sin^2(2\theta_{13}) sin^2(\Delta m^2_{32} L/4E_\nu) \\ & + \cos^2(\theta_{23}) \sin^2(2\theta_{13}) \sin^2(1.27\Delta m^2_{21} L/E_\nu) \\ & - J \sin(\delta) \sin(1.27\Delta m^2_{32} L/E_\nu) \\ & + J \cos(\delta) \cos(1.27\Delta m^2_{32} L/E_\nu) \end{aligned} \tag{3.2}$$

where

$$J = \cos(\theta_{13}) \sin(2\theta_{12}) \sin(2\theta_{13}) \sin(2\theta_{23}) \sin(1.27\Delta m^2_{32} L/E_\nu) \sin(1.27\Delta m^2_{21} L/E_\nu)$$

and considering that $|\Delta m^2_{13}| \simeq |\Delta m^2_{32}|$, since $\Delta m^2_{21}/\Delta m^2_{31} \sim 3 \times 10^{-2}$. Because of this, the ν_e appearance is expected to be observed around the maximum of the ν_μ disappearance, consequently allowing the simultaneous measurements of θ_{13}, θ_{23}, and Δm^2_{32}.

We also pointed out that the matter effects were small in T2K's case for the given energy ranges, baseline length, average electron density and expected statistics (Sec.1.2.2). Therefore, the probability amplitude depends mainly of the $\sin^2(2\theta_{13})$ value, and to a lesser extent of the δ phase as well.

Once the events are in the right time window as pointed out in the previous section, the far detector Super-Kamiokande can distinguish ν_e interactions from ν_μ by analyzing the features of the Čerenkov rings produced by the charged leptons (Sec.3.5). To be selected as a ν_e candidate, the events must fulfill the following requirements:

- it must be fully contained in the SK 22.5 kton fiducial volume, i.e. the electron must not exit the inner detector. This is important to exclude cosmic ray events and radioactivity from the surrounding rocks ;
- the visible energy E_{vis}, which is defined as the energy of an electromagnetic shower that gives a certain amount of Čerenkov light, must be larger than 100 MeV (a muon with a momentum of 300 MeV/c yields a visible energy of $\sim$110 MeV), to reduce the rock radioactivity background which produces low energy electrons ;
- have one electron like (e-like) ring and no decay electrons ;
- the reconstructed neutrino energy must be comprised between 350 and 850 MeV which corresponds to the neutrino energy range where the oscillation probability is expected to be maximal (Fig.3.15).

One of the main backgrounds expected at this level comes from ν_μ neutral current interactions that produce π^0. Neutral pions decay mostly into two photons, each γ producing an electromagnetic shower that is generally tagged by two electron like rings. Nevertheless, sometimes the two rings might overlap or one of the photons does not have enough energy to produce a ring, thus Super-Kamiokande observes only one electron like ring consequently flagging the event as a ν_e candidate. Specific cuts to discriminate such events have been studied and a dedicated detector in the off-axis near detector, the π^0 detector (P0D), will measure this contamination.

The other main source of background is the intrinsic ν_e contamination of the beam, which is an irreducible background. As we will see in further detail in section 3.2, the neutrino beam is produced mainly by the decays of charged pions through $\pi^+ \rightarrow \mu^+\nu_\mu$ ($\Gamma \sim 99.99$ %)and by the decays of charged kaons via $K^+ \rightarrow \mu^+\nu_\mu$ ($\Gamma \sim$63.5 %). The decay tunnel has been tuned so that most of the muons do not have time to decay, nevertheless some of the low energy muons do decay through $\mu^+ \rightarrow e^+\nu_e\overline{\nu}_\mu$. Also, kaons can decay through the semileptonic channel $K^+ \rightarrow \pi^0 e^+\nu_e$ ($\Gamma \sim$5 %), but these three-body decays are mainly forward going thus using an off-axis beam allows the reduction of this contamination. Pions can also decay with a ν_e in the final state, but such channels have a branching ratio smaller than 0.01 %. The intrinsic ν_e contamination has been evaluated to be 1 % but it will be measured more precisely with the off-axis near detector. The reduction table of the ν_e appearance analysis at Super Kamiokande

for an exposure of 5×10^{21} POT is given on the table 3.1.

Selection cut	CC ν_μ BG	NC ν_μ BG	Beam ν_e BG	CC ν_e signal
Fully contained, $E_{vis} > 100$ MeV	2215	847	184	243
1 e-like ring, no decay e^-	12	156	71	187
$0.35 \leq < E_\nu^{rec} \leq 0.85$ GeV	1.8	47	21	146
e/π^0 separation	0.7	9	13	103

Table 3.1: Reduction table for the ν_e appearance analysis at Super-Kamiokande as predicted by the simulation for 5×10^{21} POT exposure, assuming that $\Delta m^2_{32} = 2.5 \times 10^{-3}$ eV^2 and $\sin^2(2\theta_{23}) = 0.1$.

The expected ν_e energy spectrum is computed for different θ_{13} hypotheses with a Monte Carlo simulation. Once the real energy spectrum of the ν_e born from a ν_μ oscillation has been measured, θ_{13} is deduced from the spectrum which best fits the data.

With T2K, the existing upper limit given by the CHOOZ experiment on $\sin^2 2\theta_{13}$ should be improved by at least an order of magnitude. T2K's expected sensitivity to θ_{13} for different values of δ can be seen in figure 3.3, and is about 20 times higher than CHOOZ's sensitivity. The systematic error fraction assumed for this calculation is 10%. The sensitivity for the $\delta = 0$ hypothesis with respect to the CHOOZ limit can be seen in figure 3.4. In both figures, the beam is assumed to be running at 750 kW for five years, using the 22.5 kton fiducial volume of Super-Kamiokande.

3.1.3 Atmospheric oscillation parameters precise measurement

The other main goal of T2K is measuring precisely the atmospheric oscillation parameters, i.e. Δm^2_{32} with a precision of $\delta(\Delta m^2_{32}) \sim 10^{-4}$ eV^2 and θ_{23} with a precision of $\delta(\sin^2(2\theta_{23})) \sim 0.01$. Up to now the most precise measurements of these parameters have been given by MINOS (Sec.1.5). The measurement of these parameters in T2K is done through the ν_μ disappearance since most of the ν_μ oscillate into ν_τ which neither Super-Kamiokande nor the near detector can detect. The survival probability of the ν_μ is

$$P(\nu_\mu \to \nu_\mu) = 1 - \sin^2(2\theta_{23}) \cos^4(\theta_{13}) \sin^2(1.27\Delta m^2_{32} L/E_\nu) - P(\nu_\mu \to \nu_e) \qquad (3.3)$$

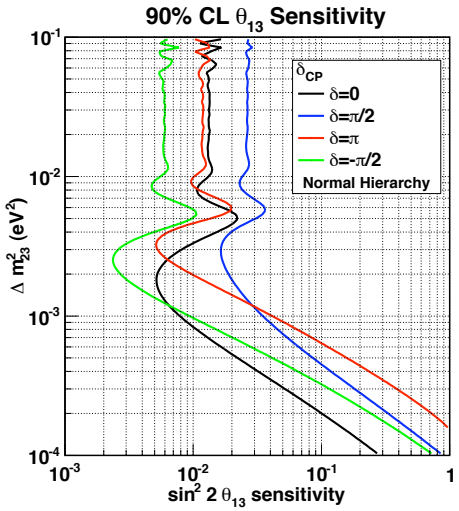

Figure 3.3: T2K sensitivity to θ_{13} at the 90% confidence level as a function of Δm^2_{23} and δ_{CP}. The following oscillation parameters are assumed: $\sin^2(2\theta_{12}) = 0.8704$, $\sin^2(2\theta_{23}) = 1.0$, $\delta m^2_{12} = 7.6 \times 10^{-5}$ eV^2, normal mass hierarchy.

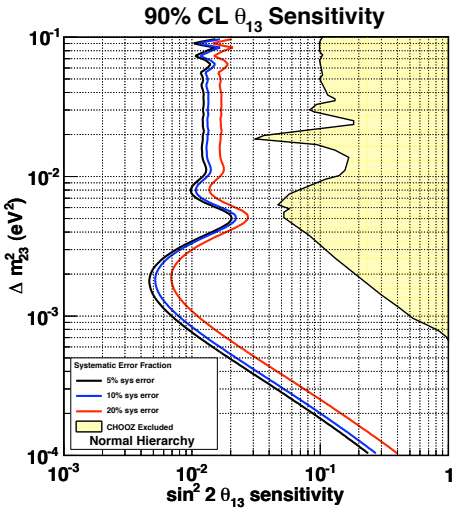

Figure 3.4: T2K sensitivity to θ_{13} at the 90% confidence level as a function of Δm^2_{23} for $\delta_{CP} = 0$. 5 %, 10 % and 20 % systematic error fractions are plotted. The yellow region has already been excluded to 90 % C.L. by the Chooz reactor experiment. The following oscillation parameters are assumed: $\sin^2 2\theta_{12} = 0.8704$, $\sin^2 2\theta_{23} = 1.0$, $\delta m^2_{12} = 7.6 \times 10^{-5}$eV^2, normal mass hierarchy.

with Δm^2_{32} in eV^2, L in km and E_ν in GeV. Once again, matter effects can be neglected.

The atmospheric oscillation parameters are obtained by doing the ratio of the oscillated ν_μ energy spectrum to the unoscillated one (Fig. 3.5), as it can be observed on figure 3.6. The unoscillated spectrum measurement which is done at the near detector and then extrapolated to the far detector will be explained in chapter 6. The ratio presents a dip at ∼600 MeV, where the maximum oscillation is expected. The position of this dip is proportional to Δm^2_{32} and its depth is proportional to $\sin^2(2\theta_{23})$. The measurement of Δm^2_{32} is therefore directly linked to the energy scale, thus it is crucial to calibrate it as precisely as possible. One calibration method which uses the decay of neutral kaons will be described in chapter 7.

The detection of the ν_μ uses mainly the CCQE channel, i.e. $\nu_\mu + n \rightarrow \mu^- + p$. The selection criteria at Super- Kamiokande are similar to the ν_e selection:

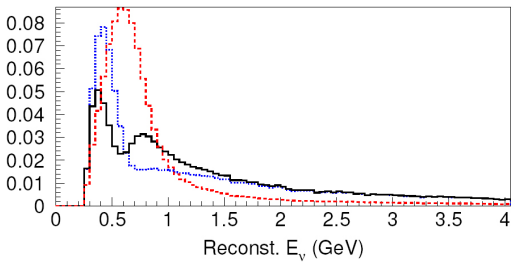

Figure 3.5: The ν_μ energy spectrum before oscillation (dashed red) and after oscillation for $\Delta m^2_{32} = 2.4 \times 10^{-3}$ eV^2 (dashed blue) and $\Delta m^2_{32} = 2.8 \times 10^{-3}$ eV^2 (black).

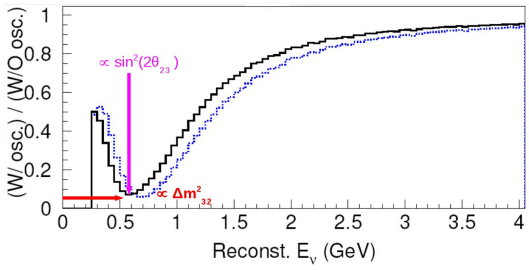

Figure 3.6: Ratio of the oscillated ν_μ spectrum to the unoscillated ν_μ spectrum.

- there must be no activity in the outer detector ;
- the event must have one muon like ring with a reconstructed energy larger than 30 MeV ;
- the reconstructed vertex must be within the 22.5 kton fiducial volume.

One of the main problems in this measurement is the extrapolation of the measured spectrum at the near detector to the far detector. The extrapolation function is obtained by the beam Monte Carlo simulation. More details on this simulation will be given in section 5.2.1. Several issues need to be dealt with caution: the divergence of the pion beam (Sec.3.2) to understand how the neutrino beam is produced), the angular size of the detectors with respect to the neutrinos, and the size of the neutrino production source. These effects are non negligible at the near detector position, whereas the last two effects can be neglected in SK since the source can be considered as point like and the angular dimension does not intervene because of the long distance between both positions.

Selection cut	CCQE	CC-nonQE	NC	Total ν_μ signal
Vertex in the fiducial volume	4114	3737	3149	11000
Fully contained	3885	3011	1369	8265
$E_{vis} \geq 30MeV$	3788	2820	945	7553
Single μ-like ring	3620	1089	96	4805

Table 3.2: Reduction table for the ν_μ disappearance analysis at Super-Kamiokande as predicted by the simulation for 5×10^{21} POT exposure, assuming that there is no oscillation.

Δm^2_{32} (eV^2)	CCQE	CC-nonQE	NC	Total nu_μ signal
No oscillation	3620	1089	96	4805
2.0×10^{-3}	933	607	96	1636
2.3×10^{-3}	723	525	96	1344
2.7×10^{-3}	681	446	96	1223
3.0×10^{-3}	800	414	96	1310

Table 3.3: Expected number of events at Super-Kamiokande for different Δm^2_{32} values as predicted by the simulation for 5×10^{21} POT exposure, assuming that $\sin^2(2\theta_{23}) = 1.0$ and $\sin^2(2\theta_{13}) = 0.0$.

The reduction table for the unoscillated hypothesis at Super-Kamiokande for an exposure of 5×10^{21} POT is given in the table 3.2. The table 3.3 shows the expected number of events for different Δm^2_{32} values after an exposure of 5×10^{21} POT and assuming $\sin^2(2\theta_{23}) = 1.0$ and $\sin^2(2\theta_{13}) = 0.0$.

T2K will measure the atmospheric parameters with a precision of $\delta(\Delta m^2_{32}) \sim 10^{-4}$ eV^2 and $\delta(\sin^2 2\theta_{23}) \sim 0.01$. Figure 3.7 shows T2K's expected sensitivities with respect to the most stringent limits given by MINOS latest measurements.

3.1.4 CP-violation search

If θ_{13} is measurable by either the current experiments or future experiments, and different from zero, it might be possible to measure δ, the PMNS matrix Dirac phase (Sec.1.2). Should this phase be also different from zero, it would mean there is CP violation in the leptonic sector and it could be the first step towards the understanding of the matter-antimatter asymmetry observed in the Universe, as described in the leptogenesis theory (Sec.1.4). The CP asymmetry in the absence of matter effects is given by

$$A_{CP} = \frac{P(\nu_\mu \to \nu_e) - P(\overline{\nu}_\mu \to \overline{\nu}_e)}{P(\nu_\mu \to \nu_e) + P(\overline{\nu}_\mu \to \overline{\nu}_e)} \simeq \frac{\Delta m^2_{12} L}{4E_\nu} \cdot \frac{\sin(2\theta_{12}}{\sin(\theta_{13})} \cdot \sin\delta. \tag{3.4}$$

Since the expected value θ_{13} is small - the best upper limit is $\sin^2 2\theta_{13} < 0.15$ at 90 % C.L. - the CP asymmetry can be large, in particular for small neutrino energies. Nevertheless, the oscillation probability amplitude is proportional to the value of $\sin^2\theta_{13}$. Therefore, the probability to observe the $\nu_\mu \to \nu_e$ oscillation decreases with θ_{13} and is relatively small with respect

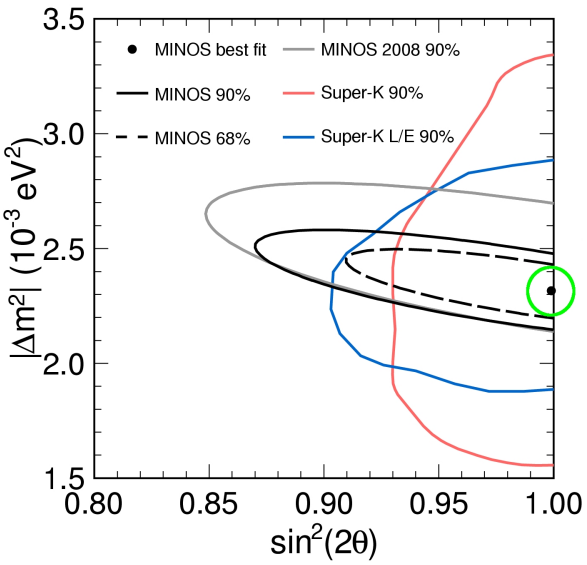

Figure 3.7: MINOS 2010 contours for the atmospheric parameters. The green contour represents T2K's expected sensitivity to the Δm^2_{32} and θ_{23} parameters: $\delta(\Delta m^2_{32}) \sim 10^{-4}$ eV^2 and $\delta(\sin^2 2\theta_{23}) \sim 0.01$.

to the $\nu_\mu \rightarrow \nu_\tau$ oscillation probability whose maximum is in the same energy range at T2K's baseline length since $\Delta m^2_{21} \sim \Delta m^2_{31}$.

Reactor neutrino experiments such as Double Chooz can measure θ_{13} directly through $\overline{\nu}_e$ disappearance but do not have the possibility of measuring the δ since the disappearance probability does not depend on δ. Since T2K searches for ν_e appearance, whose probability depends on the δ phase, T2K will attempt to measure this parameter during its second phase. This phase will consist of an upgrade in the beamline, in particular on the proton intensity that is planned to go up to 4 MW i.e. an intensity five times greater than in the first phase, and several new options for the far detector. One possibility is building a new far detector, Hyper-Kamiokande, which would be located 8 km south of Super-Kamiokande, and would be an upgraded version of the latter. The total volume of this detector would be 1 Mton (20 times SK volume) and its fiducial volume would be 0.54 Mton. With these upgrades, the statistics should increase by more than a factor of 100, the sensitivity to $\sin^2(2\theta_{13})$ should go below 10^{-3}, and δ phase measurement should go down to 10-20 degrees. Another possibility consists in building a 100 kton liquid Argon time projection chamber on the Okinoshima island, at 658 km from J-PARC with

an off-axis angle of 0.8 degree. Finally, the last considered option would be building a far detector in Korea, with an off-axis angle of about 1 degree and a baseline length of approximately 1000 km.

3.2 The neutrino beam

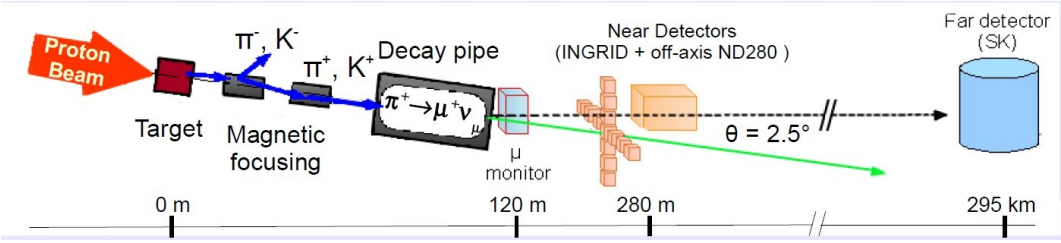

Figure 3.8: The neutrino beamline from Tokai to Super-Kamiokande.

The most important element in T2K is the neutrino beam. It needs to be understood as well as possible, meaning its production must be well controlled. To be able to accomplish T2K physics goals, backgrounds must be well understood and studied. The J-PARC facility, where the neutrino beam is produced, will be described first.

The ν_μ beam is produced at J-PARC (Tokai) by a 30 GeV proton beam colliding onto a carbon target (Fig.3.8). After the decay pipe, a muon detector monitors the neutrino beam going towards the near detector ND280. This near detector, located at 280 m from the target, is made of one on-axis detector, INGRID, and one off-axis detector. The beam reaches the off-axis far detector Super Kamiokande, a 50 kton water Čerenkov detector at Kamioka, 295 km away.

3.2.1 J-PARC accelerator complex

J-PARC (Japan Proton Accelerator Research Complex)[106] is the newly built high intensity proton accelerator facility at Tokai-mura, Ibaraki prefecture. Its construction started in April 2004 and the neutrino beamline was successfully commissioned in April 2009.

The J-PARC facility consists of three successive accelerators (Fig.3.9):

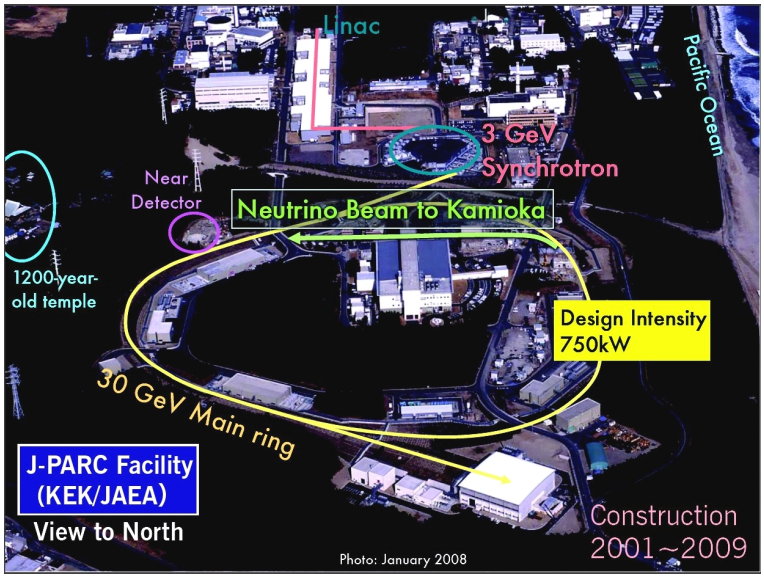

Figure 3.9: The J-PARC facility with its three accelerators.

- a linear accelerator (LINAC) that accelerates an H^- beam up to 400 MeV at nominal design (currently accelerates the beam up to 181 MeV) ;
- a rapid cycling synchrotron (RCS) where the beam is converted into an H^+ beam by charge-stripping foils and accelerated up to 3 GeV with a 25 Hz cycle ;
- the main ring synchrotron (MR), with a circumference of 1567 m, where the beam is accelerated up to 30 GeV.

The 30 GeV proton beam used for the neutrino beamline is structured in eight bunches per spill (only six until June 2010) and the design intensity is 3.3×10^{14} protons per pulse with a repetition rate of 0.31 Hz. The beam is extracted by a set of five kicker magnets within a single turn at the fast extraction point of the MR (the MR has also a slow extraction point used for the hadron beamline). The beam power achieved by the end of 2010 was greater than 100 kW (design intensity is 750 kW).

3.2.2 Neutrino beam production and monitoring

The neutrino beamline can be divided into two portions (Fig.3.10): a primary and secondary beamlines (Fig. 3.11). The primary beamline is where the proton beam is bent to point towards

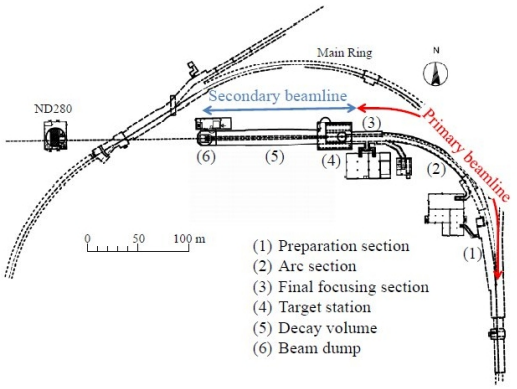

Figure 3.10: Primary and secondary beamlines.

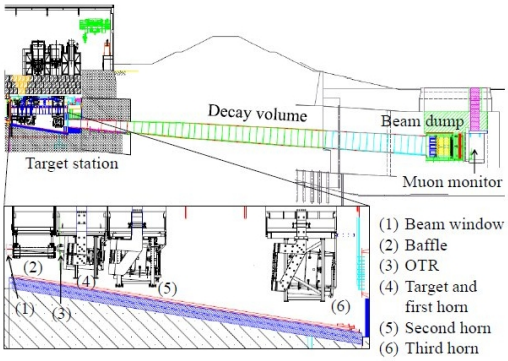

Figure 3.11: Side view of the secondary beamline.

Super-Kamiokande, with an off-axis angle of $2.515 \pm 0.04°$. To have a stable neutrino beam it is important that the proton beam is well tuned thus it is monitored by several devices: 5 current transformers to measure the beam intensity, 21 electrostatic monitors to locate precisely the beam center position, 19 segmented secondary emission monitors to observe the beam profile (center, width, and divergence), and 50 beam loss monitors.

The secondary beam starts where the proton beam collides onto the target, a 91.4 cm long $\times$ 2.6 cm diameter graphite rod. Prior to colliding onto the target, the proton beam is monitored by the Optical Transition Radiation detector. The collision produces mainly a large number of charged pions which are focused by three successive magnetic horns powered by 250-320 kA current pulses. The selected pions (positively charged pions only) decay in flight through $\pi^+ \rightarrow \mu^+ + \nu_\mu$ consequently producing the ν_μ beam. A few charged kaons are also produced, which will mainly decay via $K^+ \rightarrow \mu^+ + \nu_\mu$ but also via 3-body decays such as $K^+ \rightarrow \pi^0 + e^+ + \nu_e$, generating part of the intrinsic ν_e contamination of the beam. The other source of ν_e contamination is the muon decay through $\mu^+ \rightarrow e^+ + \nu_e + \overline{\nu}_\mu$, which adds a $\overline{\nu}_\mu$ component to the beam (though most of the $\overline{\nu}_\mu$ are created by wrong sign pion decays). These decays take place in the decay volume, a 96 m long steel tunnel. After decaying, the beam reaches the beam dump where only muons with an energy greater than 5 GeV and neutrinos pass through. The muons are detected by a downstream muon monitor [109][110] to characterize bunch-by-bunch the neutrino beam stability, intensity, and direction with a precision better than 0.25 mrad.

Finally, the neutrino beam goes through the near detector complex at 280 m from the target and reaches SK, 295 km away. The alignment, the distances between the target and the detectors, both near and far, and the time synchronization between the beam spills and the detectors are done by GPS survey. The time structure of the beam is crucial for background discrimination such as cosmic rays in the detectors.

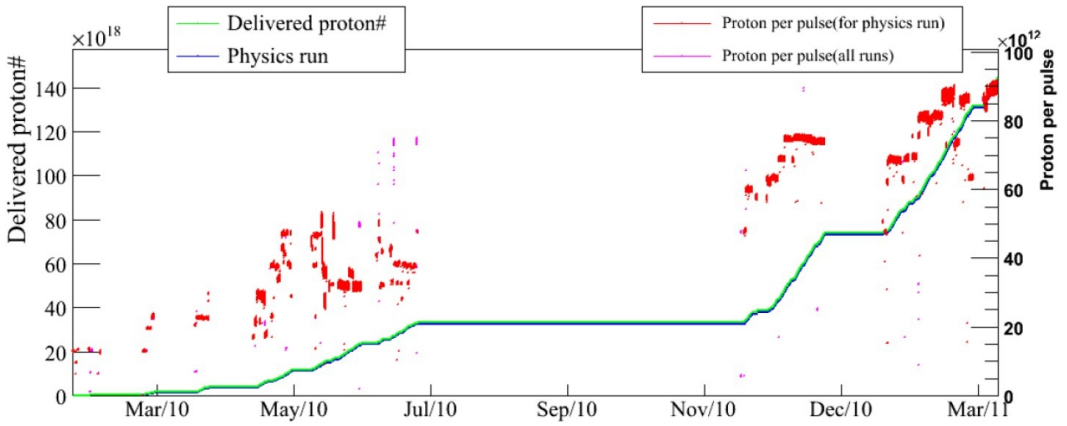

Figure 3.12: Protons on target delivered since February 2010 until the earthquake of March 2011.

The amount of POTs delivered since the beginning of the first physics run until March 2011 can be seen on figure 3.12. The flat period corresponds to the annual summer shut down. So far the near detector has successfully recorded more than 95% of the delivered beam. The analyses presented in this thesis will use only the data taken from January to June 2010.

Unfortunately, a major earthquake and tsunami hit Japan on March 11^{th} 2011 causing severe damage to the Sendai region. The Ibaraki prefecture, where J-PARC and the near detectors are located, was mainly struck by the earthquake. The material damage to the detectors, the beamline, and the surrounding buildings was not major, T2K should start taking data again at the beginning of 2012.

The expected fluxes for all neutrino components at the off-axis near detector and the far detector can be seen in figure 3.13 and figure 3.14 respectively. The peak neutrino energy is $\sim$600 MeV at an off-axis angle of 2.5°

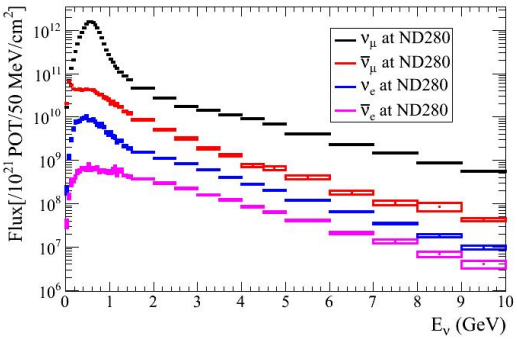

Figure 3.13: Expected ν_μ, ν_e, $\overline{\nu}_\mu$, and $\overline{\nu}_e$ fluxes at the off-axis near detector at 280 m.

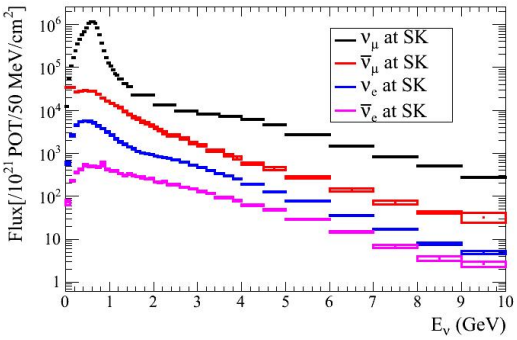

Figure 3.14: Expected unoscillated ν_μ, ν_e, $\overline{\nu}_\mu$, and $\overline{\nu}_e$ fluxes at Super-Kamiokande.

3.2.3 Why use an off-axis beam?

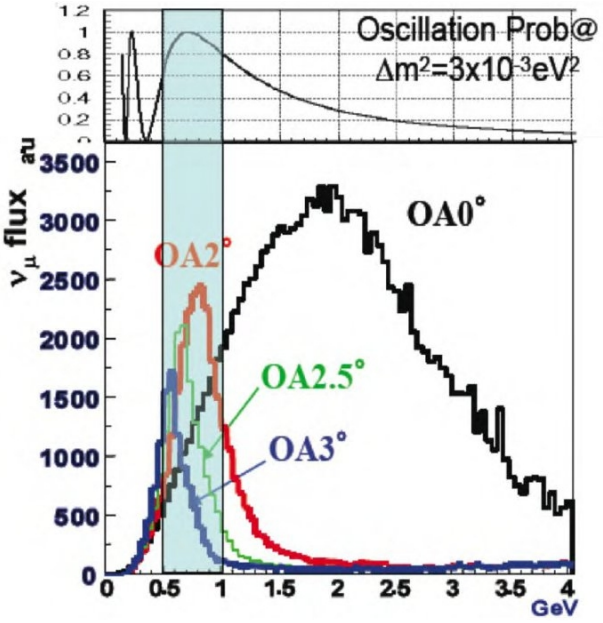

Figure 3.15: Neutrino energy spectrum for different off-axis angle and corresponding ν_e appearance oscillation probability on top.

T2K's near and far detectors are at an off-axis angle of $2.515 \pm 0.04°$ with respect to the neutrino beam direction. The off-axis configuration offers several advantages.

First of all, it allows a better focalization of the neutrino energy, thus allows to have a narrow band energy distribution and minimize the high energy tail. The off-axis angle is adjusted

to choose the neutrino energy that maximizes the neutrino oscillation probability (Fig.3.15), consequently improving the sensitivity of the experiment to the measurement of the oscillation parameters.

The off-axis has also an impact on two-body decay kinematics, in particular it enhances the $\pi^+ \longrightarrow \nu_\mu + \mu^+$ decay. Three-body decays, such as semileptonic decays of charged kaons ($K^+ \rightarrow \pi^0 e^+ \nu_e$) and muon decays ($\mu^+ \rightarrow e^+ + \nu_e + \overline{\nu}_\mu$) are mainly forward going, thus are not affected by the off-axis positioning which leads to a reduction of the beam intrinsic ν_e contamination expected in the near and far detectors.

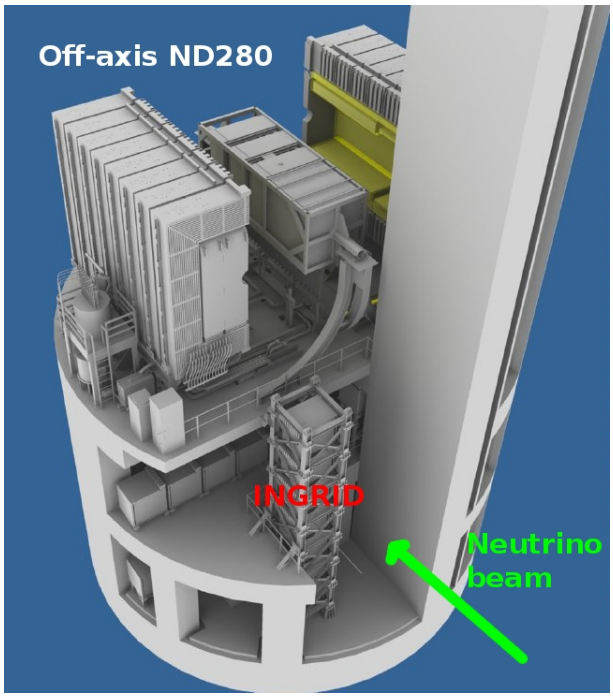

Figure 3.16: The ND280 pit, a pit of 19 m diameter and 37 m depth (first underground level). The top floor houses the off-axes near detector ND280. The horizontal branch of the on-axis detector INGRID is on the second underground level while its vertical branch spreads between the first and third underground levels.

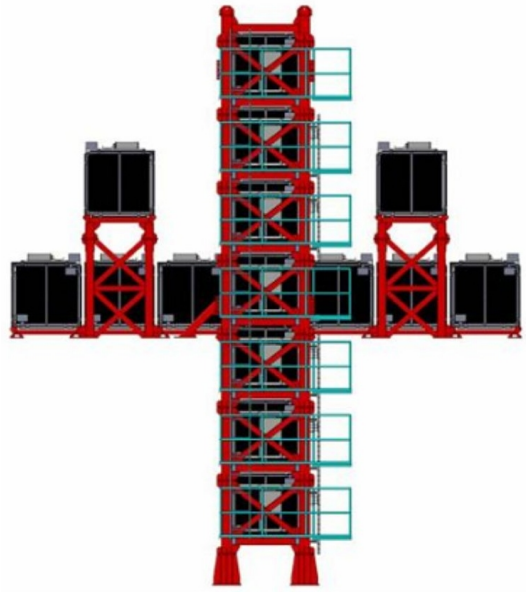

Figure 3.17: The INGRID on-axis detector design.

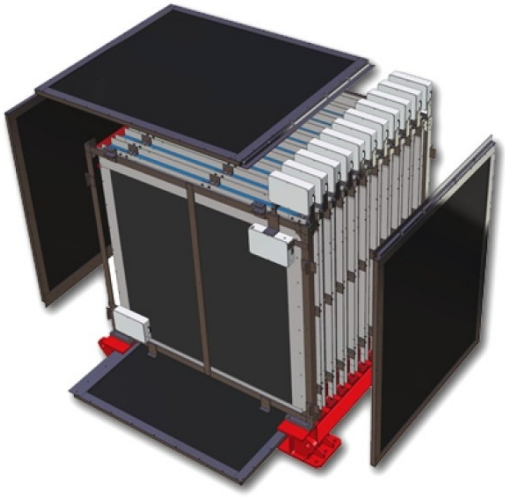

Figure 3.18: An INGRID module.

3.3 The on-axis near detector INGRID

Designed to measure the on-axis neutrino beam profile, the Interactive Neutrino GRID (INGRID) is located on the neutrino beam axis. This detector monitors directly both the neutrino beam direction and intensity, on a daily basis. INGRID is housed in the ND280 hall (Fig.3.16), a pit of 19 m diameter and 37 m depth.

The INGRID detector is made of 14 identical modules arranged as a 10 m cross which two identical branches and two additional modules located outside the main cross (Fig.3.17). The off-axis modules are used to check the neutrino beam cylindrical symmetry. The center of the INGRID cross, which is made of two overlapping modules, coincides with the center of the neutrino beam, defined as zero degree with respect to the direction of the primary proton beamline. Each module consists of a sandwich structure of nine iron plates and 11 tracking scintillator planes surrounded by veto scintillator planes (Fig.3.18). The iron is used as the neutrino target, and the total iron mass per module is 7.1 tons. The tracking planes are made of one layer of 24 scintillator bars in the horizontal direction glued to one layer of 24 vertical scintillator bars. The scintillation light is collected in each bar by a wavelength shifting (WLS) fiber. One end of the fibers is connected to a multi-pixel photon counter (MPPC), which is the

standard readout device of all the scintillator-based detectors in both on-axis and off-axis near detectors. The MPPC will be presented in further detail in section 4.1.2. The readout electronics is based on the Trip-T ASIC developed at Fermilab[111]. This electronics is used by all the scintillator based near detectors.

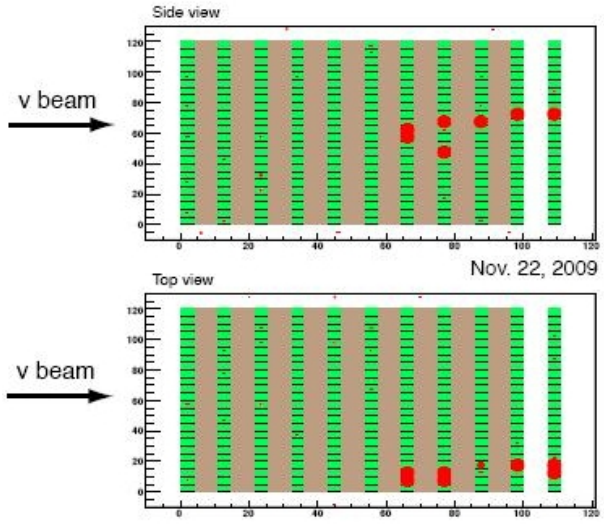

Figure 3.19: A neutrino candidate event in the INGRID detector. The neutrino enters from the left. The green cells are the scintillator bars, the gray boxes show the iron target planes. The red circles form the track of the charged particles produced by the neutrino interaction, the size of the circles is proportional to the signal size.

INGRID uses cosmic rays for calibration purposes, both on the surface prior to its installation and in the ND280 pit during beam periods. The first T2K neutrino event was seen by INGRID in November 2009. Figure 3.19 shows an event display of this event.

3.4 The off-axis near detector

Located at 280 m from the target with an off-axis angle of 2.5 degrees, the off-axis near detector (ND280) characterizes the neutrino beam before oscillation. This means measuring various quantities such as beam flux, composition, direction, neutrino energy spectra, and cross sections. The flux measurement and the absolute energy scale calibration used to measure the neutrino energy spectra will be described in chapters 6 and 7.

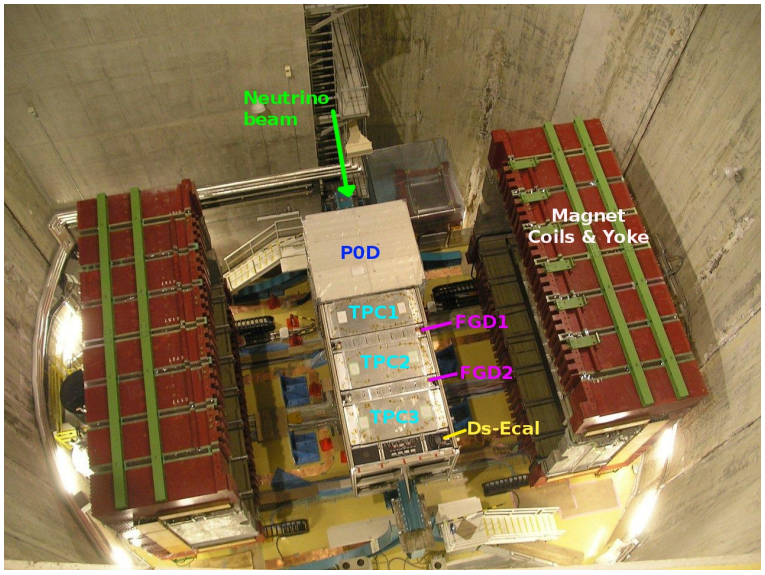

Figure 3.20: The ND280 detector in the ND280 pit at J-PARC, Tokai.

The detector is placed within a magnet refurbished from the UA1 experiment which provides a 0.2 T magnetic field. The off-axis ND280 is housed in the same pit as INGRID, on the first floor (Fig.3.20).

The off-axis ND280 is composed by a subset of different detector types: an upstream π^0 detector (P0D) and a tracker, surrounded by an electromagnetic calorimeter (downstream and barrel ECAL) and side muon range detectors (SMRD) embedded within the magnet yoke (Fig.3.21).All parts but the barrel electromagnetic calorimeter were installed and commissioned at the end of 2009, and took data for the first T2K run which was from January to June 2010. The magnet was operational and had been field mapped. The barrel electromagnetic calorimeter was installed during summer 2010 and started taking data at the end of 2010. The results presented in this thesis use the data from the first T2K run, i.e. before the barrel-ECAL installation.

3.4.1 Goals and physics requirements.

The ND280 is used to characterize the unoscillated neutrino beam, which is fundamental to measure the neutrino oscillation parameters. More precisely, as far as the ν_μ disappearance is concerned, the ND280 and in particular its tracker will measure the ν_μ spectrum and flux using

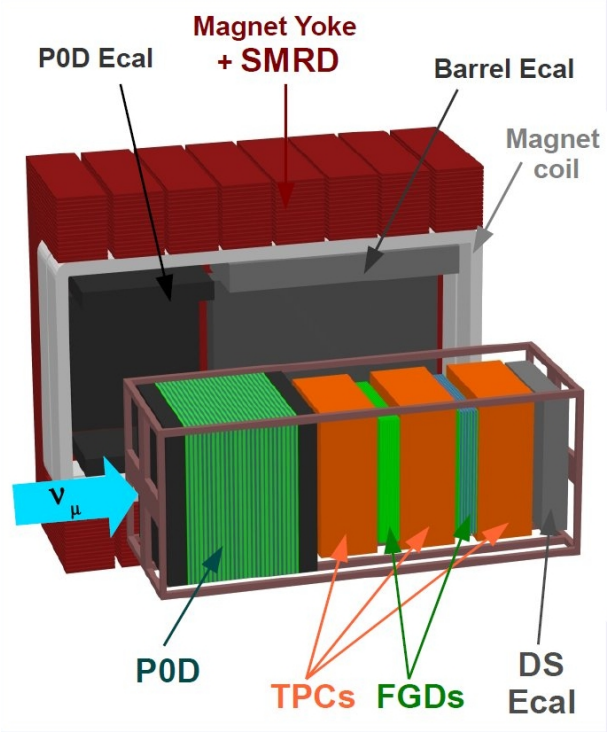

Figure 3.21: The off-axis near detector structure at J-PARC, Tokai.

mainly charged current quasi-elastic interactions (CCQE), $\nu_\mu + n \rightarrow \mu^- + p$. The neutrino energy can only be reconstructed in the CCQE case, for all the other interaction types the CCQE hypothesis is made and a transfer matrix is computed (Sec.6.3.3.4).

As for the ν_e appearance, the ND280 plays a crucial role in the measurement of the intrinsic ν_e contamination, done mainly by its tracker, and backgrounds such as the neutral current interactions producing π^0, done by the π^0 detector installed upstream the tracker. The expected intrinsic ν_e contamination is $\sim$1%.

To be able to reach the expected precision on Δm^2_{32} and θ_{23}, the absolute momentum scale must be known at the 2 % level and the precision on the neutrino flux measurement must be better than 5 %.

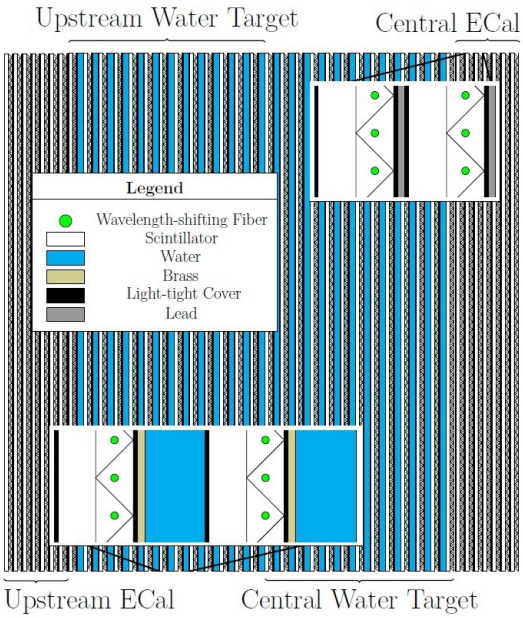

Figure 3.22: Schematic P0D design. The neutrino beam crosses the detector from the left to the right.

3.4.2 Pi-zero detector (P0D)

The π^0 detector (P0D) is installed in the upstream end of the magnet. It has been optimized to study the neutral current interactions, in particular the $\nu_\mu + n \rightarrow \nu_\mu + n + \pi^0 + X$ process on a water target (mainly on oxygen), which is one of the main backgrounds in the ν_e appearance search at Super-Kamiokande which uses also water as a neutrino target. Consequently, the measurements done with the P0D will be useful to extrapolate systematics on Super-Kamiokande.

This detector consists of 76 scintillator planes made of extruded triangular plastic scintillator bars arranged vertically and horizontally, interleaved with fillable passive water targets and lead and brass sheets (Fig.3.22). The bars are read by WLS fibers connected to an MPPC each. The whole structure can be considered as an active target, reaching a total weight of 17.6 tons. The P0D can operate with both water targets filled or empty, thus the measurement of the neutrino interaction cross-section on oxygen can be done by a simple subtraction. The segmentation of the scintillator layers is enough to reconstruct charged particle tracks and electromagnetic showers. A light injection system and cosmic rays allow the calibration of the detector. The reconstruction efficiency for neutral pions with a momentum larger than

200 MeV is 33 %. If the event is fully contained, the expected energy resolution is

$$\Delta E/E = 10\% + 3.5\%/\sqrt{E(GeV)} \tag{3.5}$$

3.4.3 ND280 tracker

The ND280 tracker, installed downstream the P0D, consists of three time projection chambers (TPC) and two fined grained detectors (FGD). This detector is optimized to study charged current interactions, in particular the CCQE process $\nu_\mu + n \rightarrow \mu^- + p$ and its main objectives are to measure the muon and electron neutrino fluxes and spectra as well as neutrino interaction cross-sections. Since both analyses presented in the thesis are based on the data taken by this detector, a detailed description of the tracker detectors, its goals and its performances will be given in chapter 4.

3.4.4 Electromagnetic calorimeter (ECAL)

The ND280 electromagnetic calorimeter (ECAL) surrounds the P0D and the trackers. It consists of plastic scintillator bars, read by a WLS fiber connected to an MPPC, interleaved with lead absorber sheets. Its coverage is almost hermetic: it will detect any charged particle leaving or entering the inner volume of the ND280. Its main goal is to measure the energy and direction of the outward (or inward) going charged particles through the detection of photons. The ECAL plays also a key role in the measurement of π^0 production.

The ECAL is made of 13 independent modules: six modules surround the tracker volume on the four sides parallel to the beam axis (Barrel ECAL), one module is placed downstream the tracker (Ds-ECAL), and six modules surround all six sides of the P0D (Fig.3.21).

3.4.5 Side muon range detector (SMRD)

The side muon range detector consists of 440 scintillator modules installed in the magnet iron yoke gaps. Each scintillator layer is read by a WLS fiber connected to an MPPC, like all scintillator based ND280 detectors (Fig.3.23). The SMRD has three main goals:

- detect muons which escape from the inner volume with large angles with respect to the beam direction and measure their momenta ;
- trigger on cosmic rays entering the ND280 (used for calibrating all ND280 detectors) ;

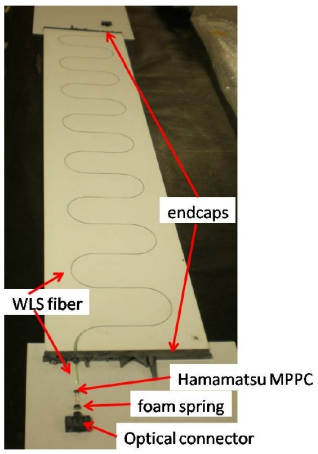

Figure 3.23: SMRD scintillator counter components.

- help identify events generated in the pit walls and magnet.

3.5 The far detector Super-Kamiokande

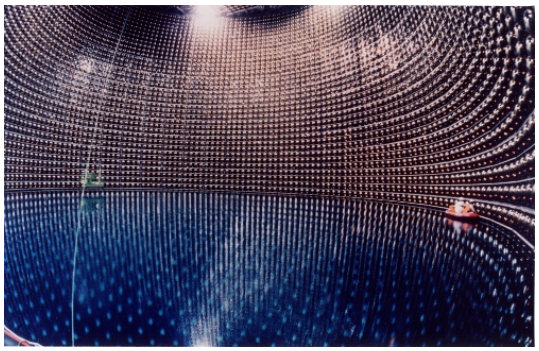

Figure 3.24: The off-axis far detector Super-Kamiokande, Kamioka.

Super Kamiokande (Fig.3.24), the largest water Čerenkov detector in the world, serves as far detector and is located at 295 km from the target. It was built within a 1 km deep mine at Kamioka (2700 m water equivalent) and has been taking data since 1996. Super-Kamiokande has produced a large number of important results for neutrino physics and currently has set the most stringent limit on proton lifetime. Super-Kamiokande has been used in several experiments such as the Super-Kamiokande experiment [22], which proved for the atmospheric

neutrino oscillations, and K2K [27], the first long baseline neutrino oscillation experiment that studied the $\nu_\mu \longrightarrow \nu_e$ oscillation with a ν_μ beam produced at KEK.

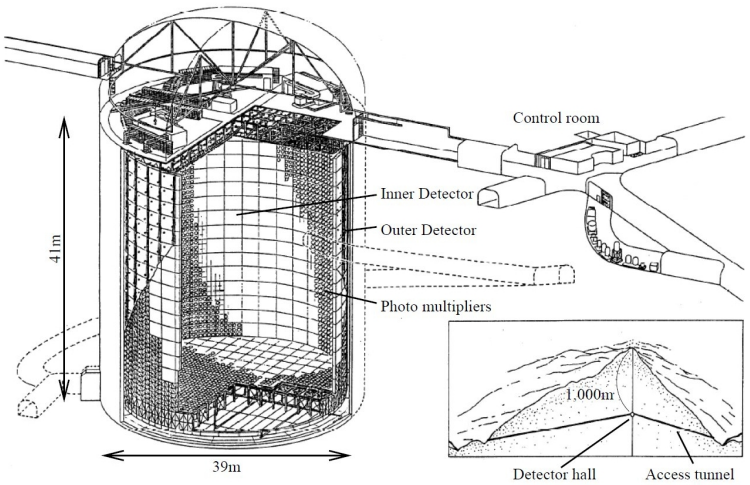

Figure 3.25: Super Kamiokande design.

Super-Kamiokande [107] consists of a cylindrical tank of 41.4 m height and 39.3 m diameter filled with 50 ktons of pure water (Fig. 3.25). This volume is divided into two sub-volumes, the inner detector which contains 32 ktons of water whose walls are covered by 11 146 inward facing 50 cm diameter photo-multipliers (PMT) (40 % surface coverage), and the outer detector surrounding the inner detector, instrumented with 1885 outward facing PMTs. The outer detector serves as an active veto and a radioactivity shield. An accident in November 2001 caused the lost of 60 % of the PMTs. The period before the accident is called SK-I phase. SK ran from December 2002 until fall 2005 (SK-II phase) with half of its PMTs redistributed evenly on the whole surface. Between fall 2005 and spring 2006, SK was re-instrumented with reinforced PMTs to prevent damage from chain reactions like the one that had caused major damage years earlier. Data taking resumed in June 2006 (SK-III phase). Since September 2009, SK runs with an upgraded PMT readout electronics (SK-IV phase) and T2K is the first experiment using this upgraded set-up.

The depth at which Super-Kamiokande is buried reduces the cosmic ray flux by five orders of magnitude with respect to the Earth's surface. Since SK has been used in several experi-

ments, its behavior is well understood. The energy scale is known to the percent level, and the software for modeling events in the detector matches calibration samples to the percent level.

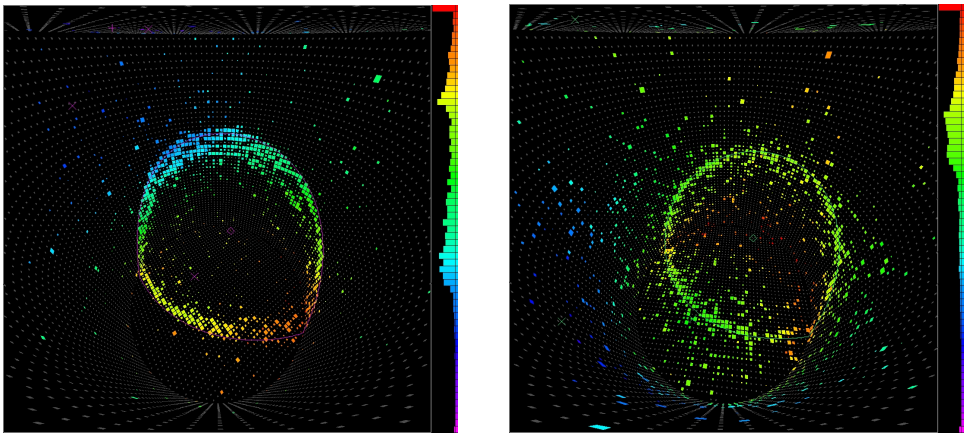

Figure 3.26: Typical muon signal (left) and electron signal (right) observed at Super-Kamiokande.

Charged particles produced by neutrino interactions are detected by the Čerenkov light cone they produce as they cross the water when their energy is above the threshold [112]. Super-Kamiokande can easily distinguish the light rings produced by muons from the ones produced by electrons. As it can be seen in Fig.3.26, muon-like rings have neat edges while electron-like rings have blurry edges due to the electron scattering in the water. The misidentification between electrons and muons is estimated to be $\sim$2 % in the sub-GeV energy range.

Chapter 4

The off-axis near detector tracker

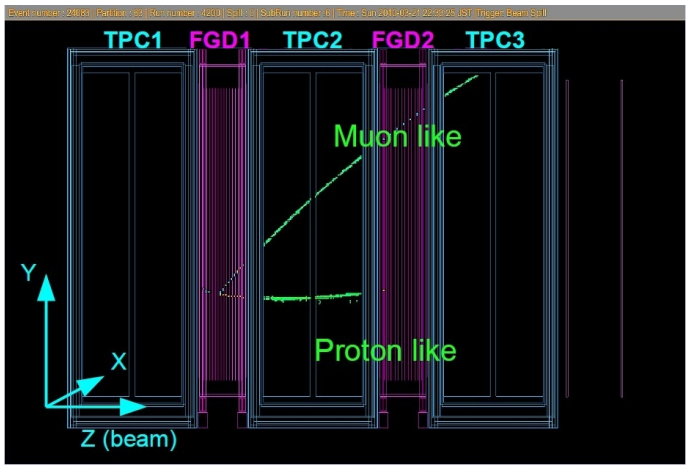

Figure 4.1: CCQE-like neutrino interaction in the first FGD of the ND280 tracker.

The charged current quasi-elastic process (CCQE), $\nu_\mu + n \rightarrow \mu^- + p$, is the dominant neutrino interaction channel at 600 MeV (Fig.2.2). As we explained in chapter 2, it is a very important channel since it is the only one that allows a full reconstruction of the neutrino energy, required for the oscillation measurements, by using only the muon momentum and angle with respect to the beam direction. Therefore, it is fundamental to reconstruct the track of the outgoing muon along with physical related quantities such as the momentum, angles, and vertex. In the off-axis near detector (ND280), this is done mainly by the tracking system.

The ND280 tracker is composed of three wireless Time Projection Chambers (TPCs) and

two massive Fine Grained Detectors (FGDs) installed in between the TPCs (Fig.4.1) and has been optimized to study the CCQE interactions. It plays a key role in the measurement of the unoscillated beam characterization, measuring ν_μ and ν_e fluxes, energy spectra and interaction rates. The measurement of the ν_e component is crucial to determine the intrinsic ν_e contamination of the beam, which is one of the main sources of uncertainty in the search for neutrino electron appearance and θ_{13} measurement. As for the ν_μ component, the tracker provides the ν_μ energy spectrum, which is extrapolated and compared to the one measured at the far detector to extract the atmospheric oscillation parameters Δm_{32} and θ_{23}. The ν_μ flux is also a non-negligible source of systematic error in the ν_e appearance search [108]. In chapters 5 and 6 we will explain how the ν_μ spectrum can be obtained using the data provided by the tracker. The two FGDs, which are not identical, will also allow the measurement of neutrino interaction cross-sections on water, which is very important for the Super-Kamiokande measurement, and on carbon.

The tracker detectors were installed at the end of 2009, and have since then been taking both neutrino beam data for physics purposes and cosmic data for calibration purposes. The analyses presented in chapters 5, 6 and 7 use the first data sample taken by the tracker, i.e. the physics run that took place between January 2010 and lasted until June 2010.

In this chapter we will first describe the FGDs goals, design, and performances (Sec.4.1). Likewise, we will then proceed to describe the TPCs in section 4.2.

4.1 The Fine Grained Detectors

The fine grained detectors (FGD) [113, 114] main purposes are to provide target mass ($\sim$1 ton each) for neutrino interactions and to measure neutrino cross-sections on water, since Super-Kamiokande's target is water, and on carbon. They are a crucial element in vertex reconstruction since given their mass, most neutrino interactions studied by the tracker take place in the FGDs. The definition of a fiducial volume in which the interaction vertex must be is crucial for background reduction in the flux measurement, as we will demonstrate in section 5.3.3, and for the matter normalization in the flux measurement (Sec.6.3.3.2). Their segmentation is good enough ($\sim$ 1 cm $\times$ 1 cm) to provide tracking of charged particles and they can also perform

particle identification based on the deposited energy.

We will first describe the FGDs design and the multi-pixel photon counters used as readout devices. We will then briefly discuss some of the FGD performance results .

4.1.1 Design

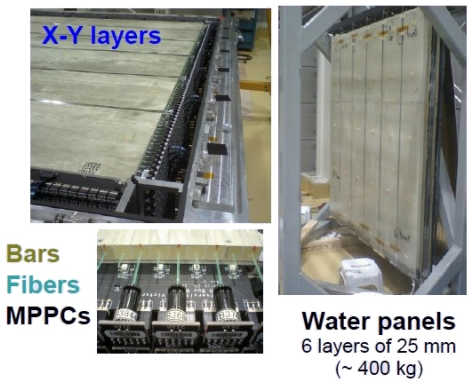

Figure 4.2: X-Y scintillator layers (top left), WLS fibers connected to their MPPC (bottom left) and FGD2 water panels (right).

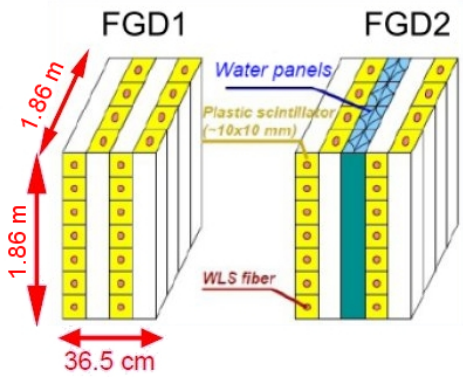

Figure 4.3: Schematic FGD design. The water layers can be seen in the second FGD.

Both FGDs are made of thin scintillator bars ($9.61 \times 9.61 \times 1864$ mm^3 each) arranged in horizontal (segmentation along the Y axis) and vertical (segmentation along the X axis) layers to provide charged particles tracking (Fig.4.2 and 4.3). The first FGD has 30 layers of 192 bars each, each layer oriented alternatively in the X and Y directions, where the X-Y plane is transverse to the beam direction. The second FGD alternates 7 X-Y scintillator layers with 6 passive water layers to measure the neutrino interaction cross-section on water, which is obtained by comparing the neutrino interaction rates measured in the first FGD to those in the second FGD.

Each bar yields an average of 30 photo-electrons per minimum ionizing particle. The scintillation light produced in the bars is collected by a wavelength shifting fiber (Ø = 1 mm). To improve light collection, one fiber tip has been mirrored by vacuum deposition of aluminium. The other tip of the fiber is connected to a multi-pixel photon counter (MPPC, Sec.4.1.2). The front-end electronics is based on the AFTER ASIC chip (Sec.4.2.3). An LED-based light injection system is used for *in situ* calibration purposes such as photo-sensor response, saturation and non-linearity.

4.1.2 The Multi-Pixel-Photon-Counters

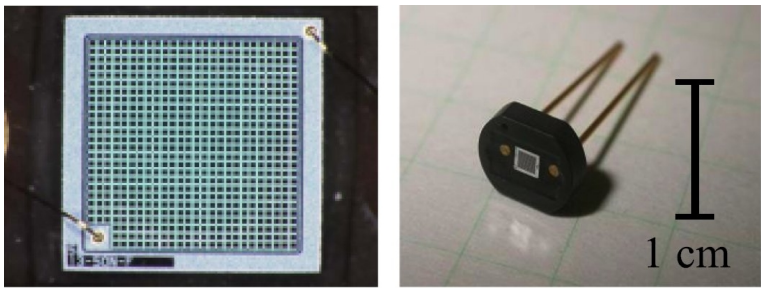

Figure 4.4: A multi-pixel photon counter. The segmentation of the MPPC can be seen on the left picture.

The Multi-Pixel Photon Counters (Fig.4.4) [115] are used in all the near detectors except for the TPCs for reading out the wave-length shifting fibers. They were specifically developed and produced for T2K by Hamamatsu Japan and the Kyoto University. It is the first time that these devices are used in such a large scale: over 52 000 MPPCs have been installed and have been taking data since late 2009. The MPPCs digitize the light signal produced by scintillation inside the bar, and have the advantage of being able to operate in a magnetic field.

Each MPPC is a 1.3×1.3 mm^2 module divided into 667 active pixels (50×50 μm^2 pixels), suited for the 1 mm diameter fibers. Each pixel works as an independent Geiger counter. At the nominal voltage of 70 V and at a room temperature of $\sim$ 25 °C, the measured dark noise rate is smaller than 1.2 MHz, the photon detection efficiency is close to 30 %, and the typical gain is of 7.5×10^5. The number of dead channels in the FGDs is on average 30 out of approximately 8500 channels, which represents less than 0.4 % of the total.

4.1.3 Performances

In this section, we will discuss briefly some of the test results on the FGDs performances.

An important calibration result is the hit efficiency, measured with through going cosmic rays (Fig.4.5). Indeed, vertex reconstruction is based on the association of TPC tracks to FGD hits. Missed FGD hits can lead to a wrongly reconstructed vertex, which can affect the efficiency and purity of event selection processes that rely on a fiducial volume (Sec.5.3.3), and bias the reconstruction of the charged particles' momentum at vertex since the exact position

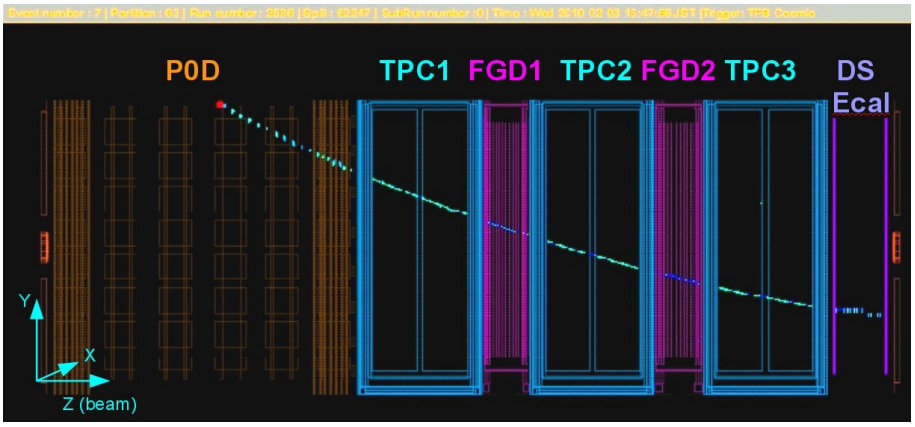

Figure 4.5: A through going cosmic ray event in the ND280.

of the vertex is required to compute the energy loss in the FGD materials.

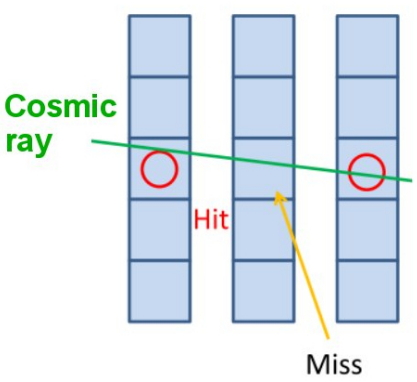

Figure 4.6: Hit efficiency principle: a hit is considered as missed if the preceding and following scintillator layers have hits. The first and last scintillator layers are excluded.

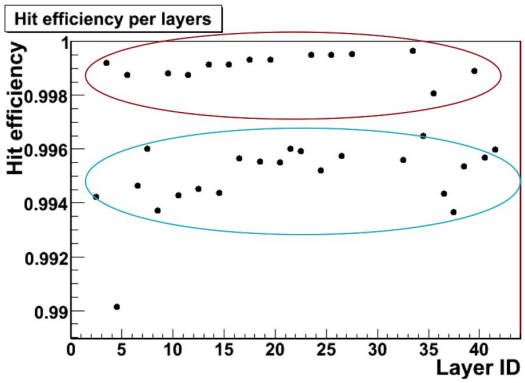

Figure 4.7: Hit efficiency for horizontal (red) and vertical (blue) layers.

Hit efficiency is defined as the number of hits divided by the total number of layers crossed (Fig.4.6). The measurement shows an efficiency higher than 99 % for all layers (Fig.4.7). The slightly higher efficiency for horizontal layers with respect to the vertical ones is due to a geometrical effect as cosmic rays are mainly downward going.

One of the first results obtained with neutrino beam data was the reconstructed timing of

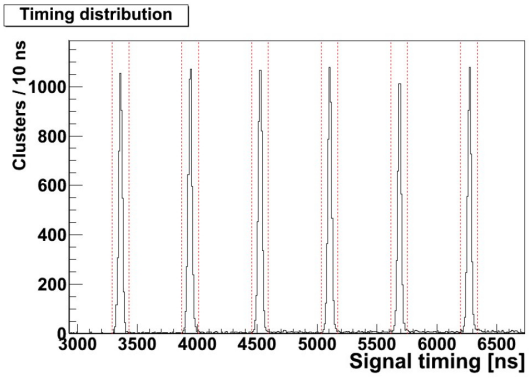

Figure 4.8: Timing resolution.

the events in the FGD (Fig.4.8). The neutrino beam delivered by J-PARC had six bunches per spill during the first data taking period (January to June 2010), with an inter-bunch time of 581 ns. This structure can be clearly seen in the FGDs, with almost no background in-between bunches. The time reconstruction is important since the TPCs cannot provide an absolute time measurement, and the time structure can be used to avoid pile-up effects i.e. to distinguish two or more neutrino interactions which took place within the same spill by tagging the events according to the bunch they belong to. Nevertheless, given the beam power at which T2K ran during the first year (50 kW on average) and that there was almost no background in between the bunches, we will not need to classify the events into time bunches for our selection process (Chap.5). The beam was upgraded to an eight-bunch structure for the second data taking period which started in fall 2010.

4.2 The Time Projection Chambers

The time projection chambers (TPC) [116] used in the ND280 tracker are wireless gaseous TPCs instrumented with Micromegas detectors on their readout planes (Fig.4.9). They serve three main purposes.

First of all, as part of the tracker, the TPCs provide high quality three dimensional reconstruction of charged particles trajectories. A good track reconstruction allows not only the measurement of physical quantities such as the momentum or energy loss, but also the selection of different neutrino interaction channels by classifying the events into different topologies

(a) (b)

Figure 4.9: Picture of the opened (left) and closed (right) inner cage of a ND280 TPC. The inner side of the readout detectors (Micromegas modules) and the field cage are shown on the left picture.

according to the number of reconstructed tracks (Sec.5.6). The TPCs provide a space point resolution of about 0.7 mm.

Their second goal is to measure momentum of the charged particles that cross the TPCs volume, through the measurement of the track's curvature induced by the 0.2 T magnetic field produced by the surrounding magnet. A transverse momentum resolution of 10% at 1 GeV is sufficient since at 600 MeV, the neutrino energy reconstruction resolution in CCQE events is limited to a 10 % level because of the Fermi momentum of the struck nucleons. The reconstruction of the momentum and angle with respect to the beam of the outgoing muons allows the measurement of the ν_μ spectrum (Chap.6) before oscillation. Nevertheless, to reach T2K physics goals on the atmospheric parameters measurements, the absolute momentum scale must be known at the 2% level. The analysis presented in chapter 7 is precisely done to check whether we can reach that level of knowledge on the absolute momentum scale and will present one possible method to calibrate it.

Lastly, the TPCs can perform particle identification using the energy deposited (dE/dx) by each particle, which is crucial to distinguish muons from electrons and protons from pions.

This allows the measurement of the beam ν_e intrinsic contamination, which needs to be known as precisely as possible to reduce the uncertainties on the search for ν_e appearance at the far detector. The resolution on the measurement of the deposited energy, which is based on a truncated mean method must be better than 10 %.

In this section we will first describe the operating principle of a wireless time projection chamber. Then we will present the T2K TPC design, in particular their readout detectors - the Micromegas bulks - and front-end electronics. Finally we will show the performances results of these detectors with both beam and cosmic data.

4.2.1 Wireless TPC operating principle

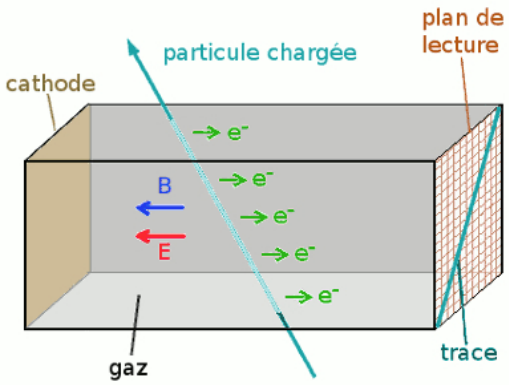

Figure 4.10: Basic TPC operation principle.

A wireless time projection chamber is a large container filled with gas, where a uniform electric drift field (and eventually a magnetic field) reigns. The cathode can be either one of the walls of the box or be placed in the middle of the the drift volume (Fig.4.10). The electric field homogeneity is ensured by an external electrostatic cage. The readout of the signal (deposited charge) is done by the detectors located at the end of the drift volume. For example, the T2K ND280 TPCs use Micromegas micro-pattern detectors.

When a charged particle crosses the TPC, it ionizes the drift gas, producing primary electrons that drift away from the central cathode and towards one of the readout planes because of the electric field. While drifting, the electrons scatter through coulombian interaction. This

scattering can be attenuated mainly by choosing the proper drifting gas and eventually with the magnetic field used to curve the charged particles trajectories. The electrons are amplified and sampled by the chosen readout detector. This detector allows the reconstruction of the two-dimensional projection of the track on the transverse to the drift plane. The third coordinate is reconstructed as a function of the drifting time which requires knowing well the drifting properties of the gas mixture (such as drifting speed) and the time T_0 at which the particle crossed the detector. The T_0 is generally provided by an external trigger, such as scintillator based detector which has a fast response time.

If the TPC is placed within a magnetic field, the trajectory of the charged particle will be a helix. For a magnetic field which is parallel to the drift direction and thus orthogonal to the readout plane, the projection of the track on the readout plane is an arc of a circle. By measuring the curvature of the projection of the track on the readout detector, the transverse momentum p_t of the charged particle can be obtained through the simple equation

$$|p_t| = 0.3 \times B \times R \tag{4.1}$$

where the transverse momentum p_t is in GeV/c, the magnetic field B in Tesla and the radius of curvature R in meters. The 0.3 factor is a unit conversion term. The total momentum p is then given by

$$p = \frac{p_t}{sin\phi} \tag{4.2}$$

where ϕ is the angle between the track and the direction of the field B. More details on the track reconstruction are given in section 5.1.1.

4.2.2 ND280 TPC design

The TPCs have a double box design to allow better isolation and field homogeneity. The inner box is filled with a 95% Ar / 3% CF_4 / 2% iC_4H_{10} drift gas mixture. Its inner walls are covered with copper strips to form the field cage, which together with the central cathode that divides the TPC in two identical drift volumes, produce the required uniform electric drift field. The gas mixture was chosen for its high drift speed, low transverse diffusion, and good performance with Micromegas detectors. The drift field currently used is about 200 V/cm. The outer box, whose walls are at ground potential, contains CO_2 which is used as an insulating gas. The detector is placed within a 0.2 T magnetic field produced by the UA1/NOMAD magnet.

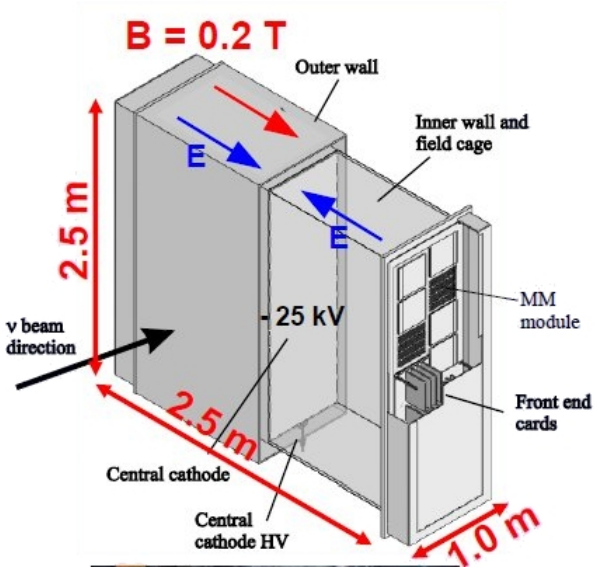

Figure 4.11: Simplified TPC design.

A simplified drawing of the TPC design is shown in figure 4.11. Each end of the two drift volumes created by the central cathode is a readout plane. The latter are instrumented with 12 bulk-Micromegas micro-pattern gaseous detectors per plane (Sec.4.2.3). There is a total of 72 Micromegas modules (35×36 cm^2 each) in all 3 TPCs corresponding to a total active surface of about 9 m^2. These are the largest TPCs ever instrumented with such devices.

The TPCs have a laser system built in for calibration purposes, in order to measure the absolute electric and magnetic field distortions, the absolute gain of the system, and gas proprieties such as electron drift velocity. The UV laser illuminates an array of aluminum dots and strips placed on the central cathode, which release electrons via the photo-electric effect (Fig. 4.12(a)). These electrons drift towards the readout planes, where they are amplified and detected, reproducing the pattern of the aluminum dots and strips (Fig.4.12(b)). Any distortion in the electron drift, due to inhomogeneous electric or magnetic field, leads to relative displacement of the expected pattern, and has an impact on the momentum measurement. Therefore, it is important to correct the field distortions since the TPCs aim to have an absolute momentum scale known at the 2 % level.

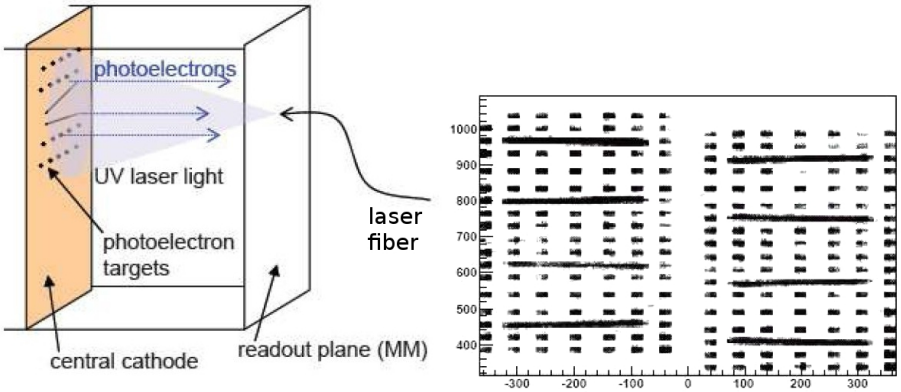

(a) (b)

Figure 4.12: (a)The TPC laser calibration system. (b) Event display of typical laser events where the aluminum dots and strips pattern can be seen. The two readout planes of a TPC are shown.

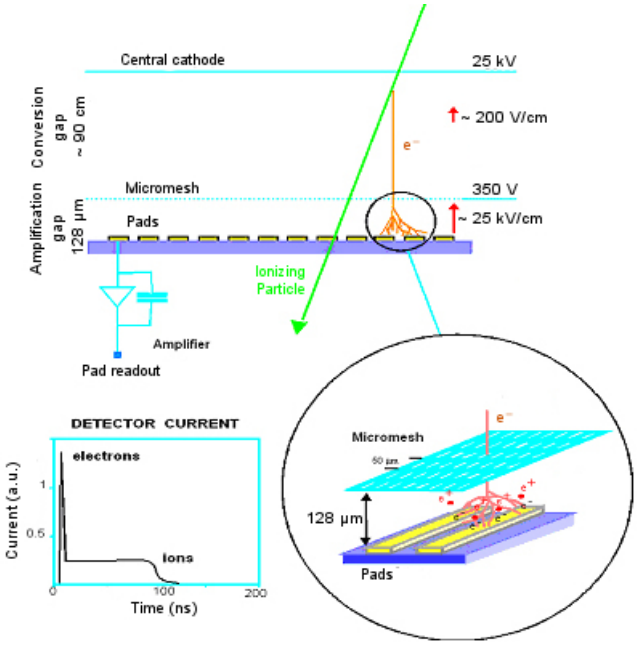

Figure 4.13: The Micromegas operating principle.

4.2.3 Micromegas Bulk and electronics

A Micro Mesh Gaseous Structure, also called Micromegas (MM), is a micro-pattern gaseous detector (MPGD) invented by I. Giomataris and G. Charpak in 1995[117]. A micro-mesh divides the gas volume into two regions: a conversion and drift region, and an amplification stage (Fig.4.13). This detector type is characterized by its uniform gain on all of its active surface, guaranteed by the uniformity of the amplification gap.

When a charged particle crosses the TPC volume, the electrons produced by the gas ionization drift towards the MM mesh, which plays the role of the anode with respect to the central cathode (drift region).

In the conversion stage, the thin woven mesh plays the role of the cathode, and the anode can be segmented into strips or pads. The electric field in the gap between the mesh (cathode) and the pads (anode) being very intense i.e. typically $\sim$25 kV/cm in T2K's case, the ionization electrons are multiplied in an avalanche, and collected by the anode with an electron collection efficiency close to 100 %. The ions produced by the gas ionization are collected by the mesh. These two signals, the electron signal and the ion signal which is delayed with respect to the electron one, are the ones that allow the detection of the charged particles. The typical signal shape can be observed in Fig. 4.13. The smallness of the gap leads to an avalanche with small size, therefore the signal rise time is short, typically a few nanoseconds for the electron signal when there is no longitudinal diffusion, and less than 100 ns for the ion signal.

The bulk-Micromegas is one type of MM detector. In this case, both the mesh and the pads are kept together by thin photo-imaged pillars forming one unique robust structure. This robustness is one of the main advantages of this type of MPGD, since it allows the instrumentation of large surfaces, with minimal dead areas in between the modules. Moreover, the technique used to produce them is suited for industrialization and mass production, thereby being a cheap alternative to wire chambers, with advantages with respect to the latter such as the uniform electric field mentioned above and its robustness.

T2K's TPC are instrumented with 72 bulk-MM, which represents a total active surface of about 9 m^2. Each module is divided into 48 rows and 36 columns (1726 active pads + 2 pads used for the high voltage delivery) with a pad pitch of 7.0×9.8 mm^2 (Fig. 4.14). The average

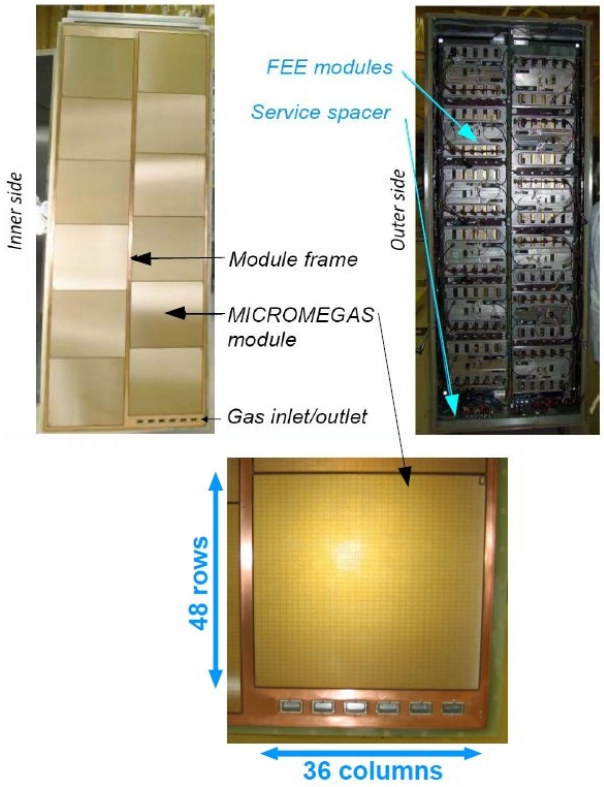

Figure 4.14: A TPC readout plane. The inner side which shows the 12 Micromegas modules can be seen in the top left picture. The top right picture shows the mounted front-end electronics. The bottom picture shows a zoom on a Micromegas module.

gain is 10^3 at a voltage of -350 V and for a 128 μm gap. This gain is high enough to have a detection efficiency close to 100 % when the detectors are operated with low-noise electronics, while reducing the probability for sparks – electric discharges between the mesh and the pads – in the amplification region and thus rendering the detector operation stable with small dead time. T2K's MM have a spatial point resolution of $\sim$700 μm at full drift distance, a time resolution of $\sim$10 ns, and low electronic noise ($<$ 700 electrons) [118].

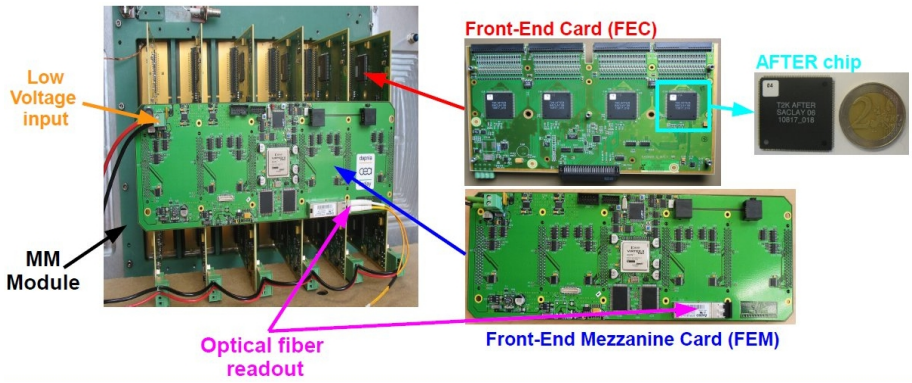

Figure 4.15: The Micromegas bulk with its front-end electronics mounted. The FEC and FEM can be seen in the middle picture.

Each Micromegas bulk is read by six front-end cards (FEC), each of them instrumented with four AFTER application specific integrated circuits (ASIC). The front-end electronics mounted on an MM module is shown in figure 4.15. The AFTER ASIC were developed at Saclay, and they are characterized mainly by their low electronic noise ($\sim$ 600 e$^-$). Their features include a sampling frequency that can go up to 50 MHz, adjustable gain, and a programmable peaking time.

A front-end mezzanine card gathers the information collected by the FECs and sends it through an optical fiber to the back-end electronics. There is a total of 124 272 electronic channels for the three TPCs.

The MM modules and electronics went through extensive test in 2006 and 2007 which validated the physics performance that could be reached with such detectors [119, 120]. In the following section we will give more recent performance results.

4.2.4 Performances

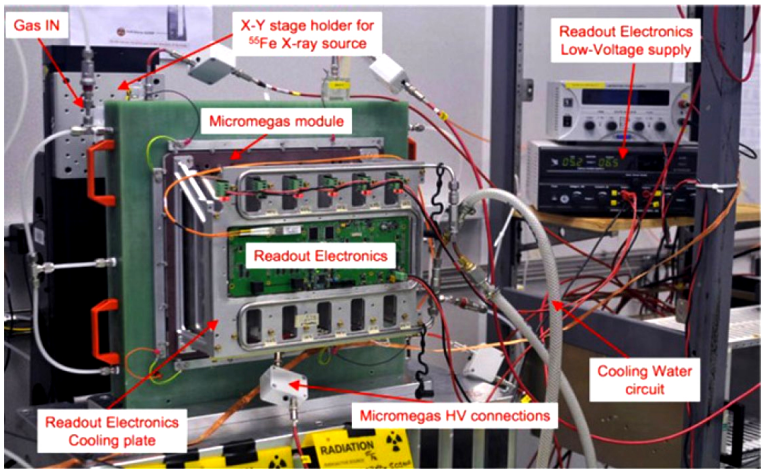

Figure 4.16: The Micromegas bulks test bench at CERN. The mechanical arm containing the calibration ^{55}Fe X-ray source used to scan the module surface can be seen.

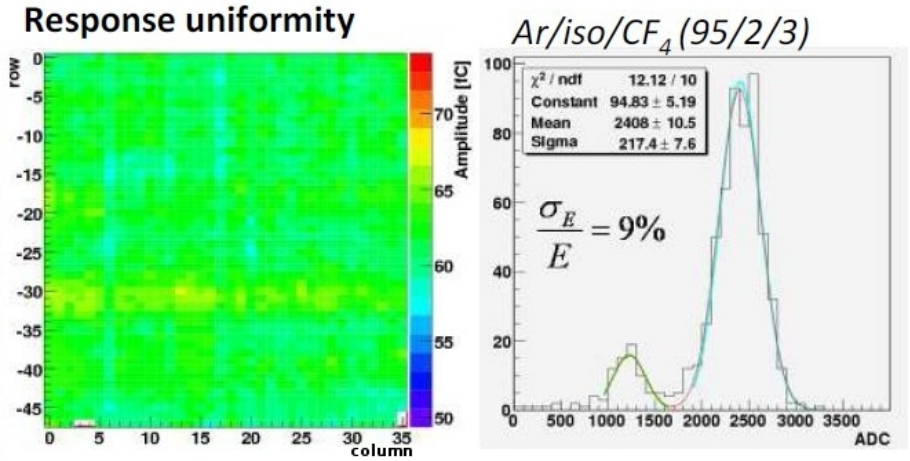

Figure 4.17: The left plot shows the uniformity of the pad per pad gain in arbitrary units. The right plot shows the energy spectrum of the ^{55}Fe source used for calibration and test purposes.

Each of the MM modules was tested prior to its installation on a test bench at CERN (Fig.4.16). I participated in some of these validation tests, which provided measurements of the gain and resolution uniformity, edge effects, and count of the number of faulty pads. The energy resolution was measured with a 5.9 keV ^{55}Fe X-ray source illuminating single pads.

The obtained spectrum (Fig. 4.17) has a resolution of about 8 % at 5.9 keV, which is also good enough to see the 2.9 keV escape line in argon. The typical r.m.s. (root mean square) dispersion or response uniformity of collected charge is better than 3 % (Fig.4.17), and only about 10 faulty pads were found out of more than 120 000 channels (<0.01 %).

These performance results take into account the differences between the channels in the routing path length from a pad to the readout connector. The path length differences might result in parasitic capacitances of a few pF, which can lead to small cross-talk effects. Using a test bench at Saclay, at the beginning of my thesis I searched for correlations between the charges measured in adjacent pads to quantify the cross-talk contribution. The measurement was done by irradiating a MM module with a collimated ^{55}Fe source, where the MM module was operated at a higher gain of about 2000, to be able to distinguish eventual cross-talk signals in the surrounding pads. We selected the pads that contained almost all of the deposited energy in a single pad (at least 95 % of the total energy). Since the fraction of energy deposited between different pads is random, the measured charges in the surrounding pads should not be correlated to that of the central pad. Any correlation between the charges is due to a cross-talk effect between the channels. We obtained that the cross-talk contribution for the pads surrounding the irradiated pad was at the level of 1 % above the noise level.

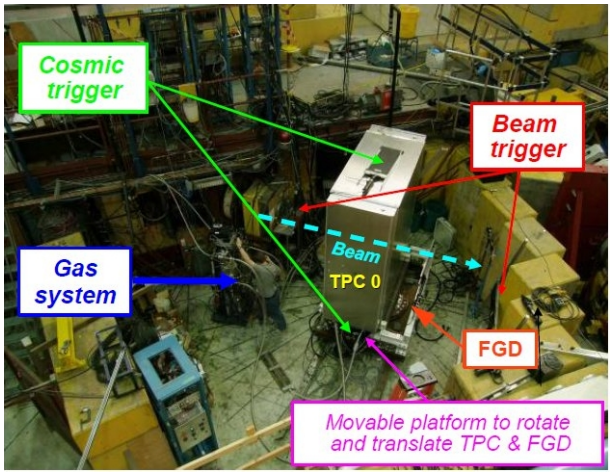

Figure 4.18: Layout of the test area at TRIUMF (Canada).

The mechanical frame of the TPCs was built at TRIUMF (Canada) while the electronics

and MM-bulks were produced by a collaboration between the CEA of Saclay and the CERN. Once the detectors and electronics were ready and tested in Europe, they were sent to TRIUMF to be mounted and tested once again, with the M11 beam which provided pions, electrons, and muons (Fig.4.18). The FGDs were also tested with this beam prior to their installation in Japan.

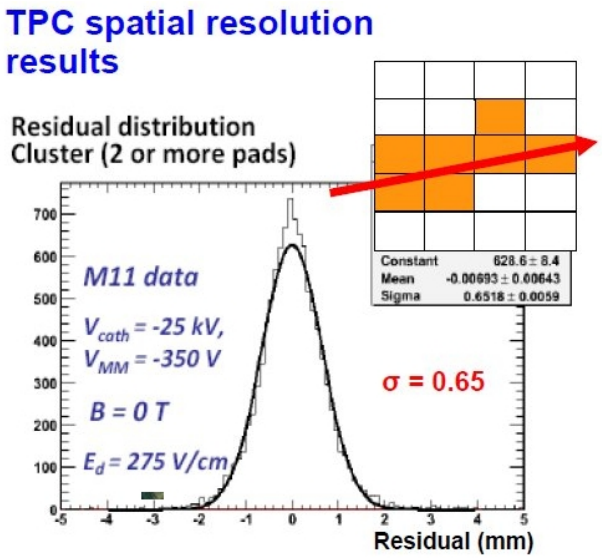

Figure 4.19: Spacial resolution measurement done at TRIUMF with beam data.

As we mentioned before, when a charged particle crosses a TPC, the deposited charge can be spread over a few pads. This neighboring pads are grouped into clusters, which are fitted to reconstruct the projection of the track on the readout plane (Sec.5.1.1). The spatial resolution is obtained through the comparison of the transverse coordinate computed by the global fit to the one resulting from a single cluster fit while fixing the other track parameters (angles and curvature). The residual distribution measured at TRIUMF is shown in figure 4.19 and the resulting spatial resolution is 650 μm at a 75 cm drift distance, which is good enough to obtain the required transverse momentum resolution of 10 % at 1 GeV.

Figures 4.20 and 4.21 show the spatial resolution as a function of the drift distance for all clusters and only for clusters consisting of two pads respectively, obtained with the T2K data. The resolution is degraded at short drift distance since the electron transverse diffusion is low and most of the clusters are just single pads, thus the resolution is limited by the pad size. The

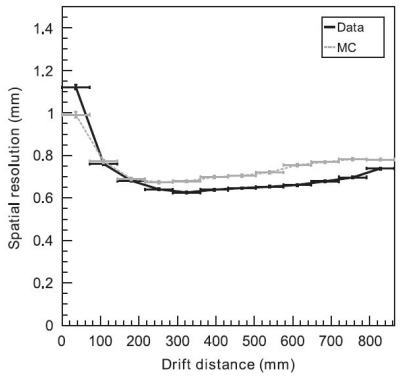

Figure 4.20: Spatial resolution per cluster as a function of the drift distance.

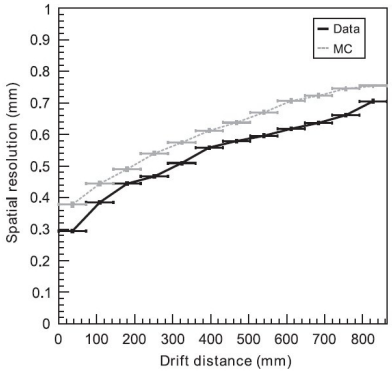

Figure 4.21: Spatial resolution as function of the drift distance for clusters made of two pads.

best resolution is obtained with clusters with two pads since the deposited charge per pad can be weighted to estimate better the true position of the point (Sec.5.1.1). Figure 4.21 shows also the dependence of the spatial resolution on diffusion, since for longer drifting distance, there is more diffusion and the resolution degrades. The results are compatible with those obtained at the TRIUMF beam tests: for a 75 cm drift distance the resolution is about 650 μm.

As for particle identification, which is one of the main goals of the TPCs, relies on the deposited energy (dE/dx), the measurement of the dE/dx resolution is also very important. The dE/dx is based on the measurement of the truncated mean of the charge deposited in each cluster (Sec.5.3.4 and [121]). The measured resolution on the energy loss is 7.8 $\pm$ 0.2% for minimum ionizing particles (Fig.4.22(a)), which is better than the 10 % requirement for the T2K physics program. With this resolution, the probability to misidentify a muon as an electron is 0.2 % for tracks with a momentum below 1 GeV/c. The distributions of the energy loss as a function of the momentum for data taken during the first T2K physics run are shown in figures 4.22(b) and 4.22(c). The data is compared to the expected curves for muons, pions, protons, and electrons, and is in good agreement with the expected values. The studied sample contained mainly negatively charged muons (Fig.4.22(b)), positively charged pions and protons (Fig.4.22(c)).

Once the data is taken, it needs to be processed so that it can be used in physics analyses. The reconstruction process will be explained in the next chapter.

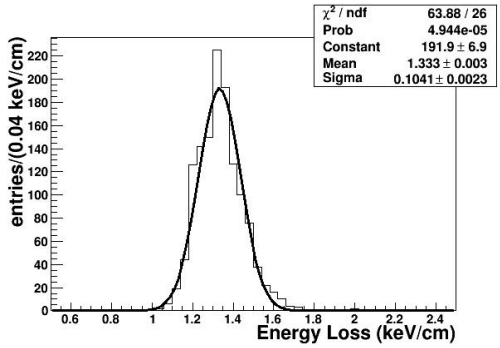

(a)

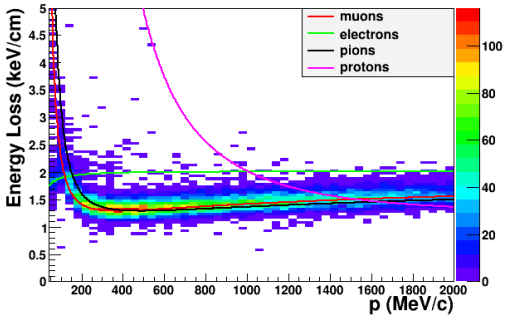

(b)

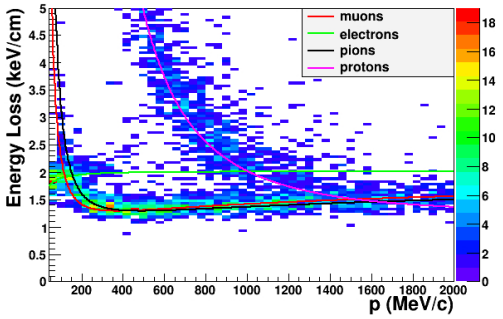

(c)

Figure 4.22: Deposited energy resolution (a) and deposited energy versus momentum for (b) negative particles and (c) positive particles.

Chapter 5

Reconstruction tools, selection criteria and validation

In this chapter we will focus on the tools and the event selection criteria used for the ν_μ flux measurement. Ideally, the flux should be reconstructed using a CCQE sample since it is the only channel that allows an accurate neutrino energy reconstruction (Sec.2.1.1). Nevertheless, for the analysis of the first T2K neutrino data, a simpler and more robust choice is measuring the flux with a charged current inclusive sample given the low statistics. Moreover, this CC-inclusive sample can serve other purposes such as being a control sample to validate the Monte Carlo (MC) simulation through data-MC comparisons and for testing the performance of high level reconstruction algorithms.

As explained in section 2.1.1, the outgoing muon momentum and angle with respect to the incoming neutrino are the physical quantities needed to compute the neutrino energy. Although the muon track is the main track we will be looking for, additional information on the event can be extracted from other tracks related to the same neutrino interaction vertex, such as the proton track. For this, the raw data taken by the ND280 detectors, and in particular by the ND280 tracker, must be processed. This means applying the detector calibration constants, matching the information taken by the different detectors, and reconstructing physical quantities or objects such as momenta, energy losses, vertices, and tracks. This is done by a series of algorithms which start at a very basic level, i.e. use the raw data provided by each detector separately, and progressively increase in complexity to go towards a reconstruction which takes into account all of the information and puts it into one unique object called a global track.

To validate this reconstruction process and be sure that the detectors are well understood, it is necessary to run simulations of the detectors and reproduce what a real neutrino event would look like. This is done through a Monte Carlo simulation which considers the detector geometry but also neutrino physics elements such as neutrino interaction cross-sections. The MC can be then used to test all of the reconstruction tools and later on to predict what should be observed with the data.

After the reconstruction, the next step before being able to measure the neutrino flux (Chap.6) is selecting an inclusive charged current sample among the neutrino interactions that took place within the FGDs of the ND280 tracker. This means tagging charged current signal events, identifying and reducing backgrounds such as the neutral current interactions and the interactions from outside the fiducial volume, and being as efficient as possible to have significant statistics while keeping a low level of contamination. This is done through a series of cuts, each of them carefully determined to yield the best result.

We will explain in section 5.1 the reconstruction principle, and focus on two different reconstruction techniques: one based on the information provided by the TPCs only, and the official full reconstruction, which takes into account all of the detectors in the ND280. Section 5.2 will introduce both the Monte Carlo simulation (MC) used to study the performances of the reconstruction tools and to predict event rates, and the neutrino data sample used for all of the analyses presented in the two last chapters of this thesis. Section 5.3 will list and describe each of the cuts performed to select the signal events for the flux measurement, the full list of cuts used for the momentum scale calibration will be given in chapter 7. In section 5.4, we will compare the MC and data selections. Then we will compare in section 5.5 the results and performance of our selection procedure with similar analyses done both with the global reconstruction tools and with TPC only objects, which will validate the use of the full reconstruction sequence. Finally, in section 5.6, we will classify the selected events into four topologies, according to the number of reconstructed tracks per event.

5.1 The reconstruction tools

The off-line software which performs the reconstruction is based on GEANT4[122] for detector simulation and on ROOT[123] for storage, handling, and analysis framework. The first step

after taking the data is calibrating it. After the calibration, the data is processed by a series of reconstruction algorithms.

We will first explain how the reconstruction of a track is done in the TPCs. Then we will introduce two different techniques to fully reconstruct an event by starting with the tracks in the TPCs. The first technique uses mainly the TPC information to fully reconstruct the event. The second technique is the official T2K reconstruction sequence which uses all of the detectors' information.

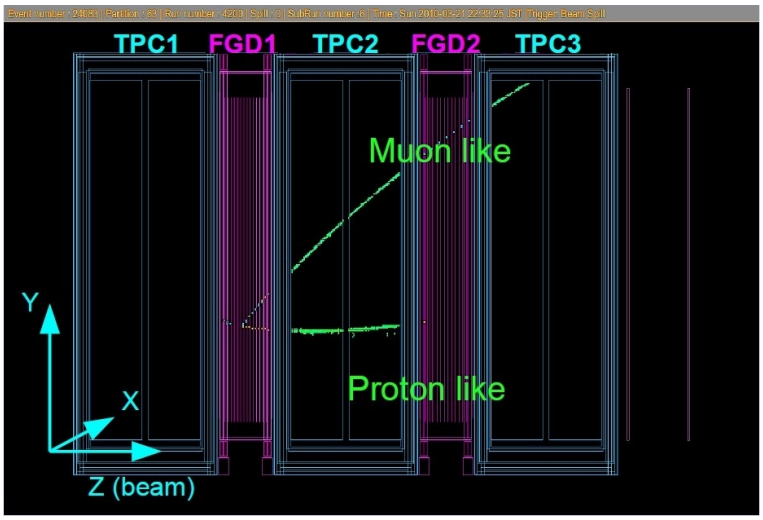

Figure 5.1: Typical neutrino event display in the near detector tracker, which shows the axes naming convention and detector numbering.

The convention for the geometrical axes naming is as follows: the Z axis is parallel to the beam direction, the Y axis is the vertical direction and the X axis is the transverse direction, parallel to the electron drift direction and magnetic field in the TPCs. The numbering of the detectors will be done as follows: TPC1 is the TPC immediately downstream the P0D, followed by FGD1, TPC2, FGD2 (which contains water targets), and TPC3 (Fig.5.1). The selection presented in this chapter and the analyses presented in chapters 6 and 7 focus on neutrino interactions that took place in FGD1 and FGD2.

5.1.1 TPC reconstruction

Charged particles which cross the TPCs ionize the gas and the ionization electrons drift towards the readout planes instrumented with Micromegas modules. These electrons deposit a certain amount of charge on the pads of the Micromegas detectors. Because of the transverse electron diffusion, which increases with the drift distance, the charge can be shared among a few adjacent pads (typically two or three pads). These charges can then be grouped into vertical or horizontal clusters by matching the waveforms – charge deposited in a pad as a function of time – which have to overlap in time and have to be consecutive in space (Fig.5.2). Since the expected tracks produced by the outgoing charged particles of the neutrino interactions tend to be horizontal i.e. parallel to the beam direction (Z axis), we will use only a vertical clustering.

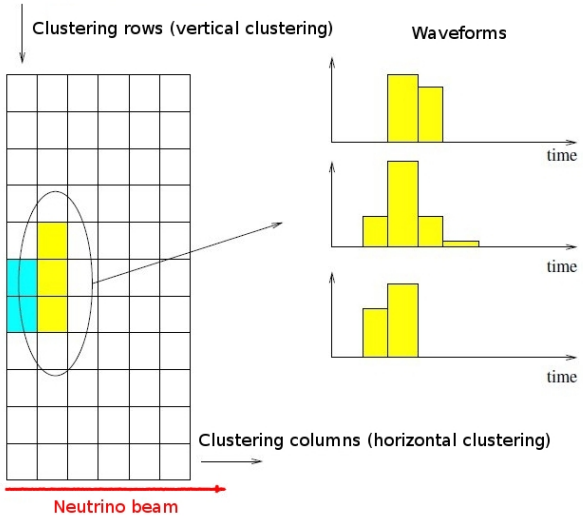

Figure 5.2: TPC clustering sketch.

Once the clustering is finished, a pattern recognition algorithm connects the adjacent clusters which overlap in time and space into segments, TPC per TPC.

The transverse – with respect to the readout plane – coordinate X is reconstructed from the drifting time, and to compute it, the time T_0 at which the track was created is required. TPCs cannot provide such kind of information because the electrons drift at a typical speed of a few cm per μs for a maximum drift distance of about 90 cm so the drifting time of the electrons is

much larger than the beam spill window (3 μs). Therefore, faster detectors signals are used to determine this T_0, such as the FGDs which provide time measurements with a resolution of a few nanoseconds, the P0D, or the Ecal. It is possible to use more than one detector to reduce the amount of false matches.

The algorithm combines the previously reconstructed segments and selects the combination which provides the longest possible track. Finally, the track is reconstructed with either a point reconstruction method or a likelihood method.

In the point reconstruction method, the position of the point cannot be estimated with a simple barycenter as the pad width is much larger than the electron cloud size. The points are reconstructed independently cluster per cluster by weighting the deposited charge per pad as described in [119].

The likelihood method uses a charge deposition distribution model to fit the track model instead of reconstructing points [124]. In both cases, the track is then fitted with an 8-parameter helix model, where the helix itself is defined by six parameters and the two additional parameters are the curvilinear abscisses of the initial and final positions of the helix . Both techniques are implemented in the off-line near detector software. The analyses presented later on use the likelihood method to reconstruct the TPC tracks.

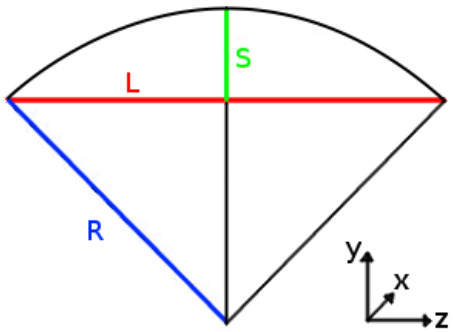

Figure 5.3: Track projection on the transverse plane with respect to the drift direction. R is the radius of curvature (blue), L is the projected track length (red), and S is the sagitta (green).

This process is repeated in each of the TPCs independently. Once the TPC track segment is reconstructed, if the magnetic field was on, then it is possible to compute the charged particle's

momentum (p_x, p_y, p_z) from the curvature of the track. In the axial uniform magnetic field $(B_x, 0, 0)$, the charged particle's trajectory is a helix. The projected trajectory on the orthogonal to the magnetic field plane is a circle arc of radius

$$R = \frac{p_t}{eB} \tag{5.1}$$

where $p_t = (p_y^2 + p_z^2)^{1/2}$ is the particle's transverse momentum, e is the electron charge, and B is the magnetic field value. Thus, the transverse momentum in GeV/c can be written as a function of the radius R expressed in meters and the magnetic field in Tesla

$$p_t \sim 0.3BR \tag{5.2}$$

The total momentum value p can be deduced from the transverse momentum and the angle ϕ between the track and the direction of the magnetic field

$$p = \frac{p_t}{\sin\phi} \tag{5.3}$$

The resolution of the momentum depends on the resolution of the transverse momentum, and the value and resolution of the angle ϕ. The resolution on the transverse momentum for a track with N equidistant points is given by the Gluckstern formula [125]

$$\frac{\sigma_{p_t}}{p_t} = \frac{\sigma_{yz} p_t}{eBL^2}\sqrt{\frac{720}{N+4}} \tag{5.4}$$

where σ_{yz} is the point resolution on the transverse plane and L the projected length of the track as defined on figure 5.3. The resolution on the angle ϕ is given by

$$\frac{\sigma_\phi}{\phi} = \frac{\sigma_x}{L}\sqrt{\frac{12(N-1)}{N(N+1)}} \tag{5.5}$$

We will show in section 5.3.1 how many clusters per track are needed to have a proper momentum reconstruction.

5.1.2 Simple reconstruction

It is possible to reconstruct the neutrino interaction vertices and compute the momentum at the vertex position, by using only the reconstructed information provided by the TPC and the calibrated FGD hits. Once the tracks have been reconstructed in the TPCs as described in the previous section, they are extrapolated into the FGDs as follows:

- TPC2 (resp. TPC3) tracks are extrapolated back to FGD1 (resp. FGD2) ;
- a circular extrapolation is used in the y-z plane since the projection of the track on this plane is a circle arc (Fig. 5.4 left side) ;
- a linear extrapolation is used in the x-z plane. The helicoidal track projection in this plane is a sinusoid but given the weak magnetic field, the projection can be approximated by a straight line (Fig. 5.4 right side).

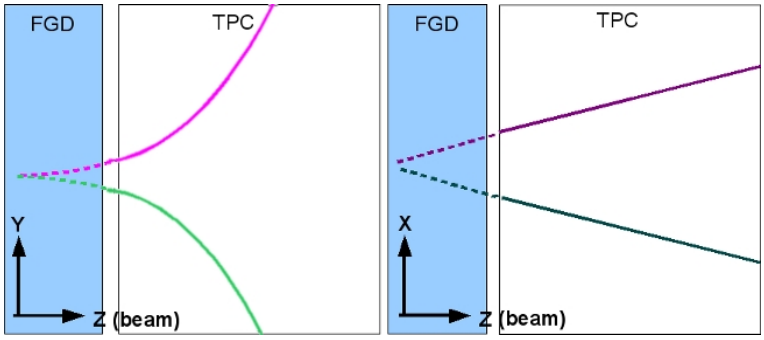

Figure 5.4: A schematic view of the TPC track extrapolation in the y-z plane (left) and x-z plane (right).

Once the tracks have been extrapolated, given the FGD granularity ($\sim$1 cm), FGD hits that are at a distance smaller than 3 cm are considered to be associated to the track. The starting point of the track in the FGD will be given by the associated hit which has the lowest z i.e. the most upstream FGD hit.

With the starting point defined, it is possible to compute the energy and momentum of the particle at the vertex since the type and amount of matter crossed by the particle is known. A simple approach to compute the energy loss in the FGDs, which is not negligible given the material density of the scintillator bars, is to consider that the curvature of the track remains the same and that the energy loss per unit of length does not depend on the momentum.

This method has the advantage of being simple and robust, and can be used as a tool for validating the performances of higher level algorithms like the global reconstruction which will be explained in the next section. A simplified version of this technique, which does not include

the FGD hit matching, is used to reconstruct vertices for the K^0_s events in the absolute momentum scale calibration presented in chapter 7. The constant energy loss approximation is rather close to reality for the pions produced by the K^0 decays, which have energies varying from 0.1 to 1 GeV. More details on this will be given in chapter 7.

5.1.3 Global reconstruction

After the TPC tracks have been reconstructed individually, the reconstruction is done in all of the other detectors, in particular in the FGD and the ECal. Since the analyses presented later on use data that was taken prior to the installation of the barrel ECal, the reconstruction used for the analysis is only based on TPC and FGD information.

The first step after the TPC reconstruction, is the same as the previous method: tracks are extrapolated into the FGDs and hits which are compatible with the track are associated to it. A first Kalman filter algorithm[126], which considers the material distribution in the detectors, is applied on both the FGD hits and TPC tracks to obtain a tracker track and improve momentum reconstruction. The energy loss in the FGDs is computed and takes into account multiple scattering within the FGDs. The unmatched hits in the FGDs are associated among them to form isolated FGD tracks. The tracker tracks are then extrapolated to the other detectors (ECAL, P0D, SMRD) and matched with the tracks reconstructed in these detectors to form the longest possible track. Once again, the full track (global track) is fitted altogether with a Kalman filter algorithm.

This is the type of tracks we will be using for the ν_μ flux measurement, except that we will only use the segments of the global track corresponding to the TPCs and FGDs.

5.2 Monte Carlo simulation and data samples

To be able to understand the data taken with the detectors, it is important to run simulations of the expected events, both to validate analysis tools and to understand the detectors. For this Monte Carlo simulations are run. In this section we will briefly describe the T2K near detector Monte Carlo simulation and then we will introduce the data sets used for the analyses presented in this thesis.

5.2.1 The near detector Monte Carlo simulation

The Monte Carlo simulation is done in three main steps: the neutrino beam simulation, the neutrino interactions generations, and the detector response simulation.

The first step in the MC simulation chain is generating the neutrino beam. It begins with the injection of 30 GeV protons into the graphite target, whose interactions with the target's nuclei and subsequent secondary particles are simulated with two different softwares. The Monte Carlo files used in our analyses were produced with the native GEANT3 [127] hadron production package GCALOR. Since then, the simulation chain has been improved, therefore when fitting the data to extract the ν_μ flux (Sec.6.2), we will use a more recent flux simulation which is based on FLUKA2008 [128] and which has been tuned to the NA61/SHINE data [129, 130], a hadroproduction experiment at CERN which uses a replica of T2K's target. The produced particles are then transferred to JNUBEAM, a specific simulation code for the J-PARC neutrino beam based on GEANT3, which was developed to predict the neutrino flux at the ND280 and Super-Kamiokande. This simulation replicates the geometry of the secondary beamline, in particular it includes the horn magnetic fields.

The second step is generating the neutrino interactions with the nuclei present in the detectors. This is done with either GENIE[131] or NEUT[68] neutrino generators. We have chosen to use NEUT, a well-known neutrino generator since it is the one used by Super-Kamiokande, which produces a list of neutrino interactions and their outgoing particles from the neutrino flux and energy spectrum simulated previously, taking into account the detector's materials distribution. NEUT's theoretical framework and parameter values were given in chapter 2. We will use GENIE, which has a different theoretical framework and parameters, to compare the results obtained with both neutrino generators and understand better the systematic errors related to the cross-sections and final state interactions in section 6.5.2.

The output of the neutrino generator is passed through the detector simulation, where GEANT4 is used to simulate the energy deposits in the detector, which is divided into small volume cells, considering all the materials that can be found in the ND280 detectors (including glue, screws and mechanical frames), size and position of the different parts of the ND280. Finally, the response of the active detectors such as the scintillator bars, fibers, TPC electron

drift, and readout electronics is simulated through a custom-written code called elecSim. The output is then treated as if it were real data, and goes through the whole reconstruction chain, explained in the previous section.

The amount of Monte Carlo produced is given in equivalent number of protons on target (POT) so that it can be compared to the data sample. For the flux analysis we use a total of $9.82 \cdot 10^{20}$ POTs. The MC numbers presented in the following sections have been normalized to the data POTs, the normalization factor being $POT_{MC}/POT_{DATA} = 33.8$.

5.2.2 The data sets

The data set used in this thesis is the data taken from January until June 2010 (called 2010a data set). I did a one month stay in Japan to participate actively in this period of data taking, both as a TPC detector expert trainee and as a shifter. The selected runs went through quality checks to ensure the data was taken in a proper environment i.e. the magnet was turned on (momentum can be measured) and that the required detectors for the analyses did not present any anomaly. For our analyses we haven chosen all runs which were flagged as good runs – no problem in any detector – or bad because of a P0D or SMRD only problem, since we will only consider FGD and TPC data. The computed POT number for these runs is $2.91 \cdot 10^{19}$ POTs. The sample we use is slightly different from the ones used by the analyses we will be comparing to for tool and selection validation, which accounts for a difference of a few percent between our numbers and the reference ones.

5.3 Inclusive charged current selection criteria

For the ν_μ flux measurement, we are interested in selecting a sample of ν_μ charged current interactions only, $\nu_\mu + N \rightarrow \mu^- + N'$. Charged current interactions are tagged by the outgoing charged lepton track, thus we look for events that have an outgoing negative muon track. The muon is, most of the time, the negative particle that carries most of the momentum among the outgoing particles. Therefore the selected track should be the highest momentum track among the negative ones, should there be more than one track.

To measure the ν_μ flux we will select interactions that take place only in either of the FGDs by defining a fiducial volume in which the reconstructed neutrino vertex must be contained.

Consequently, tracks coming from outside such as sand muons or interactions in any other part of the near detector (including the magnet), and other backgrounds such as π^0 conversions are rejected. The definition of a fiducial volume is also important since the exact number of target nuclei is required to compute the ν_μ flux. Once the fiducial volume cut has been applied, we must ensure that the selected track is compatible with the muon hypothesis and not with the electron hypothesis. This is done with the particle identification cuts.

In this section we will explain each of the cuts applied to the samples to select our charged current sample. We will first discuss the track length cut, which ensure proper momentum and energy loss reconstruction. Then we will move onto the highest momentum negative track choice. Thirdly, we will explain the fiducial volume definition. Finally we will focus on the particle identification cuts.

5.3.1 TPC track length

To properly tag a signal event, we need to have at least one reconstructed track. We require that this track has one successfully reconstructed TPC segment so that we can access all the information needed for a proper selection, such as the momentum of the particle, the deposited energy to apply the particle identification algorithms. Nevertheless, simply reconstructing a track is not sufficient to ensure the quality of the track. This is why we require that the track has a minimum number of points, each point corresponding to a cluster of Micromegas pads as defined in section 5.1.1 (for the Y and Z coordinates) with its correponding timing information (for the X coordinate).

The width of a single TPC is 72 pad columns, therefore a track crossing a single TPC should have at most 72 points unless the track spirals. Figure 5.5 shows the track length distribution, where two peaks can be observed: one at 72 points, which is the full TPC, and one at 36 points which corresponds to one Micromegas module width. Thus, tracks should have at least 18 points (1/4 of a TPC) to be sure that both the momentum and energy loss are properly reconstructed. A study done by another T2K group shows that the purity of their selection of μ candidates (from charged current interactions) is quite stable when varying the number of required points (Fig.5.6). In particular, loosening the cut does not improve the efficiency greatly since most of the tracks have more hits that required (Fig.5.5) and tightening it only decreases the efficiency of the selection.

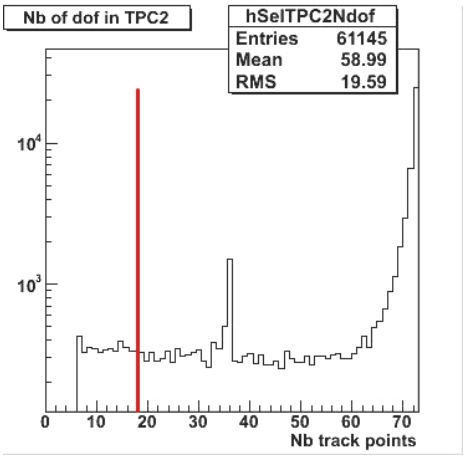

Figure 5.5: Single TPC tracks' number of points before cuts. The TPC reconstruction requires at least 6 points to reconstruct a track. The minimum number of points required for a single TPC is shown in red.

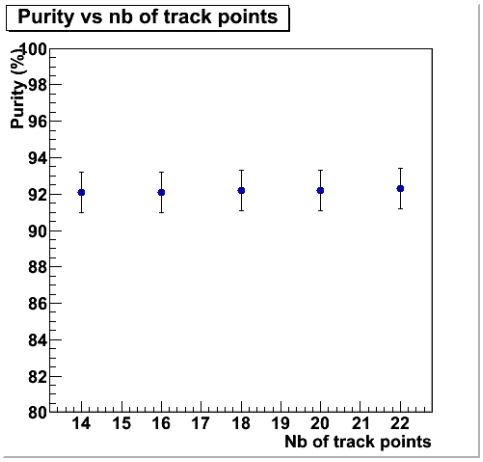

Figure 5.6: Purity of the sample vs minimum required track points as shown by another T2K group.

5.3.2 Highest momentum negative track

In true ν_μ charged current interactions, the outgoing negative muon is the lightest primary particle produced and most of the time it is the particle that carries most of momentum among the negatively charged particles. Therefore, we first select all the negative tracks and then we look for the one that has the highest momentum among them. Once we have selected the highest momentum negative track, we check if this track is the absolute highest momentum track in the event. Figure 5.7 shows that 73 % (resp. 67.4 %) of the selected tracks in the data sample (resp. MC sample) were also the highest momentum track in the event at this stage of the selection. The remaining 27 % (resp. 32.6 %) correspond to a positively charged particle, thus we cannot just select the highest momentum track but must also require that the track corresponds to a negatively charged particle.

After all the cuts up to the PID cuts have been applied, 80 % (resp. 85.3 %) of the muon candidate tracks in the data sample (resp. MC sample) are indeed the highest momentum track in the event (Fig.5.8). The differences between data and MC before and after the cuts will be explained in section 5.4.

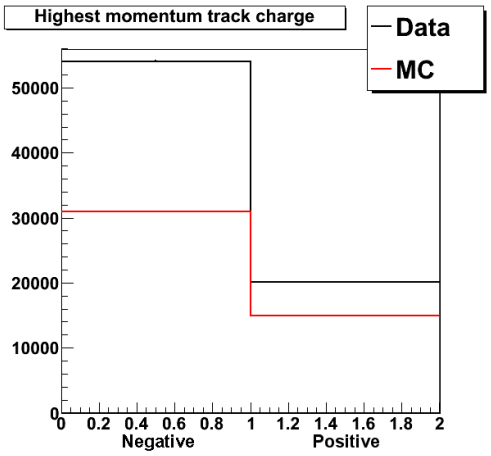

Figure 5.7: Charge distribution of the highest momentum track per event after selecting the highest momentum negative track, for both the data and the normalized to POT_{DATA} MC samples. Bin 0 represents the negative tracks and bin 1 the positive tracks.

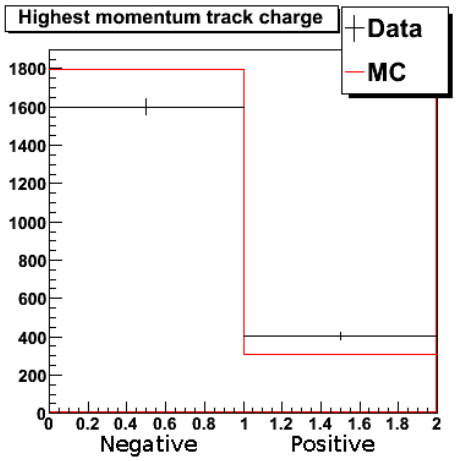

Figure 5.8: Charge distribution of the highest momentum track per event after full selection, where 0 represents negative tracks and 1 positive tracks, for both the data and the normalized to POT_{DATA} MC samples.

A short study which used both methods, i.e. choosing the highest momentum track and requiring it to be negative (method 1) or choosing the highest momentum track among the negative ones (method 2), yielded the efficiencies and purities for each method (Tab.5.1, [132]). This study was done with the latest software release and processed data from the 2010 and 2011 T2K runs, thus the numbers presented in table 5.1 are different from our results. The first method yields a data/MC ratio which is closer to one and a slightly higher purity while the second method has a higher efficiency. Both methods can be used, the choice depends on what the aim of the analysis is. In our case, we have chosen the highest efficiency method since we are only using the data of the first data taking period.

Charge misidentification has been estimated to be 1.6 % for data and 1.9 % for MC for tracks with at least 40 points [133]. We will show in section 5.4 that the contamination due to positively charged particles, due to wrong charge reconstruction, is of the order of a few percent.

	Max. momentum then neg.	Neg. then max. momentum
Selected events (data)	7307	8845
Run 1	1747	2101
Run 2	5560	6744
Ratio data/MC	1.009±0.013	1.054±0.012
CC purity	0.925±0.001	0.894±0.001
Wrong charge	0.025±0.001	0.029±0.001
CCQE	0.509±0.002	0.460±0.002

Table 5.1: Comparison between two different selection methods: selecting the highest momentum track then requiring it to be negative, or selecting the highest momentum track among the negatives ones. Run 1 is the data taking period from January to June 2010, while run 2 is the period between fall 2010 and March 2011. For our analysis we only consider the run 1.

5.3.3 Fiducial volume

The next step in the selection is defining a fiducial volume (FV) in which the reconstructed neutrino interaction vertex must be. This volume must be carefully determined because it plays a key role in the background reduction. Indeed, neutrinos do not leave any track thus it is not possible to precisely determine where they interacted. Typical backgrounds rejected by this cut are sand muons – muons which come from the natural radioactivity in the pit or from neutrino interactions with the surrounding rocks and sand – which cross the detectors, interactions which take place in the detector walls, magnet, or other detectors, and cosmic rays. Moreover, the definition of a well-known volume is needed to compute the exact number of target nuclei in it, required for the flux measurement (Sec.6.3.3.2).

A common effort between the T2K Barcelona, Geneva and Valencia groups [134] yielded the best values to define the fiducial volume, based on efficiency and purity optimizations for each FGD_i (i= 1,2) where

$$\text{Efficiency}_i = \frac{\text{true CC candidates with both true and reconstructed vertex in the FGD}_i\text{ FV}}{\text{true CC candidates with true vertex in the FGD}_i\text{ FV}} \tag{5.6}$$

$$\text{Purity}_i = \frac{\text{true CC candidates with both true and reconstructed vertex in the FGD}_i\text{ FV}}{\text{CC candidates with reconstructed vertex in the FGD}_i\text{ FV}} \tag{5.7}$$

The optimization study (Fig.5.9) shows that the best fiducial volume cuts consist in removing the most upstream along the beam direction X-Y scintillator layer of each FGD (fiducial cut on

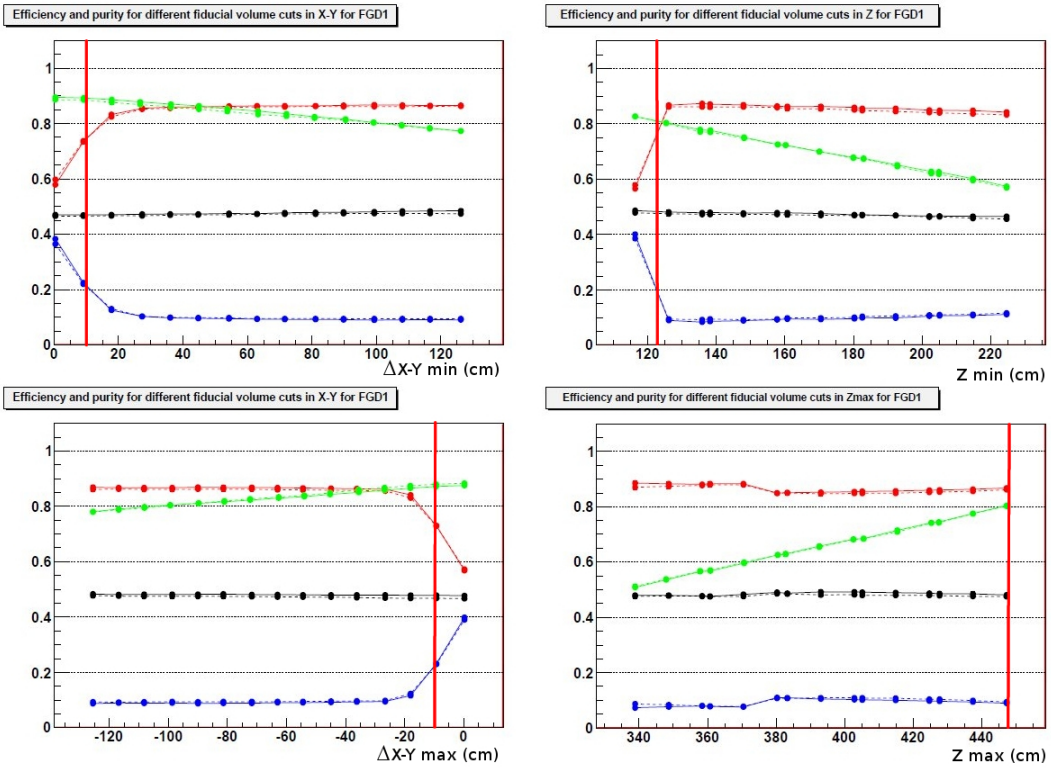

Figure 5.9: Efficiency (black), purity (red), external background (blue), and fraction of true vertices in the FGD1 FV over the total number of true vertices in FGD1 (green) as a function of $\Delta X^{fid}_{min} = \Delta Y^{fid}_{min}$ (top left), $\Delta X^{fid}_{max} = \Delta Y^{fid}_{max}$ (bottom left), Z^{fid}_{min} (top right) and Z^{fid}_{max} (bottom right) position in cm for FGD1 only. $\Delta X^{fid}_{min/max}$ (resp. $\Delta Y^{fid}_{min/max}$) is defined as the distance to the X (resp. Y) FGD edge in cm. Similar studies were done for FGD2.

the Z position, where Z is considered to be parallel to the beam axis), and removing a 10 cm wide border in the transverse plane (X and Y positions, where X is the drift axis and Y the vertical axis) (Fig. 5.10). The exact values for each cut with respect to the position of the FGD edges are given in table 5.2.

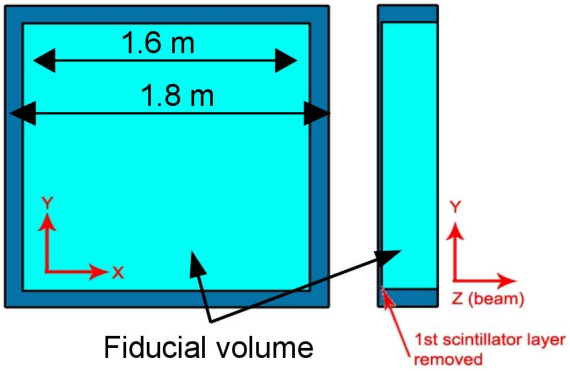

Figure 5.10: FGD fiducial volume schematic view. The dark blue areas show the removed volume.

	FGD_1 edge	FGD_1 FV cut	FGD_2 edge	FGD_2 FV cut
X_{min}	-932.17	-832.17	-932.17	-832.17
X_{max}	932.17	832.17	932.17	832.17
Y_{min}	-877.17	-777.17	-877.17	-777.17
Y_{max}	987.17	887.17	987.17	887.17
Z_{min}	115.95	123.35	1473.95	1481.35
Z_{max}	447.05	447.05	1807.05	1807.05

Table 5.2: Fiducial volume cuts with respect to the FGD physical edges.

This is the fiducial volume definition [1] that will be used for the flux analysis described in chapter 6.

[1]For comparison purposes and validation of the global tools, we use a more stringent fiducial volume which was defined prior to the fiducial volume optimization. The values for this fiducial are $|x| < 80$ cm, $|y| < 80$ cm, and $14 < z < 50$ cm for FGD1 (resp. $153 < z < 185$ cm for FGD2).

5.3.4 Particle identification

The particle identification (PID) is computed with a truncated mean method and is based on the "pull" distribution of the energy loss in the TPCs. The PID pull P_x is computed for each particle type x, where x can be a muon, proton, pion, or electron, and is defined as

$$P_x = \frac{C_{meas} - C^x_{exp}}{\sigma^x_{exp}} \tag{5.8}$$

where C_{meas} is the track measured truncated charge, C^x_{exp} is the expected deposited charge for the particle x hypothesis, and σ^x_{exp} is the uncertainty on the energy loss and on the momentum reconstruction. Further details can be found in [121].

Although theoretically these distributions should be Gaussian distributions with a mean value equal to zero and a sigma of one when the particle is really the expected one, some corrections need to be applied because of detector calibration issues. In our case, we applied an overall – the same for all TPCs and runs – rough correction to the muon and electron pull values so that they were properly centered. The correction applied on the MC is slightly different to that of the data. With the corrections done, we are ready to cut on the pull, according to which kind of particle we want to select. The pull is computed for each TPC separately, thus we will apply the cut only on the TPC track segment which is closest to the primary vertex event if the track crosses several TPCs, since cutting on all TPC segments mainly reduces the efficiency of the selection without really improving the purity of the sample[1].

First of all, we want to make sure our candidate track is compatible with the muon hypothesis. Thus we require the absolute value of the muon pull to be smaller than 2.5 [2]. Figure 5.11 shows the muon pull distribution for each TPC before the cut. Although most of the selected tracks are compatible with the muon pull hypothesis, the pull distribution presents long tails on both sides with respect to the central value. These tails are due to a calibration issue. At the time the data was processed, the fluctuations of the calibration parameters over time, i.e. their changes from one run to another, were not taken into account. Moreover, the TPC3 shows

[1] It is possible to use a likelihood cut which combines the PID information from all the TPC segments, which would not lower the efficiency. We chose not to use such method to remain simple and robust.

[2] For comparing our selection to the one using TPC objects only and for the global tools validation, we use a stricter cut on the muon pull, cutting at $P_\mu = 2$ instead of 2.5. For the flux measurement, we go back to the looser value mentioned previously.

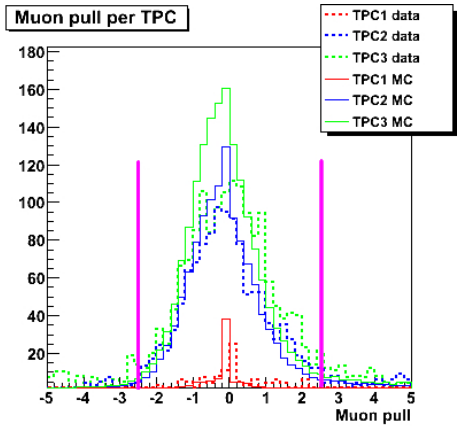

Figure 5.11: Corrected muon pull per TPC before the muon pull cut for data and MC. The magenta lines show the muon pull cut.

longer tails and a wider pull distribution than the other TPCs. Indeed, TPC3 gain fluctuated more over time than the other two TPCs and had a Micromegas module with lower gain than expected because of a faulty electronic component. Most of these calibration issues have been corrected recently but it has not been confirmed yet whether they have been fully corrected or not, which is why we have not used the most up to date data processing. This calibration issue will lead us to a few disagreements between data and MC distributions later on, which will be dealt as a systematic error on the flux measurement (Sec.6.5.2.4).

Likewise, tracks that are consistent with the electron hypothesis must be rejected. For this we require the absolute value of the electron pull to be greater than two. Figure 5.12 shows the electron pull distribution prior to the muon pull cut, which can be divided into two distributions. The distribution that has a peak at an off-centered value, corresponds to the selected tracks which are most likely to be muon tracks. The second peak, centered around 0, corresponds to the electron like tracks, which should be rejected. Figure 5.13 shows the electron pull after the muon pull cut. The muon pull cut reduces greatly the amount of tracks which were compatible with the electron hypothesis. The electron pull cut is used to further improve the electron rejection.

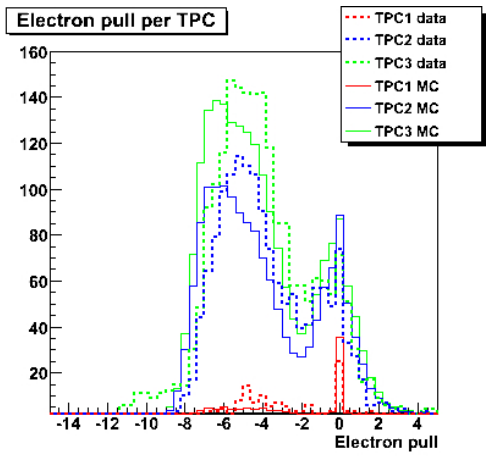

Figure 5.12: Electron pull per TPC before the muon pull cut.

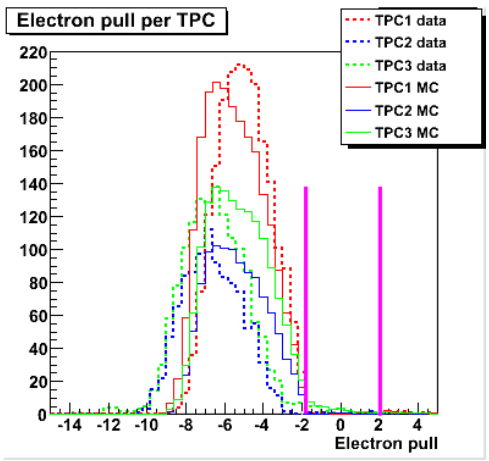

Figure 5.13: Electron pull per TPC after muon pull cut. The magenta lines show the electron pull cut.

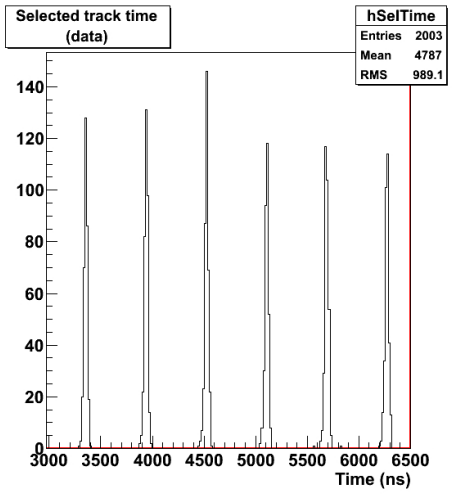

Figure 5.14: Track timing after selection, for neutrino data only. No event is seen out of the spill bunches.

5.3.5 Event pile up

As explained in section 3.2, the neutrino beam was delivered in six neutrino bunches spills during the first period of data taking. A possible source of systematical uncertainty is related to events which present more than one neutrino interaction in the FGDs for a single spill. To reduce the pile up effect, before applying the selection, it is possible to sort the tracks according to the time bunch they belong to. Although the simulated beam power used to generate the MC (100 kW) was higher than the real beam power delivered during the first period of data taking (50 kW), only a few events over several thousands had more than one neutrino interaction in the FGDs fiducial volume, therefore we deemed the track bunching not necessary. Figure 5.14 shows that in our sample there is almost no event in-between bunches. This simplification might not be valid for the second period of data taking (from fall 2010 until the earthquake in March 2011) since the beam power was increased up to about 150 kW.

5.4 Data vs. Monte Carlo selections

In this section we will compare data and MC selected events, to check the agreement between both. We will first compare the number of selected events after each cut. Then we will compare the muon candidate main distributions, such as momentum, angle with respect to the beam axis and vertex position. Finally, we will study the composition of our selected sample in terms of purity and efficiency.

5.4.1 Reduction table

Table 5.3 gives the number of events after each cut and the corresponding relative cut efficiency, defined as the ratio of the number of events after the cut to the ones before the cut. The total number of events selected in the data is 2003 events versus 2106 events for the Monte Carlo, i.e. a data/MC ratio of 95.1 %. This 5 % difference between data and Monte Carlo has not yet been fully understood. The main contribution to the discrepancy comes from a muon pull correction issue since after the FV cuts and before the PID cuts, data and MC are consistent within the statistical fluctuations.

The first difference we notice between data and MC is after the selection of the highest momentum negative track. More events are selected in the data than in the Monte Carlo. This is

Cuts	Data	Data efficiency	MC normalized	MC efficiency
Nb spills	891 328	-	388 757.8	-
1 neg. TPC track	58 596	6.6%	32 916.7	8.5%
Fiducial volume	3 114	5.3%	3 147.6	9.6%
FGD1	1 504	-	1 535.4	-
FGD2	1 610	-	1 612.2	-
Muon PID cut	2163	69.5%	2 251.8	71.5%
FGD1	1 083	72%	1 107.4	72.1%
FGD2	1 080	67.1%	1 144.4	71%
Electron PID cut	2003	90.8%	2105.9	93.5%
FGD1	1 001	92.4%	1 038.8	93.8%
FGD2	1 002	92.8%	1 067.1	93.3%

Table 5.3: Reduction table for data and normalized to data POTs Monte Carlo.

due to the important amount of sands muons – muons coming from neutrino interactions with the surrounding sand and rocks – crossing the detectors, which are not simulated in the MC and that are not yet rejected by our selection. Here they represent $\sim$42 % of the most energetic negative tracks.

The second main disagreement stands at the level of the first PID cut, the muon pull cut. Before the muon PID cut, the data/MC ratio is 99 % whereas after the cut the ratio decreases to 96 %. As explained in section 5.3.4, neither the fluctuation of the calibration constants from run to run nor the fact that TPC3 gain fluctuated more than the the gain of the other two TPCs were taken into account when correcting the muon pull distributions, leading to longer tails on the data pull distributions and an overall pull width larger for TPC3 than for the other two TPCs. This effect will be dealt as a systematic error (Sec.6.5.2.4).

One important thing which has to be pointed out is that the efficiencies in both FGDs are very close after the final cut on electron pull. Indeed, both FGDs have the same mass, and although the second FGD has additional water targets, we expect to have approximately the same amount of neutrino interactions in each.

5.4.2 Muon candidate main plots

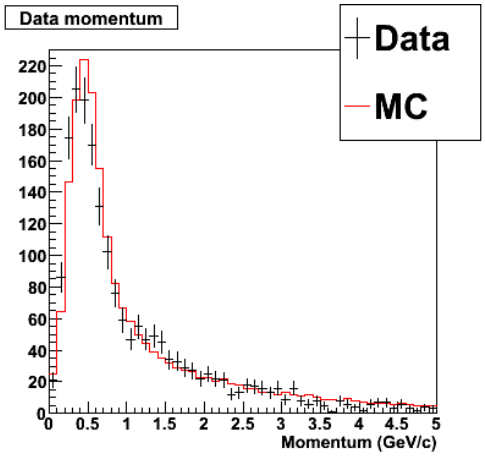

Figure 5.15: Data vs Monte Carlo reconstructed momentum at vertex for muon candidate tracks.

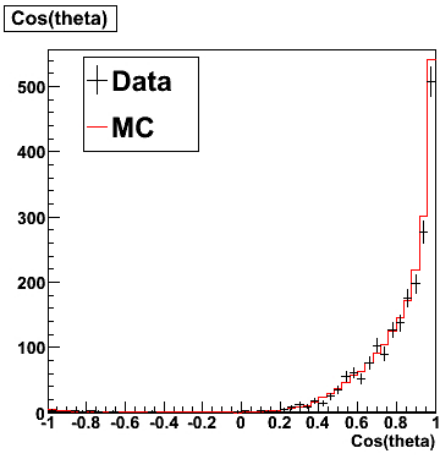

Figure 5.16: Data vs Monte Carlo reconstructed $\cos\theta$ for muon candidate tracks, where θ is the angle of the outgoing track with respect to the neutrino beam direction.

As explained in section 2.1.1, neutrino energy reconstruction requires the muon momentum and angle with respect to the incoming neutrino to be known. Figure 5.15 shows the reconstructed momentum at vertex of the muon candidate tracks for neutrino data and MC (normalized to the data POTs) after all cuts have been applied. There is an overall good shape agreement between Monte Carlo and data, although a small MC excess around the 500 MeV region can be seen. The cosine of the angle θ (track angle with respect to the ND280 Z axis) is shown in figure 5.16. We notice that most of the tracks are forward going ($\cos\theta > 0$). Although the neutrino beam reaches the near detector with an angle of 2.5 °, we will consider that the beam axis is parallel to the Z axis. Therefore, θ will be used as an approximation of the angle of the outgoing muon with respect to the neutrino beam direction.

Also, it is important to look for any anomalies in the position of the reconstructed vertex since it is needed to define the fiducial volume and also because it could indicate a reconstruction issue or a wrongly simulated effect or background. Figure 5.17 shows the position of the reconstructed muon candidate vertex for both data and MC samples, which are in good agreement. The X distribution is flat as expected since the neutrino beam is homogeneous in the X direction. The Y distribution presents a small negative slope. Indeed, the neutrino beam is up-

ward going with an angle of 2.5° with respect to the Z direction thus more events are expected in the bottom part of the tracker (negative Y). Finally, the Z distribution shows clearly the FGDs internal structure, in particular the empty areas correspond to the FGD2 water targets. Also, the efficiency increases with Z because the multiple scattering and energy loss dicrease as the vertex gets closer to the FGD edge.

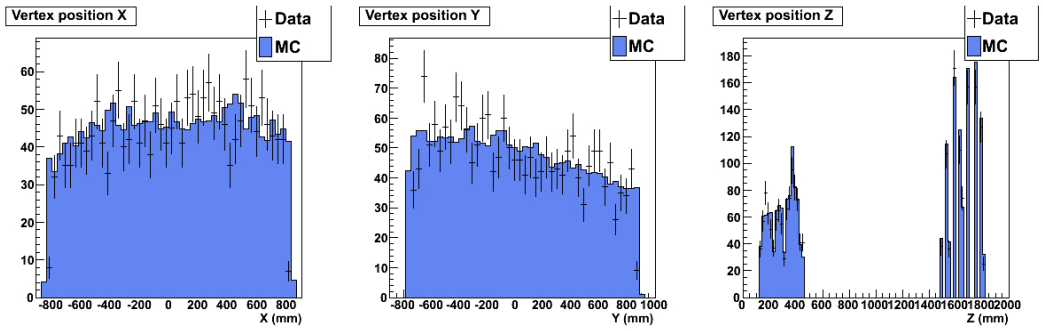

Figure 5.17: Reconstructed μ^- candidate vertex position for data and MC.

5.4.3 Selection purity and efficiency

Using the MC truth information, the selection efficiency and purity for a given ν_μ interaction channel i (CCQE, CC1π, etc.) in a defined fiducial volume (FV) can be computed as follows:

$$\text{Eff}_\text{i} = \frac{\text{Selected true } \nu_\mu \text{ with reconstructed and true vertex in the FV for the channel i}}{\text{Generated } \nu_\mu \text{ in the FV for channel i}} \quad (5.9)$$

$$\text{Purity}_\text{i} = \frac{\text{Selected true } \nu_\mu \text{ with reconstructed and true vertex in the FV for the channel i}}{\text{Total number of CC candidate events with reconstructed vertex in the FV}} \quad (5.10)$$

Both the efficiencies and purities for each interaction channel are summarized in table 5.4. The selected tracks come mainly from charged current interactions as expected, with a CC inclusive purity of 84.35 %. The main contributions are CCQE interactions (42.71%) and single π production (23.94 %) events. Neutral current contamination accounts only for 2.7% while other neutrino contributions, such as the $\overline{\nu}_\mu$, ν_e, and $\overline{\nu}_e$ interactions (selected events which have passed all the cuts, but whose parent neutrino was not a ν_μ) are below the percent level.

The main contamination in our sample is the "out-of-FV" tracks, i.e. tracks whose reconstructed vertex is within the FV but not their true vertex. Figure 5.18, which presents the

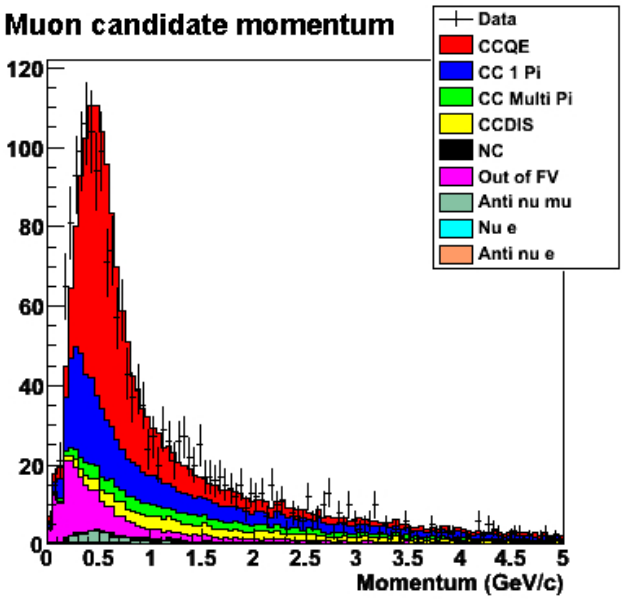

Figure 5.18: Reconstructed μ^- candidate momentum break down into true interaction channels.

	Selected evts.	Generated evts.	Efficiency	Purity
CCQE	30 389	69 046	44.01 %	42.71 %
CC1π RES	15 109	34 917	43.27 %	21.24 %
CC1π COH	1 924	3 036	63.37 %	2.7 %
CC Multi-π	5 693	10 476	54.34 %	8 %
CCDIS	6 104	11 385	53.61 %	8.58 %
CC Other	792	1 483	53.41 %	1.11 %
True CC	60 011	130 343	**46.04 %**	**84.35%**
NC	1892	52 193	-	2.66 %
$\overline{\nu}_\mu$	699	8 060	-	0.98 %
ν_e	143	3 486	-	0.2 %
$\overline{\nu}_e$	40	415	-	0.06%
Out of FV	8 361	-	-	11.75 %
Total CC-like events	71 146	-	-	-

Table 5.4: Overall selection efficiency per interaction channel, computed with the MC sample. The numbers have not been normalized to the data POTs.

distribution of the different interaction channels as a function of the reconstructed muon candidate momentum, shows that these out-of-FV tracks correspond mainly to low momentum particles. The curvature of these tracks is large, in particular in the FGDs where they lose more energy. Consequently, the reconstruction can miss hits which should be associated to this track and considers the tracks starts in the FGD when it actually came from outside the FV. Figures 5.19 and 5.20 show the position of the true vertices for the selected MC events tagged as out-of-FV, where we can see that these tracks come from all sides. Later on, when we define the event topologies in 5.6 for the flux analysis, we will demonstrate that it is mainly events with only one reconstructed track which have the highest contamination.

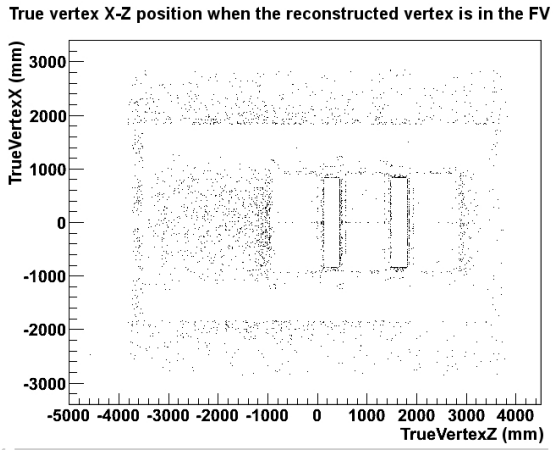

Figure 5.19: MC true vertex position in the X-Z plane for events which have a reconstructed vertex in the FV but a true vertex out of it.

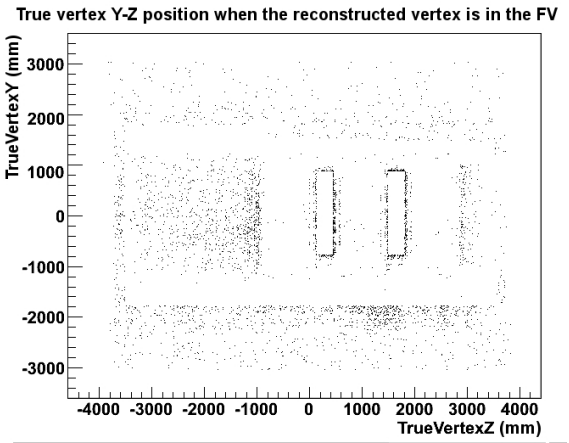

Figure 5.20: MC true vertex position in the Y-Z plane for events which have a reconstructed vertex in the FV but a true vertex out of it.

The inclusive charged current sample break down into true particle types, i.e. as a function of the true particle name of the selected track, is given in the table 5.5. After all cuts have been applied, the sample is mainly made up of muons (86.75 %) as expected, where 5.3 % of the selected muons have a true vertex out of the fiducial volume. The main sources of contamination are pions, mainly negative ones but also positive ones, due to charge misidentification. The energy loss curve as a function of the momentum for pions is very close to that of the muons, therefore it is very difficult to distinguish them from muons with PID cuts only. The cut on both muon pull and electron pull proves to be very efficient to reject the electrons since the electron contamination is below the percent level.

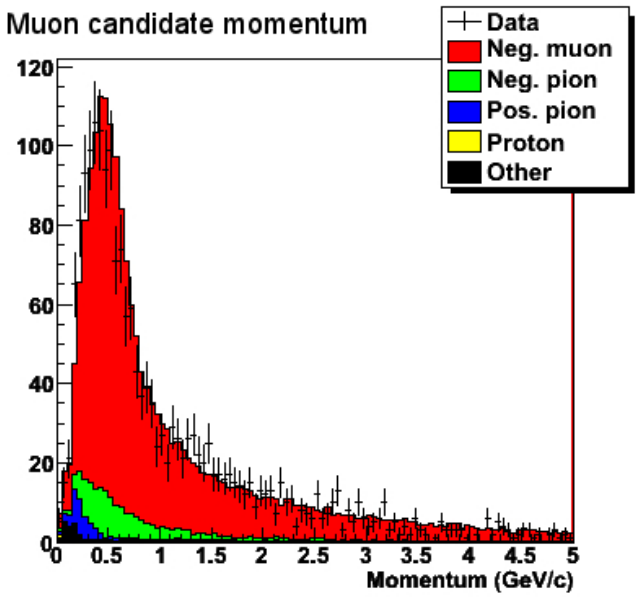

Figure 5.21: Muon candidate momentum break down into true particle types.

True Particle	Ratio
μ^-	86.75%
π^-	8.37%
e^-	0.3%
π^+	2.7%
Proton	0.93%
μ^+	0.7%
e^+	0.08%
Other	0.14%

Table 5.5: True particle type for normalized MC.

Positive pions, along with the other positively charged particles, have been selected as a consequence of a misidentified charge. In our sample we have 4.41 % of tracks which have a misidentified charge. We notice that the main contamination sources after the π^- (8.37 %) comes from π^+ (2.7 %) and protons (0.93 %).

5.5 Global reconstruction tools validation

To validate the recently developed global tools which use higher level reconstruction algorithms, we compared basic distributions with two other analyses carried out by other T2K groups. The first reference analysis, which we will call *R1* [135], is an analysis done by the T2K Barcelona group which also uses global tracks and uses very similar cuts. This comparison was done to show that we could reproduce previous results. The second reference analysis, *R2* [136], is based only on TPC tracks and uses the simple reconstruction explained in section 5.1.2. By comparing our results with the latter, we can prove that lower reconstruction algorithms yield similar results to the global reconstruction ones, which validates the global tools performance.

It is important to perform such cross-checks because the results presented in an updated version of the R2 analysis were approved for the first T2K oscillation papers [108, 137]. Later on, all analyses will only be done at the global reconstruction level. Thus the CC inclusive sample can be used both as a control sample to compare data to MC (done in previous section) and to validate the different higher level reconstruction algorithms.

Both reference analyses were done prior to the optimization of the selection cuts. Therefore, although the cuts are done in the same order, the values for each cut might not be exactly the ones used for the flux measurement described in the next chapter. The cuts are as follows

- 1) Select global tracks that have at least one TPC segment ;
- α) TPC segments must have at least 18 points (1/4 of a TPC) ;
- 2) Select the negative tracks ;
- 3) Pick the track with the highest momentum among the negative tracks in the event as the muon candidate ;
- 4) Fiducial volume cuts: $|x| < 80$ cm, $|y| < 80$ cm and 14 cm $< z <$ 50 cm for FGD1 (resp. $153 < z <$ 185 cm for FGD2) ;
- β) No track in TPC1 (and TPC2) with more than 18 points when the reconstructed vertex is in the FGD1 FV (resp. FGD2 FV) ;

- γ) The muon candidate reconstructed momentum must be higher than 50 MeV ;
- 5) PID cut on the muon pull: $|\text{pull}_\mu| < 2$ on the TPC segment that is closest to the vertex ;
- 6) PID cut on the electron pull: $|\text{pull}_e| > 2$ on the TPC segment that is closest to the vertex ;

where cuts α through γ are applied only in the comparison to R2.

We will first cross-check our selection with the global reference analysis R1. We will then move on to the validation of the global tools by comparing our selection to the R2 analysis.

5.5.1 Cross-check of our selection with another global analysis

The global reconstruction based analysis we use as reference will be called *R1* while our own analysis will be called *A1*. Both analyses use global tracks, where the matching between the TPC tracks and the FGD hits is done with a Kalman filter method which takes into account multiple scattering (Sec.5.1.3).

	Data		MC	
Cuts	R1	A1	R1	A1
Nb. spills	880768	891328	388499	389147
1 neg. TPC track	60965	61267	35569	35410
Fiducial volume	3148	3170	3006	3014
FGD1	-	1541	-	1474
FGD2	-	1629	-	1540
PID cuts	1803	1892	1874	1911
FGD1	-	943	-	943
FGD2	-	949	-	968

Table 5.6: Comparison between the reference analysis R1 and our analysis (A1).

The table 5.6 shows the number of events selected by both analyses after each cut. Although the initial samples used by both analyses are slightly different, there is an overall good agreement both on MC and data as expected since the criteria and tools used for the selection are the same. There is a small difference at the PID level, showing that A1 has slightly better

efficiency than R1. This is because in A1 we cut only on the TPC segment that is closest to the vertex whereas R1 cuts on all TPC segments. If we were to do the same, we would have 82 events less, leading to 1810 events in the end, which is compatible with the 1803 events obtained by R1. This brief cross-check proves that it is possible to reproduce the selection.

5.5.2 Comparison with a lower reconstruction level based analysis

After proving that we can obtain the same results as other analyses which use the global reconstruction, we will now compare our results with an analysis based on a lower level reconstruction, the TPC reconstruction, done by the T2K Saclay group. This reference analysis will be referred to as *R2*. Since this analysis is based on a lower level reconstruction tool, it uses the simple extrapolation method described in 5.1.2 to do the matching between the FGD hits and TPC tracks. This method tends to decrease the acceptance since the extrapolation "tube" has a constant width, thus does not take into account the multiple scattering whereas the Kalman filter method used in the global reconstruction, takes into account the multiple scattering and enlarges the acceptance as the particle is produced further upstream in the FGDs.

Although it is not possible to apply the cuts in the exact same order as in R2, to get as close as possible to the selection done in R2, we must add three cuts, α through γ, applied in the order stated previously:

- α) the track must have at least one TPC segment of 18 points ;
- β) there must be no track in TPC1 (and TPC2) with more than 18 points when the reconstructed vertex is in the FGD1 FV (resp. FGD2 FV) ;
- γ) the muon candidate reconstructed momentum must be higher than 50 MeV ;

Our analysis with the extra cuts will be referred as *A2*.

The cut α on the track length is added to check the quality of the track being looked at. If the track is too short, the error on the reconstructed momentum can be very large and the short track can actually be a segment of a broken track i.e. a track which is long but that has been reconstructed as several shorter tracks. This cut, which was not originally part of the selection done with the global tools, has been kept for all analyses now performed in T2K. Vetos on TPC1 (and TPC2) are necessary in the R2 analysis, since there is no matching between the track segments in different TPCs to form a global track, to ensure the rejection of interactions

which took place upstream the FGDs, in particular to reject interactions that took place in the P0D (just upstream of TPC1). These vetoes also decrease the number of events with backward going tracks. Putting a lower limit on momentum is mainly to eliminate low energy electrons, which are one of the sources of contamination in the sample.

The table 5.7 shows how the number of selected events evolves when we move from an analysis similar to R1 to the R2 analysis by adding the extra cuts before any PID cuts. The numbers are given from the data sample only, to illustrate the evolution. We obtain similar results with the MC. Because the reconstructed objects used by A2 and R2 are very different, we cannot give the evolution of the number of events at any stage of the selection, but only after the fiducial volume cut and before the PID cuts.

	R1	A1 (std cuts)	$>$ 18 pts	No TPC1	No TPC2	p $>$ 50 MeV (A2)	R2
Fiducial vol.	3148	3170	3017	2703	2555	2278	2136
FGD1	-	1541	1453	1261	1261	1114	1062
FGD2	-	1629	1524	1442	1294	1164	1074

Table 5.7: Evolution from the global analysis R1 to the TPC reconstruction based analysis R2, before the PID cuts.

Table 5.8 shows the selected number of events after each cut for both A2 and R2 analyses. The agreement between both selections is good for MC and data up to the fiducial volume and TPC veto cuts. After the PID cuts, we see that both analyses numbers do not match and that numbers between the selected events in FGD1 and FGD2 are not the same either. We will try to explain the different sources of these disagreements.

First, we will compare the basic distributions of the selected events up to the fiducial volume cut and before the PID cuts, to search for and explain any differences. Figure 5.22 shows the muon candidate kinematical distributions such as the reconstructed momentum at the assumed ν interaction vertex and the angle θ with respect to the Z axis (assumed to be the neutrino beam axis), the reconstructed vertex position in the transverse plane (X and Y position), the track length, and the muon pull. All the distributions but the ones for cos θ and the track length

Cut	Data		MC	
	R2	A2	R2	A2
Nb spills	889797	891328	394566	389147
Fiducial vol. + veto	2136	2278	2193	2225
FGD1	1062	1114	1132	1095
FGD2	1074	1164	1061	1130
PID cuts	1455	1624	1482	1677
FGD1	768	825	766	835
FGD2	687	799	716	842

Table 5.8: Comparison between R2 and our analysis A2.

seem to have a good agreement.

Our selected sample presents more events at large angles because of the TPC-FGD matching method. R2 uses a simple approach to do the matching, i.e. extrapolates the TPC track into the FGD with a circle on the YZ plane and a straight line on the XZ plane. To find the starting point of the tracks, which is then assumed to be the ν interaction vertex, one looks for the most upstream FGD hit within a 3 cm radius thus keeping a constant radius of the extrapolated tube whereas the global analyses use a Kalman filter algorithm, which broadens the volume as the tracks goes further into the FGD, taking into account the increase in multiple scattering. Consequently, it increases the angle acceptance and explains why we have more tracks at a larger angle.

The track length distribution shows that our sample has tracks which have more than 72 points (which is the total number of Micromegas columns in a single TPC). The number of degrees of freedom, which are the number of track points minus the eight parameters of the helix fit, is the only information provided at the global track level concerning the track length. Nevertheless, this number of degrees of freedom is not always computed properly. In particular when a long track is mistakenly broken into smaller tracks which are then re-matched together to reform the long track, the numbers of degrees of freedom for each piece of the broken track are added several times, thus leading to a longer than expected track. This happens sometimes for tracks which spiral in the TPC, each branch of the spiral being considered as a separate

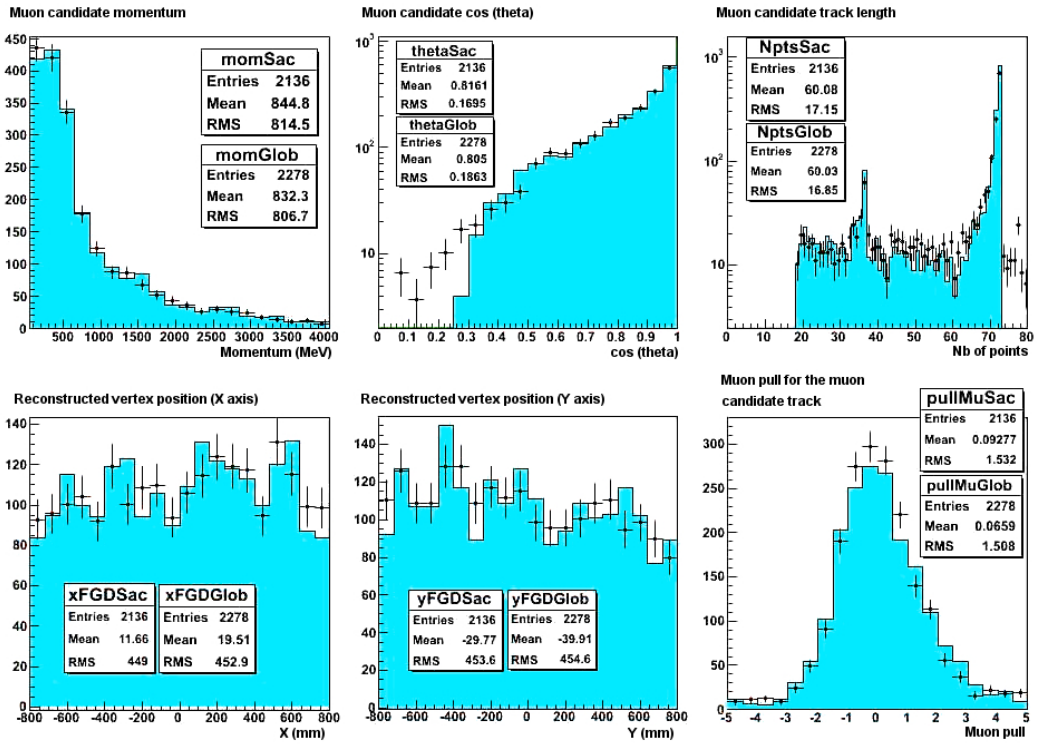

Figure 5.22: Basic plots distributions for the R2 (blue histogram) and A2 (black dots) analyses. Top row: muon candidate momentum (left), angle with respect to the Z axis (middle), and track length given in number of track points (right). Bottom row: reconstructed vertex position in the X (left) and Y directions (middle), and muon pull distribution (right), before the PID cuts.

track, or for tracks which cross the central cathode. It is a well-known bug which has been corrected in posterior software releases and data processing batches. This does not affect our analysis since we only have an inferior boundary on the track length.

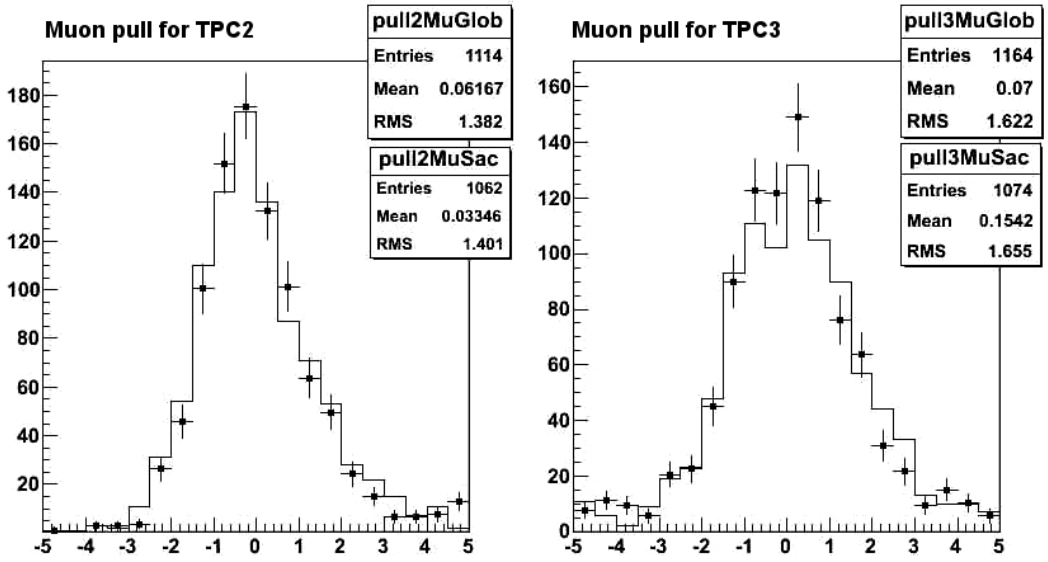

Figure 5.23: Muon pull distributions for TPC2 (left) and TPC3 (right). The dots represent our A2 analysis while the full histogram corresponds to the reference analysis R2.

As the table 5.8 demonstrates, the main disagreement between both analyses is at the level of the first PID cut, i.e. the muon pull cut. In figure 5.22, the muon pulls are seemingly in good agreement, nevertheless when we split the distributions as a function of the TPC (Fig.5.23), we realize that there is a disagreement between our muon pull which is narrower than the R2 analysis one, and also a difference between the TPC2 and TPC3 which shows a broader distribution. There is no TPC1 pull since we have a TPC1 veto. The main identified sources of disagreement up to now is related to the pull correction explained in 5.3.4:

- the pull correction is not done in the same way. Pull corrections are necessary because of a calibration problem which was not well understood at the time, thus leading to different ways for correcting it in the R2 and A2 analyses. This issue has been mostly solved in the most recent data processing release ;

- the pull should be corrected run per run and not one single correction for all runs since there seems to be a more important variation over time on TPC3 values than on TPC2

which leads to an overall pull that is broader if not corrected properly.

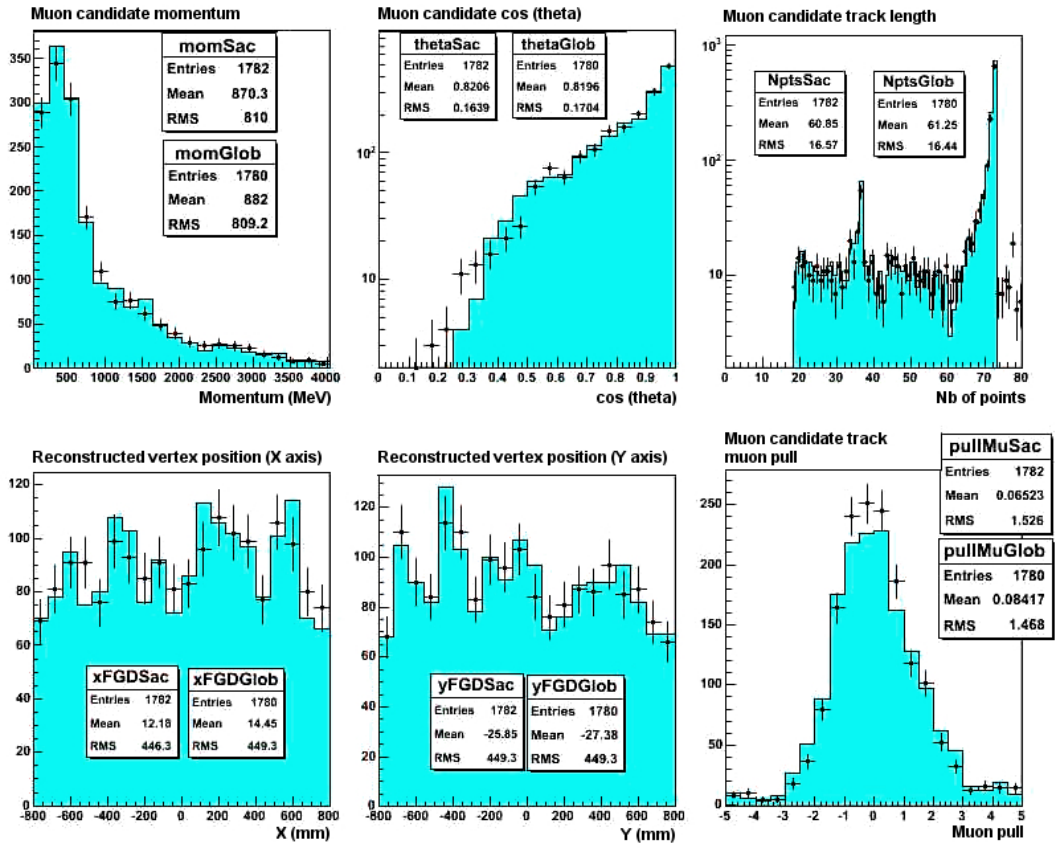

Figure 5.24: Basic plots distributions for the R2 (blue) and A2 (points) analyses 1780 common events. Top row: muon candidate momentum (left), angle with respect to the Z axis (middle), and track length given in number of track points (right). Bottom row: reconstructed vertex position in the X (left) and Y directions (middle), and muon pull distribution (right), before the PID cuts.

Figure 5.24 shows the same basic distributions as 5.22, but only for the 1780 common events between both analyses, which represents 84.3 % of the selected events in the R2 analysis and 78 % of the selected events in the A2 analysis. The agreement between these common samples is good, therefore other than the disagreements induced by the PID correction, the remaining discrepancies observed before come from the events which are not common to both analyses.

Figures 5.25 and 5.26 show the muon candidate momentum and θ angle distributions for the 356 events selected by R2 but not by A2 and the 498 events selected by A2 but not by R2,

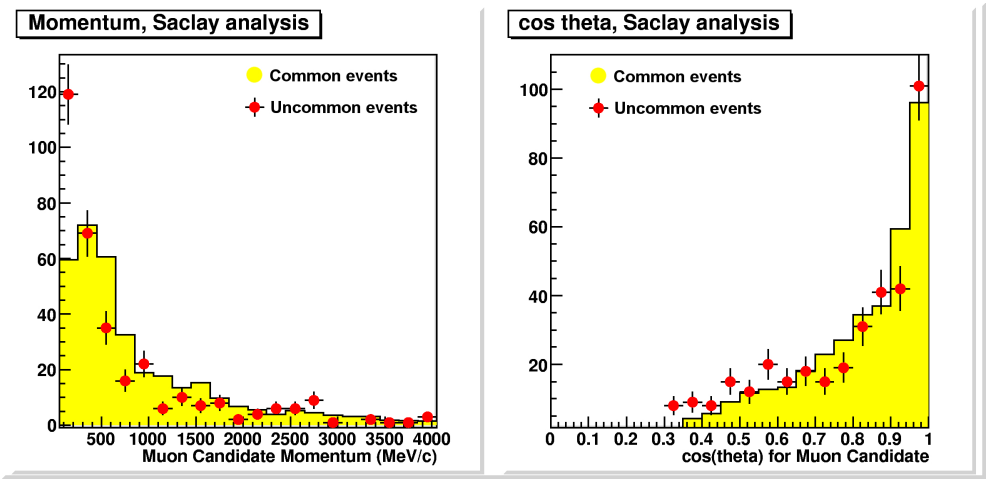

Figure 5.25: Muon candidate momentum (left) and cosine of the angle at vertex for common events (yellow histograms) and selected events by R2 but not by A2 (red dots), before the PID cuts. The distributions of the common events have been normalized to the 356 events selected by R2 but not by A2.

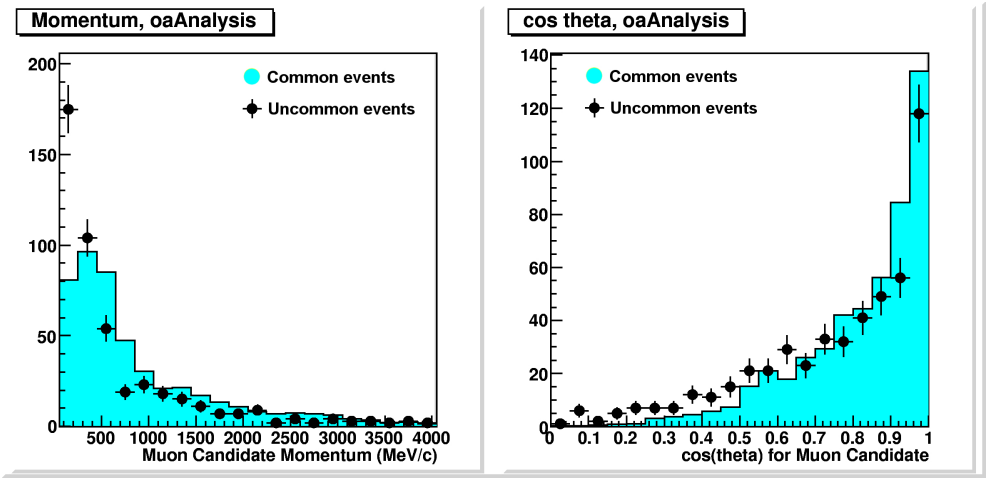

Figure 5.26: Muon candidate momentum (left) and cosine of the angle at vertex for common events (blue histograms) and selected events by A2 but not by R2 (black dots), before the PID cuts. The distributions of the common events have been normalized to the 498 events selected by A2 but not by R2.

compared to the same distributions obtained for the common events to A2 and R2. In both cases most of the uncommon events are either at low muon momentum or at large angle.

For the 498 events selected in A2 but not R2, as we explained before, the R2 has a smaller acceptance for large θ angles (small $\cos\theta$ values) than the A2 analysis because of the FGD-TPC matching algorithm. Also, the R2 analysis has a higher probability to miss FGD hits at low energy because of the transverse diffusion and select events which are not selected by A2 because the missed hits have been properly matched to the TPC in A2 and might lead to an out of fiducial volume event.

Reason	Nb. events
From runs used in R2 but not A2	14
Unexplained lost before FV cut	133
Vertex X or Y not in FV	54
Vertex Z not in FV	87
FGD1	28
FGD2	59
Total edge effects	**141**
Unexplained	68

Table 5.9: Origin of the events selected by the R2 analysis but not by the A2 analysis.

As for the 356 selected in R2 but not A2, we briefly studied their origins. The details can be found in table 5.9. The main sources of disagreement are the following:

- A few data runs were used by R2 but not by A2 because they were flagged by the data quality group as having FGD or TPC problems during the data taking (14 events) ;
- "Edge effects" caused by the different TPC-FGD matching techniques. These events, which have a reconstructed vertex close to the edges of the fiducial volume and have slighly different positions in R2 and A2, passed the FV cut in R2 but not in A2 (141 events). These effects are more frequent at low momentum (more multiple scattering) and large angle .

Nevertheless, 201 events (133 before the FV cuts and 68 after the FV cuts) remain unexplained. A few of these events were visually scanned and did not show any anomaly. Concerning the events lost before the FV cut, one explanation could be that the charge reconstruction is done differently in each analysis, leading to a different selection of wrong charge tracks in one analysis or the other. As for the remaining 68 events, the visual scan showed events which had more than one reconstructed track, where each analysis picked a different track as the muon candidate. Once again this could be related to a wrong vertex reconstruction or a charge reconstruction and charge misidentification issue.

We can conclude that both reconstruction techniques yield similar results, despite a few disagreements which have been mostly understood. The global reconstruction is therefore validated, and we shall use it in the flux measurement analysis presented in the following chapter. Although the TPC-reconstruction based R2 analysis proved to be robust and was used in the first T2K oscillation analyses, from now on, all T2K physics analyses will be done with the higher level global reconstruction algorithms.

5.6 Event topologies

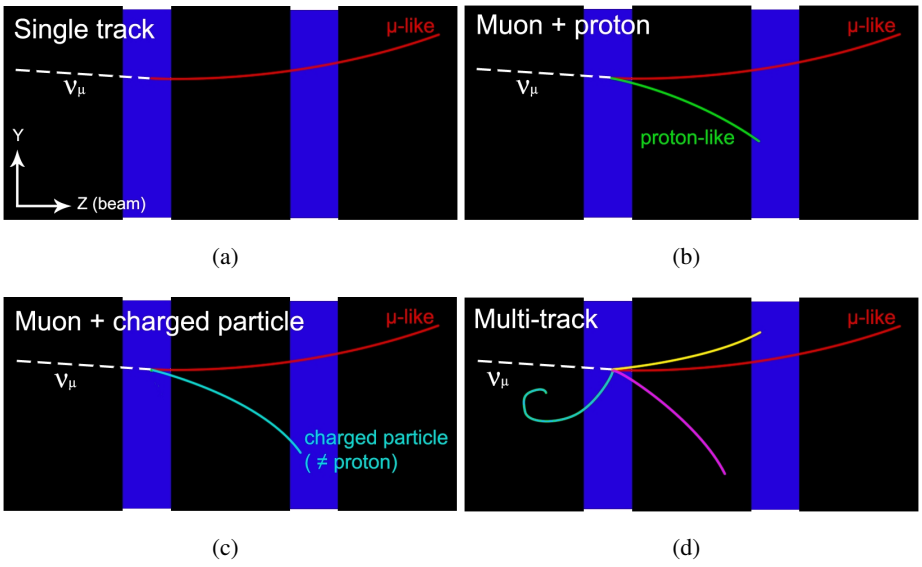

Figure 5.27: Topologies: (a) Single track, (b) Muon + proton, (c) Muon + MIP, and (d) Multi-track.

Once the events have gone through the selection phase, as described in the previous chapter, they can be sorted into four topologies, according to the number and the nature of reconstructed tracks. The choice of the topologies was done to enhance a particular neutrino interaction mode for each topology and to provide additional information on backgrounds. These topologies can be used in several analyses, and in particular they will be used to do the ν_μ flux measurement presented in the next chapter.

The four categories or topologies are defined as follows:

- Single track topology (Fig.5.27(a)): these are the events which have only one successfully reconstructed track, i.e. the muon candidate track ;
- Two-track category with proton (Fig.5.27(b)): the event has a second track, other than the muon candidate track, which is consistent with a proton-like track, i.e. a track that has at least 18 points, is positively charged, has a momentum greater than 200 MeV, and a deposited truncated charge (variable used to compute the PID pulls, which is proportional to the energy loss) greater than 800 a.u. (Fig.5.28) ;
- Two-track category without proton (Fig.5.27(c)): Same as the previous topology, except that the second track is not compatible with the proton hypothesis, it can be any minimum ionizing particle (MIP) ;
- Multi-track category (Fig.5.27(d)): any event that passes the cuts with at least three tracks including the muon candidate.

For all topologies that have more than one track, all of the secondary tracks, other than the muon candidate, must have at least 18 points for the same reasons as put forward in section 5.3.1. Moreover, they must be consistent with the ν interacton vertex, which is assumed to be at the muon track origin, within a radius of 10 cm (Fig.5.29).

Table 5.10 summarizes the contribution from the different ν interaction channels to each event topology. As expected, the "single track" and the "muon + proton" topologies enhance the CCQE channel while the "muon + MIP" topology enhances the channels with single or multi-pion production . Finally, the DIS interactions and multi-pion production are dominant in the "Multi-tracks" topology.

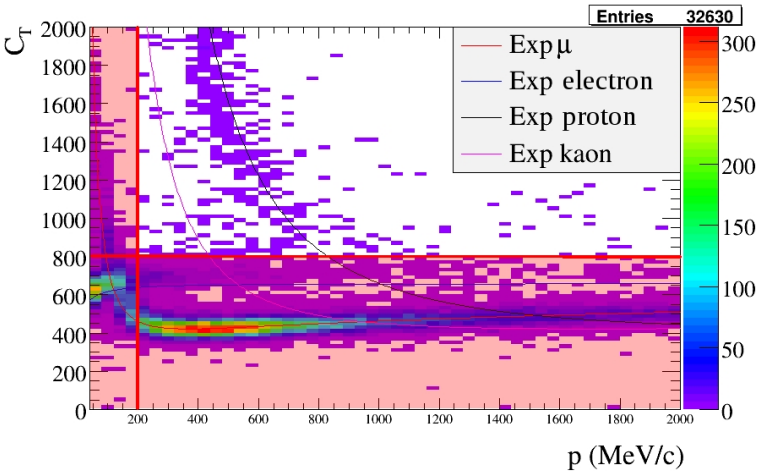

Figure 5.28: Truncated charged C_T (equivalent to energy loss) in arbitrary units (a.u.) versus momentum. The dots show the measured truncated charge, the lines show the expected values for each particle type.

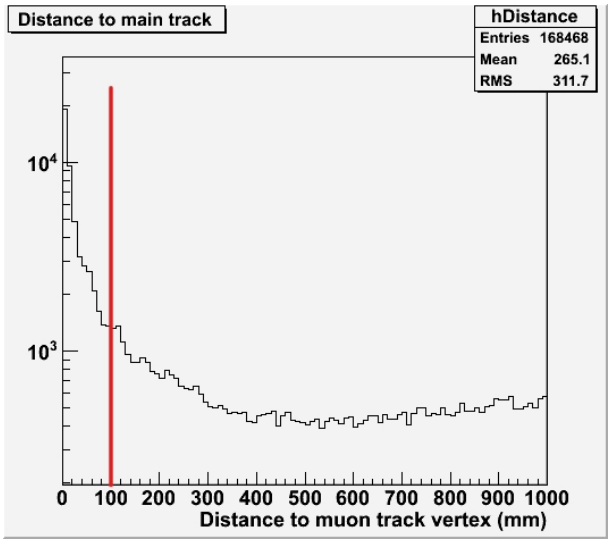

Figure 5.29: Distance between the origin of the muon candidate track and the origin of the secondary tracks, for the MC charged current inclusive sample. The red line shows the cut at 10 cm.

	Single track	Mu + proton	Mu + MIP	Multi-tracks
CCQE	**51.92%**	**50.67%**	17.76%	4.54%
CC1π RES	20.67%	27.44%	**28.64%**	14.79%
CC1π COH	2.36%	0.28%	8.02%	0.79%
CCMultiπ	5.01%	7.96%	15.07%	**20.27%**
CCDIS	3.13%	3.47%	15.22%	**39.39%**
CC other	0.75%	1.39%	1.84%	2.63%
True CC	83.84%	91.21%	86.55%	82.41%
NC	1.73%	3.44%	4.40%	6.55%
$\overline{\nu}_\mu$	0.48%	0.58%	3.22%	2.16%
ν_e	0.07%	0.28%	0.29%	0.94%
$\overline{\nu}_e$	0.03%	0.03%	0.16%	0.15%
Out of FV	13.85%	4.47%	5.38%	7.80%

Table 5.10: Neutrino interaction true type contribution to each topology.

In chapter 2 we showed that the neutrino energy could be reconstructed accurately only for CCQE events. Since the first two topologies enhance the CCQE channel, the resolution on the reconstructed neutrino energy in these topologies will be better than in the other topologies, leading to a better ν_μ flux fit (Sec.6.4).

Figure 5.30 shows the muon candidate momentum break down into ν interaction types per topology. An excess of MC with respect to the data can be seen in the single track topology, while all the other topologies show a small MC deficit. A few hints which could explain these excess and deficits will be given in the next chapter, in section 6.5.2.3.

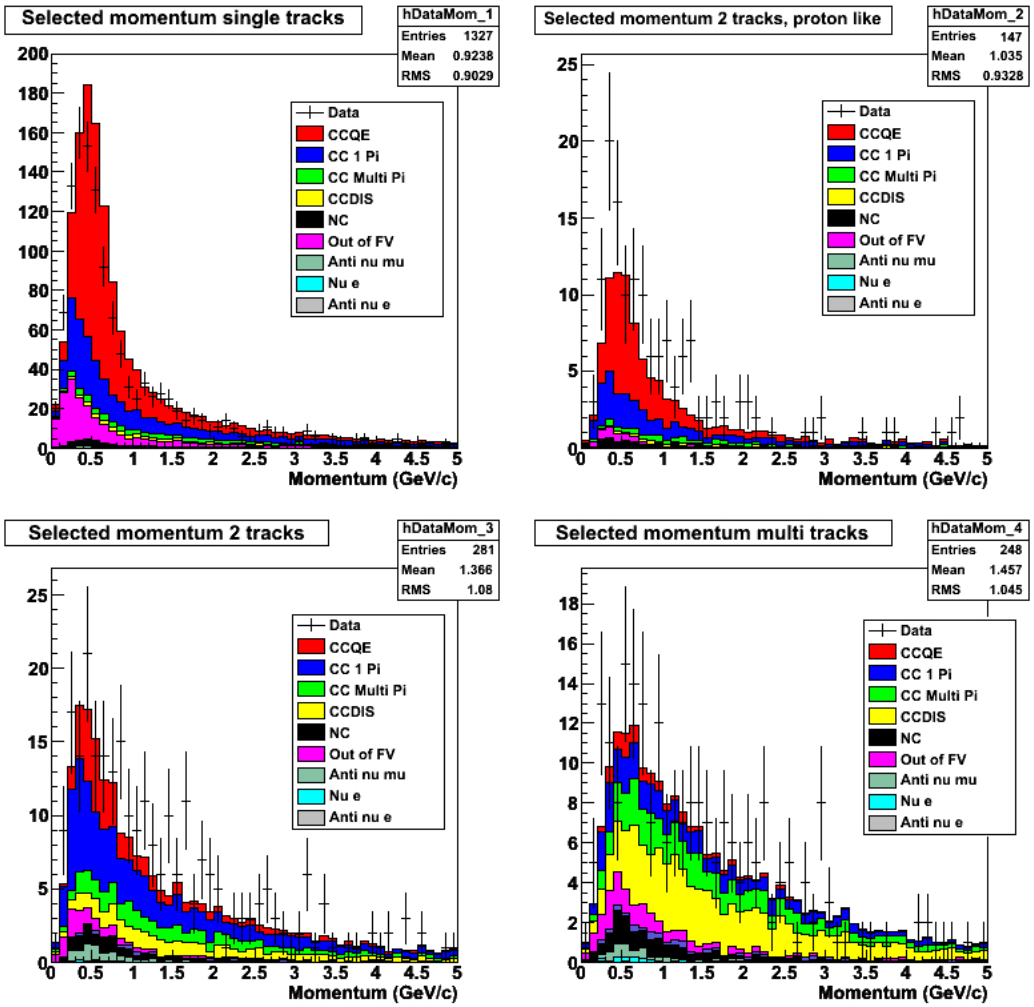

Figure 5.30: Muon candidate momentum per topology break down into true interaction types.

Chapter 6

Neutrino muon flux in the off-axis near detector

In section 3.1.1 we explained how T2K measures the oscillation parameters. In particular, we showed that ν_μ disappearance analysis required to know as precisely as possible the unoscillated ν_μ flux and energy spectrum at the near detector position so that it could be extrapolated to the far detector and compared with the oscillated spectrum. As we will explain later on, the measurement of the ν_μ flux plays also a role in the ν_e appearance analysis.

So far, the analyses presented in the first T2K publications have used only a near/far detector normalization ratio based on the data obtained with the updated R2 analysis, while the shape of the spectrum was given by the Monte Carlo simulations. In this chapter, we will show a first attempt to measure the actual ν_μ flux at the ND280, based on an inclusive charged current ν_μ interaction sample. The selection criteria applied on both the data and MC samples were given in the previous chapter.

To begin with, we will explain in section 6.1 with further details the motivation for the ν_μ flux measurement. Then in section 6.2, we will present the flux predictions done by the T2K beam group, which will be used as a reference to compare to the ν_μ flux at the near detector. We will explain in section 6.3 the neutrino energy reconstruction and the flux measurement principle, first from a theoretical point of view and then from a practical point of view, including the different technical difficulties the measurement implies. In section 6.4, we will present the validation of the method with the MC simulation. We will then move on to presenting the

results on data and the systematic errors in section 6.5. We will conclude on the results obtained and we will briefly discuss an alternative method to do the flux measurement in section 6.6.

6.1 Physics motivations

In this section we will present the physics motivations to measure the ν_μ flux. We will first focus on the motivations related to the ν_μ disappearance analysis and then on the motivations related to the ν_e appearance analysis.

6.1.1 ν_μ flux for the ν_μ disappearance search

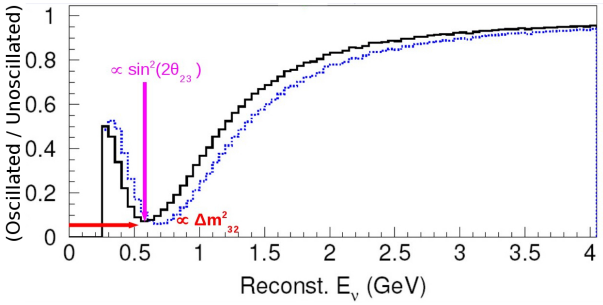

Figure 6.1: Ratio of the oscillated ν_μ spectrum to the unoscillated ν_μ spectrum for $\Delta m^{32} = 2.4 \times 10^{-3}$ eV^2 (dashed blue) and $\Delta m^{32} = 2.8 \times 10^{-3}$ eV^2 (black).

We have already shown that the measurement of the atmospheric oscillation parameters is directly related to the measurement of both the oscillated and the unoscillated ν_μ energy spectrum, the latter being deduced from the measured ν_μ spectrum at the near detector. Indeed, the ν_μ disappearance measurement requires both the shape and the normalization of the unoscillated spectrum to compute the spectra ratio and extract the oscillation parameters (Fig.6.1). In particular, the shape of the spectra must be well understood at the sub-GeV neutrino energy range since that is where the maximum oscillation occurs. We will show in section 6.1.2 that the high energy tail must also be well understood for the ν_e appearance analysis.

The extrapolation of the near detector (ND) measurements to predict the expected number of events at the far detector (FD) is done as follows

$$N_{FD}^{exp}(\theta, \Delta m^2) = N_{ND}^{obs} \times Prob_{\nu_\mu \to \nu_{e,\tau}}(\theta, \Delta m^2) \times (N_{FD}^{MC}/N_{ND}^{MC}) \tag{6.1}$$

where N_{ND}^{obs} is the number of observed events at the near detector and N_{FD}^{MC}/N_{ND}^{MC} is the extrapolation factor derived from the beam MC simulation. Since $Prob_{\nu_\mu \to \nu_{e,\tau}}(\theta, \Delta m^2)$ depends on the neutrino energy E_{ν_μ}, N_{ND}^{obs} and N_{FD}^{MC}/N_{ND}^{MC} must also be known as a function of E_{ν_μ}. For T2K's first publications, the ND280 group produced an integral measurement of the total rate of ν_μ interactions in the ND280 tracker, expressed as a ratio $R_{data/MC}$ of the rate in data to the predicted rate in the Monte Carlo

$$R_{data/MC} = 1.061 \pm 0.028(stat.)^{+0.044}_{-0.038}(det.sys.) \pm 0.039(phys.model). \quad (6.2)$$

This measurement was used to normalize the beam group's predictions for the interaction rates at Super-Kamiokande. Nevertheless, the produced muon momentum spectrum and angle distribution (from which E_{ν_μ} is computed) presented in the different publications do not include yet the full differential systematics and corrections required to do a quantitative comparison of the agreement between data and MC as a function of the muon momentum. Therefore, as far as the ν_μ energy spectrum shape is concerned, only spectra simulated by the T2K beam group have been used. In this chapter we will put forward a new approach to measure not only the event rates but also the shape of the ν_μ energy spectrum.

6.1.2 ν_μ flux for the ν_e appearance search

While the ν_μ disappearance analysis is directly linked to the ν_μ spectrum, the latter plays also an important role in the ν_e appearance search. The uncertainty on the ν_e appearance measurement is dominated by the uncertainty on the expected backgrounds. As explained in sections 3.1.2 and 3.2, one of the main backgrounds is the intrinsic ν_e contamination in the ν beam, due to the charged kaons, pions, and muons decays. The uncertainty on the intrinsic ν_e flux accounts for about half of the total background uncertainties therefore to be able to measure the spectrum of the ν_e produced by the $\nu_\mu \to \nu_e$ oscillation, the intrinsic ν_e energy spectrum must be measured as precisely as possible. The other half of the background uncertainties is due to the neutral current π^0 interactions.

Figure 6.2 shows the contribution from each type of neutrino parent to the total intrinsic ν_e spectrum at Super-Kamiokande. The distribution is dominated by the kaon contribution at high energy ($E_\nu > 1$ GeV), while at the maximum oscillation energy range (below 1 GeV) the pion contribution is also important. The contribution from each neutrino parent to the error envelope of the intrinsic ν_e energy spectrum at Super-Kamiokande is given in figure 6.3, and shows that

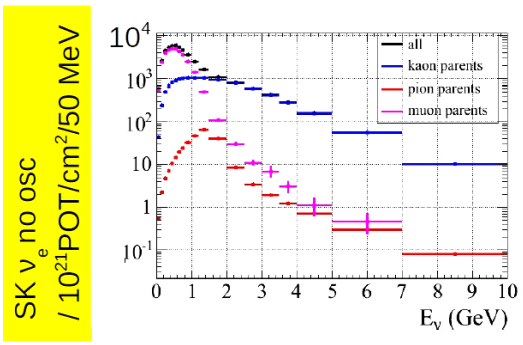

Figure 6.2: Predicted intrinsic ν_e energy spectrum at Super-Kamiokande in the no-oscillation hypothesis. The contributions from each type of neutrino parent to the total ν_e spectrum are shown.

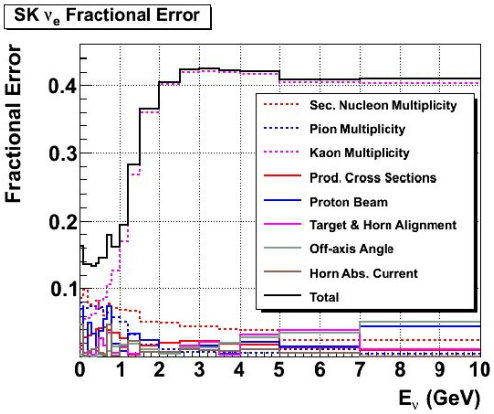

Figure 6.3: Predicted intrinsic ν_e background error envelope at Super-Kamiokande. The contributions from each type of neutrino parent to the total error are shown.

the overall uncertainty in the oscillation region ($E_\nu < 1$ GeV) is of the order of 15 %, which leads to an 8.5 % systematic error on the background prediction for the ν_e appearance search [108].

At neutrino energies larger than 1 GeV, the error on the intrinsic ν_e energy spectrum is largely dominated by the kaon contribution error, while in the oscillation region (below 1 GeV) both the pions and kaons errors are dominant. Since the expected intrinsic ν_e contamination is of the order of 1 %, it is difficult to directly measure it at the near detector. Therefore both the kaon and pion contributions must be well understood.

The kaon contribution, i.e. the kaon multiplicity, can be studied using the ν_μ energy spectrum since at high neutrino energies the kaon contribution is also dominant (Fig.6.4). The energy dependent uncertainties are given on figure 6.5.

To summarize, the ν_μ spectrum is needed at low neutrino energies to study the ν_μ disappearance and at high neutrino energies to constrain the kaon multiplicity which introduces the largest error on the measurement of the intrinsic ν_e contamination. Because of this, a recent analysis has been done to study the high energy tail of the neutrino energy spectrum, using two

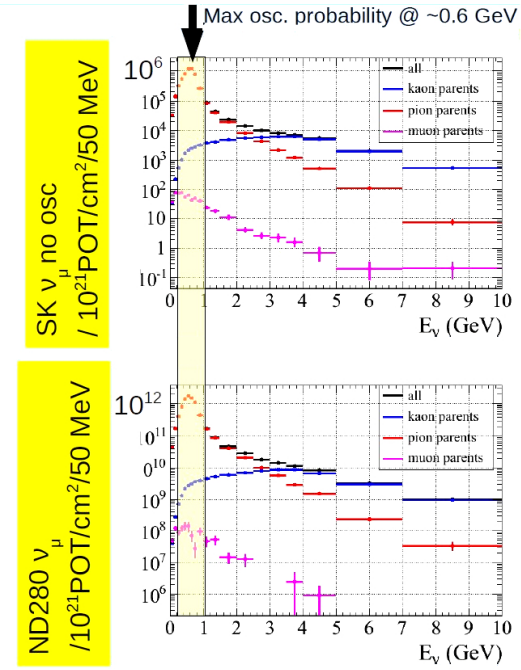

Figure 6.4: Predicted unoscillated ν_μ energy spectrum at Super-Kamiokande (top) and at the ND280 (bottom). The contributions from each type of neutrino parent to the total ν_μ spectrum are shown.

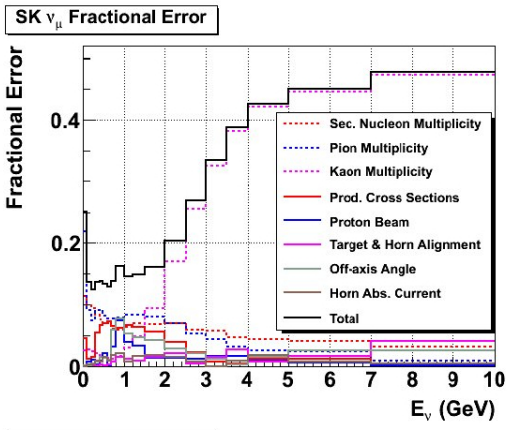

Figure 6.5: Predicted ν_μ energy spectrum error envelope at Super-Kamiokande. The contributions from each type of neutrino parent to the total error are shown.

large energy bins ($E_\nu > 2$ GeV and $E_\nu < 2$ GeV) [138]. In this chapter we will present an analysis which uses a more refined energy binning to study ν_μ energy spectrum at both low and high energies.

Besides the oscillation analyses, the ν_μ flux predictions at the near detector can be used for cross-section measurements.

6.2 Flux predictions

In section 5.2.1 we described the whole MC simulation chain. Now we will focus on the first step which is the simulation of the neutrino flux.

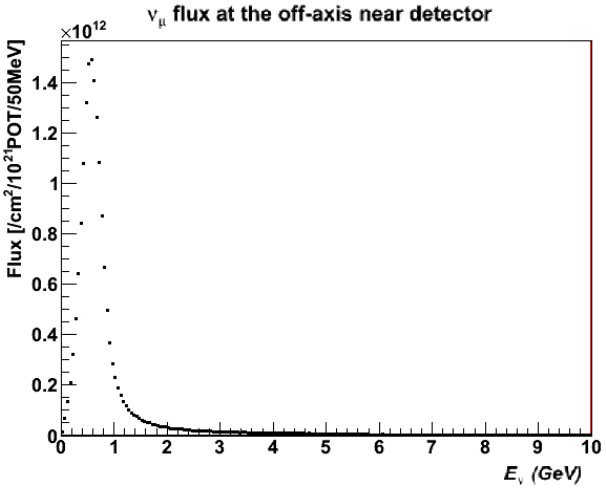

Figure 6.6: ν_μ flux used to generate the MC sample and to compare to the measured ν_μ flux.

As we will describe in the following sections of this chapter, the ν_μ flux measurement consists actually in comparing the expected number of events per reconstructed energy bin to the observed ones, which allows us to measure how far the predicted spectrum is from the observed one by fitting flux factors, defined as the ratio of the measured flux to predicted one, for given true energy bins.

Since our MC sample was generated with an older version of the flux prediction which was based on the GEANT3 hadron production package GCALOR, we will use the same flux

release as the one used to generate the MC to test and validate the flux measurement algorithm. This flux prediction can be seen on figure 6.6. The peak energy is at about 600 MeV, and the energy spectrum shows a long high energy tail.

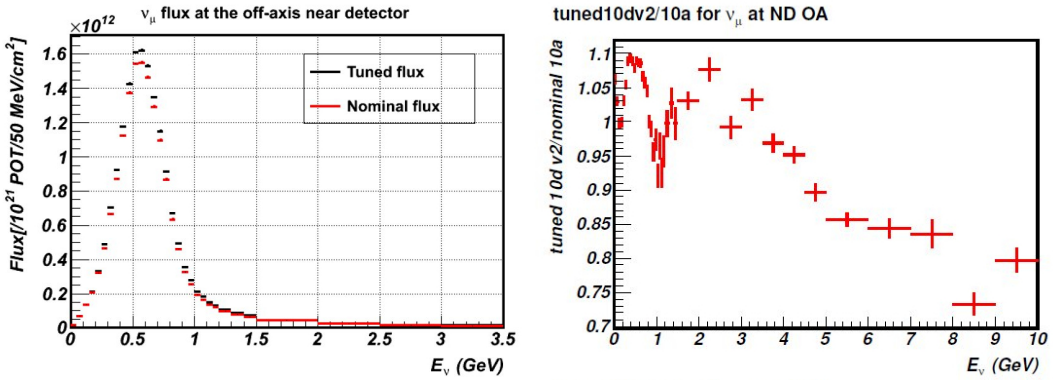

Figure 6.7: ν_μ flux prediction before and after tuning to the SHINE data at ND280, used as a reference in the ν_μ flux measurement on real neutrino data (left). Ratio of the tuned ν_μ flux to the nominal flux at ND280 (right).

More recent flux predictions have been done since the MC was produced, with improved absolute flux uncertainties. These newer flux releases are based on FLUKA2008[128] to simulate the proton interactions inside the carbon target. The outgoing particles are then processed by JNUBEAM, a specific simulation code for the J-PARC neutrino beam based on GEANT3, which was developed to predict the neutrino flux at the ND280 and at Super-Kamiokande. This simulation replicates the geometry of the secondary beamline, in particular it includes the horn magnetic fields and decay volume. Finally, the flux prediction is adjusted using the data provided by NA61/SHINE [129, 130], a hadroproduction experiment at CERN which uses two different targets, one thin carbon target and a replica of T2K's target. SHINE measures the particle production from carbon at T2K proton beam energy (30 GeV) and covers almost all of the relevant pion phase-space for the ν_μ production at T2K.

The main sources of uncertainty in the flux predictions are the kaon and pion multiplicities, as well as the production cross-sections. The pion multiplicity introduces an up to 20 % uncertainty (mostly for low ν energies), while the kaon multiplicity introduces an up to 20-25 % error (mostly at high ν energies) [139, 140]. The production cross-sections add a 10 to 50 % errors, which depends of the type of interaction process that is being considered. Therefore,

SHINE data on pion and kaon production is really useful to reduce those uncertainties. The flux uncertainties are energy dependent, and range from 10-15 % at low energy ($E_\nu < 2$ GeV) to 40 % at high neutrino energies (Fig.6.5 and Fig.6.3).

For now, only the 2007 run pion SHINE data on thin target has been processed and used to tune the flux prediction, reducing the errors mainly at ν energies below 1 GeV. There can still be a substantial improvement of the absolute flux uncertainties once the 2007 kaon data, 2007 T 2K replica target pion and kaon data, and the full 2009 run data are processed and included in the flux predictions. For further details on T2K flux predictions, refer to [141].

Once the prediction has been tuned to the data, the predicted ν_μ flux varies by about ± 10 % for neutrino energies below 3 GeV (Fig.6.7). This tuned flux will be used as a reference to be compared to the measured ν_μ flux on real neutrino data.

6.3 Flux measurement principle

Using a method similar to the one used in K2K to measure the neutrinos fluxes [142], the principle of our flux measurement relies on fitting the measured neutrino energy spectrum with a likelihood function, to compare the computed expected number of events for a given reconstructed energy – which depends on the true ν_μ fluxes per true energy bin – to the observed number of events for the same reconstructed energy. The sample chosen to do the measurement is the inclusive charged current sample defined in the previous chapter, where the muon candidates were chosen with following criteria:

- the event must have at least one global track with a TPC segment that has at least 18 points ;
- the highest momentum track is selected among the tracks corresponding to negatively charged particles ;
- the starting point of the track must be within the defined FGD fiducial volume (Tab.5.2) ;
- the track must be consistent with the muon hypothesis at less than 2.5 σ and incompatible with the electron hypothesis at more than 2 σ.

After applying all the cuts, 2003 events were selected as muon candidates.

The flux measurement can be done by fitting the reconstructed energy spectrum of the full inclusive charged current sample, or by fitting simultaneously the four reconstructed energy spectra of the inclusive charged current sample divided into the four topologies introduced in the previous chapter (Sec.5.6).

In this section we will explain how the expected number of events is computed for different values of the measured ν energy. First, we will explain the general flux measurement principle. Then, we will explain how to apply the method concretely.

6.3.1 Neutrino energy reconstruction

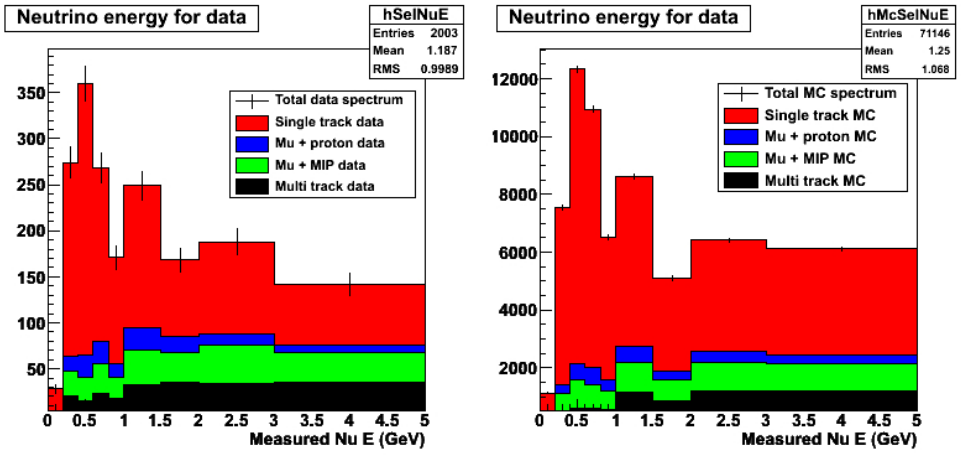

Figure 6.8: Reconstructed ν_μ energy assuming the CCQE hypothesis for data (left) and MC (right). The contribution from each event topology is shown.

To do the flux measurement we must first reconstruct the neutrino energy from the muon momentum and muon angle with respect to the incoming neutrino. As explained in section 2.1.1, the neutrino energy can only be reconstructed accurately when the process is a CCQE interaction. Therefore, we assume that all selected events are of CCQE type. In this case, the incoming neutrino energy is given by

$$E_\nu^{CCQE} = \frac{m_P^2 - m_\mu^2 - m_{Neff}^2 + 2m_{Neff}E_\mu}{2(m_{Neff} - E_\mu + p_\mu \cos\theta)} \tag{6.3}$$

where m_P is the proton mass, m_{Neff} is the neutron mass minus the binding energy, E_μ and p_μ are the energy and momentum of the outgoing μ^-, and θ is the angle of the outgoing muon with respect to the incoming neutrino. The neutron binding energy has been set to 25 MeV, as measured by [70] since the most abundant atom having at least one neutron in the FGDs is carbon (Tab. 6.2). The obtained neutrino energy spectrum is shown on figure 6.8. We measure the neutrino energy up to 5 GeV, and we have divided the measured energy into nine energy bins as defined on table 6.1. The energy binning was chosen so that all energy bins have enough population to do a fit, which is why higher neutrino energy bins, which are less populated, must be larger than the lower energy bins.

Bin e^{ν}_{meas}	e^{ν}_{meas} range (GeV)
1	0 - 0.2
2	0.2 - 0.4
3	0.4 - 0.6
4	0.6 - 0.8
5	0.8 - 1
6	1 - 1.5
7	1.5 - 2
8	2 - 3
9	3 - 5

Table 6.1: Neutrino energy binning.

Figure 6.9 shows the neutrino energy resolution for the MC true CCQE events, fitted by a triple Gaussian. Since the energy is computed from the reconstructed momentum, the energy resolution is limited by the same three contributions that determine the momentum resolution: the Fermi momentum of the struck nucleus (which generates an irreducible uncertainty on the true muon momentum of about 10 %), the TPC momentum reconstruction resolution, and the energy loss correction applied to the measured TPC momentum to take into account the energy lost in the FGDs. The fit shows that the central Gaussian has a bias of about 40 MeV, which is mainly due to the energy loss correction applied on the reconstructed momentum, and a width of about 11 % at 600 MeV (peak energy of the neutrino beam). The tails are mainly due to the energy loss corrections and the muon momentum reconstruction itself.

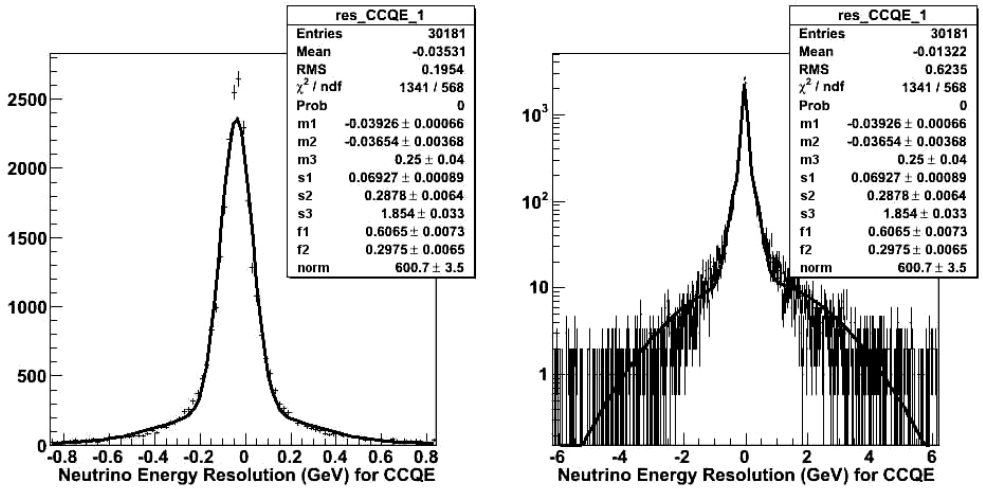

Figure 6.9: ν_μ energy resolution for true CCQE events only, with normal scale (left) and logarithmic scale (right). The distribution has been fitted by a triple Gaussian, where m_i and s_i the sigma are the mean and σ of each Gaussian, and f_i the fraction of the corresponding Gaussian with respect to the triple Gaussian.

6.3.2 The flux measurement principle

Once the neutrino energy has been computed, for each reconstructed neutrino energy bin e_{meas}, the probability of observing n_{obs} events knowing that we expect n_{exp} events for the same measured neutrino energy bin is given by the Poisson distribution:

$$P(n_{obs}|n_{exp}) = \frac{e^{-n_{exp}} \times n_{exp}^{n_{obs}}}{n_{obs}!}. \tag{6.4}$$

Therefore, the full likelihood function – without splitting the events into topologies– can be written as

$$\mathcal{L}_{full} = \prod_{e_{meas}=1}^{9} \frac{n_{exp}(e_{meas})^{n_{obs}(e_{meas})}}{e^{n_{exp}(e_{meas})}} \tag{6.5}$$

The term $n_{obs}!$ from equation 6.4 has been removed since it is a constant and therefore does not intervene when maximizing the likelihood. For practical reasons, we will minimize

$$-ln(\mathcal{L}_{full}) = \sum_{e_{meas}=1}^{9} n_{exp}(e_{meas}) - n_{obs}(e_{meas}) \times ln(n_{exp}(e_{meas})) \tag{6.6}$$

which is equivalent to maximizing $\mathcal{L}_{full}$.

If we consider the four topologies – single track (1), muon + proton (2), muon + MIP (3), and multi-tracks (4) – then we must minimize

$$\sum_{i_{topo}=1}^{4} -ln(\mathcal{L}_{full}^{i_{topo}}) \tag{6.7}$$

where $\mathcal{L}_{full}^{i_{topo}}$ is the likelihood computed as in equation 6.5 but for each topology separately.

While the $n_{obs}(e_{meas})$ are obtained directly from the reconstructed ν_μ energy spectrum, either from the data sample or the MC sample, the expected number of events $n_{exp}(e_{meas})$ is computed as a function of a given true neutrino energy e_{true} as follows

$$\begin{aligned} n_{exp}(e_{meas}) = &\int_0^\infty n_{exp}(e_{true}) de_{true} \times P(e_{meas}|e_{true}) \\ &+ n_{exp}^{outofFGD}(e_{meas}) + n_{exp}^{\overline{\nu}_\mu}(e_{meas}) + n_{exp}^{\nu_e}(e_{meas}) + n_{exp}^{\overline{\nu}_e}(e_{meas}) \end{aligned} \tag{6.8}$$

where $P(e_{meas}|e_{true})$ is the probability to reconstruct the true neutrino energy e_{true} as a neutrino energy in the e_{meas} bin, which in practice will be replaced by the neutrino interaction type k_{proc} and topology i_{topo} dependent "transfer matrices" (Sec.6.3.3.4), and $n_{exp}^{background}(e_{meas})$ are the expected contributions from the different background sources, i.e. the contributions from the out-of-FGD, the $\overline{\nu}_\mu$, the ν_e, and the $\overline{\nu}_e$ events. Since these contributions are fixed, we will assign them systematic errors, as it will be explained in section 6.5.2.

The expected number of events for a given true neutrino energy $n_{exp}(e_{true})$ depends on:

- the real physical flux, which we want to measure and that can be written as the predicted flux $\Phi(e_{true})$ for a given true neutrino energy e_{true} multiplied by a flux factor $f(e_{true})$, where the latter are the fitted parameters ;
- the number of atoms of each type (j_{atom}) in the fiducial volume $N_{j_{atom}}$;
- the cross-sections $\sigma_{j_{atom},k_{proc}}$ for different neutrino interaction processes (k_{proc}) on different nuclei ;
- the selection efficiencies $\epsilon_{k_{proc}}(e_{true})$ defined as the ratio of the number of selected events to the number of generated events per interaction type for the given true neutrino energy in the fiducial volume.

Some simplifications have been made to ease the calculation:

- although the FGDs are made of several nuclei, we consider only the three main atomic components (Tab.6.2): carbon, hydrogen, and oxygen ;
- the interaction processes have been grouped into four categories: CCQE only ($k_{proc} = 1$), CCDIS only ($k_{proc} = 3$), NC ($k_{proc} = 4$) which groups all neutral current interactions, and CCRES ($k_{proc} = 2$) which includes all remaining charged current interactions such as incoherent and coherent single pion production, and multi-pion production.

Taking into account these new categories, $n_{exp}(e_{true})$ can be written as

$$n_{exp}(e_{true}) = f(e_{true})\Phi(e_{true}) \times \sum_{j_{atom}=C,H,O} N_{j_{atom}} \sum_{k_{proc}=1}^{4} \sigma_{j_{atom},k_{proc}} \times \epsilon_{k_{proc}}(e_{true}). \tag{6.9}$$

Therefore, measuring the ν_μ flux is equivalent to fitting the $f(e_{true})$ flux factors, which indicate how far the measured flux is from the predicted flux. We expect these flux factors to be close to one.

If we consider the event topologies, the calculation is the same, except that it is done individually for each topology.

6.3.3 Practical approach

Now that we have explained the general principle of the flux measurement, we can focus on the technical part of how each of the required elements is obtained. First, we will remind which flux predictions are used for each of the studied samples (Sec.6.3.3.1). Second, we will list the number of atoms of each type comprised in the fiducial volume (Sec.6.3.3.2). Third, we will present the different cross-sections used and the uncertainties assigned to each of them (Sec.6.3.3.3). Fourth, we will show how the probability $P(e_{meas}|e_{true})$ of reconstructing an energy e_{meas} from a true energy e_{true} is measured (Sec.6.3.3.4). Fifth, we will explain how the efficiencies for each process type are computed (Sec.6.3.3.5). Finally we will discuss a few technical details that must be taken into account to properly compute the number of expected events (Sec.6.3.3.6).

6.3.3.1 Used flux predictions

The flux predictions used when studying the neutrino data sample and the MC sample are not the same for the reasons given in section 6.3.3.1. To be consistent with the MC, we use the flux

prediction that was used to generate the MC whereas for the data we use the most up-to-date flux prediction, which has been tuned with the NA61/SHINE data and have lower uncertainties. The predicted fluxes and uncertainties are shown in section 6.2.

6.3.3.2 Number of nuclei in the fiducial volume

To compute the flux, it is necessary to know how many atoms of each kind there is in our fiducial volume (Eq.6.9). The fiducial volume comprises the two FGDs, which are mainly made of plastic scintillator bars and water for the second FGD. The table 6.2 summarizes the detectors atomic composition, including the scintillator bars, water, glue and support. As it can be seen on the table, the most abundant atoms are carbon, oxygen and hydrogen. We will neglect in the calculation of the flux the contribution due to the other atom types.

N atoms (in 10^{28})	Hydrogen	Carbon	Oxygen	Others
FGD1 total	4.88±0.06	4.80±0.02	0.15±0.01	0.05±0.01
FGD2 total	5.93±0.03	2.68±0.01	1.69±0.01	0.03±0.01
FGD1 fiducial	3.76±0.05	3.69±0.02	0.12±0.01	0.04±0.01
FGD2 fiducial	4.59±0.02	2.01±0.01	1.35±0.01	0.03±0.01

Table 6.2: Atomic composition of each FGD given in 10^{28} atoms, for the total volume per detector and for the fiducial volume.

The atomic composition is manually computed from the provided material densities, taking into account the FGDs dimensions. Since the exact spatial distribution of these material densities is not given, we cannot compute the number of atoms in the fiducial volume with a 100 % accuracy. The fiducial volume removes the most upstream scintillator layer Z wise, and a border of 10 cm in the X-Y plane but we cannot exactly compute the number of atoms that were removed with respect to the total FGD volume, in particular the atoms removed from the water targets in the FGD2. Thus, we assume that within the fiducial volume the material densities are homogeneous. This assumption might introduce a bias in our flux measurement. Indeed, the first step of the flux algorithm validation with the MC simulation, which consists in fixing the flux factors to compare the computed expected number of events to the observed number of events (Sec.6.4), showed an excess on the total number of expected events of 3.2 % which most likely due to a difference between the calculation of the number of atoms in the fiducial volume and the volume that is actually implemented in the MC. Therefore, an overall

correction of -3.2 % has to be applied on the expected number of events to compensate for this excess, and we assign a conservative systematic error of 1.6 % on this correction.

6.3.3.3 Cross-sections

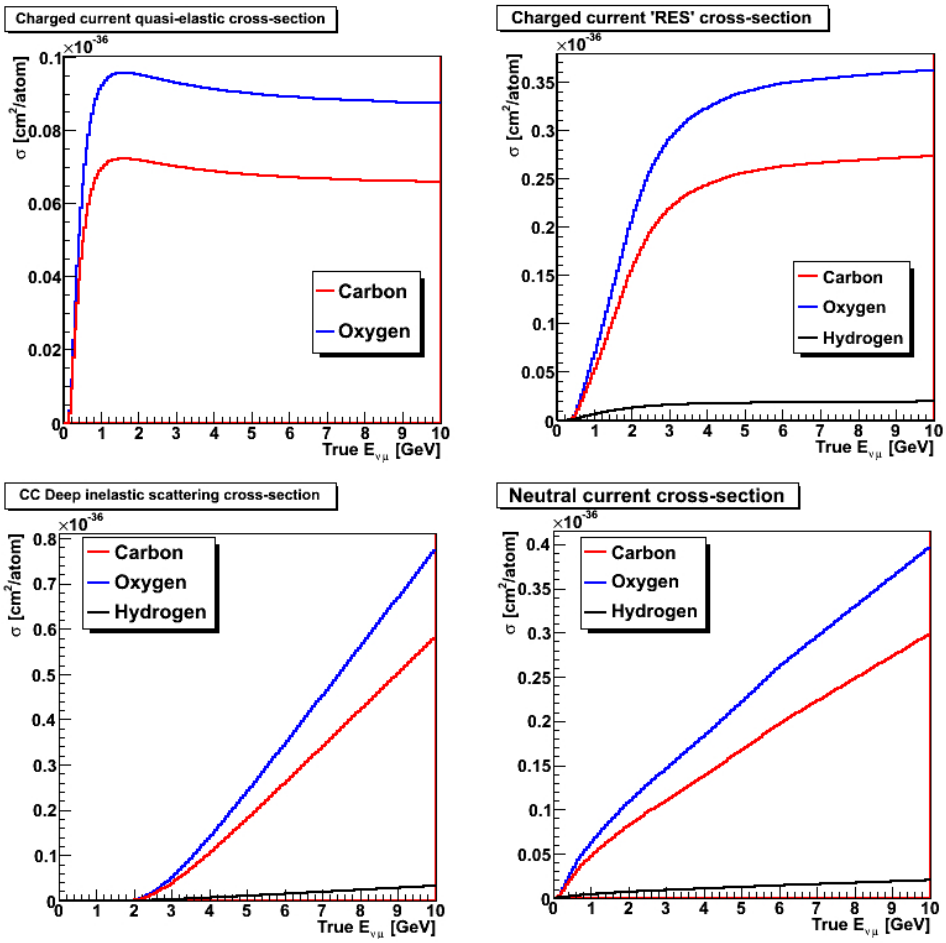

Figure 6.10: Neutrino cross-sections on carbon (red), oxygen (blue), and hydrogen (black) for the CCQE (top left), CCRES (top right), CCDIS (bottom left) and NC (bottom right) interaction categories. ν_μ cannot interact with hydrogen nuclei via the CCQE channel since there is no neutron.

The neutrino interaction cross-sections are computed using the prescriptions indicated in chapter 2. To be able to keep a reasonable amount of events in each energy bin, we have divided the different interaction types into four categories as follows

- Charged current quasi-elastic (CCQE): This process is a category by itself since most of

the events are CCQE, and because it is the only process where the neutrino energy can be reconstructed accurately ;

- Charged current deep inelastic scattering (CCDIS) ;
- Other charged current, dominated by the resonant charged current single pion production (CCRES) ;
- Neutral current (NC): since it is a background in our charged current selection, we do not separate the neutral current processes into sub-types.

Figure 6.10 shows the different cross-sections as a function of the true neutrino energy, per atom type and per interaction category.

Deduced from the cross-section uncertainties presented in chapter 2 and from [86], the uncertainties for each interaction category are summarized in the table 6.3. These errors are split in two large energy bins, i.e. $E_\nu < 2$ GeV and $E_\nu > 2$ GeV, and the energy bins are considered to be fully correlated. For the CCQE and NC processes we have only considered a normalization error and no shape variation.

	$E_\nu < 2$ GeV	$E_\nu > 2$ GeV
CCQE	25 %	25 %
CCRES	45.9 %	29.9 %
CCDIS	30 %	25 %
NC	36 %	36 %

Table 6.3: Uncertainties for each interaction category as a function of the true neutrino energy.

Since the CCQE and CCDIS are single process categories and the NC processes had already been assigned systematic error, we only needed to compute the systematic for the CCRES category. The CCRES break down into single processes for the full inclusive charged current sample is given on table 6.4. The composition of the CCRES category changes from one topology to another, but as a first approach we have neglected these differences. To compute the systematic error for the overall CCRES, we re-weighted the individual process systematics σ_i by their corresponding q_i fraction as follows

$$\sigma_{CCRES} = \sqrt{\sum_i q_i \times \sigma_i^2}. \tag{6.10}$$

	$q_i(E_t^\nu < 2$ GeV)	$\sigma_i(E_t^\nu < 2)$	$q_i(E_t^\nu > 2$ GeV)	$\sigma_i(E_t^\nu > 2$ GeV)
CC 1π incoh.	0.772	30 %	0.540	20 %
CC 1π coh.	0.132	100 %	0.041	100 %
CC other	0.016	30 %	0.048	25 %
CC multi π	0.080	30 %	0.371	25 %

Table 6.4: CCRES category break down into single processes with their respective systematic errors as a function of the neutrino true energy.

6.3.3.4 Transfer matrices (energy resolution)

Equation 6.8 shows that to compute the expected number of events for a given measured neutrino energy e_{meas}, we need the probability $P(e_{meas}|e_{true})$ of reconstructing energy e_{meas} knowing that we have e_{true} i.e. we need to know the energy resolution. In practice, this probability is not an analytical function, but a set of matrices called the transfer matrices which depend on the interaction category and the topology (Fig.6.11). While the matrix elements for the true CCQE events are mainly along the diagonal, the other matrices have off-diagonal elements that contribute to small reconstructed energies for true neutrino energies that spread up to energies higher than 10 GeV. Therefore, these matrices depend on the neutrino interaction type and on the event topology.

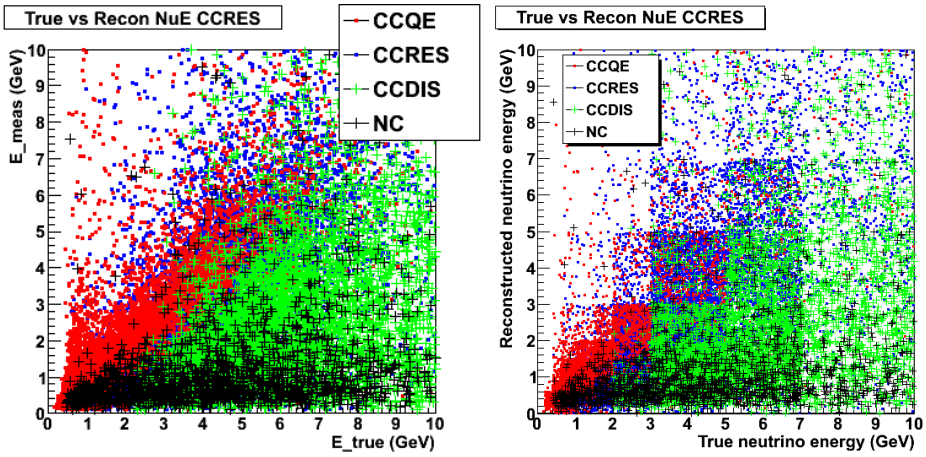

Figure 6.11: Scatter plot of the reconstructed ν energy as a function of the true ν energy, for the 4 interaction categories with a 50 MeV binning (left) and with the rough binning (right).

Given the limited statistics and the complex nature of these matrices, in particular for the interactions that are not CCQE, we must slice the true energies into a binning similar to the measured energy binning, defined in table 6.1 with two additional bins from 5 to 7 GeV and from 7 to 10 GeV since we can integrate the true energy contributions to the measured energy for true energies up to 10 GeV. To reduce statistical fluctuations, for each true energy slice, we fit the measured energy distribution with a triple Gaussian:

$$P(e_{meas}|e_{true}) = \frac{f_1}{\sqrt{2\pi\sigma_1^2}} e^{-\frac{(e_{meas}-\mu_1)^2}{2\sigma_1^2}} + \frac{f_2}{\sqrt{2\pi\sigma_2^2}} e^{-\frac{(e_{meas}-\mu_2)^2}{2\sigma_2^2}} + \frac{1-f_1-f_2}{\sqrt{2\pi\sigma_3^2}} e^{-\frac{(e_{meas}-\mu_3)^2}{2\sigma_3^2}} \tag{6.11}$$

These are the functions that will be used as $P(e_{meas}|e_{true})$ (Fig.6.12).

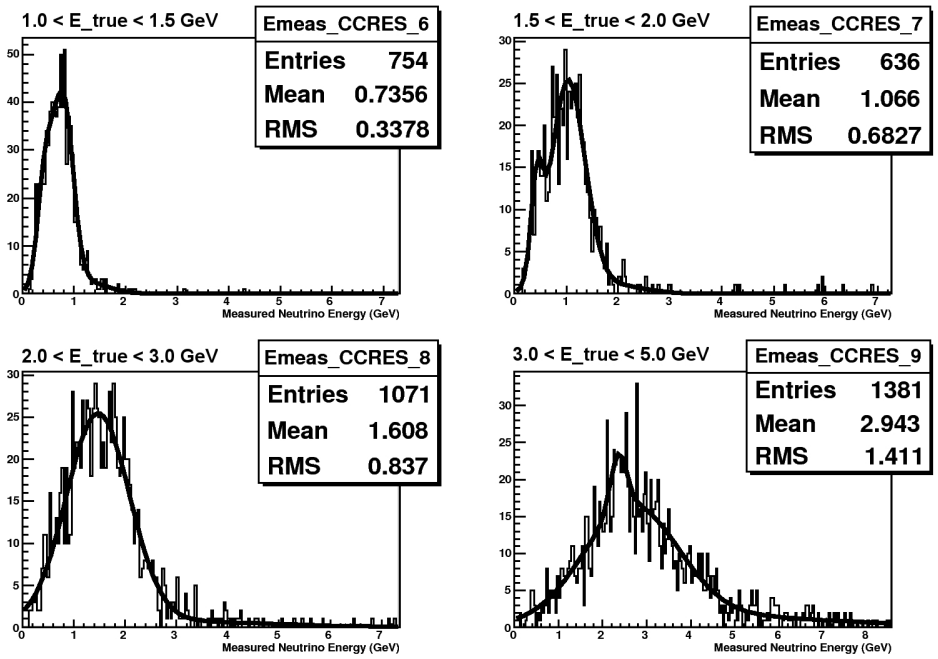

Figure 6.12: An example of the triple Gaussian used to fit the measured energy distributions for the CCRES process, where the 2 track topologies are combined (Muon + proton and muon + MIP), in a given true neutrino energy slice: 1.0-1.5 GeV (6), 1.5-2.0 GeV (7), 2.0-3.0 GeV (8), and 3.0-5.0 GeV.

When using the four topologies in the fit, the transfer matrices should also be split accordingly because the energy resolution is not the same for each topology since they enhance different neutrino interaction types. For the CCQE process, since it is the only case where

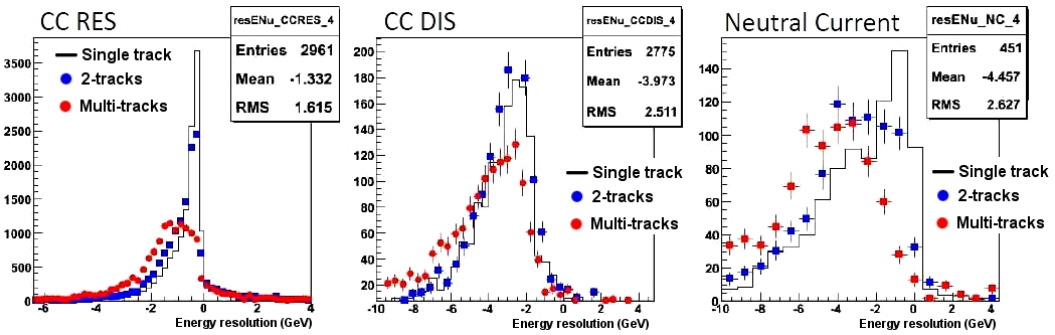

Figure 6.13: Energy resolution for the CCRES (left), CCDIS (middle) and NC (right) processes, for the single track topology (black histogram), the grouped "muon + proton" and "muon + MIP" topologies (blue dots) and for the multi-track topology (red dots).

the ν energy can be properly reconstructed, there is no difference on the the energy resolution between the topologies, thus the CCQE matrix does not need to be separated. Nevertheless, for the CCRES, CCDIS and NC processes, which are less populated, we cannot separate these matrices into all four topologies in all cases. Therefore, we will group the topologies that have similar energy resolution shapes for a given neutrino interaction type. Figure 6.13 shows the energy resolution for the CCRES, CCDIS and NC processes. The "muon + proton" and "muon + MIP" energy resolution distributions have similar shapes in these processes, so they have been grouped together. The "single tracks" do not require to be grouped with other topologies since they are the most abundant. The "multi-track" events cannot be grouped with the other topologies since their energy resolution is too different from the others.

In theory we should not use a higher energy boundary but the flux predictions and cross-sections are only provided for neutrino true energies up to 10 GeV. Therefore, we must add a correction to account for the events with true energies larger than 10 GeV per process and per energy bin. The contributions from true neutrino energies larger than 10 GeV are small for the CCQE and CCRES categories but they are not negligible for the CCDIS and NC processes, as it can be seen on figure 6.14.

6.3.3.5 Efficiencies

As equation 6.9 shows, we need to compute the selection efficiency for each interaction category. In fact, this efficiency can be divided into two different efficiencies: a global efficiency

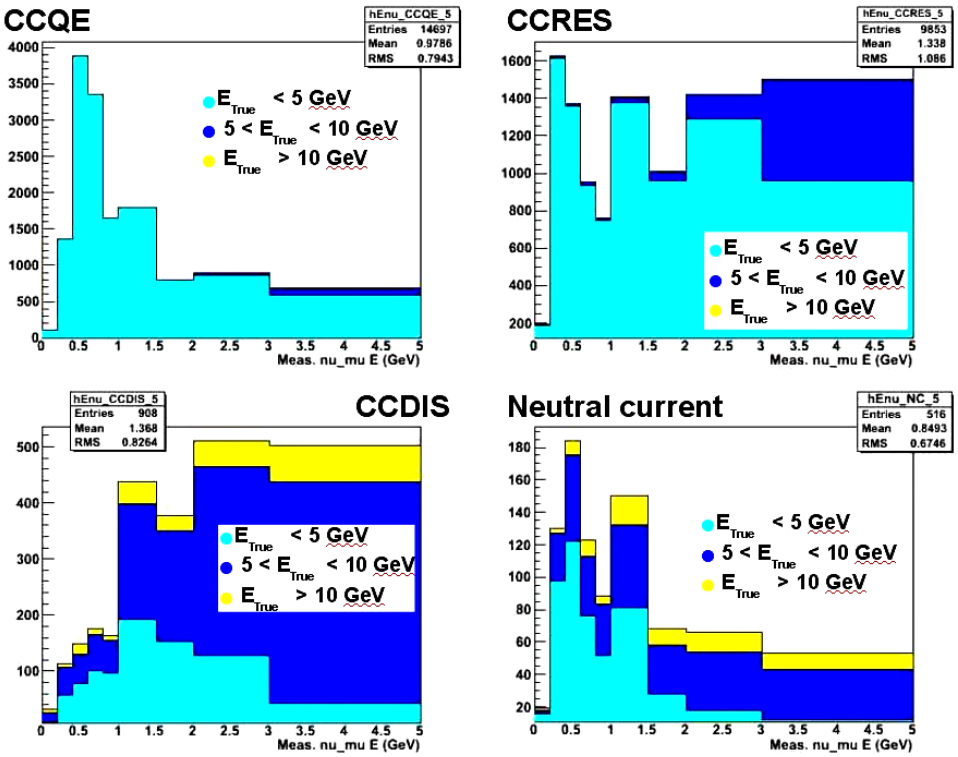

Figure 6.14: Contribution to the measured neutrino energy from true neutrino energies $5 < E_\nu < 10$ GeV (dark blue) and $E_\nu > 10$ GeV (yellow) as a function of the interaction type. To take into account the contribution of the $E^\nu_{true} > 10$ GeV on the $E^\nu_{meas} < 5$ GeV, the applied correction factor is the ratio of the total histogram divided by the sum of the histograms for $E^\nu_{true} < 5$ GeV (light blue) and for $5 < E^\nu_{true} < 10$ GeV (dark blue). This correction does not depend on the topology.

and a relative efficiency.

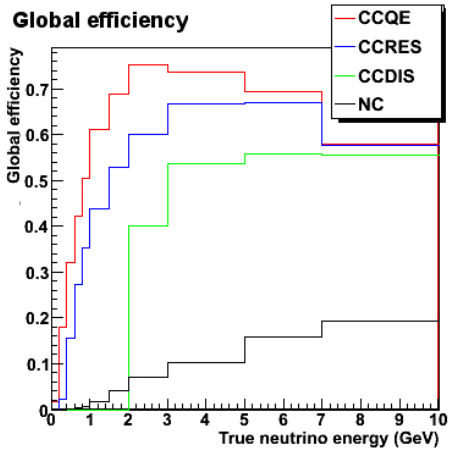

Figure 6.15: Global efficiencies for the each interaction category.

The global selection efficiency is defined as the ratio of the selected events to the generated events per interaction type as a function of the true energy in the fiducial volume (Fig.6.15). After obtaining the efficiencies per energy bin and per interaction type, the histograms are fitted with a six-parameter function $\epsilon_{global}^{k_{proc}}(e_{true})$ as follows

$$\epsilon_{global}^{k_{proc}}(e_{true}) = (par(0) + par(1)e_{true} + par(2)e_{true}^2 + par(3)e_{true}^3) \times (par(4) + e_{true})^{par(5)}. \tag{6.12}$$

Figure 6.16 shows the fitted distributions. The CCQE efficiency and CCRES efficiencies increase rapidly in the first energy bins. The CCDIS efficiency is zero below 2 GeV, which is the minimum energy required to produce CCDIS interactions.

The relative efficiency is defined at the ratio of the number of selected events for an interaction category k_{proc} in a given topology to the total number of k_{proc} events selected. In the fit with topologies, it is the product of the global efficiency and the relative efficiency that is used in the calculation of expected events for each topology.

Figure 6.17 shows an example of the relative efficiencies per topology for the CCQE process. From the single track and muon + proton plots we can observe that the proton starts to be detected at a true neutrino energy of about 1 GeV since the efficiency in the single track

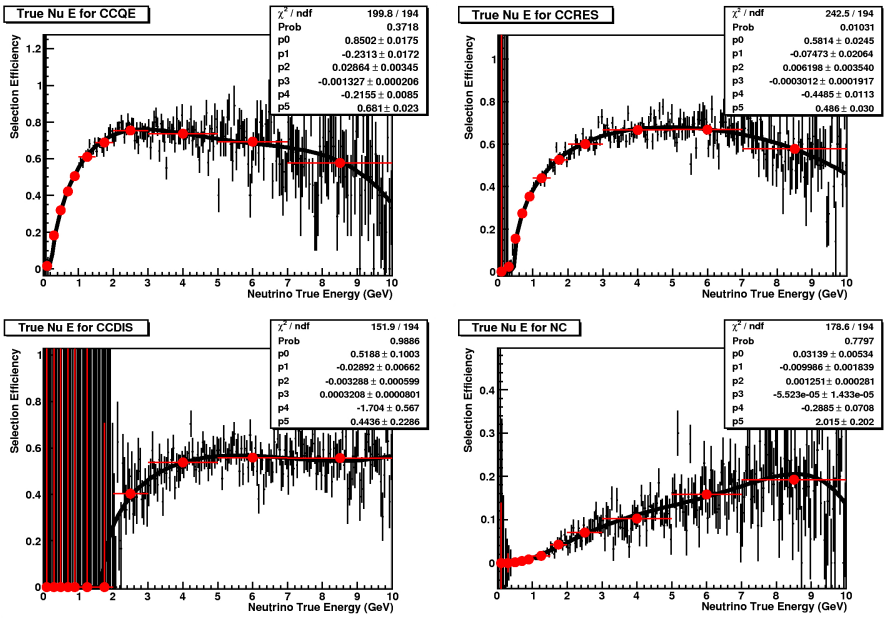

Figure 6.16: Fitted global efficiencies per interaction category. The red dots represent the efficiencies binned in the 9 energy bins defined on table 6.1.

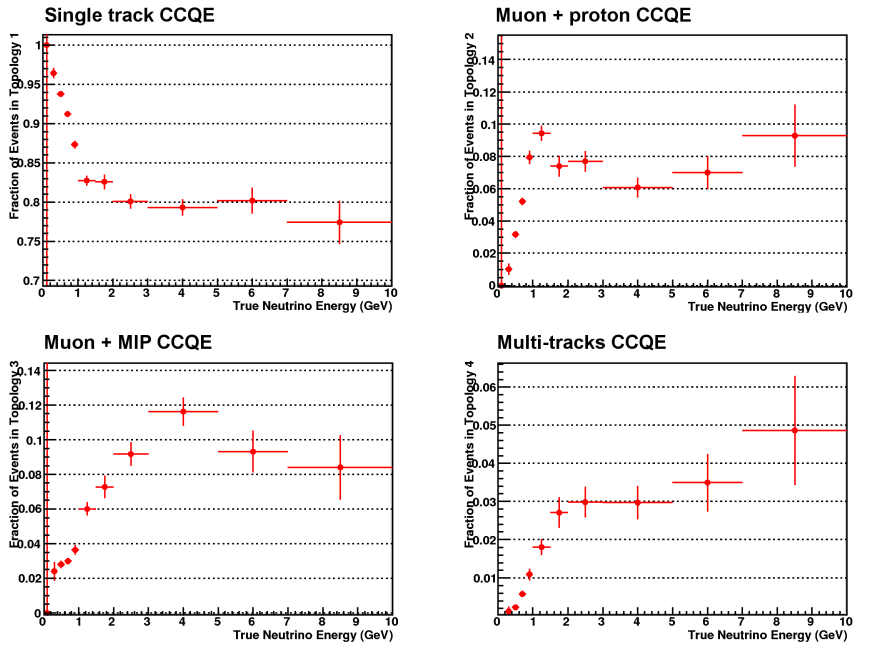

Figure 6.17: Binned relative CCQE efficiency per topology as a function of the true neutrino energy.

topology drops while the muon + proton one increases, meaning that some events from the first topology have migrated to the second one. Although there should not be any CCQE in the muon + MIP topology, protons can be misidentified as a π^+ for proton energies above 1 GeV because the energy loss curves of pions and protons get closer. This effect can be seen for true neutrino energies of a few GeV, as the muon + MIP plot shows. The last plot shows that the fraction of CCQE in the multi-tracks topology is very low.

6.3.3.6 Integration into large energy bins

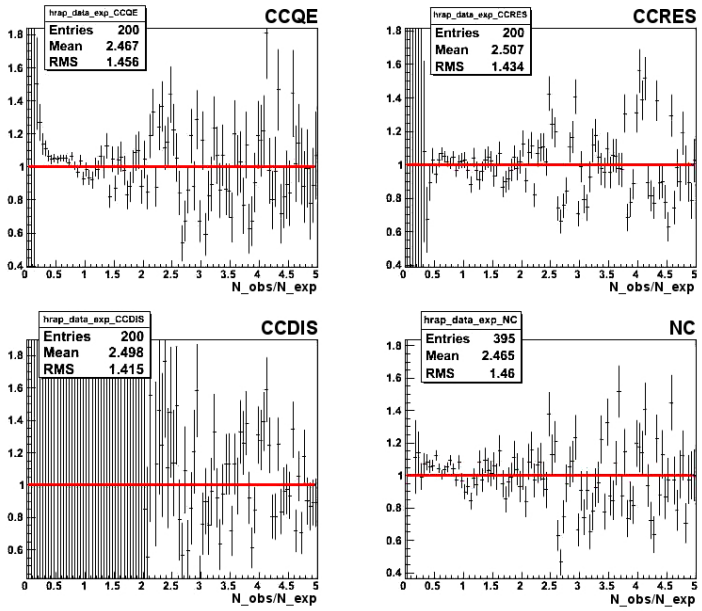

Figure 6.18: Ratio of the observed events in the MC sample to the expected events computed from Eq.6.9 for each interaction category.

As explained in section 6.3.3.4, we must slice the true energies into bins which have enough statistics to compute the corresponding transfer matrix elements. To compute the number of expected events in a large true energy bin we must therefore integrate the contributions from Eq.6.9 within that bin. Since the flux predictions and the cross-sections are provided in 50 MeV energy bins by the T2K beam and cross-section working groups, the expected number of events N_{exp}^{large} for a large true energy bin i_L is then given by

$$N_{exp}^{large} \propto \int_{E_{min}(i_L)}^{E_{max}(i_L)} \phi(E_{true}) \times \sigma(E_{true}) \times \epsilon(E_{true}) dE_{true} \tag{6.13}$$

where the dE steps are 50 MeV steps, E_{min} is the large true energy bin lower limit and E_{max} is the upper limit. The transfer matrix elements, since they are fitted with triple Gaussians, are integrated using the standard *erf* functions.

At low energy, the efficiency, the predicted flux, and the cross-section functions increase rapidly, so the integral of the product of the three values is not equal to the product of the mean values for each 50 MeV bin. Thus, we must apply a correction proportional to the ratio of the true number of MC events in the true energy bin to the computed number of events in the same bin to compensate for the binning effect at low energy (Fig.6.18), in particular for the CCQE process, and to a lesser extent for the CCRES and NC categories. There is no binning effect on the CCDIS process since the CCDIS relative efficiency is zero at low neutrino energies.

6.3.3.7 Backgrounds

To get as close as possible to the measured neutrino spectrum, we must take into account as many backgrounds as possible. Figure 6.19 shows the contributions from each neutrino interaction category and backgrounds to the measured neutrino spectrum per topology. There are five different expected backgrounds: the neutral current interactions, the out-of-FV events, the $\overline{\nu}_\mu$, the ν_e, and the $\overline{\nu}_e$. As table 6.5 indicates the main background is for all topologies the out-of-FV contribution, which will be assigned a systematic error (Sec.6.5.2), followed by the neutral current interactions and the other minor backgrounds.

While the neutral current background is modeled and can be varied simultaneously with the neutrino flux, the out-of-fiducial volume, the $\overline{\nu}_\mu$, the ν_e, and the $\overline{\nu}_e$ cannot be described by a precise model although they must be taken into account in the calculation of the expected number of events. Therefore, each of these backgrounds is simply added, e_{meas} bin per e_{meas} bin, to the expected number of events for the considered e_{meas} bin (Eq.6.8). Figure 6.20 shows the contribution of each of these unfitted backgrounds as a function of the measured neutrino energy.

6.4 Validation with the Monte Carlo simulation

Prior to fitting the data, it is necessary to validate the flux fitting program with the MC sample. The cross-checks done can be split into two categories: the cross-checks done with the full MC

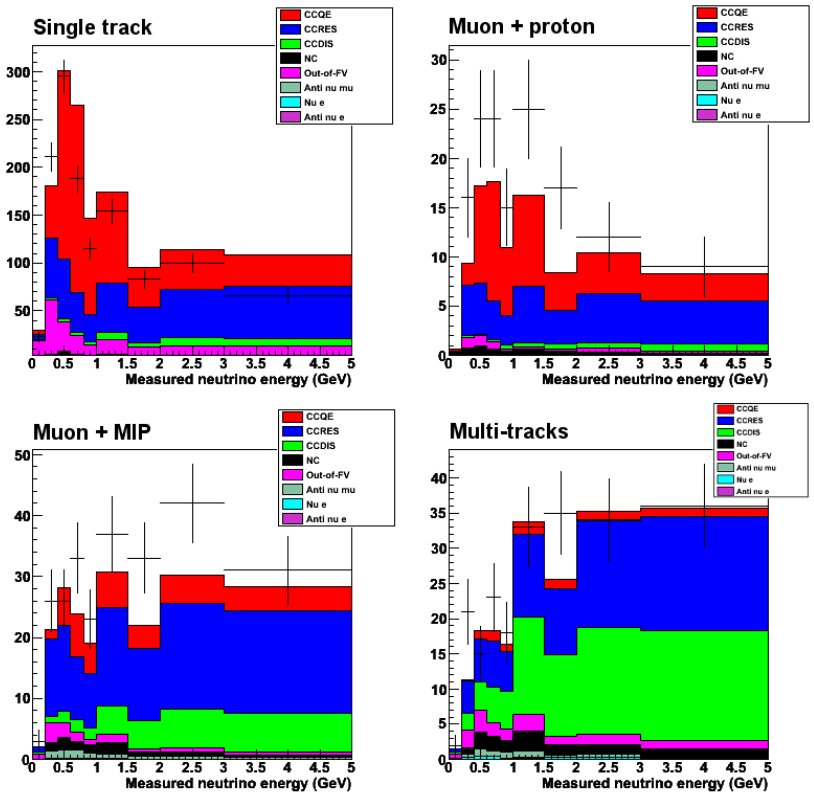

Figure 6.19: Reconstructed neutrino energy spectrum per event topology. The contribution from each interaction category and backgrounds is shown.

	Single track	Mu + proton	Mu + MIP	Multi-tracks
CCQE	51.92%	50.67%	17.76%	4.54%
CCRES	28.79%	37.07%	53.57%	38.48%
CCDIS	3.13%	3.47%	15.22%	39.39%
True CC	83.84%	91.21%	86.55%	82.41%
NC	1.73%	3.43%	4.40%	6.54%
$\overline{\nu}_\mu$	0.48%	0.58%	3.22%	2.16%
ν_e	0.07%	0.28%	0.29%	0.94%
$\overline{\nu}_e$	0.03%	0.03%	0.16%	0.15%
Out of FV	**13.85%**	**4.47%**	**5.38%**	**7.80%**
Backgrounds	16.16%	8.79%	13.45%	17.59%

Table 6.5: Neutrino interaction true type contribution to each topology.

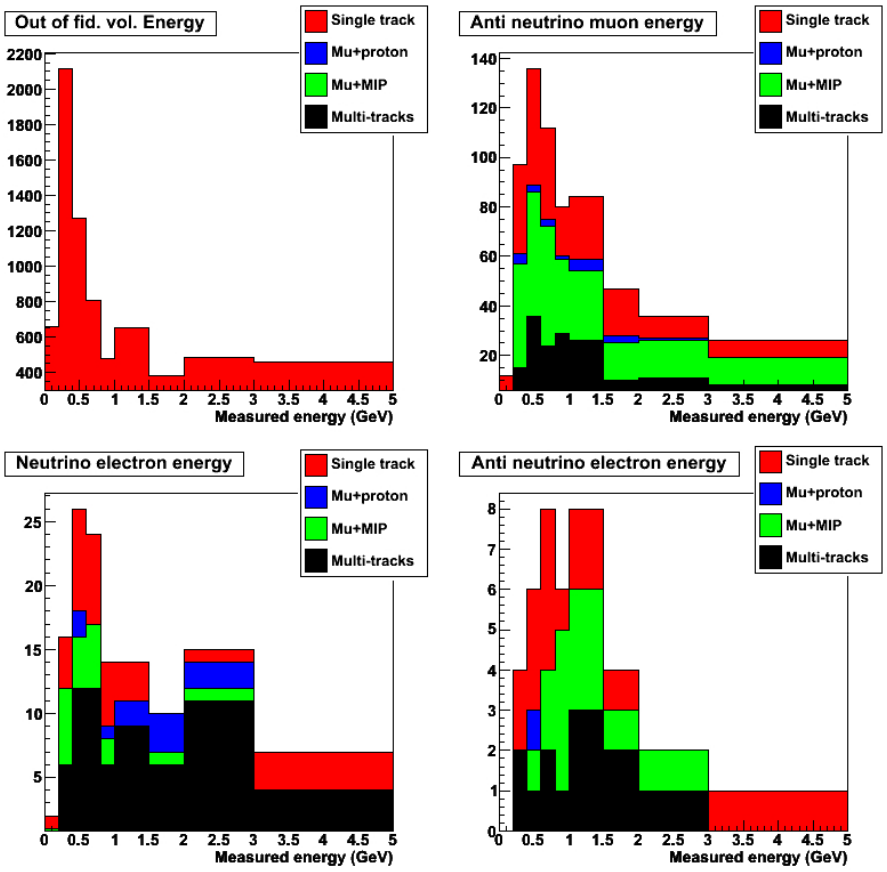

Figure 6.20: Reconstructed neutrino energy for events with a true vertex out of the fiducial volume (top left), and for events whose parent is an $\overline{\nu}_\mu$ (top right), a ν_e (bottom left), or an $\overline{\nu}_e$ (bottom right).

sample and the cross-checks done with MC samples with a number of POTs equivalent to the data POTs. The results obtained with the MC samples will be used as reference to understand the fit results on data.

6.4.1 Cross-checks with full MC sample

The first cross-check is the most fundamental one, and consists in verifying that the calculated expected number of events is in good agreement with the measured number of events in the same true energy bin and then in the same reconstructed energy bin per topology and per interaction category, while fixing the flux factors to 1.

Figures 6.21 and 6.22 compare the expected number of events from equations 6.8 and 6.9 to the observed number of events in the MC sample per true energy bin, for different neutrino interaction processes or for different event topologies. Figures 6.23 and 6.24 show a similar comparison, but per measured energy bin. After correcting the 3.2 % excess due to the number of atoms normalization mentioned in section 6.3.3.2 (which was observed the first time this cross-check was done), all figures show that the prediction and the measured spectra are in good agreement.

Once we are sure the calculation of the expected events is properly done, the second test consist in fitting the flux factors for the full sample without the event topologies (average fit) and taking into account the four topologies (4-topology fit). This allows to check for any bias and to check that the different χ^2 distributions are as expected.

Two types of χ^2 can be computed to quantitatively measure the quality of our fit: a spectrum χ^2 and a flux χ^2.

The spectrum χ^2, which indicates how well the shape of the energy spectrum is reproduced, is defined as

$$\chi^2_{spectrum} = \sum_{i=1}^{9} \frac{(N_{obs} - N_{exp})^2}{\sigma^2_{obs}} \tag{6.14}$$

with $\sigma_{obs} = \sqrt{N_{obs}}$.

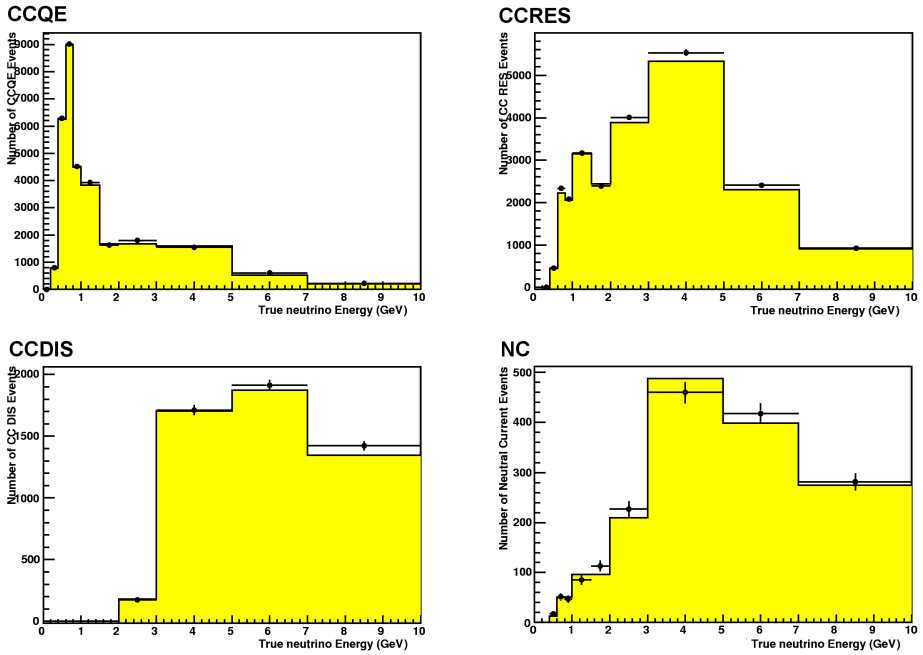

Figure 6.21: Predicted number of events (yellow) vs observed number of events in the MC sample (dots) as a function of the true neutrino energy for each ν interaction type.

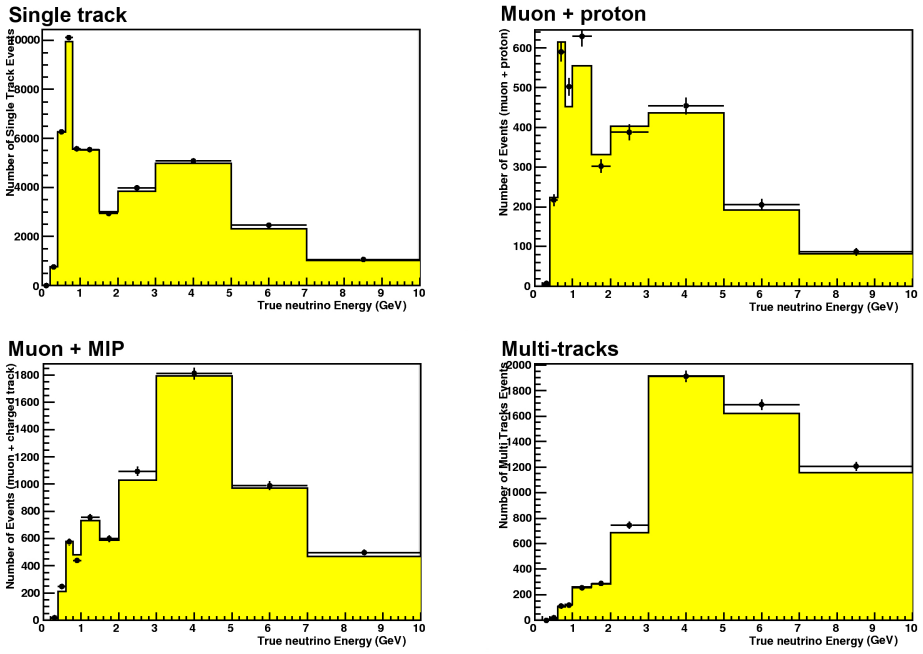

Figure 6.22: Predicted number of events (yellow) vs observed number of events in the MC sample (dots) as a function of the true neutrino energy for each event topology.

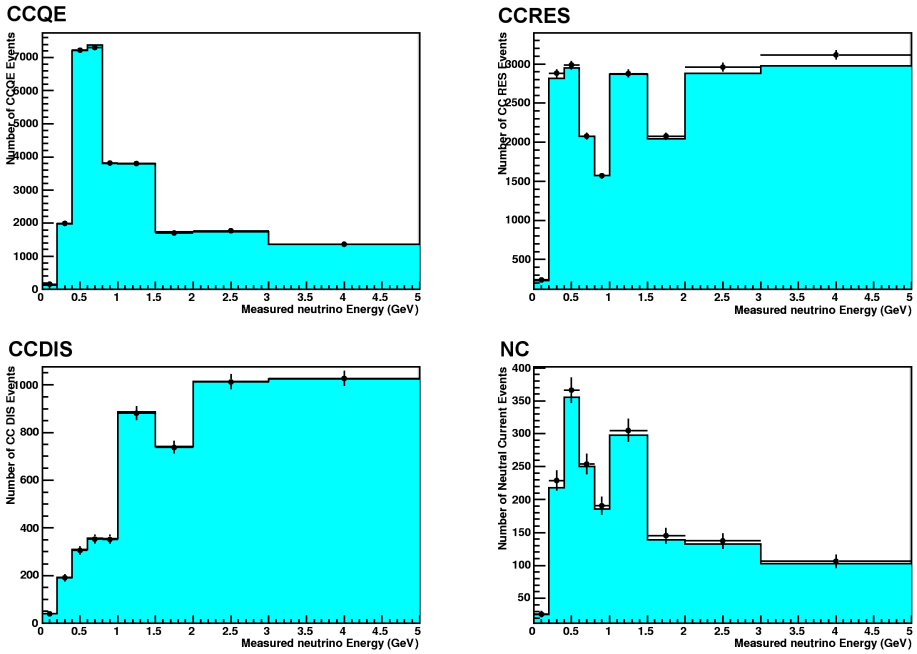

Figure 6.23: Predicted number of events (blue) vs observed number of events in the MC sample (dots) as a function of the measured neutrino energy for each ν interaction type.

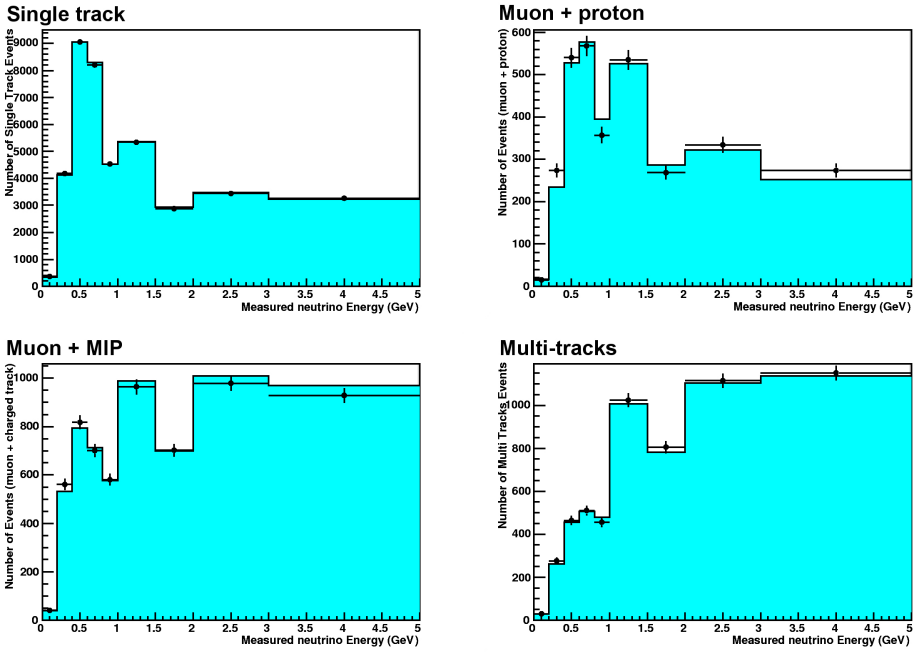

Figure 6.24: Predicted number of events (blue) vs observed number of events in the MC sample (dots) as a function of the measured neutrino energy for each event topology.

Average fit	f_2	f_3	f_4	f_5	f_6	f_7	f_8	f_9
f_2	1	**-0.307**	-0.061	0.019	-0.010	-0.012	0.021	-0.018
f_3	**-0.307**	1	**-0.489**	0.059	0.030	-0.043	0.028	-0.020
f_4	-0.061	**-0.489**	1	**-0.582**	0.116	-0.030	-0.003	0.003
f_5	0.019	0.059	**-0.582**	1	**-0.601**	0.272	-0.116	0.046
f_6	-0.010	0.030	0.116	**-0.601**	1	**-0.709**	0.331	-0.159
f_7	-0.012	-0.043	-0.030	0.272	**-0.709**	1	**-0.752**	0.386
f_8	0.021	0.028	-0.003	-0.116	0.331	**-0.752**	1	**-0.748**
f_9	-0.018	-0.020	0.003	0.046	-0.159	0.386	**-0.748**	1

Table 6.6: f_i flux factors correlation coefficients for the average fit without topologies.

4 Topologies fit	f_2	f_3	f_4	f_5	f_6	f_7	f_8	f_9
f_2	1	**-0.319**	-0.040	0.020	-0.018	0.012	-0.003	-0.003
f_3	**-0.319**	1	**-0.498**	0.080	0.021	-0.032	0.014	-0.004
f_4	-0.040	**-0.498**	1	**-0.593**	0.128	-0.046	0.017	-0.012
f_5	0.020	0.080	**-0.593**	1	**-0.591**	0.263	-0.104	0.037
f_6	-0.018	0.021	0.128	**-0.591**	1	**-0.695**	0.293	-0.117
f_7	0.012	-0.032	-0.046	0.263	**-0.695**	1	**-0.715**	0.320
f_8	-0.003	0.014	0.017	-0.104	0.293	**-0.715**	1	**-0.693**
f_9	-0.003	-0.004	-0.012	0.037	-0.117	0.320	**-0.693**	1

Table 6.7: f_i flux factors correlation coefficients for the fit with topologies.

The flux χ^2, which indicates how close to the predicted flux we are, must be computed while taking into the full covariance matrix of the flux factors fit because the flux factors for each true energy bin are highly correlated between themselves, in particular the flux factors from neighbouring bins (Tab.6.6 and 6.7). Therefore, the flux χ^2 are computed as follows:

$$\chi^2_{flux} = \overrightarrow{F}^T \times \text{COV}^{-1} \times \overrightarrow{F} \tag{6.15}$$

where $\overrightarrow{F} = (f_1 - 1, ..., f_9 - 1)$ and COV^{-1} is the inverted covariance matrix.

The average fit has 9 energy bins and fits 8 flux parameters, therefore there is only 1 degree of freedom (dof) for the spectrum χ^2. As for the fit with topologies, there are 9 energy bins per topology but only 8 fitted parameters thus number of degrees of freedom is 28 for the spectrum χ^2. We expect the flux χ^2 to be consistent with an 8 dof χ^2 distribution while the spectrum χ^2 should be consistent with the χ^2 distributions for 1 dof (resp. 28 dof) for the average fit (resp. fit with topologies).

	Average fit	4-topology fit
f_1	1 (fixed)	1 (fixed)
f_2	1.087 ± 0.138	1.097 ± 0.128
f_3	1.024 ± 0.031	1.020 ± 0.029
f_4	0.984 ± 0.028	0.987 ± 0.027
f_5	1.003 ± 0.053	0.986 ± 0.049
f_6	1.002 ± 0.059	1.032 ± 0.051
f_7	0.966 ± 0.115	0.936 ± 0.093
f_8	0.985 ± 0.081	0.982 ± 0.064
f_9	1.053 ± 0.034	1.014 ± 0.028
Spectrum χ^2	1.9 (1 dof)	22.2 (28 dof)
Flux χ^2	6.02	3.33

Table 6.8: Fitted flux factors f_i for each true energy bin number i, for the average fit and the 4-topology fit.

The results of the fits are given in table 6.8. All flux factors are consistent with 1 and the χ^2 are within the expected values. Although the errors are large because of the important correlations between the energy bins –due to the large energy resolutions – the 4-topology fit has

smaller errors than the average fit. Because the topologies enhance a given interaction channel (Sec.5.6), the reconstructed energy resolutions are better for the CCQE-enhanced topologies.

	Single track	Mu+Proton	Mu+MIP	Multi-tracks
f_2	1.10 ± 0.13	11.13 ± 11.10	2.74 ± 2.93	1.00 ± 4.83
f_3	1.02 ± 0.03	1.09 ± 0.20	1.05 ± 0.53	5.13 ± 7.99
f_4	0.98 ± 0.03	1.07 ± 0.12	0.84 ± 0.31	1.62 ± 1.57
f_5	1.01 ± 0.05	0.64 ± 0.18	1.56 ± 0.72	0.68 ± 1.48
f_6	1.02 ± 0.05	1.22 ± 0.18	0.62 ± 0.67	1.23 ± 0.97
f_7	0.97 ± 0.10	0.67 ± 0.36	1.21 ± 0.74	0.49 ± 1.75
f_8	0.96 ± 0.07	1.01 ± 0.28	1.04 ± 0.27	1.35 ± 0.82
f_9	1.03 ± 0.04	1.15 ± 0.14	0.91 ± 0.08	0.98 ± 0.13
Flux χ^2	3.24	13.35	5.23	2.34

Table 6.9: Fitted flux factors and error, for each topology separately.

The third test consists in fitting each topology individually as if it were the average fit, to check if each of the topologies is properly modeled. The detailed parameters values and errors are given in table 6.9. Again, the central values do not show any bias and the flux χ^2 have values consistent with the 8-dof χ^2 distribution, which is not yet a Gaussian distribution. For certain true energy bins, the error on the single track fit is better than the 4-topology fit. Indeed, the single track category is the most populated category and is enriched in CCQE events, thus its energy resolution is better.

6.4.2 Cross-checks with equivalent to POT$_{data}$ MC samples

In section 5.2, the amount of POTs for the MC sample and the data samples were given, showing that the MC sample is equivalent to 33.7 times the data sample in terms of POT. Therefore, to further test the quality of our fit and to establish a reference to compare to the data fit, we divide the full MC sample into 33 POT$_{data}$ equivalent samples by randomly splitting the MC events.

We first check the flux factors fitted values for each fit type – with or without topologies – and look for any anomaly such as a bias.

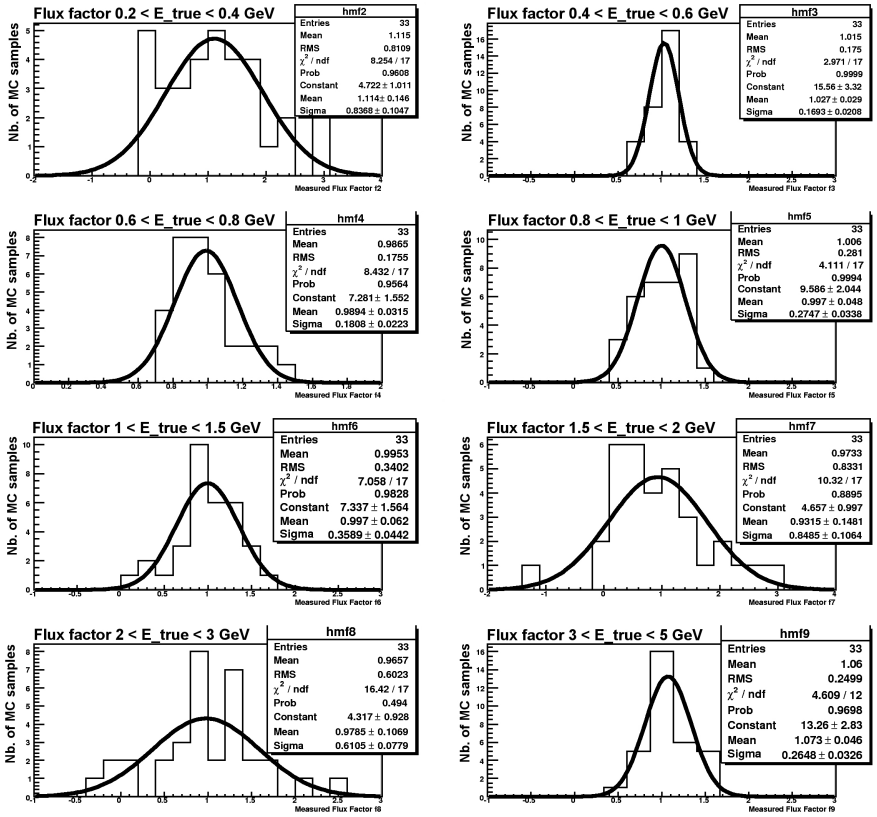

Figure 6.25: Flux factor f_i distributions for the average fit, fitted by a Gaussian.

Figure 6.25 shows an example of the f_i distributions fitted by a Gaussian for the average fit. Table 6.10 summarizes the fitted mean values and dispersion of each f_i distribution for both the average and the 4-topology fits. All the f_i distributions have a mean value consistent with 1. No particular bias is observed.

With each of the fitted f_i and their corresponding error σ_i for the 33 MC samples, we can compute sample per sample the pull for each f_i:

$$Pull_i = \frac{f_i - 1}{\sigma_i} \tag{6.16}$$

Figure 6.26 shows as example of the pulls for the f_i resulting from the 4-topology fit and their Gaussian fits. Table 6.11 summarizes the pull values and widths for both fit types. All pulls

	Average fit		4-topologies fit	
	Mean	σ	Mean	σ
f_2	1.114 ± 0.146	0.831 ± 0.105	1.135 ± 0.142	0.782 ± 0.116
f_3	1.027 ± 0.029	0.169 ± 0.021	1.008 ± 0.032	0.181 ± 0.022
f_4	0.989 ± 0.032	0.181 ± 0.022	0.989 ± 0.030	0.170 ± 0.021
f_5	0.997 ± 0.048	0.275 ± 0.034	0.992 ± 0.053	0.302 ± 0.038
f_6	0.997 ± 0.062	0.359 ± 0.044	1.026 ± 0.058	0.331 ± 0.044
f_7	0.932 ± 0.148	0.849 ± 0.106	0.936 ± 0.106	0.608 ± 0.078
f_8	0.979 ± 0.107	0.611 ± 0.078	0.955 ± 0.078	0.424 ± 0.060
f_9	1.073 ± 0.046	0.265 ± 0.033	1.014 ± 0.033	0.190 ± 0.023

Table 6.10: Mean and σ of the Gaussian which fits the f_i distribution obtained from the 33 data-equivalent MC samples.

have a mean value consistent with 0 and a width consistent with 1 as expected, which proves that the errors on the flux factors have been well estimated.

	Average fit		4-topologies fit	
	Mean	σ	Mean	σ
f_2	0.115 ± 0.174	0.999 ± 0.124	0.176 ± 0.183	1.048 ± 0.130
f_3	0.103 ± 0.171	0.980 ± 0.121	0.042 ± 0.176	1.009 ± 0.125
f_4	-0.115 ± 0.184	1.056 ± 0.131	-0.067 ± 0.188	1.079 ± 0.134
f_5	0.018 ± 0.157	0.903 ± 0.111	-0.042 ± 0.173	0.995 ± 0.123
f_6	0.030 ± 0.177	1.015 ± 0.126	0.115 ± 0.175	1.004 ± 0.124
f_7	-0.038 ± 0.220	1.262 ± 0.156	-0.103 ± 0.191	1.094 ± 0.136
f_8	-0.068 ± 0.212	1.218 ± 0.150	-0.091 ± 0.188	1.077 ± 0.134
f_9	0.250 ± 0.219	1.256 ± 0.155	0.079 ± 0.194	1.114 ± 0.139

Table 6.11: Pull distributions mean and width for each f_i distribution.

We showed earlier on the correlation matrices obtained when fitting the full MC sample, which revealed a strong correlation between the fitted flux factors for adjacent true neutrino energy bins. With the 33 sub-samples, we can directly observe the correlation between the flux factors. For example, figure 6.27 shows the correlation between f_3 and f_4. The linear fit yields

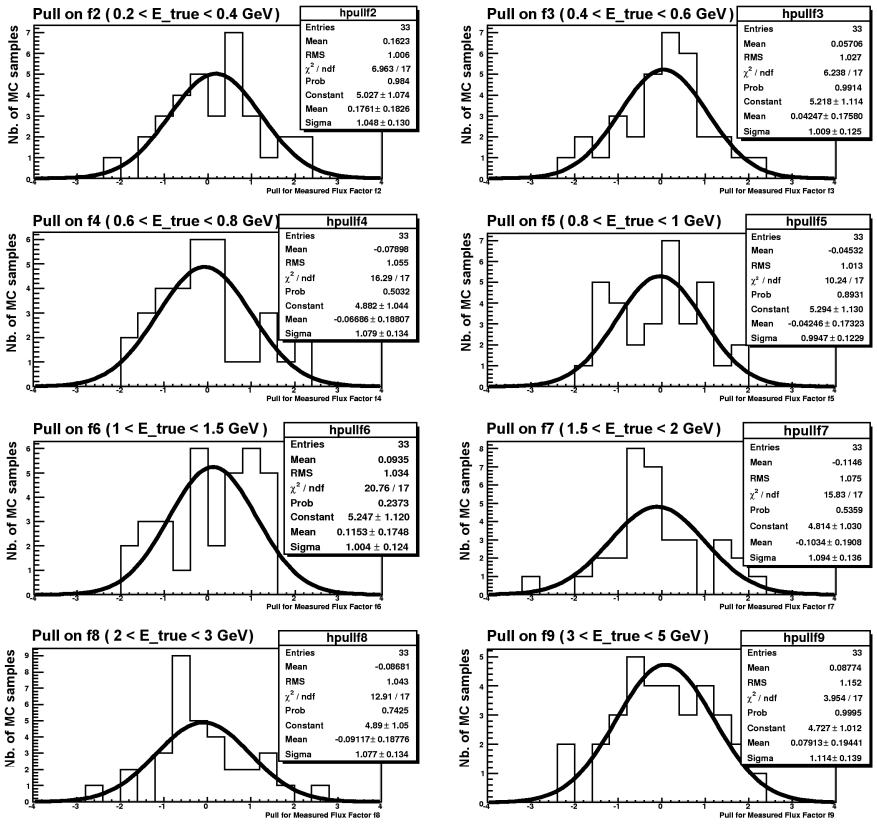

Figure 6.26: Pull distributions for each f_i for the 4-topology fit obtained with the 33 data-equivalent MC samples, fitted by a Gaussian.

a correlation of 0.57 which is close to the one given in the correlation matrix.

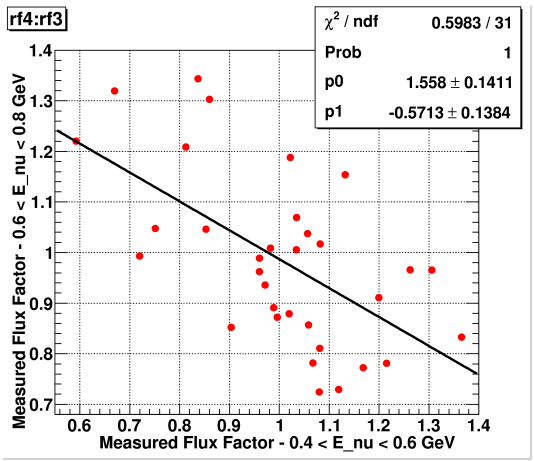

Figure 6.27: Correlation between fitted values of the f_3 and f_4 flux factors.

As done previously with the full MC sample, we can also evaluate the quality of our fits by computing the flux and spectrum χ^2. Figure 6.28 shows the distribution of the flux χ^2 and the expected χ^2 function for 8 degrees of freedom. All of the flux χ^2 are in agreement with the expected values.

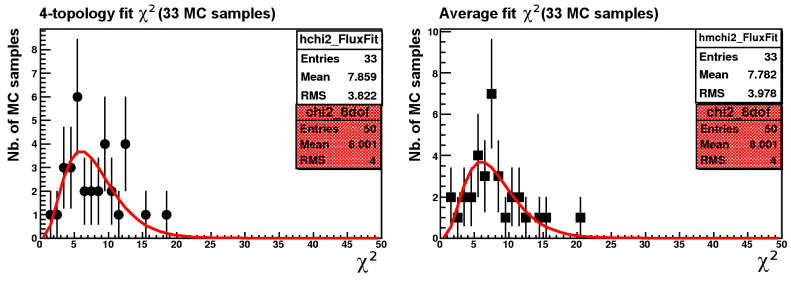

Figure 6.28: Flux χ^2 distributions (dots) for the 4-topology (left) and the average (right) fits compared to the 8-degrees of freedom χ^2 (red curve).

If we focus on the 4-topology fit, and compute the total spectrum χ^2 by adding the 4 partial χ^2 (Fig.6.29), it is consistent with the 28 degrees of freedom χ^2 function. The partial spectrum χ^2 are also plotted in the same figures, their sum yields the total spectrum χ^2. These partial χ^2, which do not have a meaning on their own, are shown on the bottom four plots of same figure. The top left plot shows the "averaged" spectrum χ^2 computed as if the fit was the average fit,

i.e. computed for the summed up spectrum instead of topology per topology, but with the flux factors fitted with the topologies.

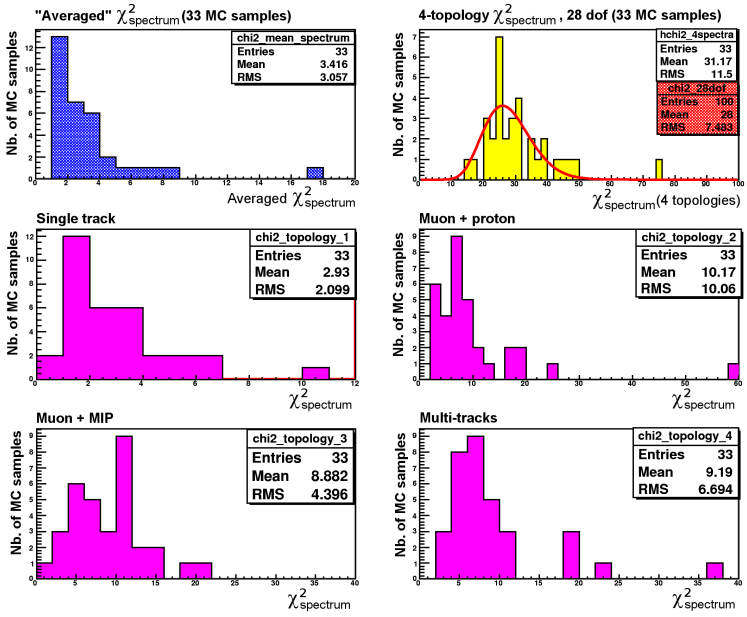

Figure 6.29: Top left: "Averaged" spectrum χ^2. Top right: total spectrum χ^2. 4 bottom plots: Partial spectrum χ^2 per topology.

Finally, now that each fit type has been individually tested and has proved to work fine, we can compare the average fit to the 4-topology fit.

One of the advantages of the 4-topology fit is that the errors are smaller than for the average fit. The ratios of the 4-topology to the average fit flux factor errors are shown in figure 6.30. Indeed, for all the measured energy bins, the ratio is smaller than 1. The errors are 10 to 20 % better when using the 4-topology fit configuration.

The next comparison between the fit configurations consists in computing the differences between the f_i values obtain the 4-topology fit and the average fit (Fig.6.31). Each of the obtained distributions can be fitted with a Gaussian, whose mean value and σ are given in table 6.12. Both fitting methods are consistent since all the mean values are consistent with 0. The σ of the distributions represent the average dispersion between the values obtained with one

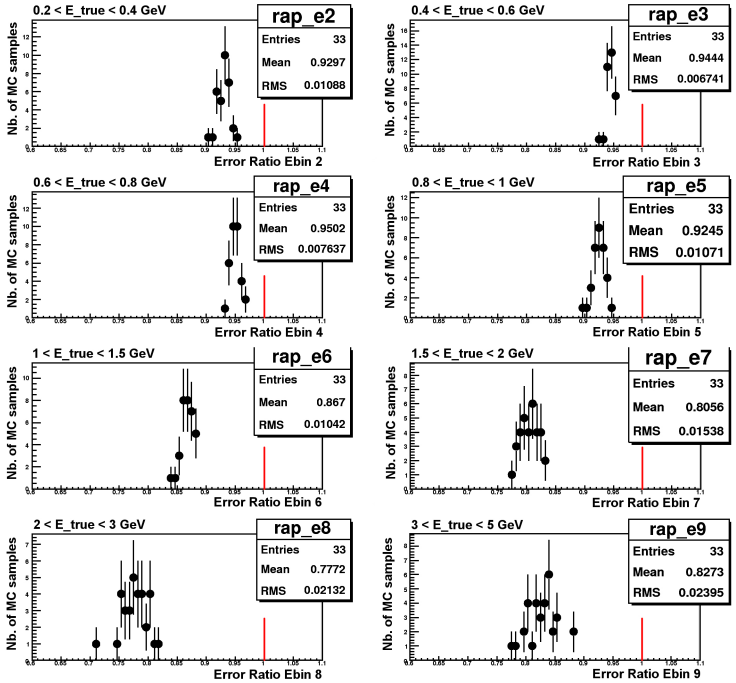

Figure 6.30: Ratio of the flux factors error computed with the 4-topology fit to the flux factor error computed with the average fit, for the 33 MC samples. The red line shows when the ratio is 1.

	Mean	σ
f_2	0.015 ± 0.056	0.323 ± 0.040
f_3	-0.004 ± 0.011	0.064 ± 0.008
f_4	0.001 ± 0.009	0.054 ± 0.007
f_5	-0.016 ± 0.021	0.120 ± 0.015
f_6	0.032 ± 0.033	0.191 ± 0.024
f_7	-0.024 ± 0.083	0.474 ± 0.058
f_8	0.012 ± 0.065	0.372 ± 0.046
f_9	-0.040 ± 0.020	0.132 ± 0.016

Table 6.12: Difference between the fitted f_i for the 4-topology fit minus the average fit.

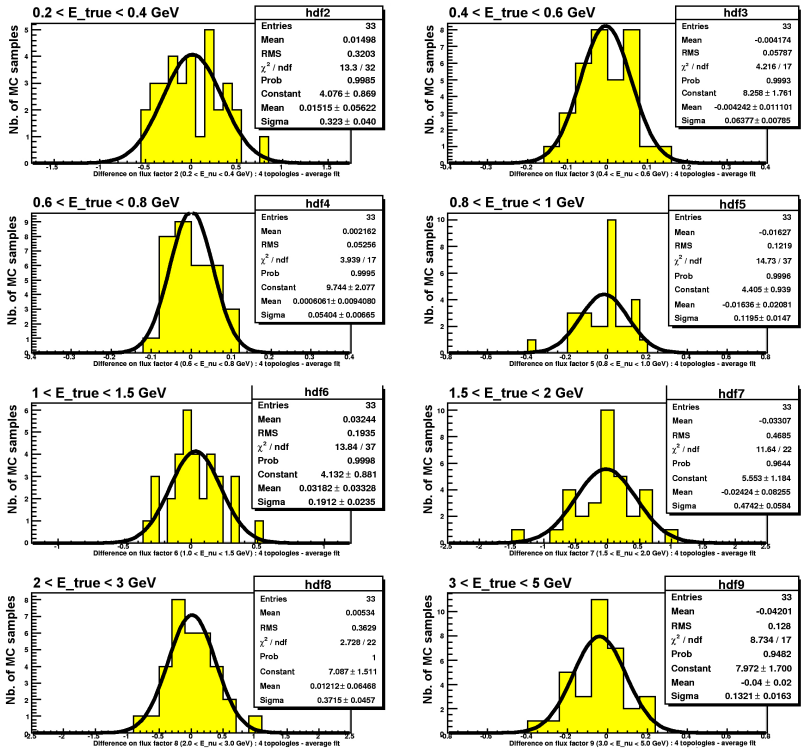

Figure 6.31: Distributions of the difference between the fitted f_i for the 4-topology fit minus the average fit.

method compared to the other.

To summarize, we can conclude that the flux fit, with both average and 4-topology configurations, is well understood and stable enough to be used to fit real data.

6.5 Results on neutrino data and systematic errors

Now that the fit has been validated with the MC, we can finally fit the data. One additional correction must be done at this stage, to take into account the bias produced by the muon pull cut. As explained in section 5.4, because of an issue with the muon pull PID calibration and correction, there is a 4 % difference between the number of events in selected in the data sample and the MC sample. We will therefore normalize the expected number of events by 0.96.

We will first present the results obtained with both the average and 4-topology fits (Sec.6.5.1) and then we will discuss the main sources of systematic errors (Sec.6.5.2) such as the out-of-fiducial volume contribution , the cross-section uncertainties and a few hints on the final state interaction (FSI) errors. We will also discuss the other sources of uncertainty, relative to the different corrections made.

6.5.1 Data fit results

Table 6.13 summarizes the fit results with both the average and the 4-topology fits on the data sample. The errors are large because of the large correlations between neighbouring energy bins and because of the low statistics, but the parabolic approximation to compute them seems to be good since the MINOS errors are almost symmetric and close to the parabolic errors. The flux χ^2 cannot be directly computed as we did for the MC, since now we must take into account the errors on the flux predictions and the systematics of our analysis.

The average fit shows an overall good agreement between the prediction and the measured spectrum (Fig.6.32).

The 4-topology fit has smaller errors than the average fit as expected. Nevertheless, if we compare the predicted number of events to the observed ones per measured energy bin and per topology, we see that there is an overall prediction excess in the single track topology while all

	Average ($\pm$ MINOS err.)	4-topology ($\pm$ MINOS err.)
f_1	1 (fixed)	1 (fixed)
f_2	$3.813 \pm 0.825 \left(^{+0.843}_{-0.813}\right)$	$2.821 \pm 0.756 \left(^{+0.772}_{-0.744}\right)$
f_3	$1.101 \pm 0.160 \left(^{+0.162}_{-0.159}\right)$	$1.167 \pm 0.153 \left(^{+0.155}_{-0.151}\right)$
f_4	$0.627 \pm 0.141 \left(^{+0.144}_{-0.141}\right)$	$0.577 \pm 0.134 \left(^{+0.137}_{-0.134}\right)$
f_5	$0.893 \pm 0.305 \left(^{+0.313}_{-0.306}\right)$	$0.725 \pm 0.287 \left(^{+0.295}_{-0.287}\right)$
f_6	0.789 ± 0.365 ($\pm$ 0.374)	$1.175 \pm 0.328 \left(^{+0.335}_{-0.334}\right)$
f_7	$1.333 \pm 0.686 \left(^{+0.715}_{-0.705}\right)$	$0.810 \pm 0.587 \left(^{+0.610}_{-0.595}\right)$
f_8	$1.524 \pm 0.453 \left(^{+0.470}_{-0.463}\right)$	$1.423 \pm 0.396 \left(^{+0.409}_{-0.400}\right)$
f_9	$0.712 \pm 0.191 \left(^{+0.199}_{-0.189}\right)$	$0.920 \pm 0.178 \left(^{+0.183}_{-0.176}\right)$
Spect. χ^2	1.87 (1 dof)	77.91 (28 dof)

Table 6.13: Fitted flux factors f_i for each true energy bin number i, for the full fit and the fit with topologies. The statistical errors are given.

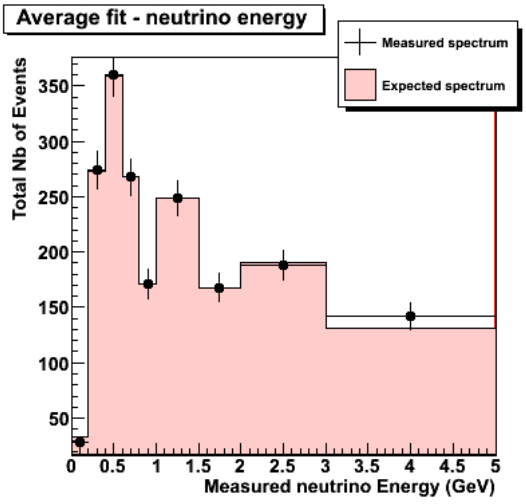

Figure 6.32: Comparison between the expected number of events (orange histogram) and the observed ones (dots) as a function of the measured neutrino energy for the average fit.

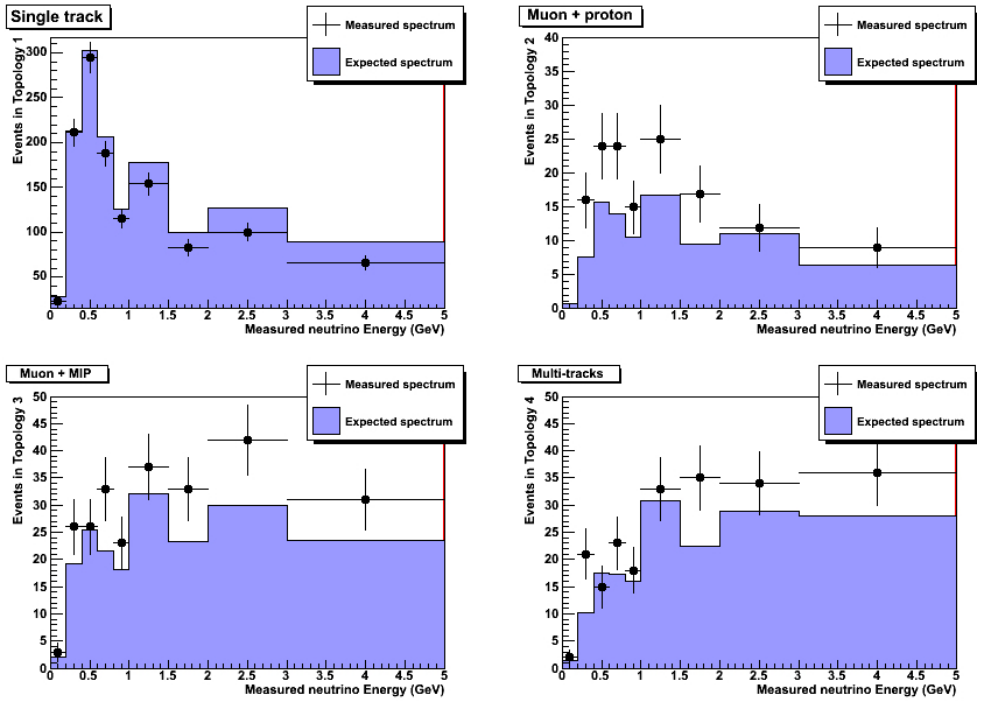

Figure 6.33: Comparison between the expected number of events (blue histogram) and the observed ones (dots) as a function of the measured neutrino energy per topology for the 4-topology fit.

the other topologies present a prediction deficit (Fig.6.33).

To quantify this disagreement, we computed once again the spectrum $\chi^2_{spectrum}$ and a new χ^2, the difference between the average fit and the 4-topology fit χ^2_{diff}.

The total $\chi^2_{spectrum}$ for the data is 77.91, which is too high to be consistent with the values show on top left plot of figure 6.29. The partial $\chi^2_{spectrum}$ are

$$\begin{aligned} \chi^2_{spectrum}(Singletrack) &= 27.488; \\ \chi^2_{spectrum}(\mu + p) &= 19.707; \\ \chi^2_{spectrum}(\mu + MIP) &= 15.822; \\ \chi^2_{spectrum}(Multi - track) &= 14.892. \end{aligned} \tag{6.17}$$

Each of the values is relatively high compared to the partial $\chi^2_{spectrum}$ distributions given in figure 6.29.

The difference between fit types χ^2_{diff}, which is an estimator of the agreement between both fit configurations, is defined as

$$\chi^2_{diff} = \sum_{ie_{meas}=1}^{9} \left(\frac{f_i^{4topo} - f_i^{average}}{\sigma_{diff}} \right)^2 \tag{6.18}$$

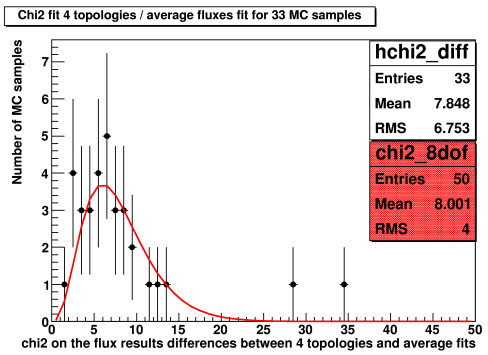

Figure 6.34: χ^2_{diff} distribution computed for the 33 MC samples. For the data, $\chi^2_{diff} = 21.17$.

The χ^2_{diff} for each of 33 MC samples, computed with the values given in table 6.12, are shown in figure 6.34. Their distribution is consistent with a 28 degrees of freedom χ^2 distribution as expected. To compute the data χ^2_{diff} we use the same σ_{diff} than the MC. The computed

χ^2_{diff} for the data is 21.17, which is as the very limit of the acceptable χ^2_{diff} values.

Therefore, both χ^2 values show that the 4-topology fit is not well understood.

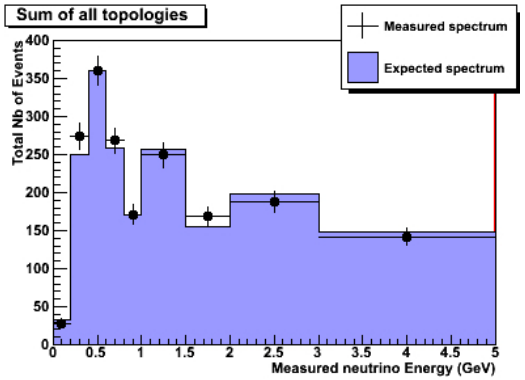

Figure 6.35: Comparison between the expected number of events (blue histogram) and the observed ones (dots) as a function of the measured neutrino energy for all topologies added up.

Although the individual topologies show a disagreement, there is no disagreement between the prediction and the observed spectrum when all topologies are added (Fig.6.35). This means the problems is not related to the overall fit with topologies itself, but rather with the distribution of the events between the topologies.

Since the largest systematics are expected to come from the neutrino interactions cross-sections, we fitted the relative fractions of each charged current interaction category while fixing the other flux factors to 1, to check whether the agreement increased or not (Tab.6.14). The fitted fractions show much larger variations than the systematic errors assigned to each of the interaction categories (Tab.6.3), in particular for the CCQE fraction. Indeed, the CCQE process is dominant in the single track and muon + proton topologies, but while there is an excess of expected events in the single track topology, in the muon + proton topology there is a prediction deficit. Therefore, the fit tries to compensate simultaneously the contradictory variations. Neither the agreement between the observed and the expected number of events per topology nor the spectrum χ^2 are improved (Fig.6.36). Therefore the disagreement is not due the fraction of each process. A few elements which can explain this disagreement are given

later on in section 6.5.2.3.

	4-topology fit
f_{CCQE}	0.628 ± 0.064
f_{CCRES}	1.449 ± 0.143
f_{CCDIS}	1.117 ± 0.311

Table 6.14: Fitted relative fractions for the different processes.

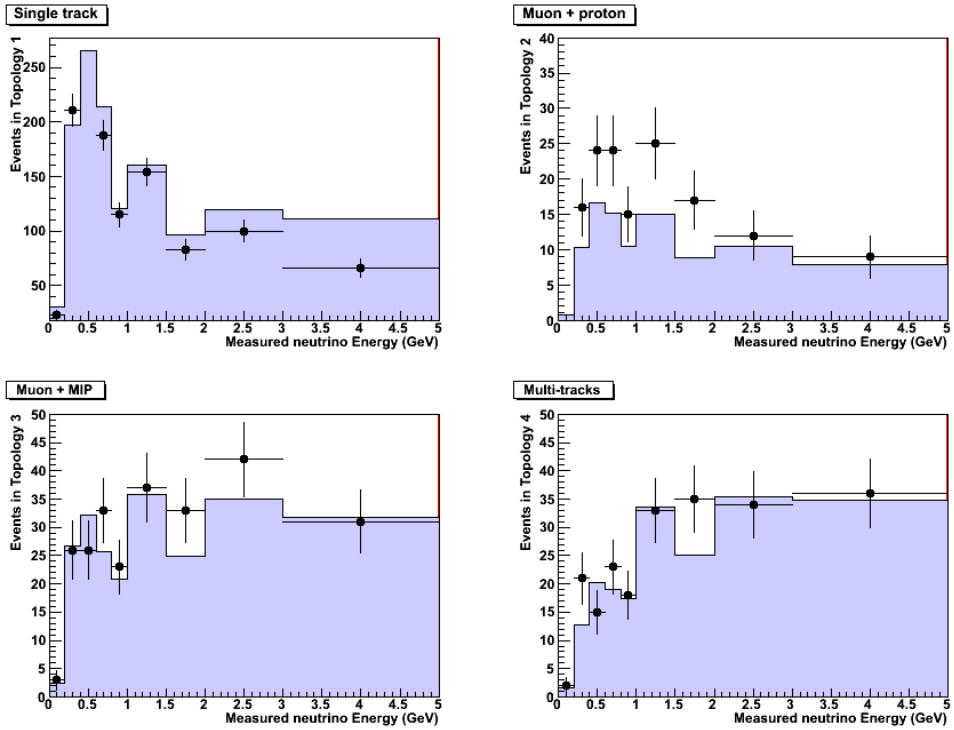

Figure 6.36: Comparison between the expected number of events (blue histogram) and the observed ones (dots) when the process fractions are simultaneously fitted, as a function of the measured neutrino energy per topology.

For now we can conclude that the average fit works well with data, but that the 4-topology fit needs further investigation to understand the event distribution disagreement between the topologies and requires further testing.

6.5.2 Systematic errors

In this section we will review the main sources of systematic errors for the flux measurement. We will start with the cross-section related uncertainties and the out-of-FV induced errors. Then we will discuss the final state interaction (FSI) related issues. Finally, we will summarize the other sources of systematic errors such as the ones assigned to the various manual corrections we did on the flux algorithm.

6.5.2.1 Cross-sections uncertainties

The uncertainties on the neutrino interaction cross-sections are large, therefore we expect the systematics associated to them on the flux factors to be large. To compute these systematics, we applied $\pm$ 1 $\sigma_{k_{proc}}$ variations on each of the cross-sections for each atom type, independently for each interaction category k_{proc}, and re-fitted the data sample. The $\sigma_{k_{proc}}$ can be found in table 6.3. The resulting fluctuations on the fitted flux factors with respect to the values given in table 6.13 will be assigned as systematic errors on the latter.

	Average fit				4-topology fit			
	CCQE	CCRES	CCDIS	NC	CCQE	CCRES	CCDIS	NC
f_2	$^{+0.462}_{-0.433}$	$^{+0.941}_{-0.781}$	$^{+0.015}_{-0.012}$	$^{+0.038}_{-0.036}$	$^{+0.279}_{-0.296}$	$^{+0.780}_{-0.653}$	$^{+0.003}_{-0.003}$	$^{+0.017}_{-0.017}$
f_3	$^{+0.255}_{-0.175}$	$^{+0.118}_{-0.100}$	$^{+0.002}_{-0.002}$	$^{+0.013}_{-0.013}$	$^{+0.305}_{-0.197}$	$^{+0.105}_{-0.076}$	$^{+0.000}_{-0.000}$	$^{+0.008}_{-0.008}$
f_4	$^{+0.160}_{-0.104}$	$^{+0.058}_{-0.045}$	$^{+0.002}_{-0.002}$	$^{+0.006}_{-0.005}$	$^{+0.150}_{-0.097}$	$^{+0.044}_{-0.037}$	$^{+0.001}_{-0.001}$	$^{+0.007}_{-0.007}$
f_5	$^{+0.248}_{-0.153}$	$^{+0.067}_{-0.043}$	$^{+0.005}_{-0.005}$	$^{+0.008}_{-0.008}$	$^{+0.124}_{-0.099}$	$^{+0.125}_{-0.120}$	$^{+0.000}_{-0.001}$	$^{+0.003}_{-0.003}$
f_6	$^{+0.079}_{-0.068}$	$^{+0.223}_{-0.133}$	$^{+0.010}_{-0.008}$	$^{+0.020}_{-0.019}$	$^{+0.310}_{-0.193}$	$^{+0.099}_{-0.041}$	$^{+0.014}_{-0.010}$	$^{+0.023}_{-0.022}$
f_7	$^{+0.147}_{-0.123}$	$^{+0.343}_{-0.300}$	$^{+0.048}_{-0.044}$	$^{+0.016}_{-0.016}$	$^{+0.003}_{-0.079}$	$^{+0.325}_{-0.332}$	$^{+0.021}_{-0.030}$	$^{+0.006}_{-0.007}$
f_8	$^{+0.195}_{-0.153}$	$^{+0.113}_{-0.071}$	$^{+0.008}_{-0.003}$	$^{+0.004}_{-0.005}$	$^{+0.242}_{-0.175}$	$^{+0.045}_{-0.018}$	$^{+0.015}_{-0.005}$	$^{+0.019}_{-0.017}$
f_9	$^{+0.088}_{-0.074}$	$^{+0.292}_{-0.202}$	$^{+0.074}_{-0.074}$	$^{+0.010}_{-0.010}$	$^{+0.044}_{-0.046}$	$^{+0.444}_{-0.276}$	$^{+0.096}_{-0.097}$	$^{+0.008}_{-0.009}$

Table 6.15: f_i flux factors variations due to 1 σ-fluctuations on the cross-section for each interaction category and for both fit configurations.

Table 6.15 shows the detailed contribution of each of the interaction processes to the cross-section systematic error. The combined variations of the flux factors due to the cross-section variations are shown in table 6.16.

	Average		4-topology	
f_2	-0.894	+1.049	-0.717	+0.828
f_3	-0.202	+0.281	-0.211	+0.323
f_4	-0.113	+0.170	-0.104	+0.156
f_5	-0.159	+0.257	-0.156	+0.176
f_6	-0.151	+0.237	-0.199	+0.327
f_7	-0.328	+0.377	-0.343	+0.326
f_8	-0.169	+0.225	-0.177	+0.248
f_9	-0.228	+0.314	-0.296	+0.457

Table 6.16: Overall f_i flux factors variations due to cross-section 1σ-fluctuations.

As expected, the systematic errors induced by the cross-sections are of the same order of magnitude than the uncertainties on the cross-sections. Both fit configurations yield similar systematic errors. In particular, the error on f_2 is large because the second true energy bin has low statistics and because it is highly correlated to the third true energy bin which is more populated. Thus, a small variation on the third energy bin leads to a stronger variation on the second energy bin.

Nevertheless, with more statistics it would be possible to fit simultaneously the relative fractions of each process and the flux factors, thus turning this systematic partially into a statistical error.

6.5.2.2 Out-of-fiducial volume contamination

The out-of-fiducial volume (out-of-FV) events are the main contamination source in our selected sample (Tab. 5.4). There is no theoretical model to describe them therefore they cannot be accurately predicted by a calculation. Nevertheless, we know they are correlated to the neutrino fluxes since most of them come from beam neutrino interactions taking place outside of the FGDs (surrounding rocks/sand, magnet, etc.). Therefore, we can predict their contribution to the measured energy spectrum with the MC simulation, which for now does not accurately reproduce reality since it does not include the sand muons. Indeed, a simulation of the sand muons is currently being developped.

These out-of-FV events are therefore considered as one of the main potential sources of systematic errors in the flux fit. Two types of uncertainty can be computed from this contribution: an out-of-FV normalization error and an out-of-FV measured energy spectrum shape error.

	Average	4-topology
f_2	$\pm$ 0.715	$\pm$ 1.708
f_3	$\pm$ 0.039	$\pm$ 0.060
f_4	$\pm$ 0.023	$\pm$ 0.039
f_5	$\pm$ 0.019	$\pm$ 0.025
f_6	$\pm$ 0.030	$\pm$ 0.061
f_7	$\pm$ 0.031	$\pm$ 0.042
f_8	$\pm$ 0.010	$\pm$ 0.039
f_9	$\pm$ 0.050	$\pm$ 0.065

Table 6.17: f_i fluctuations when the fraction of out-of-FV is simultaneously fitted.

To compute the systematic error due to the out-of-FV normalization, we can fit the global out-of-FV fraction (which is normally fixed to 1) and observe what fluctuations it produces on the fitted f_i. The fitted out-of-FV fractions in the average and 4-topology fit configurations are

$$f_{out}^{average} = 0.705 \pm 0.303 \quad \text{and} \quad f_{out}^{4-topology} = 0.506 \pm 0.239. \tag{6.19}$$

Both fitted fractions are consistent with 1 at 1 or 2 σ. These fractions were also fitted with the MC sample and the values were also consistent with 1 for both fit configurations. Table 6.17 shows the observed f_i fluctuations, which will be assigned as the out-of-FV normalization systematics.

To study the uncertainties produced by a shape variation of the out-of-FV measured energy spectrum, we split the latter into three categories according to where the true neutrino interaction vertex is: the magnet, the electromagnetic calorimeter (ECAL) or the π^0 detector (P0D), and the tracker volume which is not part of the fiducial volume (Fig. 6.37). We will suppose that these three distributions are not correlated thus they can fluctuate independently from each other. To have a visible shape modification, we will vary the relative fractions of

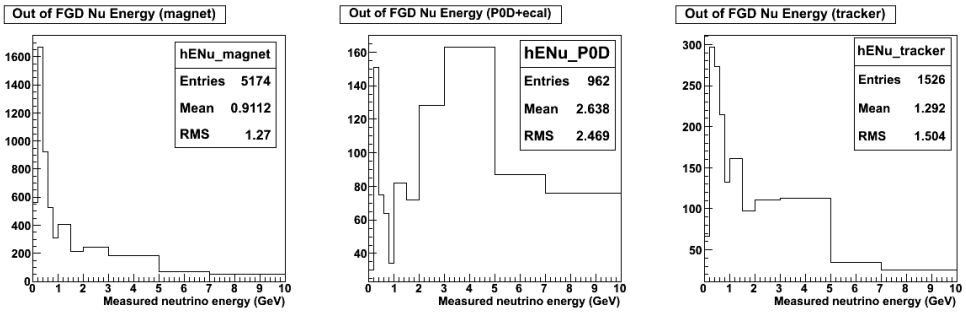

Figure 6.37: From left to right: Magnet, Ecal+P0D, and tracker components of the out-of-FV contribution to the measured neutrino energy distribution.

the ECAL+P0D and tracker components by $\pm$ 50 %. Since we only want to study the shape induced errors, we will keep the total fraction of out-of-FV constant, using the magnet distribution to absorb the ECAL+P0D fluctuation or the tracker fluctuation since it is the most populated category.

	Average		4-topology	
f_2	-0.277	+0.460	-0.520	+0.110
f_3	-0.025	+0.018	-0.039	+0.008
f_4	-0.011	+0.012	-0.020	+0.000
f_5	-0.020	+0.011	-0.049	+0.004
f_6	-0.021	+0.009	-0.020	+0.000
f_7	-0.007	+0.029	-0.045	+0.002
f_8	-0.024	+0.010	-0.005	+0.017
f_9	-0.027	+0.079	-0.018	+0.012

Table 6.18: Out of FV shape systematics per f_i for the average and 4-topology fits.

Table 6.18 summarizes the fluctuations on the f_i with respect to the values given in 6.13 induced by the out-of-FV contribution shape variation. These fluctuations will be assigned as the out-of-FV shape systematic errors.

Table 6.19 presents the combined out-of-FV shape and normalization systematic errors. The combined normalization and shape errors are reasonable since they are of the order of a few percent, except for f_2 which has a large error for the reasons stated in section 6.5.2.1.

	Average		4-topology	
f_2	-0.767	+0.850	-1.786	+1.712
f_3	-0.046	+0.043	-0.072	+0.061
f_4	-0.026	+0.026	-0.044	+0.039
f_5	-0.027	+0.022	-0.055	+0.025
f_6	-0.037	+0.031	-0.064	+0.061
f_7	-0.032	+0.042	-0.061	+0.042
f_8	-0.026	+0.014	-0.039	+0.043
f_9	-0.057	+0.094	-0.067	+0.066

Table 6.19: Combined out-of-FV shape and normalization systematics.

6.5.2.3 Final state interactions

The disagreement for each separate event topology between the expected and the measured neutrino energy distributions can be due to apparent event migrations from one topology to another, since there is an overall excess of expected events in the single track topology while there is an average deficit on all of the other topologies. After the neutrino interaction with the nucleus, the outgoing proton or pions can be re-absorbed by the nuclear medium through final state interactions (FSI) therefore a biased estimation of this process rate could explain these apparent event migration. Indeed, an overestimation of the re-absorption rate in the MC simulation would lead to a migration from the topologies with more than one track to the single track topology as observed. To get a first estimate of the effect induced by the theoretical model used to compute the FSI, we compared the NEUT results with the ones obtained with another neutrino generator, GENIE[131], which uses a different theoretical framework.

Since we only want to study the differences caused by the different theoretical models used by the neutrino generators other than the cross-sections, we replaced the NEUT relative efficiencies (Sec. 6.3.3.5) by the ones obtained with GENIE. This study can only be done for the 4-topology fit configuration since we need the separation into topologies to see the effects of the FSI. Figure 6.38 shows the relative efficiencies for the CCRES interaction category for each topology obtained with both neutrino interaction generators. We can see that the relative efficiencies are different, in particular for the muon + proton and multi-track topologies. This will lead to different values for the fitted flux factors.

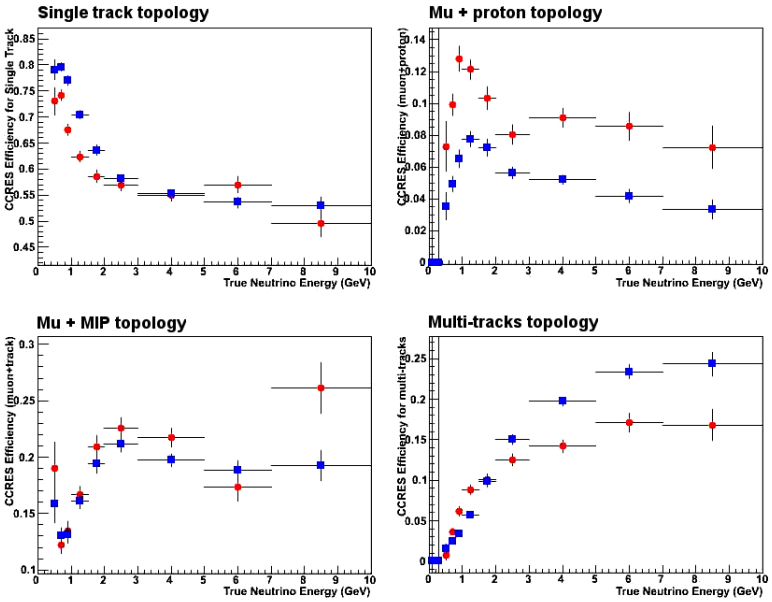

Figure 6.38: Comparison between the GENIE (red) and NEUT (blue) relative efficiencies for the CCRES interaction type per topology.

	NEUT	GENIE	Diff. GENIE - NEUT
f_2	2.821	2.724	-0.097
f_3	1.167	1.162	-0.005
f_4	0.577	0.567	-0.010
f_5	0.725	0.707	-0.019
f_6	1.175	1.140	-0.035
f_7	0.810	0.632	-0.178
f_8	1.423	1.574	+0.151
f_9	0.920	0.915	-0.005

Table 6.20: Fitted flux factors comparison between NEUT and GENIE for the 4-topology fit.

Table 6.20 shows the comparison between the results obtained with both neutrino interaction generators NEUT and GENIE. GENIE yields on average smaller flux factors than those fitted with NEUT. The largest differences between both generators are for the CCRES processes, whereas there is a good agreement between both for the CCQE processes. Indeed, the

largest variation on the fitted flux factors can be seen for the true neutrino energies comprised between 1 and 3 GeV (flux factors f6, f7, and f8), which is the region where the CCRES interactions are dominant.

The agreement between the measured spectrum and the GENIE predicted spectrum is improved for the two track topologies (muon + proton and muon + MIP) as it can be seen on figure 6.39 while the disagreement in the multi-tracks topology increases. Also, the $\chi^2_{spectrum}$ is smaller for the GENIE fit, in particular for the two track topologies but not for the multi-track topology (Tab. 6.21).

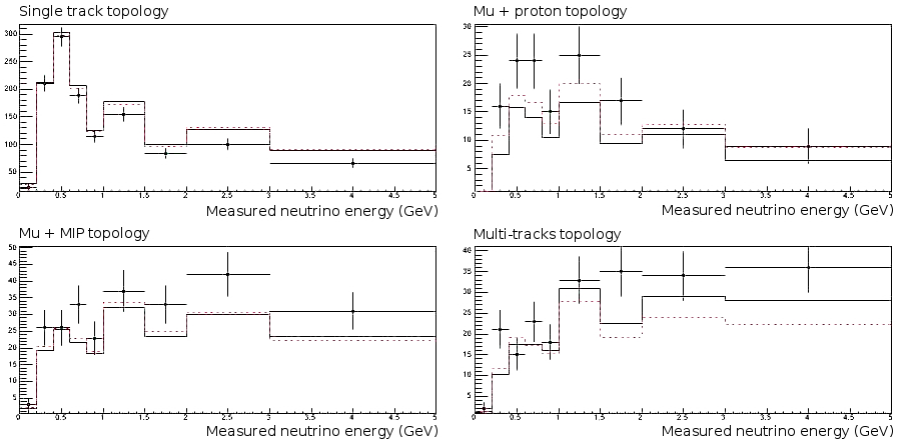

Figure 6.39: Comparison between the measured energy spectrum (dots) and the predicted spectra by NEUT (black histogram) and GENIE (dashed histogram).

	NEUT	GENIE
$\chi^2_{spectrum}$	77.9	71.2
$\chi^2_{spectrum}$(single track)	27.5	25.9
$\chi^2_{spectrum}$(μ^- + Proton)	19.7	8.9
$\chi^2_{spectrum}$(μ^- + MIP)	15.8	13.0
$\chi^2_{spectrum}$(Multi-tracks)	14.9	23.4

Table 6.21: Total spectrum χ^2 and contribution from each topology to the total $\chi^2_{spectrum}$.

We can conclude that the theoretical framework does have an impact on the apparent event migration between topologies and could partially explain the disagreement between the mea-

sured energy spectrum and the predicted one when comparing the energy spectra topology per topology. More detailed studies of theoretical models and in particular of the FSI parameters should be pushed further. Other sources of disagreement could be a reconstruction problem or some detector systematic. A possible way to explore this issue is using a more sophisticated reconstruction in the FGD, and looking for FGD-only tracks – tracks which did not reach the TPC – which are consistent with the neutrino interaction vertex. Also, we could try refining the definition of the different topologies.

Although they were computed with the 4-topology fit configuration, we will use for now the difference between the fitted flux factors as the systematic error due to the choice of the theoretical model for the average fit as well.

6.5.2.4 Other sources of uncertainty

We have assessed two of the main sources of systematic errors in the flux measurement, the cross-sections and the out-of-FV, and we have hints on the third main source of uncertainty, the final state interactions. Nevertheless, these are not the only sources of systematic errors. For instance, we must assign three more systematic errors, introduced by the two manual corrections we did on the calculation of the expected number of events and the one introduced by the contributions from neutrino energies greater than 5 GeV.

The first additional error is related to the number of nuclei in the fiducial volume normalization. We applied an overall -3.2 % correction on the expected number of events to compensate the predicted excess. We assign a conservative error of $\pm$ 1.6 % for this correction.

The second additional source of systematic error is the correction we applied when fitting the data, to take into account the 4 % of data deficit with respect to the MC caused by the muon pull cut. Once again, we assign a conservative error of $\pm$ 2 %.

As explained in section 6.3.3.4, although we measure neutrino energies up to 5 GeV, the flux for true neutrino energies higher than 5 GeV do contribute to the measured energies because of the spreading of the transfer matrices (energy resolution). Nevertheless, the flux factors of the 5-7 GeV, 7-10 GeV, and greater than 10 GeV bins are not fitted. Therefore, we will assign a systematic error to take into account their contribution. To estimate this error, we

	Average	4-topology
f_2	$\pm$ 0.007	$\pm$ 0.001
f_3	$<$ 0.001	$\pm$ 0.001
f_4	$\pm$ 0.003	$\pm$ 0.001
f_5	$\pm$ 0.002	$\pm$ 0.001
f_6	$\pm$ 0.013	$\pm$ 0.010
f_7	$\pm$ 0.126	$\pm$ 0.119
f_8	$\pm$ 0.156	$\pm$ 0.184
f_9	$\pm$ 0.231	$\pm$ 0.269

Table 6.22: Summary of the systematics related to the $E_\nu > 5$ GeV contributions.

applied $\pm$ 30 % variations on the total flux factors – normally fixed to 1 – for each of these extra energy bins, which corresponds to the uncertainty on the beam prediction at high energy. Table 6.22 summarizes the f_i fluctuations with respect to the reference values given in table 6.13, and shows that the errors are similar for both fit configurations. Since the contributions from high true neutrino energies to the low measured energies is small, the systematics for the first measured energy bins are small. The contribution from higher energies starts to be important for measured energies greater than 1 GeV, i.e. for the flux factors f_6 and above. This can be clearly observed on the computed systematics, the systematics go up to 27 % for the last measured energy bin.

6.6 Conclusion

The flux fitting algorithm has been thoroughly tested and validated with MC, proving that it is stable for both the average and 4-topology configurations. The fit on data works fine for the average configuration but the 4-topology configuration has put forward some issues related to the distribution of the events between the different topologies. This disagreement can be explained by event migrations from one topology to another due to an under/over-estimated value in the MC simulation of the proton and pion re-absorption rates which come from the final state interactions. More studies to confirm this hypothesis need to be done, which could imply reviewing the theoretical framework used to model the neutrino interactions.

The final results for the flux factors f_i given by the average fit configuration are summarized in table 6.23 with the statistical and the detailed systematic errors. The results with the combined systematic errors are given in table 6.24. Figure 6.40 shows the agreement between the fitted flux and the predicted flux as a function of the true neutrino energy. The dominant systematic error is the one due to cross-section uncertainties, which clearly constrains the precision of our measurement. Nevertheless, all systematics have not been computed yet, in particular detector and reconstruction systematics have yet to be evaluated.

	Average fit	Xsec	Out-of-FV	Th. Model	E > 5 GeV	N_{atom}	$Pull_\mu$
f_2	3.813 ± 0.825	$^{+1.049}_{-0.894}$	$^{+0.850}_{-0.767}$	± 0.097	± 0.007	± 0.016	± 0.020
f_3	1.101 ± 0.160	$^{+0.281}_{-0.202}$	$^{+0.043}_{-0.046}$	± 0.005	< 0.001	± 0.016	± 0.020
f_4	0.627 ± 0.141	$^{+0.170}_{-0.113}$	$^{+0.026}_{-0.026}$	± 0.010	± 0.003	± 0.016	± 0.020
f_5	0.893 ± 0.305	$^{+0.257}_{-0.159}$	$^{+0.022}_{-0.027}$	± 0.019	± 0.002	± 0.016	± 0.020
f_6	0.789 ± 0.365	$^{+0.237}_{-0.151}$	$^{+0.031}_{-0.037}$	± 0.035	± 0.013	± 0.016	± 0.020
f_7	1.333 ± 0.686	$^{+0.377}_{-0.328}$	$^{+0.042}_{-0.032}$	± 0.178	± 0.126	± 0.016	± 0.020
f_8	1.524 ± 0.453	$^{+0.225}_{-0.169}$	$^{+0.014}_{-0.026}$	± 0.151	± 0.156	± 0.016	± 0.020
f_9	0.712 ± 0.191	$^{+0.314}_{-0.228}$	$^{+0.094}_{-0.057}$	± 0.005	± 0.231	± 0.016	± 0.020

Table 6.23: Flux factors f_i fitted with the average fit configuration. The detailed contribution of the systematic errors is given.

	Average $\pm$ stat. $\pm$ syst.
f_2	$3.813 \pm 0.825\ ^{+1.354}_{-1.182}$
f_3	$1.101 \pm 0.160\ ^{+0.285}_{-0.209}$
f_4	$0.627 \pm 0.141\ ^{+0.174}_{-0.119}$
f_5	$0.893 \pm 0.305\ ^{+0.260}_{-0.164}$
f_6	$0.789 \pm 0.365\ ^{+0.243}_{-0.162}$
f_7	$1.333 \pm 0.686\ ^{+0.438}_{-0.396}$
f_8	$1.524 \pm 0.453\ ^{+0.314}_{-0.278}$
f_9	$0.712 \pm 0.191\ ^{+0.402}_{-0.331}$

Table 6.24: Final results obtained with the average fit.

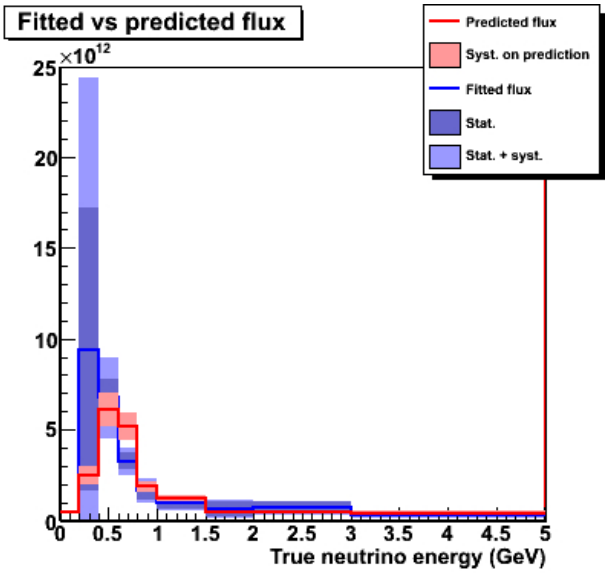

Figure 6.40: Comparison between the fitted flux as a function of the true neutrino energy (blue) with the statistical and systematic errors, and the predicted flux as a function of the energy (red) with the systematic errors.

Both systematic and statistical errors on the fitted flux factors can still be greatly improved. Now the amount data taken is about 5 times the amount of data we used, so the statistical errors can be reduced by a factor 2 and eventually more parameters, such as the process fractions, can be simultaneously fitted. Moreover, in the newest data processes and software releases, problems such as the energy loss calibration and pull correction should be solved thus reducing part of the systematic errors. Nevertheless, a better understanding of the out-of-FV background is required.

The method presented in this chapter is one of the possible methods to measure the ν_μ flux. Another method is currently being developed, which consists also in maximizing a likelihood $\mathcal{L}(\vec{o}, \vec{b}, \vec{x}, \vec{n}, \vec{s})$ defined as

$$\mathcal{L}(\vec{o}, \vec{b}, \vec{x}, \vec{n}, \vec{s}) = \mathcal{L}_{beam}(\vec{b}) \times \mathcal{L}_{xsec}(\vec{x}) \times \mathcal{L}_{ND280}(\vec{b}, \vec{x}, \vec{n}) \times \mathcal{L}_{SK}(\vec{b}, \vec{x}, \vec{s}, \vec{o}) \qquad (6.20)$$

where $\vec{o}$ are the oscillation parameters, $\vec{b}$ the beam flux prediction parameters, $\vec{x}$ the cross-section inputs, $\vec{n}$ the ND280 systematics, and $\vec{s}$ the Super-Kamiokande systematics. This method allows the flux and cross-section parameters to be changed in a coherent way for the near detector ND280 and the far detector SK. Moreover, the individual likelihoods can be given

by a simple χ^2. For example, $\mathcal{L}_{ND280}$ can be written as

$$\mathcal{L}_{ND280} = \frac{1}{2}\sum_{ij}\left(N^i_{obs} - N^i_{exp}(\vec{b},\vec{x})\right) V^{-1}_{ij}\left(N^j_{obs} - N^j exp(\vec{b},\vec{x})\right) \tag{6.21}$$

where $V = V_{stat} + V_{syst1} + V_{syst2} + ...$ is the covariance matrix including both systematic and statistical components. If the covariance matrix is diagonal, then $\mathcal{L}_{ND280}$ can be simply written as a standard χ^2

$$\mathcal{L}_{ND280} = \frac{1}{2}\sum_{i}\left(\frac{N^i_{obs} - N^i_{exp}}{\sigma_i}\right)^2. \tag{6.22}$$

While our method relies on an energy binning, this method uses a two-dimensional binning in the muon candidate momentum and angle with respect to the incoming neutrino, with two categories of events: 1 CCQE enhanced sample and one background enhanced sample. This method is more suitable for an oscillation analysis, because it allows the partial cancellation of certain systematic errors between the ND280 and Super-Kamiokande, in particular the one related to the cross-sections. But for now, this method is still under study and a simple and robust method like the one we have shown in this chapter was needed to have a first look at the ν_μ energy spectrum and to search for the the eventual difficulties that such a measurement can face.

Chapter 7

Tracker absolute momentum scale calibration

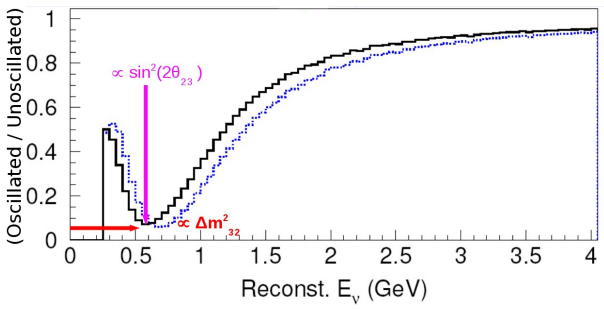

Figure 7.1: Ratio of the oscillated ν_μ spectrum to the unoscillated ν_μ spectrum for $\Delta m^{32} = 2.4 \times 10^{-3}$ eV^2 (dashed blue) and $\Delta m^{32} = 2.8 \times 10^{-3}$ eV^2 (black).

One of the objectives of T2K is measuring Δm^2_{23} with greater precision than ever before, thus it is necessary to understand and evaluate all possible sources of error. As we showed in section 3.1.3, this measure is directly correlated with the ν_μ energy and hence the μ momentum at which there is a maximal ν_μ disappearance rate (Fig.7.1). Therefore, one of the main sources of uncertainty on this measurement is the absolute momentum scale. A previous study showed that this scale had to be calibrated with a precision better than 2% so that the systematic error is smaller than the expected statistical error $5.10^{-5} eV^2$ for 5.10^{21} POTs. The energy scale of Super-Kamiokande must be also known at the same level of about 2 % (Fig.7.2).

The main reason for the momentum scale, and thus the neutrino energy scale, to be shifted is the magnetic field distortions. As equation 5.2, the momentum reconstruction is directly pro-

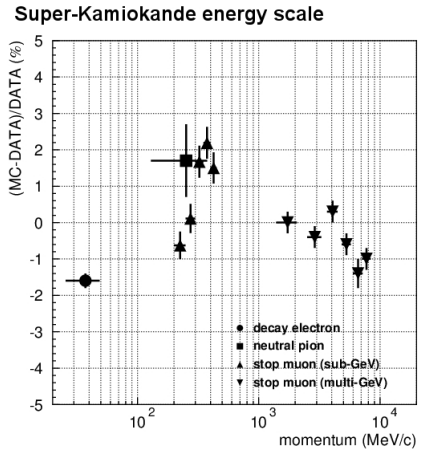

Figure 7.2: Absolute energy scale studies at Super-Kamiokande. The resulting MC/Data difference is shown for each sample, the error is taken to be the maximum deviation from zero: +2.19 % and -1.6 %.

portional to the magnetic field thus any distortion on the magnetic field would be translated into a momentum shift. Indeed, although the main component of the magnetic field B is parallel to the drift axis X, it also has some small transverse components which could bias the momentum reconstruction. To be able to correct these magnetic field distortions as much as possible, a careful mapping of the magnetic field was done and devices such as the TPC-laser calibration system allow the monitoring of such distortions.

In this chapter we will present one possible way to perform the absolute momentum scale calibration using the decay of neutral short kaons (K^0_s) into charged pions and study the feasibility of this method. For this, we will describe in section 7.1 the calibration method and the selection criteria. Since this analysis was done prior to the development of several of the tools described in the previous chapters (in particular the PID and global reconstruction algorithms), we will also describe the vertex reconstruction technique and the energy loss estimation method. In section 7.2, we will give the results of the K^0_s invariant mass reconstruction and possible background rejection cuts. We will then present two alternative calibration methods in section 7.3. Finally, we will conclude on the feasibility of the calibration with K^0_s method.

7.1 Momentum scale calibration principle

The calibration of the absolute muon momentum and thus of the neutrino energy scale relies in comparing the reconstructed mass or energy of a known object to the true expected value for such object. Different methods are possible, and we will explain other techniques than the one we chose in section 7.3. The choice we made is to reconstruct the invariant mass of the K^0_{short} (K^0_s) using the $K^0_s \rightarrow \pi^+\pi^-$ decay channel because of its simple topology. We will focus on the neutrino interactions that take place in the tracker only, and in particular in the FGDs.

In this section, we will first discuss the K^0_s production in T2K. Then we will explain the calibration principle and the selection criteria. Finally, we will describe the technical aspects of the method, such as the track extrapolation, vertex reconstruction, and energy loss estimation.

7.1.1 K^0 production

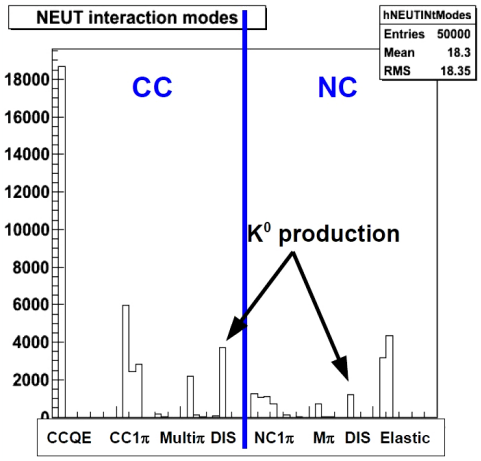

Figure 7.3: Generated number of events per interaction channel.

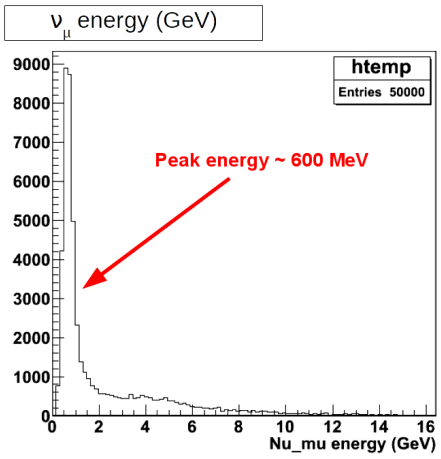

Figure 7.4: T2K ν_μ energy spectrum. The peak energy is about 600 MeV.

K^0_s are mainly produced in the ND280 dense detectors such as the P0D or the FGDs through the deep inelastic scattering channel $\nu_\mu + p/n \rightarrow \nu_\mu/\mu^- + mesons + (p,n)$ (Chap. 2). Because of the minimum neutrino energy threshold, only about 10 % of the total ν interactions are DIS events (Fig.7.3). Moreover, since the K^0 mass is 497.614 ± 0.024 MeV/c^2, the K^0_s can only be produced if the incident neutrino has an energy of at least 1 GeV. Given the T2K ν_μ energy spectrum, only the high energy tail neutrinos meet the requirement (Fig. 7.4) and

consequently, the expected number of K_s^0 is small.

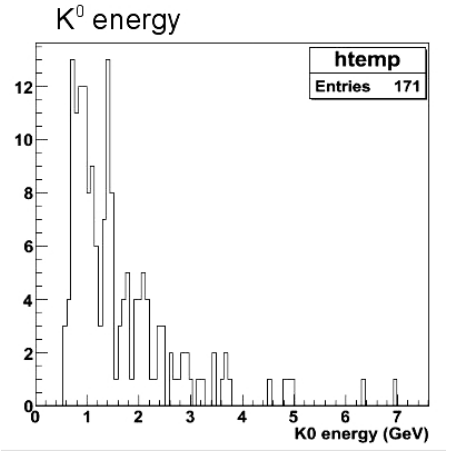

Figure 7.5: K_s^0 total energy spectrum for 50 000 neutrino interactions generated in the FGD1. The K_s^0 must be subtracted to obtain the K_s^0 kinetic energy.

At the time this analysis was done, no massive Monte Carlo sample had been produced yet thus I ran a quick MC simulation, based on the GENIE [131] neutrino generator, using the whole ND280 basket (the volume where all of the detectors except for the SMRDs are contained) as a target and the predicted neutrino flux at the near detector. This sample shows that out of 50 000 generated neutrino interactions – half of the neutrino interactions expected per year per ton of detector at nominal 750 kW beam power – only 171 K_s^0 are produced (Fig.7.5) i.e. 0.3 % of the generated events have a K_s^0 in their final state. This number does not take into account the eventual losses that might occur during the reconstruction and selection process, therefore the number of K_s^0 which can successfully be reconstructed after the full processing of the data is even smaller. The aim of the study presented in the following sections is to show that the required level of knowledge on the energy scale can be reached even with low statistics.

7.1.2 Calibration principle and selection criteria

K_s^0 decay mainly via two channels: $K_s^0 \rightarrow \pi^+\pi^-$ with a branching ratio $\Gamma_i/\Gamma = 69.20$ % and $K_s^0 \rightarrow \pi^0\pi^0$ with a branching ratio $\Gamma_i/\Gamma = 30.69$ %. Since the tracker is optimized to study charged particles, the only decay channel used for the calibration is the one with charged pions in its final state. Therefore, an error on the energy scale of the π^+ and π^- affects the

reconstructed K^0_s mass accordingly.

Given their average energy (Fig.7.5), the K^0_s mean free path in an FGD is typically a few centimeters ($\beta\gamma c\tau \sim 5$ cm) so they most likely decay within the same detector where they are produced. As a result, the outgoing charged pions energy loss in the subsequent detector must be taken into account. We will explain how this energy loss is computed in section 7.1.6.

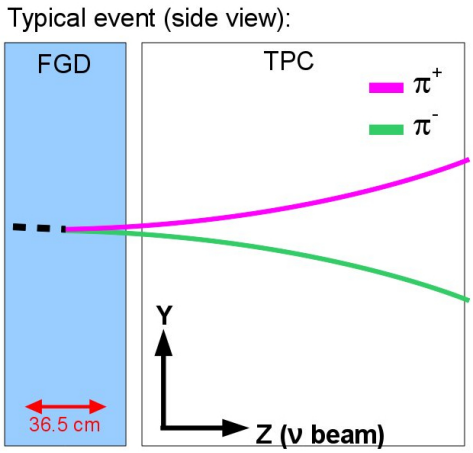

Figure 7.6: Simplified schematic view of a $K^0_s \to \pi^+\pi^-$ event.

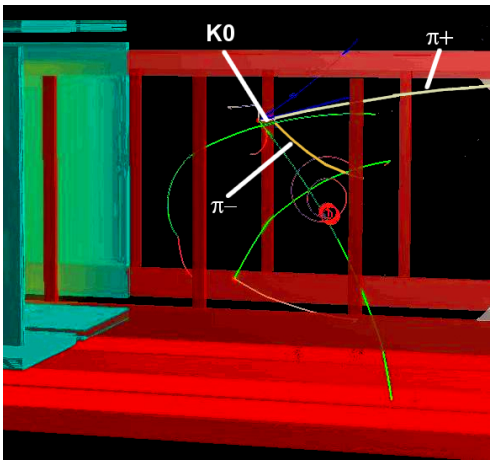

Figure 7.7: ν_μ DIS interaction event display with a $K^0_s \to \pi + \pi^-$. Only the generated true tracks are shown.

A typical K^0_s candidate event must therefore have at least two tracks with opposite curvatures. A simplified view of the typical candidate is shown in figure 7.6 while figure 7.7 shows a real neutrino interaction with a K^0_s in its final state. Since real DIS events have a complex topology, a first approach to the problem can be done with a mono-energetic K^0_s particle gun. For this, a sample of 10 000 K^0_s was generated in the FGD1 volume, with a kinetic energy of 500 MeV (expected K^0_s average energy is about 1 GeV, Fig.7.5). This amount of generated events is almost 30 times the number of expected K^0_s in a year at nominal power per ton of target material.

Once the charged pions tracks have been reconstructed, the K^0 mass is deduced from their momenta and angle at vertex as follows:

$$m^2_{K^0} = 2\left(m^2_\pi + \sqrt{m^4_\pi + m^2_\pi(p^2_+ + p^2_-) + p^2_+ p^2_-} - p_+ p_- \cos\theta\right) \tag{7.1}$$

where m_π is the charged pion mass, p_+ (resp. p_-) is the π^+ (resp. π^-) momentum at vertex, and θ the angle between the outgoing π^+ and π^- at vertex.

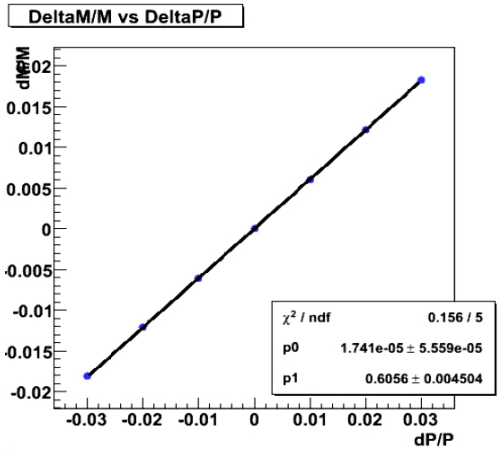

Figure 7.8: Relative variation of the K^0_s invariant mass as a function of a relative momentum variation.

To estimate the effect of a relative momentum variation on the reconstruction of the invariant mass, we manually shifted the true MC momenta and recomputed the K^0_s mass. Figure 7.8 shows that a relative variation on the momentum of $\Delta p/p = 2$ % is equivalent to a relative shift on the invariant mass of $\Delta m/m = 1.2$ %.

To summarize, the following criteria must be respected to select an event as a K^0 decay candidate:

- There must be at least two reconstructed tracks, and since the kaons have been generated exclusively in the FGD1, both tracks must be in TPC2 ;
- The tracks must have opposite sign curvatures and the curvature error σ must be smaller than 2×10^{-5} mm^{-1}. This cut is important to reduce the long tails on the measured momentum resolution, which strongly bias the reconstructed K^0_s mass (Sec.7.1.5) ;
- Both tracks are extrapolated to the nearest FGD (in our case FGD1) as it will be described in section 7.1.3, and the angle at vertex between the tracks is computed ;
- π^+ and π^- energy loss and momentum at vertex are computed ;

- the K^0 mass is reconstructed and compared to the expected value.

The PID tools were not fully functional at the time this analysis was done, therefore we did not use any cut based on PID information, which would have been very useful to reject photon conversion e^+/e^- pairs in particular.

7.1.3 Track extrapolation

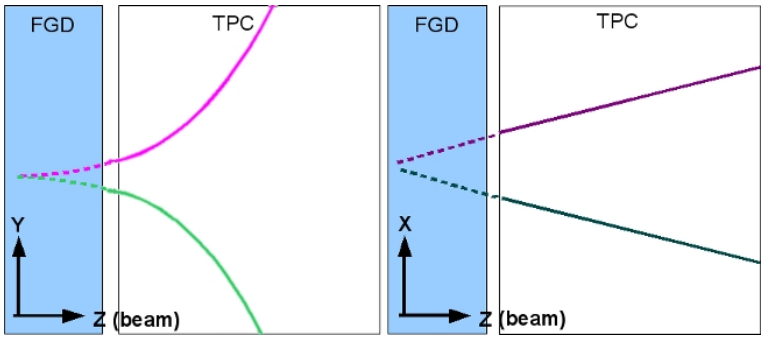

Figure 7.9: Schematic view of the TPC π^+ and π^- track extrapolation into the FGDs.

This analysis was done prior to the development of the global reconstruction algorithms, thus we used a simple method based only on the TPC reconstruction to compute the K^0 decay vertex position and to estimate the outgoing pions energy loss. Given the magnetic field orientation (parallel to the X axis), the helicoidal tracks are projected as an arc of a circle on the YZ plane and given the small curvature of the tracks, the projected sinusoid on the XZ plane can be approximated by a straight line (Fig. 7.9).

There are three different cases that need to be considered for the projection on the YZ plane:

- The extrapolated tracks do not cross: this happens generally when there is a wrong association of positive and negative curvatures. This type of event is rejected since it is not possible to compute the angle between the tracks at the vertex ;
- The extrapolated tracks have only 1 intersection point (tangent tracks). This type of event is also rejected, for the same reason as the previous case ;
- The extrapolated tracks have two intersection points.

Only the third case yields candidates for the calibration. In this case, four additional situations must be considered:

- Both points are out of the basket: the combination is rejected because the energy loss cannot be computed ;
- One point is in the basket, the other is outside. Only the point inside the basket is used to compute K^0_s mass ;
- Both points are in the basket but in different sub-detectors (i.e. one in P0D and one in FGD). The point which is closest to the first TPC track point is chosen ;
- Both points are in the same sub-detector volume. The vertex is given by the mean position of the two points.

7.1.4 Vertex and angle at vertex reconstruction

The intersection of the π^+ and π^- extrapolated tracks, described in the previous section, is taken as the reconstructed vertex position. The intersection of the π^+ and π^- projected arcs of circle on the Y-Z plane gives the Y and Z position, while the intersection of the π^+ and π^- projected straight lines on the X-Z planes gives the X and once again the Z position. While the X and Y vertex coordinates are uniquely defined by the preceding method, the Z coordinate can be obtained with both. After several tests, the Z computed by the circles intersection proved to be more accurate than the estimation using the straight lines.

Figure 7.10 shows the residual between the reconstructed vertex position and the generated true vertex position. The agreement for the X and Y coordinates is good, and there is no visible correlation between the residual and the position. The dispersion for the X and Y residuals is of the order of 1 cm, which is the FGD granularity. Nevertheless the Z residual has a long tail, showing that the reconstructed value is overestimated, and seems to be correlated to the true Z position of the vertex in the FGD (no correlation once out of the FGD) but the dispersion due to this correlation remains of the order of a few centimeters, which is consistent with the FGD granularity. This correlation is due to the approximation made when assuming that the track curvature is constant in the FGDs, although it should vary since the pions lose a non-negligible amount of energy in the FGDs.

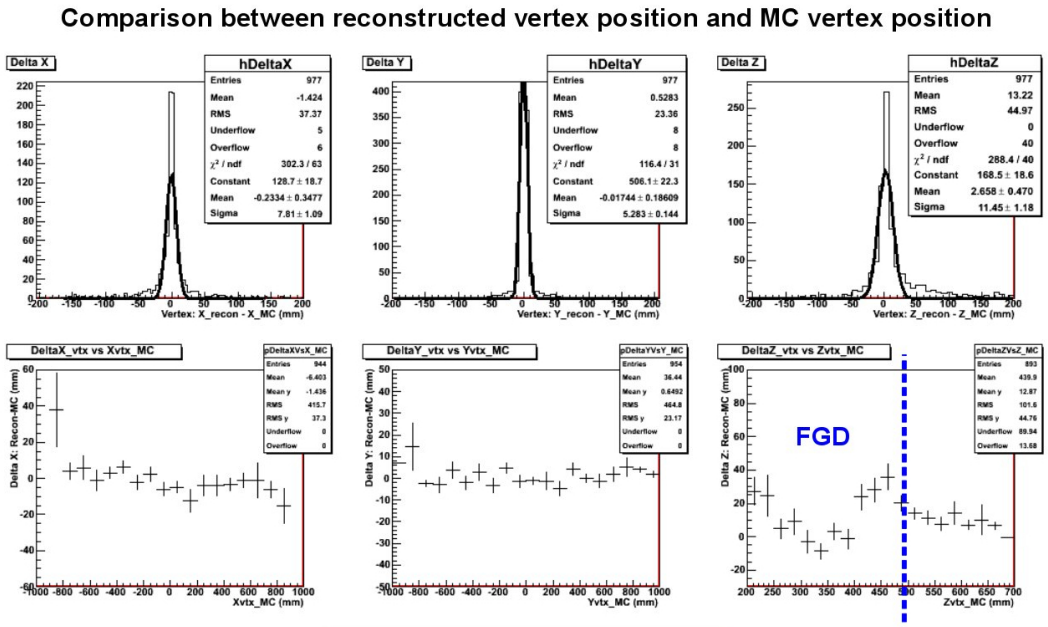

Figure 7.10: Top row: Distributions of the residuals (reconstructed - true) on the vertex reconstructed X (left), Y (middle), and Z (right) coordinates. Bottom row: Mean residual versus the true vertex position for the X (left), Y (middle), and Z (right) coordinates. The dashed blue line shows the downstream FGD1 edge (Z wise).

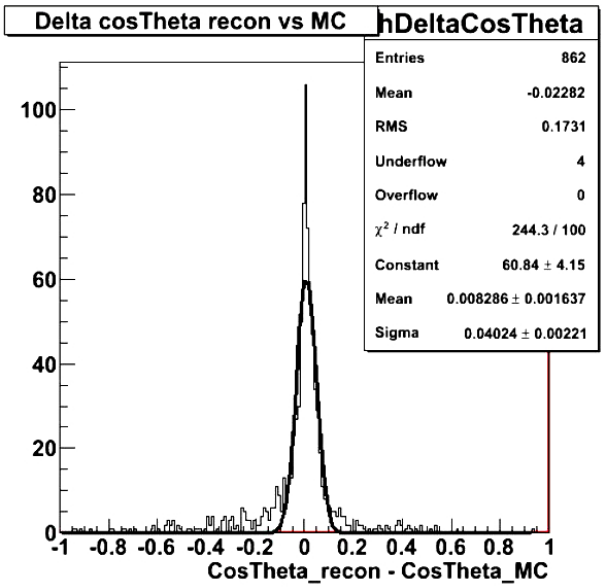

Figure 7.11: Residual between the reconstructed angle at vertex and the true angle at vertex.

Once the vertex has been determined, the angle between the pion tracks can be computed, using the tangents to the tracks at the vertex. The residual of the reconstructed angle to the true angle is shown in figure 7.11. There is a good agreement between the true and the reconstructed angles but the distribution has long tails on both sides.

7.1.5 TPC Momentum reconstruction

Since the reconstruction of the mass depends on the pion momentum reconstruction and the angle between the pion tracks at the vertex, it is important that each of these elements is properly computed. In particular, the pion momentum at vertex is computed by adding to the measured momentum of the pions in the TPCs a correction to account for the energy loss in the FGD, which will be presented in the next section.

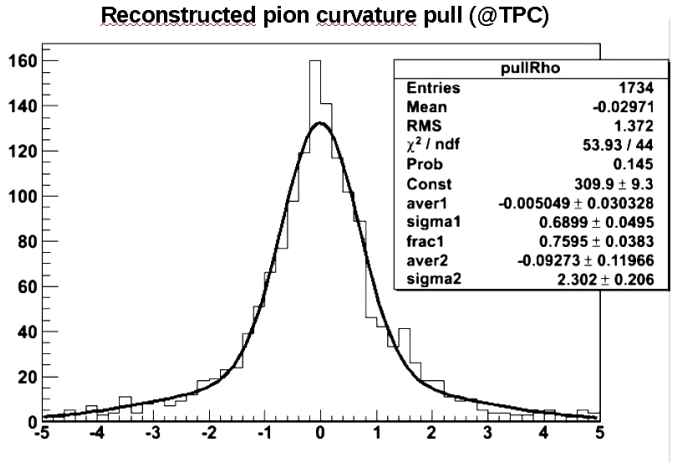

Figure 7.12: Pull of the pion track curvature measured by the TPCs, fitted by a double Gaussian.

In this section we will focus on the measurement of the pion momentum in the TPCs. As explained in section 5.1.1, the physical quantity directly measured by the TPCs is the curvature ρ, which is proportional to the inverse momentum. Figure 7.12 shows the pull distribution of the measured curvature to the true curvature. The distribution, which should be a Gaussian centered at 0 with a sigma of 1, presents in reality very long tails and must be fitted by a double Gaussian. These tails, which introduce a bias in the momentum reconstruction, correspond to tracks with a large curvature error. Therefore, we introduce a cut on the curvature error: $\sigma_\rho < 2.10^{-5}$ mm^{-1}.

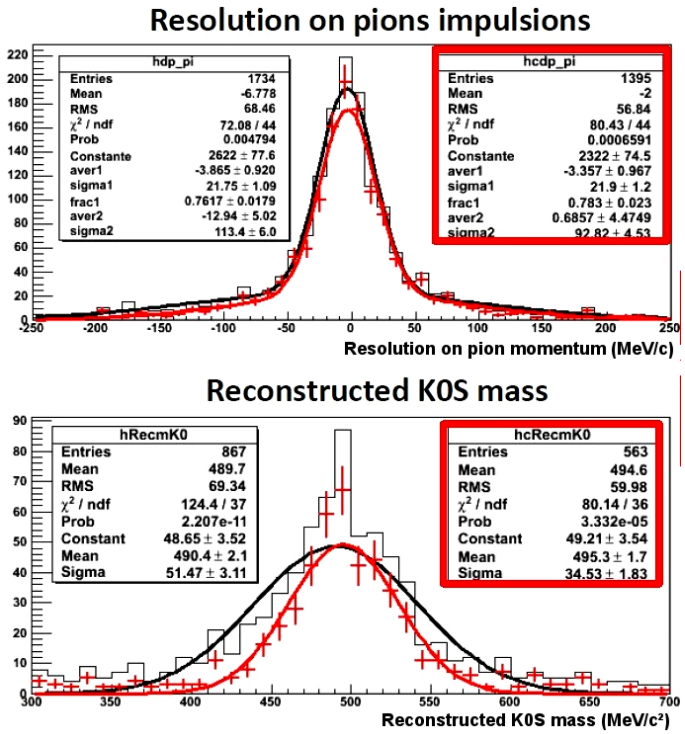

Figure 7.13: Top: Resolution of the reconstructed pion momentum in the TPCs before the curvature error cut (black) and after the cut (red). Bottom: reconstructed K^0 mass without the curvature error cut (black) and with the cut (red).

Figure 7.13 shows the effect of the curvature error cut on the reconstructed momentum and on the reconstructed mass. The relative efficiency of this cut is 80.5 % for the pion, which results in an 64.9 % efficiency for the kaons since two pions are required. Although we lose a few events, the bias on the reconstructed momentum is reduced by about 15 MeV and the reconstructed mass is closer by about 5 MeV to the expected K^0_s mass.

7.1.6 Energy loss correction

The energy loss ΔE is computed with a simple approach, considering that the energy loss per length unit is constant, as follows

$$\Delta E = \rho_{FGD} \times L_{FGD} \times \Delta E/\Delta x + \Delta E_{wall} \tag{7.2}$$

where $\rho_{FGD} = 1.06$ g.cm^{-3} is the average density of the FGD1 (which is made of scintillator bars only), L_{FGD} is the distance traveled by the pion in the FGD active volume, $\Delta E/\Delta x = 1.9$ MeV.g^{-1}.cm^2 is the average energy loss per cm for pions in carbon, and $\Delta E_{wall} = 2$ MeV is the estimated energy lost when a charged particle crosses the FGD and TPC walls.

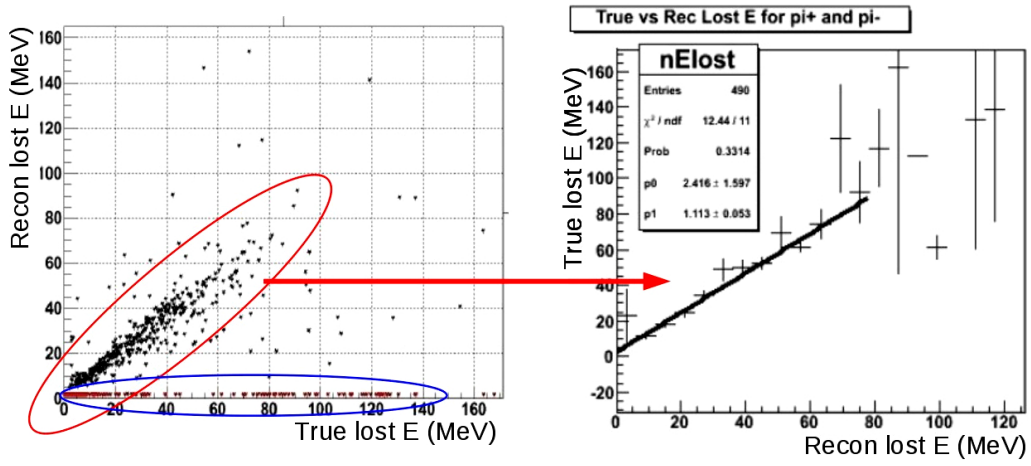

Figure 7.14: Reconstructed energy loss as a function of the MC true energy loss (left). Average true energy loss as a function of the reconstructed energy loss (right).

Figure 7.14 shows the reconstructed energy loss as a function the true energy loss. The plot can be divided into two parts. The first part, circled in blue on the left-handed plot, shows vertices whose energy loss is constant and equal to the energy lost when the charged particles

cross the FGD and TPC walls. These points have been wrongly reconstructed in the small gap between the FGD and TPC instead of within the FGD active volume. The second part, circled in red on the left-handed plot, shows the vertices which have been properly reconstructed within the FGD active volume. The right-handed plot shows that the reconstructed energy loss is in good agreement with the true energy loss when the vertex has been properly reconstructed, although the reconstructed energy loss seems to be slightly underestimated by a few MeV with respect to the true energy loss. This disagreement is most likely due to a small underestimation of the energy lost when crossing the detector walls.

The estimated energy loss is then applied as a correction to the momentum measured in the TPCs to obtain the momentum of the pions at the K^0_s decay vertex.

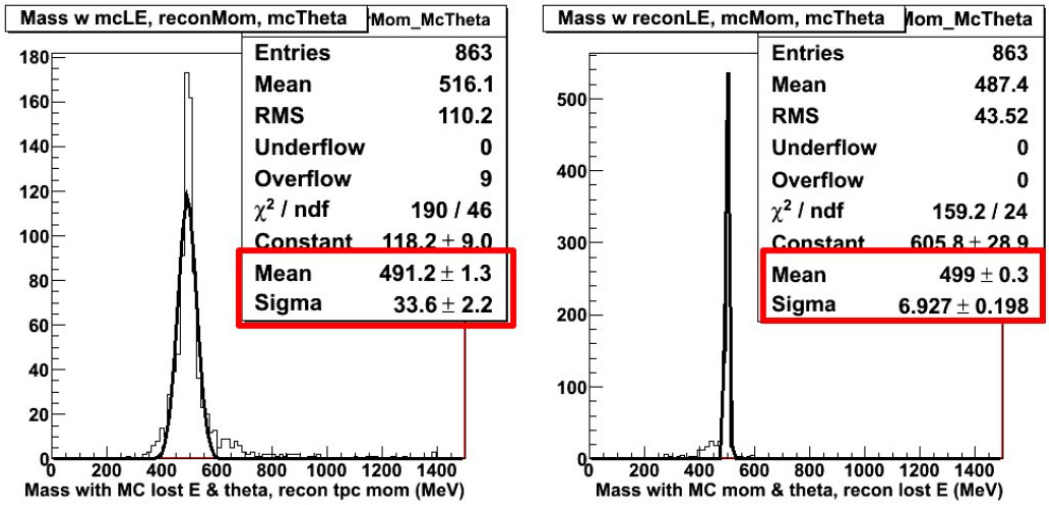

Figure 7.15: Reconstructed K^0 mass with the TPC reconstructed momentum and the true energy loss and true angle and momentum (left), and with the reconstructed energy loss and the true TPC momentum and angle at vertex (right).

To understand the impact on the final results of each reconstructed parameter, i.e. the π momenta in TPC, the π energy loss in the FGD, and the (π^+, π^-) angle, we can compute the invariant mass of the system using only one reconstructed value: the reconstructed energy loss or the reconstructed TPC momentum. Figure 7.15 shows the reconstructed K^0_s mass when using either the TPC reconstructed momentum and the true energy loss and true angle and momentum (left) or the reconstructed energy loss and the true TPC momentum and angle at

vertex (right). We can see that both the resolution and the bias on the central value of the K_s^0 invariant mass are mainly limited by the TPC momentum reconstruction itself, therefore we will consider that our energy loss and angle reconstruction is good enough for our analysis. Nevertheless, the long tails observed on the reconstructed angle distribution and energy loss (directly related to the tails observed on the reconstructed vertex position), do bias the central value of the computed K_s^0 mass but to a lesser extent than the reconstructed momentum tails.

7.2 K_s^0 invariant mass

Once all the required parameters haven been properly reconstructed, we can finally computed the invariant mass of the $\pi^+\pi^-$ system and compare it to the expected $K^0 = 497.6$ MeV/c^2 mass, and check if we fulfill the requirements on the momentum scale knowledge. We will first present the results of our analysis. Then we will give the main sources of error in our measurement and finally we will discuss the different backgrounds that will need to be rejected when doing a full analysis with real neutrino events.

7.2.1 Results

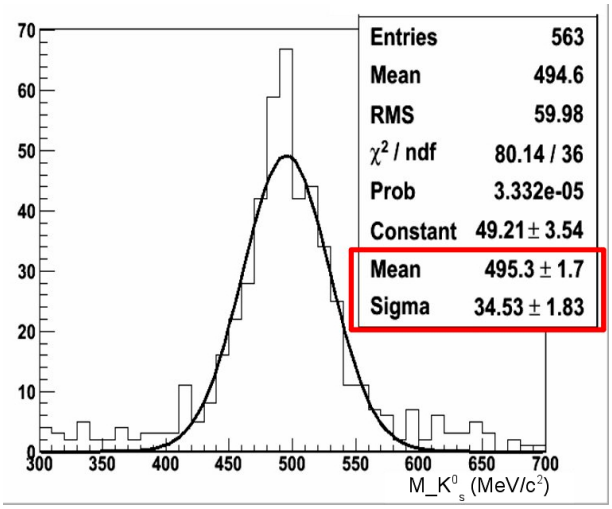

Figure 7.16: Reconstructed K^0 mass.

After applying all the reconstruction algorithms and selection criteria, we select 563 candidate events out of 10 000 generated events with the K_s^0 particle gun. The reconstructed invariant mass of the $\pi^+\pi^-$ system is 495.3 ± 1.7 MeV/c^2 (statistical error only), which is

consistent with the expected K^0 mass. This is equivalent to $\Delta m/m = 0.34$ %.

Nevertheless, this result was obtained with a pure K_s^0 sample, with higher statistics than the one expected for a year of data taking at nominal power (about 340 K_s^0 for 100 000 neutrino interactions per ton, for 10^{21} POTs at 750 kW beam power). If we extrapolate our results to the expected number of events with a simple $\sqrt{N}$ law, we obtain that for 340 K_s^0, the invariant mass is $M_{K_s^0} 495.3 \pm 9.2$ MeV/c^2 so $\Delta m/m = 1.85$ %.

Since each FGD weights about 1 ton each, we expect to have twice as many K_s^0 thus the error on the invariant mass can be divided by $\sqrt{2}$ leading to a $\Delta m/m$ of 1.3 %, which is slightly higher than the 1.2 % required to fulfill the 2 % level on the absolute momentum scale. Therefore, with improved reconstruction algorithms and additional cuts on the quality of the reconstructed angle and on the energy loss – to remove the long tails on their respective distributions, which cannot be neglected once the cut on the reconstructed momentum error has been applied –the calibration of the tracker with this method is feasible.

7.2.2 Backgrounds

Until now we studied the ideal case of a pure K_s^0 sample. As shown on figure 7.7, true neutrino events with a K_s^0 in the final state are much more complex, since they present a complicated topology with a large amount of tracks. Since the DIS events are rare, the backgrounds are abundant and must be well understood. Although we did not have enough time to study these backgrounds, we will introduce two cuts that can be very effective against them.

One of the main sources of contamination expected for this analysis is the photon conversion into an electron-positron pair. These photons can come from the decay of a neutral pions, which are produced at a much higher rate than neutral kaons. As proved in chapter 5, PID cuts are highly efficient to discriminate electrons from muons and pions.

A standard cut used by many experiments to select K_s^0 events is a cut on the kaon flight distance or on K_s^0 flight / $\sigma(K_s^0$ flight). Indeed, the K_s^0 travels a distance of a few centimeters before decaying, therefore by cutting on the distance between the primary neutrino interaction vertex and the K_s^0 decay vertex, it is possible to reject a large amount of background coming from the decay of longer lifetime particles and also from wrongly associated positive-negative

track pairs. Nevertheless, to properly apply this cut, all vertices (primary and secondary) must be reconstructed with a precision better than the centimeter. Currently there is work being done on the reconstruction of both primary and secondary vertices but the results are not yet available for our studies.

7.3 Calibration alternatives

The calibration of the momentum scale can be done with other methods than the one presented in this chapter. In this section we will briefly present one different method to do the absolute momentum scale calibration, based on the $\pi^0 \rightarrow \gamma\gamma$ decay, and one method for a relative momentum scale calibration, based on the intersections points of the energy loss curves as a function of momentum.

7.3.1 π^0 decay with double photon conversion

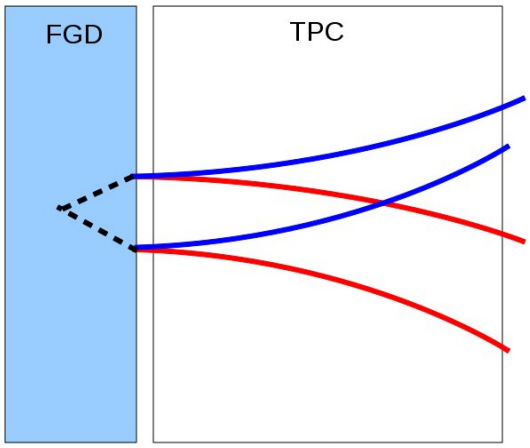

Figure 7.17: Schematic view of a $\pi^0 \rightarrow \gamma\gamma$ decay with double photon conversion. The dashed lines are the photons, the red lines are the electrons, and the blue lines are the positrons.

One alternative method to do the absolute momentum scale calibration of the tracker is to use the $\pi^0 \rightarrow \gamma\gamma$ decay, followed by a double photon conversion into electron-positron pairs. A simplified schematic view of such an event is given on figure 7.17. An advantage of this method is the abundant π^0 production in the FGDs and P0D, either through charged current or neutral current neutrino interactions, as opposed to the scarce K^0_s production. The principle is the

same as the K^0_s study, i.e. the two e^+e- pairs allow the reconstruction of the photon energies and with both photons reconstructed, the invariant mass of the system can be computed and compared to the expected π^0 mass. The disadvantage of this method is that it requires more tracks to be successfully reconstructed and matched together, and that it also needs an energy loss correction for the photons that convert in the FGDs. This additional conversion stage can be problematic since it adds an additional reconstruction step which might introduce additional systematics. Also, this method is most accurate when both photons convert, implying the reconstruction of four tracks instead of two. Nevertheless, most of the time only one photon converts into an e^+e^- pair, thus the second photon must be accurately reconstructed by the electromagnetic calorimeter. Once again, this might introduce a new systematic since it would imply the use of a completely different detector.

7.3.2 Energy loss intersection

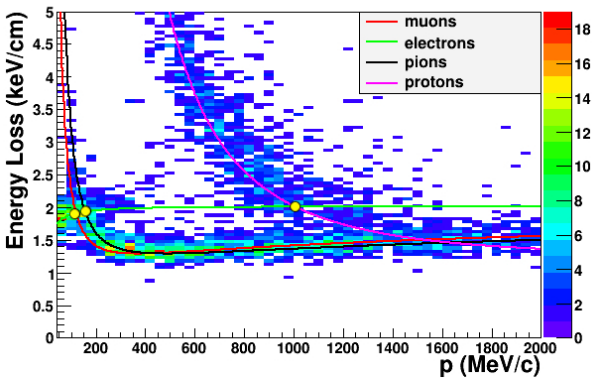

Figure 7.18: Energy loss as a function of momentum for positively charged particles. The yellow dots show the 3 intersection points that can be used for the relative momentum scale calibration.

Since the absolute momentum scale calibration requires a significant amount of statistics to be done, it is possible to do a relative momentum calibration of the tracker with a smaller amount of data. This could be useful to compare different run periods for example. The principle relies on the reconstruction of the energy loss curves intersections. The three intersection points can be seen on figure 7.18: electron-muon, electron-pion and electron-proton. By measuring the position of such points, one can measure the drift over time of the momentum scale. This method is independent of the overall calibration and of the systematic errors. Studies show that this method can be used until it is possible to do an absolute calibration.

7.4 Conclusion

The aim of the analysis presented in this chapter was to prove the feasibility of the tracker absolute momentum scale calibration by reconstructing the invariant mass of the K^0. When this analysis was done, no vertexing tools had been developed yet and the ND280 reconstruction algorithms were not yet as efficient as they are now. This partially explains why so few events reached the final step of the selection although the sample used was 100 % pure in K^0 and thus we should have had about two thirds of the generated amount as candidates since the $K^0 \rightarrow \pi^+\pi^-$ branching ratio is 69.20 %. The long tails on the resolution of the reconstructed momentum and the low reconstruction efficiency have been greatly improved in the latest software releases. Also, many potential candidates were lost when extrapolating the TPC tracks into the FGDs. Now, with the higher level algorithms which have proved to work efficiently as demonstrated in the previous chapters, a higher amount of events should reach the final stage of the selection and increase the selection efficiency. The global reconstruction tools should also allow a better reconstruction of both the primary and secondary vertices, and a better estimation of the energy loss since the information of all the ND280 detectors is used.

Despite the technical problems and the low efficiency we had at the time the study was performed, this calibration method has proved to be feasible, but requires further studying and testing with the newest software tools. The expected backgrounds are very large and extracting the K^0_s signal could prove to be challenging, therefore an in-depth study of the backgrounds must be done.

Chapter 8

Conclusion

T2K's objectives are to measure for the first time the θ_{13} angle through the search of ν_e appearance in a ν_μ beam and to measure with great precision the atmospheric neutrino oscillation parameters through the study of ν_μ disappearance. We have shown that both of these oscillation analyses require to understand well the ν_μ flux, either at low energy to measure the oscillation parameters themselves in the ν_μ disappearance channel or at high energy to constrain as much as possible the expected backgrounds in the ν_e appearance channel. It is from this perspective that I attempted a first neutrino muon flux measurement at the ND280, based on an inclusive charged current interaction sample, and the calibration of the near detector tracker absolute momentum scale. As far as the hardware is concerned, I actively participated in the Micromegas modules tests done prior to their installation in the TPCs and on the first period of data taking by spending over a month in Japan, as a shifter and as a TPC detector expert trainee.

The main part of my thesis work was to do a first ν_μ flux measurement at the near detector. Indeed, the published T2K oscillation analyses have only used the beam Monte Carlo predictions for the shape of the neutrino energy spectrum. We did not seek to realize a precise measurement of the ν_μ flux but rather to prove that the measurement could be done with a simple and robust technique, adapted to the study of the first T2K data. Several reconstruction tools were developed within the T2K collaboration during my thesis, thus the analysis I made for the flux measurement, in particular the selection process, was also very useful to validate and cross-check the performance of the newly developed high level reconstruction algorithms. Moreover, our analysis was necessary to explore and localize the different difficulties

that would need to be solved to do a precise measurement.

The first stage of the ν_μ flux measurement was choosing the most adequate sample to perform the measurement. Using a charged current quasi-elastic sample would have been the most appropriate choice for this measurement since it is the only case where the neutrino energy can be accurately reconstructed. Nevertheless, given the small statistics of the first T2K data sample, we chose to do the measurement with an inclusive charged current sample to have more statistics but also to keep the selection at a simple and robust level. This CC-inclusive sample was also used as a control sample for validating the Monte Carlo simulations, by comparing the MC to the real data, and for testing the global reconstruction algorithms by comparing our selection to another analysis which used simpler reconstruction methods.

The next stage was the flux measurement itself. For this, we used a K2K-alike method, based on a likelihood fit to compare the expected number of events for a given measured neutrino energy to the observed ones. The part that proved to be most difficult was how to deal with the low statistics. Because of this, we used an irregular energy binning, we regrouped certain neutrino interaction channels together to keep only four main interaction categories, and we had to find the right balance between using as much information as possible by dividing our sample into four event topologies and regrouping these topologies for computing the transfer matrices elements. Actually, finding the proper way to compute these transfer matrices and how to model the selection efficiencies was one of the most challenging parts of the analysis.

The results of the flux measurement on the first T2K data sample showed that the average fit worked fine and that the measured flux as a function of the neutrino energy was consistent with the prediction, once the systematics errors had been taken into account. Nevertheless, the fit with the events split into four topologies requires further investigation to understand the apparent event migration between topologies. As we explained, these migrations could be directly related to the theoretical framework used to model the final state interactions. From the systematics point of view, the main contributions were the cross-section uncertainties and the out of the fiducial volume contribution. A better understanding of the neutrino cross-sections is required to do a more precise flux measurement. With a more sophisticated selection, it is possible to reduce the out of FV contamination, but this would also require higher statistics.

And finally, to understand the final state interactions systematics, an in-depth study is needed.

During the first year of my thesis I worked on the calibration of the absolute momentum scale of the near detector tracker. The calibration was based on the reconstruction of the invariant mass of the K^0_s using the $K^0_s \rightarrow \pi^+\pi^-$ decay channel. At the time this analysis was done, most of the reconstruction tools were not yet very efficient, thus part of the work done for this analysis consisted in developing tools such as simple vertexing algorithms or energy loss estimations. We studied a pure sample of K^0_s as a first approach to test the method. By extrapolating our results to the number of K^0_s expected in a nominal year for both FGDs, we found that $\Delta m/m = 1.3$ %, which is slightly above the required 1.2 % uncertainty on the mass to reach a knowledge on the absolute momentum scale at the level of 2 %. Therefore, the calibration proved to be feasible but required more sophisticated tools. Nevertheless, the expected backgrounds for this measurement are important, so extracting the K^0_s signal could prove to be difficult.

The analyses presented in this thesis were only the first step towards more refined studies. There is room for improvements in both analyses. Many upgrades have been done on the software, in particular our main issues related to the PID pull correction and vertex reconstruction have been mostly dealt with. Also the data sample that can be used is much larger than the one we used, so the statistical errors on the ν_μ flux measurement would be reduced, and eventually more parameters such as the different interaction processes fractions could be fitted.

T2K recently observed the first indications of a $\nu_\mu \rightarrow \nu_e$ oscillation in the 1.43×10^{20} POT data sample accumulated since early 2010[108]. Six events passed all the selection cuts at the far detector Super-Kamiokande. If we consider a three-flavor neutrino oscillation scenario with $|\Delta m^2_{32} = 2.4 \times 10^{-3}$ eV^2, $\sin^2 2\theta_{23} = 1$ and $\sin^2 2\theta_{13} = 0$, then expected number of events would have been 1.5$\pm$0.3 (syst.). Under these hypotheses, the observed number of ν_e candidates have an equivalent significance of 2.5 σ. The allowed regions for $\sin^2 2\theta_{13}$ are shown on figure 8.1. Now that these first candidates have been found, it's more important than ever to do the calibration and the flux measurement to reduce as much as possible the errors and increase the significance of T2K oscillation results.

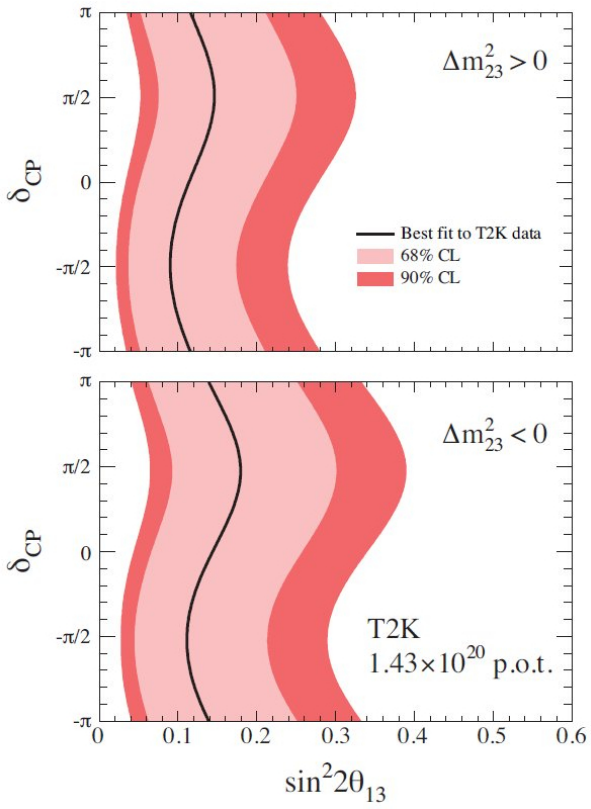

Figure 8.1: The 68 % and 90 % C.L. regions for $sin^2 2\theta_{13}$ for each value of δ_{CP}, consistent with the observed number of events in the three-flavor oscillation case for normal (top) and inverted (bottom) mass hierarchy. The other oscillation parameters are fixed. The best fit values are shown with solid lines.[108]

References

[1] A. SLOSAR U. SELJAK AND P. MCDONALD. *JCAP*, **0610**(014), 2006. 3, 12, 22

[2] J. LESGOURGUES AND S. PASTOR. *Phys. Rept.*, **429**(307), 2006. 3, 12, 22

[3] W. PAULI. *Physics Today*, **31**(27, translation in English), 1978. 4

[4] E. FERMI. *Z. Phys.*, **88**(161), 1934. 4

[5] J. CHADWICK. *Proc. R. Soc. London (A)*, **136**(692), 1932. 4

[6] E. MAJORANA. *Nuov. Cim.*, **5**:171–184, 1937. 4

[7] C.L. COWAN AND F. REINES ET AL. *Science*, **124**(103), 1956. 5

[8] G. DANBY ET AL. *Phys. Rev. Lett.*, **9**(36), 1962. 5

[9] K. KODAMA ET AL. [DONUT COLLABORATION]. *Phys. Lett. B*, **504**(218), 2001. 5

[10] S.L. GLASHOW. *Nucl. Phys.*, **22**(579), 1961. 5

[11] S. WEINBERG. *Phys. Rev. Lett.*, **19**(1264), 1967. 5

[12] A. SALAM. **Weak and Electromagnetic Interactions**. *Elementary Particle Theory, Proc. 8th Nobel Symp.*, **367**, 1968. 5

[13] D. DECAMO ET AL. [ALEPH-DELPHI-L3-OPAL]. *Phys. Lett. B*, **276**(247), 1991. 5, 19

[14] R.J. DAVIS ET AL. *Phys. Rev. Lett.*, **20**(1205), 1968. 6

[15] B. PONTECORVO. *Zh. Eksp. Teor. Fiz.*, **34**(247), 1958. 7

[16] V. GRIBOV AND B. PONTECORVO. *Phys. Lett. B*, **28**(493), 1969. 7

[17] N. NAKAGAWA Z. MAKI AND S. SAKATA. *Prog. Theor. Phys.*, **28**(870), 1962. 7, 14

[18] W. HAMPEL ET AL. [GALLEX COLLABORATION]. *Phys. Lett. B*, **420**:114–126, 1998. 7

[19] J.N. ABDURASHITOV ET AL. *Astropart. Phys.*, **25**:349–354, 2006. 7

REFERENCES

[20] M. ALTMANN ET AL. [GNO COLLABORATION]. *Phys. Lett. B*, **616**(174), 2005. 7

[21] K.S. HIRATA ET AL. [KAMIOKANDE-II COLLABORATION]. *Phys. Rev. Lett.*, **63**(16), 1989. 7

[22] S. FUKUDA ET AL. [SUPERKAMIOKANDE COLLABORATION]. *Phys. Rev. Lett.*, **86**(5651), 2001. 7, 74

[23] Q.R. AHMAD ET AL. [SNO COLLABORATION]. *Phys. Rev. Lett.*, **87**(071301), 2001. 7

[24] K. EGUCHI ET AL. [KAMLAND COLLABORATION]. *Phys. Rev. Lett.*, **90**(021802), 2003. 8

[25] R. BECKER-SZENDY ET AL.[IMB COLLABORATION]. *Phys. Rev. D*, **46**(3720), 1992. 9

[26] Y. FUKUDA ET AL. *Phys. Rev. Lett.*, **81**(8), 1998. 9

[27] E. ALIU ET AL. [K2K COLLABORATION]. *Phys. Rev. Lett.*, **94**(081802), 2005. 9, 27, 75

[28] M. GULER ET AL. [OPERA COLLABORATION]. Technical Report CERN-SPSC-2000-028. LNGS-2000-25. SPSC-P-318, CERN, 2000. 9, 28

[29] H. LIPKIN. *Phys. Lett.*, **B579**(355), 2004. 11, 13

[30] L. STODOLSKY. *Phys. Rev. D*, **58**(036006), 1998. 11, 13

[31] B. KAYSER. *Phys. Rev. D*, **24**(110), 1981. 11, 13

[32] N. CABIBBO. *Phys. Rev. Lett.*, **10**(531), 1963. 14

[33] M. KOBAYASHI AND T. MASKAWA. *Prog. Th. Phys.*, **49**(652), 1973. 14

[34] L. WOLFENSTEIN. *Phys. Rev. D*, **17**(2369), 1978. 16

[35] S.P. MYKHEYEV AND A.YU. SMIRNOV. *Sov. J. Nucl. Phys.*, **42**(913), 1985. 16

[36] J. BOUCHEZ. *Cours de la* $24^{ème}$ *école d'été de Gif*, pages 92–231. 1992. 18

[37] JN. BAHCALL AND C. PE NA GARAY. *New J. Phys.*, **6**(63), 2004. 18

[38] R.N. MOHAPATRA AND G. SENJANOVIC. *Phys. Rev. Lett.*, **44**(912), 1980. 21

[39] R. ARNOLD ET AL. *Nucl.Phys. A*, **765**:483–494, 2006. 22

[40] H.V. KLAPDOR-KLEINGROTHAUS ET AL. *Eur. Phys. J.*, **A12**:147–154, 2001. 22

[41] C. ARNABOLDI ET AL. [CUORICINO]. *Phys. Rev. C*, **78**(035502), 2008. 22

[42] I. ABT ET AL. *arXiv:hep-ex/0404039v1*, 2004. 22

[43] M. DANILOV ET AL. *Phys. Lett. B*, **480**:12–18, 2000. 22

[44] CH. WEINHEIMER ET AL. *Phys. Lett. B*, **460**:219–226, 1999. 22

[45] V.M. LOBASHEV ET AL. *Phys. Lett. B*, **460**:227–235, 1999. 22

[46] K. ASSAMAGAN ET AL. *Phys. Rev. D*, **53**(6065), 1996. 23

[47] R. BARATE ET AL. [ALEPH COLLABORATION]. *Eur. Phys. J.*, **C2**:395–406, 1998. 23

[48] KATRIN COLLABORATION. **LOI**. *arXiv:hep-ex/0109033v1*, 2001. 23

[49] PARTICLE DATA GROUP. **Review of Particle Physics**. *Journal of Physics G*, **37**(7A), 2010. 23, 37, 228

[50] A.D. SAKHAROV. *Pisma Zh. Eksp. Teor. Fiz.*, **5**(32), 1967. 24

[51] F.R. KLINKHAMER AND N.S. MANTON. *Phys. Rev. D*, **30**:2212–2220, 1984. 24

[52] E. NARDI S. DAVIDSON AND Y. NIR. *Phys. Rep.*, **466**(105), 2008. 25

[53] S. ABE ET AL.[KAMLAND COLLABORATION]. *Phys. Rev. Lett.*, **100**(22), 2008. 26, 227

[54] D.G. MICHAEL ET AL. [MINOS COLLABORATION]. *Phys. Rev. Lett.*, **97**(19), 2006. 27, 227

[55] P. ADAMSON ET AL. [MINOS COLLABORATION]. *Phys. Rev. Lett.*, **97**(191801), 2006. 28

[56] N.AGAFONOVA ET AL. [OPERA COLLABORATION]. *Phys. Lett. B*, **691**:138–145, 2010. 28, 29, 228

[57] M. APOLLONIO ET AL. [CHOOZ COLLABORATION]. *The European Physical Journal C - Particles and Fields*, **27**:331–374, 2003. 28, 29, 55, 228

[58] MINOS COLLABORATION. *arXiv:1006.0996v1 [hep-ex]*, 2010. 30

[59] MINOS COLLABORATION. *http://www.fnal.gov/pub/presspass/press_releases/minos-electron-neutrinos-20110624.html*, 2011. *http://theory.fnal.gov/jetp/talks/MINOSNue_2011June24.pdf*. 30

[60] F. ARDELLIER ET AL. [DOUBLE CHOOZ COLLABORATION]. *arXiv:hep-ex/0606025*, 2006. 30

[61] T2K COLLABORATION. **Letter of intent**. *http://neutrino.kek.jp/jhfnu/loi/loi.v2.030528.pdf*. 30, 51

[62] DAYA BAY COLLABORATION. *http://dayawane.ihep.ac.cn/docs/experiment.html*. 30

[63] J.K. AHN ET AL. [RENO COLLABORATION]. *arXiv:hep-ex/1003.1391*, 2010. 30

[64] S. PALOMARES-RUIZ O. MENA-REQUEJO AND S. PASCOLI. *Phys. Rev. D*, **72**:053002, 2005. 33

[65] LAGUNA COLLABORATION. **The Laguna project**. *http://www.laguna-science.eu/*. 33

[66] O. BENHAR. *Acta Phys. Pol B*, **40**:2389, 2009. 35, 37

[67] E.J. MONIZ R.A. SMITH. *Nucl. Phys. B*, **43**:605, 1972. Erratum: **B101**, 547 (1975). 36

[68] Y. HAYATO. *Nucl. Phys. Proc. Suppl.*, **112**(171), 2002. NuInt01. 36, 105

[69] S. ZELLER. *3rd NO-VE International Workshop on Neutrino Oscillations in Venice*, 2006. 37, 228

[70] E.J. MONIZ ET AL. *Phys. Rev. Lett.*, **26**:445–448, 1971. 39, 148

[71] C.H. LLEWELYN-SMITH. *Phys. Rep. C*, **3**:261, 1972. 39

[72] J. UDÍAS J.A. CABALLERO J.L. HERRAIZ, M.C. MARTÍNEZ. *Acta Phys. Pol B*, **40**:2405, 2009. 39

[73] R. BRADFORD A. BODEK, S. AVVAKUMOV AND H.S. BUDD. *J. Phys. Conf. Ser.*, **110**(082004), 2008. 39

[74] S. BARISH ET AL. *Phys. Rev. D*, **16**(3103), 1977. 39

[75] S. BONETTI ET AL. *Nuovo Cim.*, **38**(260), 1977. 39

[76] M. POHL ET AL. *Nuovo Cim.*, **26**(332), 1979. 39

[77] N. ARIMENISE ET AL. *Nucl. Phys. B*, **152**(365), 1979. 39

[78] A.S. VOVENKO ET AL. *Yad. Fiz.*, **30**(1014), 1979. 39

[79] S. BELIKOV ET AL. *Z. Phys.*, **320**(625), 1985. 39

[80] J. BRUNNER ET AL. *Z. Phys. C*, **45**(551), 1990. 39

[81] R. GRAN ET AL. [K2K COLLABORATION]. *Phys. Rev. D*, **74**(052002), 2006. 40

[82] X. ESPINAL AND F. SANCHEZ. *AIP Conf. Proc.*, **967**(117), 2007. 40

[83] M. DORMAN ET AL. [MINOS COLLABORATION]. *AIP Conf. Proc.*, **1189**(133), 2009. 40

[84] A.A. AGUILAR-AREVALO ET AL. [MINIBOONE COLLABORATION]. *Phys. Rev. D*, **81**(092005), 2010. 40, 41, 228

[85] V. LYUBUSHKIN ET AL. [NOMAD COLLABORATION]. *Eur.Phys.J. C*, **63**:355–381, 2009. 41

[86] PATRICK DE PERIO AND T2K NEUTRINO INTERACTION WORKING GROUP. *Private communication*, 2011. 41, 45, 154

[87] S. DYTMAN. *Acta Phys. Pol B*, **40**:2445, 2009. 42

[88] D. REIN AND L.M. SEHGAL. *Annals Phys.*, **133**(79), 1981. 42

[89] A.A. AGUILAR-AREVALO ET AL. [MINIBOONE COLLABORATION]. *Phys. Rev. Lett.*, **103**(081801), 2009. 43

[90] D. CASPER. *Nucl. Phys. Proc. Suppl.*, **112**(161), 2002. 43

[91] A. RODRIGUEZ ET AL. [K2K COLLABORATION]. *Phys. Rev. D*, **78**(032003), 2008. 43

[92] G.M. RADECKY ET AL. *Phys. Rev. D*, **25**(1161), 1982. 43

[93] R.H. NELSON. PhD thesis, Fermilab, 2010-09. 44

[94] M. HASEGAWA ET AL. [K2K COLLABORATION]. *Phys. Rev. Lett.*, **95**(252301), 2005. 45

[95] K. HIRAIDE ET AL. [SCIBOONE COLLABORATION]. *Phys. Rev. D*, **78**(112004), 2008. 45

[96] M. TZANOV. **Review of Neutrino Deep Inelastic Scattering Results**. *AIP Conference Proceedings*, **1222**:243–247, 2010. 47

[97] E. REYA M. GLUCK AND A. VOGT. *Eur. Phys. J. C*, **5**(461), 1998. 47

[98] A. BODEK AND U.K. YANG. 2003. arXiv:hep-ex/0308007. 47

[99] K. ABE ET AL. *Phys. Rev. Lett.*, **56**(1107), 1986. 49

[100] C.H. ALBRIGHT ET AL. *Phys. Rev. D*, **14**(1780), 1976. 49

[101] J-P. VIALLE P. MUSSET. *Phys. Rep. C*, **39**(1), 1978. 49

[102] J.E. KIM ET AL. *Rev. Mod. Phys.*, **53**(211), 1981. 49

[103] S.L. GLASHOW. *Nucl. Phys.*, **22**:579, 1961. 49

[104] A. SALAM AND J. WARD. *Phys. Lett.*, **13**:168, 1964. 49

[105] S. WEINBERG. *Phys. Rev. Lett.*, **19**:1264, 1967. 49

[106] KEK-REPORT 2002-13 AND JAERI-TECH 2003-044. **J-PARC Technical Design Report**. *http://hadron.kek.jp/∼accelerator/TDA/tdr2003/index2.html*, 2003. 52, 62

[107] Y. FUKUDA ET AL. *Nucl. Instrum. Meth.*, **A501**(418), 2003. 52, 75

[108] T2K COLLABORATION. **Indication of electron neutrino appearance from an accelerator-produced off-axis muon neutrino beam**. *arXiv:1106.2822v1 [hep-ex]*, 2011. 54, 78, 123, 142, 217, 218, 238

[109] K. MATSUOKA ET AL. *Nucl. Instrum. Meth. A*, **623**:385–387, 2010. 64

[110] K. MATSUOKA ET AL. *Nucl. Instrum. Meth. A*, **624**:591–600, 2010. 64

[111] P. RUBINOV L. BELLANTONI. **Bench test of first Trip-T prototypes**. *D0 Note*, **4845**, 2005. 69

[112] P.A. ČERENKOV. **Visible emission of clean liquids by action of γ radiation**. *Doklady Akademii Nauk SSSR*, **2**(451), 1934. 76

[113] T2K COLLABORATION. **The T2K experiment**. *arXiv:1106.1238v2 [physics.ins-det]*, 2011. 78

[114] F. BLASZCZYK. **T2K near detector tracker**. *Proceedings of Science*, **ICHEP 2010**(484). 78

[115] F. RETIÈRE ET AL. *Nucl. Instrum. Meth. A*, **610**:378–380, 2009. 80

[116] N. ABGRALL ET AL. *Nucl. Instrum. Meth. A*, **637**:25–46, 2011. 82

[117] I. GIOMATARIS ET AL. *Nucl. Instrum. Meth. A*, **560**:405–408, 2006. 88

[118] S. ANVAR ET AL. *Nucl. Instrum. Meth. A*, **602**:415–420, 2009. 90

[119] J. BOUCHEZ ET AL. *Nucl. Instrum. Meth. A*, **574**:425, 2007. 90, 101

[120] S. ANVAR ET AL. *Nucl. Instrum. Meth. A*, **602**:415–520, 2009. 90

[121] C. GIGANTI. *Particle Identification in the T2K TPCs and study of the electron neutrino component in the T2K neutrino beam*. PhD thesis, Université Paris Sud 11, 2010. 94, 113

[122] S. AGOSTINELLI ET AL. *Nucl. Instrum. Meth. A*, **506**:250–303, 2003. 98

[123] F. RADEMAKERS R. BRUN. *Nucl. Instrum. Meth. A*, **389**:81–86, 1997. 98

[124] P. POFFENBERGER D. KARLEN AND G. ROSENBAUM. *Nucl. Instrum. Meth. A*, **555**:80, 2005. 101

[125] R.L. GLUCKSTERN. *Nucl. Instrum. Meth.*, **24**:381, 1963. 102

[126] J.A. HERNANDO A. CERVERA-VILLANUEVA, J.J. GOMEZ-CADENAS. **RecPack, a general reconstruction toolkit**. *Nuclear Science Symposium Conference Record*, **3**, 2003 IEEE. 104

[127] COMPUTING APPLICATION SOFTWARE GROUP AND GENEVA NETWORKS DIVISION, CERN. **GEANT3, a detector description and simulation tool**. 1993. 105

[128] **FLUKA version 2008.3c**. *http://www.fluka.org/fluka.php*, 2008. 105, 145

[129] N. ABGRALL ET AL. **Report from the NA61/SHINE experiment at the CERN SPS**. *Technical Report CERN-SPSC-2010-025*, **SPSC-SR-066**, 2010. 105, 145

[130] N. ABGRALL ET AL. **Measurements of cross sections and charged pion spectra in proton-carbon interactions at 31 GeV/c**. *Preprint: CERN-PH-EP-2011-005*, 2011. 105, 145

[131] C. ANDREOPOULOS ET AL. *Nucl. Instrum. Meth. A*, **614**:87–104, 2010. 105, 188, 200

[132] E. MAZZUCATO. **Private communication**. 109

[133] C. GIGANTI M. IEVA F. SÁNCHEZ J. CARAVACA RODRÍGUEZ, R. CASTILLO. **Charge misidentification in local and global reconstruction in the 2010a data**. *T2K technical note (internal)*, 2011. 109

[134] M. IEVA L. MONFREGOLA M. RAVONEL F. SÁNCHEZ P. STAMOULIS G. WIKSTROM A. CERVERA, F. DUFOUR. **Inclusive neutrino muon CC analysis using the entire ND280 detector**. *T2K technical note (internal)*, **v1**, 2010. 110

[135] F. SÁNCHEZ. **Study of neurrent interactions in the ND280 tracker**. *T2K technical note (internal)*, **v1**, 2010. 123

[136] A. LONGHIN M. ZITO C. GIGANTI, F. BLASZCZYK. **Study of neutrino charged current interactions in the ND280 tracker**. *T2K technical note (internal)*, **v1**, 2010. 123

[137] T2K COLLABORATION. 2011. 123

[138] P. DE PERIO C. GIGANTI B. JAMIESON D. KARLEN S. OSER F. SÁNCHEZ C. BOJECHKO, J. CARAVACA RODRÍGUEZ. **Extending the run 1 ν_μ CC analysis in the ND280 tracker with a high-momentum bin**. *T2K technical note (internal)*, 2011. 144

[139] T2K BEAM GROUP. **Neutrino flux uncertainty for 10a data analysis**. *T2K technical note (internal)*, 2011. 145

[140] T2K BEAM GROUP. **Beam update for 2010a nue analysis using Run I+II**. *T2K technical note (internal)*, 2011. 145

[141] V. GALYMOV. **Predicting the neutrino flux at T2K**. *Talk at NuFact'11, Geneva*, 2011. 146

[142] K2K COLLABORATION. *Phys. Rev. D*, **74**(072003), 2006. section VII. 146

List of Figures

List of Tables

Acknowledgements

Well, I might start by saying I am not very good at writing this kind of text. Nevertheless, there are many people I would like to thank for being there and supporting me all along my career, not only during my Ph.D. but also before. Without them, I would probably not have made it this far.

First of all, I owe a big thanks to all of my family, in particular my parents, Rosa and Gérard, and my little brother Gal. I want to thank you for always being there when I needed you the most, be it in the good or the bad situations.

Then I must thank all of the Saclay T2K group, Marco, Olivier, Eddy, Jerôme and Andrea (who are no longer part of the group but who helped me understand many things), François (who unfortunately is not with us anymore), Alain, Denis, Claudio, Michael, Chiraz, and in particular Sandrine, my advisor, and Georges. Sandrine and Georges, thank you for being so patient with me, always answering my questions and supporting me all along. Although we faced a few difficulties, I really enjoyed working with you and I did learn many things that will be very useful from now on. I would like to thank Jacques as well, without whom I would not have got my "bourse de thèse". I enjoyed being part of the T2K collaboration so I hope we will be able to work together again in the future.

I would like to thank all of my committee members, Thomas, Hiro, Marcos, Gérard, and Cristina for reading my thesis and being there the day of the defense. In particular, I would like to thank Hiro, who came from far away for just a couple of days, for all of his constructive comments.

Finally, I thank everyone who was there in the past, Chang Kee for always giving me good advice, Patrick for answering all of my questions on the cross-sections and helping me to compile NEUT on a 64-bit machine, Costas and Jim for helping me with GENIE, Federico for teaching me so many things. Of course, I do not forget all of my friends, specially Laurine and Marion, who were always there to listen me whine. The list is long and could go on for pages so I will stop here, hoping no one will get upset I did not mention them.

Thank you very much everyone!